N° d'ordre : UEB/UR1 **ANNÉE 2015**

**THÈSE / UNIVERSITÉ DE RENNES 1**
*sous le sceau de l'Université Européenne de Bretagne*

pour le grade de

**DOCTEUR DE L'UNIVERSITÉ DE RENNES 1**

*Mention : Physique*

**Ecole doctorale (Science de la Matière)**

présentée par


# Ramona Mhanna

Préparée à l'unité de recherche UMR 6251, IPR
et à l'Institut Laue-Langevin, ILL
Institut de Physique de Rennes
UFR Sciences et Propriétés de la Matière


---

# Confinement-induced nano-segregation of binary liquids with amphiphilic interactions

**Soutenance prévue à Rennes le 29 octobre 2015**

devant le jury composé de :

**Natalie MALIKOVA**
Chargée de Recherche CNRS, Univ. Paris 6 / *rapportrice*

**Patrick JUDEINSTEIN**
Directeur de Recherche CNRS, CEA Saclay / *rapporteur*

**Marianne IMPEROR-CLERC**
Directrice de Recherche CNRS, Univ. Paris-sud / *examinatrice*

**Renaud DENOYEL**
Directeur de Recherche CNRS, Univ. d'Aix-Marseille / *examinateur*

**Ronan LEFORT**
Maître de Conférences, Univ. Rennes 1 / *examinateur*

**Denis MORINEAU**
Directeur de Recherche CNRS, Univ. Rennes 1 / *directeur de thèse*

**Bernhard FRICK**
Chercheur, Institut Laue-Langevin, Grenoble / co-*directeur de thèse*

# *ACKNOWLEDGEMENTS:*

I did my PhD in co-direction between the Institute of Physics of Rennes (IPR) (nanosciences and materials department) and the Institute of Laue Langevin. My utmost thanks and sincere gratitude go to my thesis directors (Dr. Denis MORINEAU and Dr. Bernhard FRICK) and my co-director (Dr. Ronan LEFORT) whose continued support and encouragement made this project possible.

Denis, know that your words of wisdom and advice have always been received with highest degrees of respect. Your support, confidence and commitment to this project were instrumental to its successful completion. A wise saying that I have recently heard is: “don’t pick a job, pick a boss, as your first boss is the biggest factor in your career success. A boss who doesn’t trust you won’t give you opportunities to grow. ” I couldn’t have picked more wisely, you are my role model and you have inspired me in so many ways both at the personal and scientific levels and for that I’ll be forever grateful. I extend my thanks and gratitude to Bernhard who has shown me that there is no limit to aspiration. It was a great honor and a privilege to work with you and I’ll always be looking up to you when I think of dedication to science. I genuinely appreciate your honesty, persistence and fruitful scientific discussions which have been invaluable for the thesis. My sincere gratitude also goes to Ronan who has played a great role in this thesis and enormously attributed to its success. I am greatly thankful for your assistance, advice and support and I am quite happy that I had the opportunity to work with someone with such scientific and human qualities.

I would also like to express my gratitude towards all the jury members (Renaud DENOYEL “jury president”, Marianne IMPEROR-CLERC, Patrick JUDEINSTEIN and Natalie MALIKOVA for accepting to be a part of this long process. In your own ways, you have each added to this project and helped shape me both as a student and a researcher.

Much gratitude goes to the management of the IPR (Jean-Pierre LANDESMAN) and the ILL (Helmut SCHOBER) for welcoming me in their institutes. My appreciation extends to all the IPR and ILL staff for making me feel like home over the last three years. A particular thanks goes to the members of the nanosciences department and the administrative service at the IPR as well as the student body at the ILL.

A very special thought goes to my friends in France (in particular Rennes and Grenoble) and Lebanon for being there for me. I have a special place in my heart for all of you, thank you for

being my big family. In addition, I would like to thank some teachers or rather mentors who inspired me to become who I am today. A huge thanks goes to you Dr. Daoud, Dr. Fares, Dr. Hala, Miss Nyola, Miss Abir, Mr. Majid, Miss Sumer and Mr. Hamad.

Last but not least, I want to dedicate this thesis to my father (my hero, my supporter, my everything), my loving mother, my sisters, my brothers, my sister in law and my extended family who have always supported me. I am so lucky to have you. Your faith in me, your unconditional love and my eagerness to make you proud served as a driving force in my work.

This project has been, without any doubt, the largest test of my own commitment, spanning three years away from my family and loved ones. But I have not achieved this alone. Along the way, I have received so much support from too many people to count. I definitely wouldn't have done it if some of you weren't in my life. Thank you for all the gracious sacrifices you have made for me while I realized this goal. Though you may not see your names here, know that your various contributions have not gone unnoticed or unappreciated.

**TABLE OF CONTENTS:**

# CHAPTER I:

# SCIENTIFIC CASE

# Chapter I: Scientific Case

## I.A. Introduction

The study of the novel properties of matter at the nanoscale has led to an intensive research activity over multiple scientific disciplines giving rise to the term renowned as nanosciences. In the same aspect, the reduction of the volume accessible to molecular fluids via confinement in pore widths equivalent to a few molecular diameters has proven capable of the drastic modification of their static and dynamical properties compared to the bulk counterparts.

Nanoconfinement has retained a constant attention during the last decades both for a fundamental-scientific and industrial-technological interest. The manipulation of fluids in nanochannels and their behavior at the nanoscale plays an intrinsic role in many phenomena offering opportunities in many applications such as: oil recovery, catalysis, separation processes, sensors, biotechnology and nanofabrication.[1] Moreover, confinement has also been reported important for many applications in lubrication, adhesion and drug delivery.[2] However, despite the large interest and multiple approaches, no thorough understanding of the behavior of nanoconfined systems has been achieved yet. Hence, with the little scientific background on this topic, the design and control of such processes remains largely empirical. This brings the scientific community to reconsider a set of problems in condensed matter regarding the topic of confinement.

Recent studies have supplied prevailing evidence that the properties under spatial confinement shouldn't be accounted in terms of the bulk analogs. It has been shown that the change in the thermodynamic balance between enthalpy and the system's disorder induces structural frustration and surface phenomena leading to the radical alteration of the liquid's spatial correlations and dynamics.[3, 4] Thus, restricted geometries have been reported to have remarkable consequences on first-order phase transition behavior (melting, freezing, solid-solid) leading to either a plain temperature shift, a change in the nature of the transition or the complete introduction-disappearance of phases.[5, 6] It has also been reported to modify the fluid dynamics in terms of structural relaxation and glassy behavior. [7-9] Furthermore, confinement-induced structural modification has also been described in the literature. Recent studies have shown that nanoconfinement caused changes in density and heat capacity (which are static

properties) [9] as well as the formation of interfacial macroclusters and new self-assembled phases in nanoassociating mixtures.[10-13]

Two main perspectives were approached in the attempt of understanding the influence of nanoconfinement on the behavior of molecular condensates. The first is based on the surface effect through the introduction of a wall interface leading to a competition between liquid-wall and liquid-liquid forces. The nature of these interactions and their balance is a critical element for the development of new surface-driven phases under confinement.[14, 15]

The other perspective is the so-called finite size effect. It emphasizes that restricted geometries imply "cut-off" effects on the growth of any correlation or cooperativity lengths which is bounded by the pore size. This is a topic of unsettled debate as this simple view gets more complicated by additional parameters such as surface effects, low-dimensionality and disorder [16, 17] in addition to experimental artifacts. Moreover, when confined within a pore with a typical size of a few molecular diameters, both static and dynamical properties can be strongly altered. A possibility not accounted for in many studies.

To put our project in this context, we present below the current state of knowledge on topics related to our work. The detailed advancements in the research field of nanoconfinement have been reported elsewhere.[5, 6, 18, 19] In this contribution, it is not my intention to achieve a comprehensive review but rather address a selection of examples on confinement studies with a particular emphasis on the structural and dynamical aspects of the confined molecular phases.

I will initially address confinement effects on phase transitions (melting-freezing), dynamics (glass transition, relaxation times) and structure (density, self-assemblies). The confinement-induced physical phenomena will then be interpreted in terms of surface and finite size effects which will be thoroughly discussed. I will then proceed to highlight some studies on binary mixtures under confinement. Light will be particularly shed on some recent studies that demonstrate pieces of evidence on microphase separation of binary mixtures under confinement either at the proximity of the bulk phase separation or, more interestingly, in fully miscible systems. The inspiring studies in this aspect will facilitate the introduction of the aim of the study and the detailed structure of the thesis will finally be concluded.

# I.B. Confinement Effects

## I.B.1. Effect on Phase Transitions

### I.B.1.1. Melting /Crystallization in Confinement:

In the recent decades, confinement effects on the liquid-solid phase transitions have been intensively studied.[5, 18, 20, 21] Experimental as well as theoretical approaches have indicated that the confinement of liquids in small pores has enormous impact on their first-order thermodynamic properties and phase transitions.[22]

Remarkable decrease of the melting temperatures have been witnessed over a broad range of confined organic compounds.[23] These pioneering studies have been measured by DSC in silica pores (Controlled Pore Glasses GPC) of variable sizes [23, 24] and showed that the melting temperature in the pores is reduced with diminishing pore size (Fig. I-1). In most studies the melting temperature variation (ΔTm) is negative and in a direct proportionality with the inverse of the pore diameter. A behavior which is in agreement with model predictions based on macroscopic thermodynamic considerations.

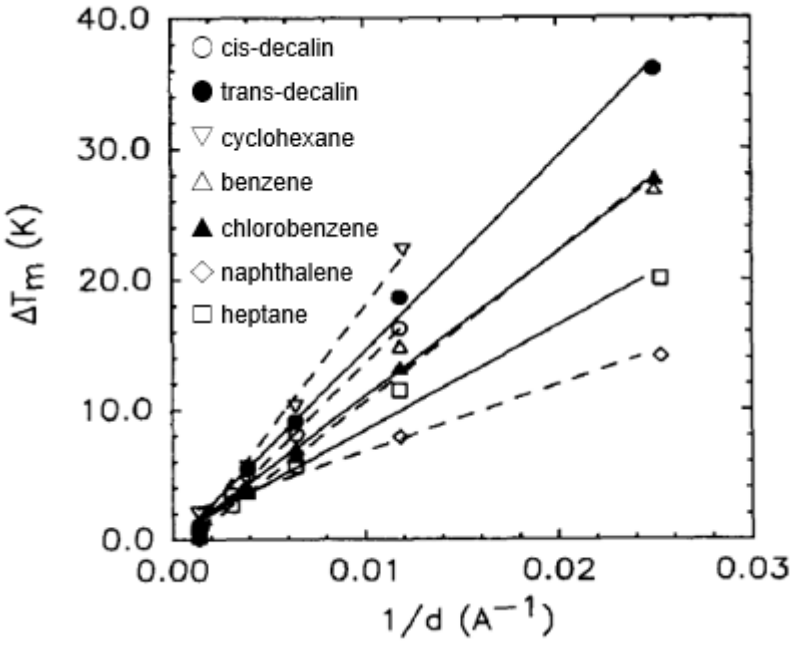


Figure I-1: Experimental values of ΔTm for different molecules as a function of the inverse pore diameter. The lines through the data are linear regression fits used to calculate the values of $\sigma_{sl}$. [23]

The Gibbs-Thomson formalism is the simplest method used to interpret the melting point depression (ΔTm) under confinement where $\Delta Tm = T_{confined} - T_{bulk}$. This model predicts that ΔTm is given by equation (I-1):

$$\Delta T_m = \frac{4\sigma_{sl} T_m}{d\Delta H_f \rho_s} \quad \text{(I-1)}$$

Where $\sigma_{sl}$ is the energy of the solid-liquid interface, Tm is the bulk melting temperature, d is the pore diameter, $\Delta H_f$ is the enthalpy of fusion of the bulk liquid and $\rho_s$ is the solid density.

Even though the Gibbs-Thomson formalism succeeds to reproduce and interpret the results of many studies in the literature,[5, 18, 20] it fails to explain certain cases where the melting temperature was shifted to higher values. The limitation of this approach is its founding on macroscopic aspects that can't be valid at the molecular scale and its non-explicit consideration of the interaction between the confined phase and the porous matrix. A subsequent introduction of a parameter α which accounts for the ratio of the matrix/fluid and fluid/fluid interactions was able to explain the increase in the melting temperature under confinement in terms of strong surface interactions.[25]

Moreover, changes in ΔTm seem to obey the formalism for pores equivalent to at least 20 times the Van der Waals diameter.[26] A remarkable deviation from this prediction is however observed, for the smaller sizes between 10-20 times the molecular diameter. For instance, for small pores, the distinction between the interface and bulk-like phases is not possible anymore and surface effects span over the entire volume of the confined system. This has been illustrated in the neutron diffraction studies on confined benzene in MCM-41 and SBA-15 (Fig. I-2).[27]

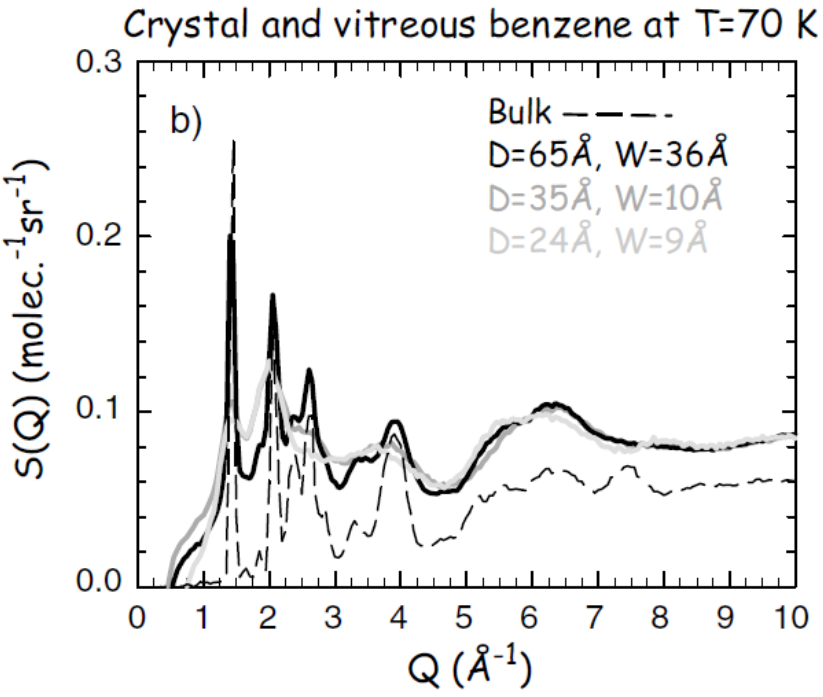


Figure I-2: S(Q) of benzene at 70 K (dashed line) and confined in various matrices of diameter D (solid lines) [27]

The Neutron Structure Factor S(Q) for the confined liquid at 70K permits the discrimination between crystalline and amorphous phases upon tuning the pore diameter by moving from MCM-41 to the larger pore-sized SBA-15.

In sufficiently large pores (D= 6.5nm), the stable bulk crystallization is reproduced in the confined benzene with a slight peak broadening due to defects and finite-size effects. As the pore size diminishes (D= 3.3nm), a highly defective structure appears leading to an amorphous solid for the smallest pore size (D= 2.4nm). In this region the structure of the confined phases generally remains amorphous (even at very low temperatures) and crystallization in that range is either partially or totally suppressed.[16, 27] This phenomenon also correlates with the glassy dynamics observed upon the cooling of the confined liquid, with an apparent signature of a dynamical arrest at lower temperatures**.**

Thus, the suppression of crystallization in nanopores and the formation of amorphous structures upon decreasing temperatures grants a rare opportunity to extend the liquid state's stability range and allows the observation of a new transition: the glass transition. Moreover, this phenomenon has raised many questions regarding the relaxation processes in confined geometries and their potential link to the dynamics of deeply super-cooled liquids.

### I.B.2.Effect on Dynamics

#### I.B.2.1. Concept of Glass Transition

As mentioned in the previous section, cooling a liquid below its melting point does not necessarily lead to crystallization. The system could rather persist in a metastable equilibrium state, becoming a super-cooled liquid. Upon further cooling, the viscosity and structural relaxation time (α) can vary over 14 orders of magnitude. The super-cooled state will eventually cease to exist reaching a state which deviates from equilibrium; *i.e*., the glassy state.

The glassy state is characterized by a relaxation time that significantly exceeds the characteristic time of the experiment. The glass transition is not thermodynamic in nature, but rather kinetic; therefore, it noticeably depends on the conditions of handling, especially the cooling rate which is demonstrated in Fig. I-3 (A) where the cooling of the liquid either led to crystallization or to two glassy states (a) and (b) with the cooling rate of (b) being faster than that of (a).[28]

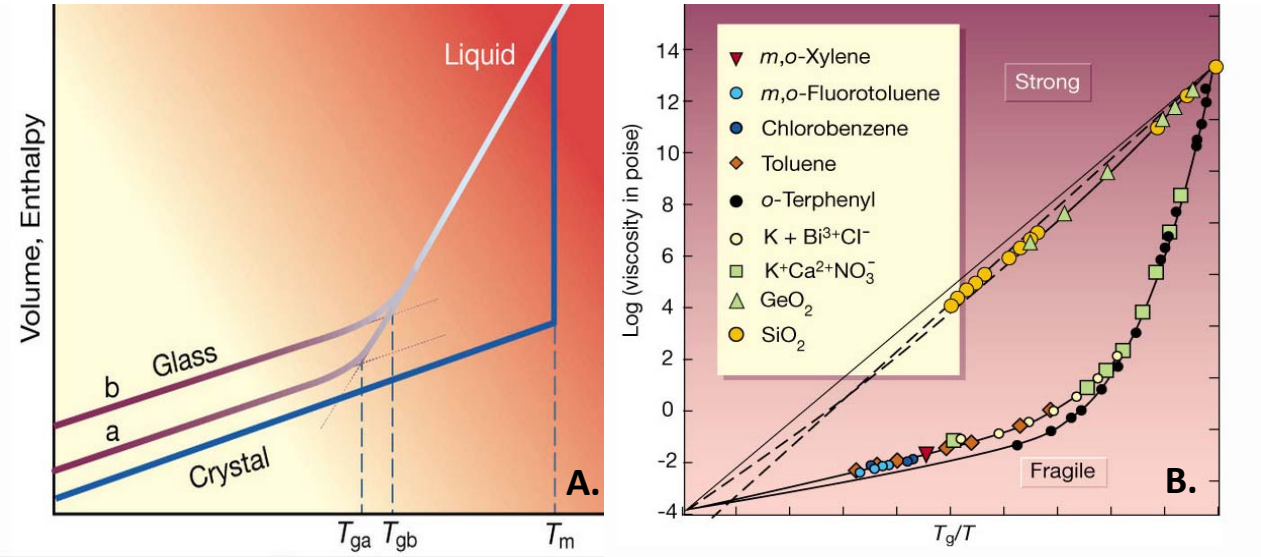


Figure I-3: The change in volume or enthalpy versus temperature; (B): the evolution of the viscosity as a function of Tg / T, Angell diagram (right). [28]

Glass-forming materials can be classified according to the change of their viscosity (or relaxation time) with Tg/T into two main categories: "Strong" liquids following an Arrhenius behavior and "Fragile liquids". The latter comprise many organic systems and are characterized by deviations from simple Arrhenius and Debye laws to a "super-Arrhenius" behavior,[29] *i.e.*, they witness an escalation in the activation energy of their main relaxation time around the glass transition temperature which is represented by the Angell diagram in Fig. I-3 (B).[28]

Super-cooled liquids hold a remarkable property having the decay of their structural relaxation function distinct from the simple form of the Debye-type (exponential). This decay is rather expressed in terms of the stretched-exponential (Kohlrausch) relaxation function.[29-31] This non-Debye type of relaxation, can be interpreted by two approaches: either the relaxation of the relaxing units is intrinsically non-exponential and homogeneous at low temperature, or the relaxing units follow a Debye mode but each has a different relaxation time. The latter time distribution being attributed to the heterogeneity in the dynamics of the liquids.[32, 33]

Adam and Gibbs suggested a model in an approach to explain the behavior of liquids in the vicinity of the Tg temperatures.[34] This model introduced the concept of cooperative rearrangements in the relaxation modes of molecules present in different parts of system. The salient thermodynamic and kinetic features were then interpreted as an outcome of the cooperative nature of the relaxation modes of super-cooled liquids expressed at the nanoscale in terms of spatial/temporal dynamical heterogeneities [30, 35] demonstrated in Fig. I-4.

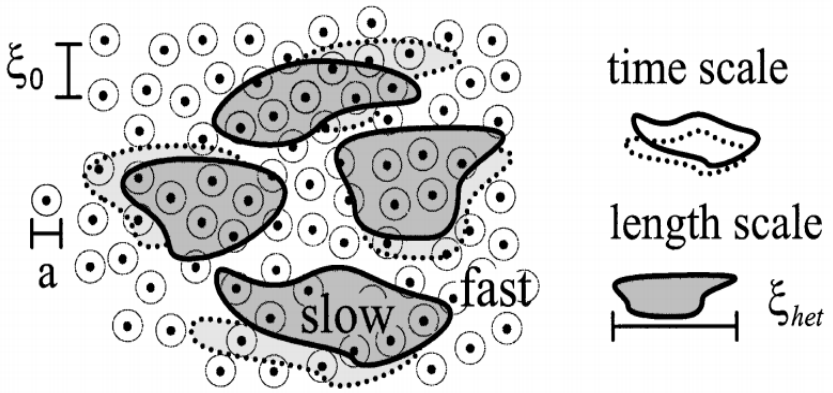


Figure I-4: Temporal fluctuations and length scale of dynamical heterogeneities in supercooled liquids. [35]

The collective dynamics concerning a few molecules is affiliated with a characteristic distance known as the cooperativity length $\xi_{het.}$ The size of such a Cooperative Rearranging Region was estimated by Donth to be in the nanometer range and equivalent to a few molecular diameters. [36] The presence of such a characterization length implied that samples bearing dimensions equivalent to this CRR (example: in the case of spatial nanoconfinement), may encounter the so-called finite size effects, a topic that will be addressed in the following section.

The pursuit of understanding the cooperative dynamics of the glass transition motivated the introduction of the concept of confinement of super-cooled liquids. In this aspect, various experimental methods (quasielastic neutron scattering, dielectric spectroscopy...) and MD simulations with extended accessible timescales (1ps to 1000s) have been performed to study the distinct signatures of confinement on the relaxation processes of the glass transition.[27, 37-40] This approach turned out to be elusive as these studies revealed that the Tg and the molecular dynamics may vary significantly under different confining environments.[18, 27] Nevertheless, it has introduced a new phenomenal field of research with its own fundamental interest.

### I.B.2.2. Dynamics of Confined Super-cooled Liquids

#### *I.B.2.2.i. Finite size Effect*

The study of the dynamics of confined super-cooled liquids although inconclusive, provided a general trend of Tg decrease. This has been illustrated by the study of salol in coated porous glass where the relaxation rates were reduced in the confined geometry compared to the bulk (Fig. I-5).[41] This can be interpreted in terms of the influence of the finite size effect on the cooperativity of the molecular reorientations of the glass-forming liquids.

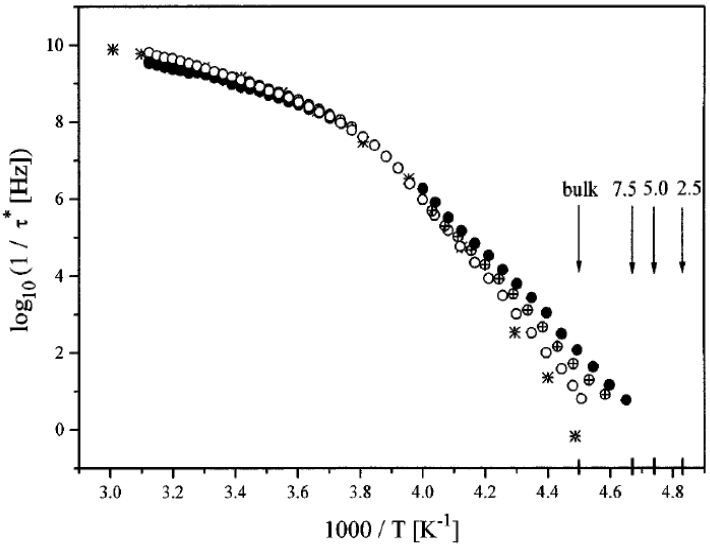


Figure I-5: Activation plot for salol confined to coated pores: ○: 7.5nm, ⊕: 5nm, ●: 2.5 and ✳ for the bulk. The arrows indicate the calorimetric glass transition temperatures for the different pore sizes and bulk salol.[41]

At high temperatures the cooperativity length is less than the diameter of the pores granting equivalence between the bulk and the confined geometry. Upon decreasing the temperature the noticeable deceleration in the glassy dynamics is attributed to the growth of cooperative rearrangement regions also known as frustration limited domains.[34, 42] This is an observation associated to the super-Arrhenius behavior of the relaxation time of fragile liquids. The correlation length of these CRR units keeps on increasing with the decreasing temperature until the finite-size effects imposed by the confining matrix limit their extension beyond the pore size. Therefore, due to this ‘‘cut-off effect’’ the structural relaxation of the confined liquid is accelerated compared to the bulk where the dynamics are increasingly retarded due to the unhindered growth of the cooperativity length.[41] However, this outcome is not systematic and no general conclusions can be withdrawn as some studies have reported constant or even increasing Tgs. An observation that can be attributed to the liquid’s interaction with the pore wall (surface effects).[18, 20, 27, 43, 44]

### *I.B.2.2.ii. Surface Effect*

MD simulations were performed in an approach to disentangle the effect of the surface roughness on the relaxation times of confined liquids.[38] A significant outcome of this study is the witnessed increase in Tg close to the wall in the case of interaction with the rough surface. On the other hand, a reduction in Tg has been detected in the proximity of the smooth wall.

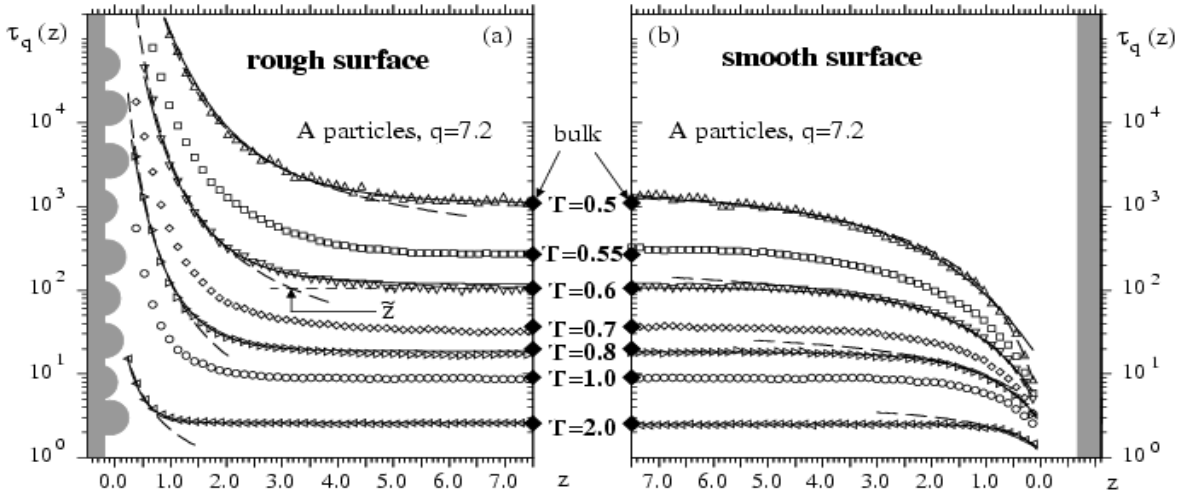


Figure I-6: Relaxation time as a function of particle distance from the wall for (a) rough and (b) smooth surfaces at different temperatures. The large diamonds are the bulk values and the long dashed curves and the solid ones show the simulation fits. [38]

The propagation of this boundary effect as a function of the distance from the pore wall has also been investigated. The study revealed the gradient recovery of the bulk behavior as we go further from the wall into the inner-pore (Fig. I-6). This distribution of relaxation times is commonly interpreted as a consequence of the surface induced dynamical heterogeneity in the system related to the spatial extension of this surface-wall effect which leads to a magnification of the non-Debye character of the structural relaxation process.[37, 39-41]

The nature of the surface morphology (roughness, chemical nature, structure) and the resultant fluid-wall interaction, can determine whether the acceleration or deceleration of the dynamics of the interfacial liquid molecules takes place. The situation gets even more complicated with the introduction of other confinement effects such as the finite size of the confining matrix. Hence, the attitude of liquids under confinement is often ambiguous and related to complex phenomena with several convoluted effects which in turn lead to non-systematic results in the literature preventing the extraction of any definitive conclusions regarding this topic.[18, 20, 38]

### *I.B.2.2.iii. Competition between the Different Effects*

As mentioned earlier, the current level of understanding of the dynamics of glass-forming liquids in confinement doesn't permit the extraction of universal behaviors of the glass transition. This is demonstrated by the study of the glass transition of toluene as a function of the pore size of a series of mesostructured porous silicates (Fig. I-7).[9]

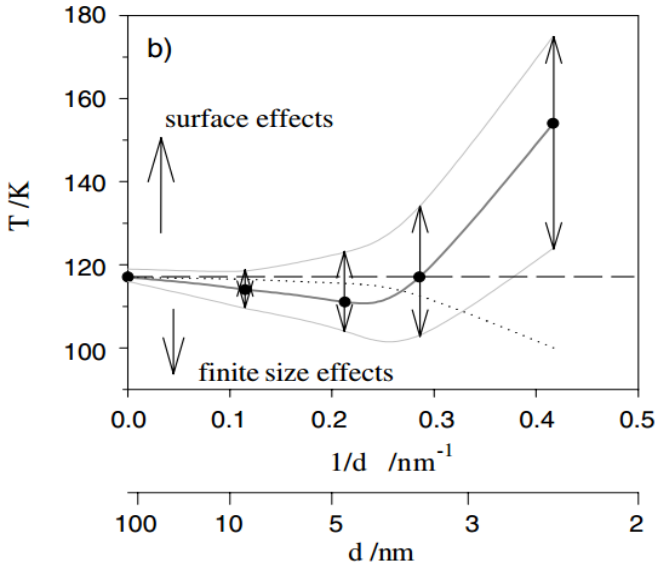


Figure I-7: The Glass transition versus the pore diameter for toluene confined in MCM-41 and SBA-15 nanopores. Dashes illustrate the Tg of bulk toluene, the points represent the average bulk Tg at the same density in the pore and the arrows represent the Tg region. [9]

The non-monotonic variation of Tg certainly emphasizes the presence of competing size and surface effects in the confined geometry, of which the relative contributions is system dependent. For instance, in small pores a remarkable increase in Tg is observed favoring interpretations based on the surface boundary effects. In such pores (widths equivalent to a few molecular diameters) most of the confined molecules can interact with the corrugated walls that act as blocking boundary conditions causing the reduction of their mobility.

In larger pore sizes, Tg is reduced to a value smaller than that of the bulk (<120 K). This is a common signature of another effect that has been discussed earlier *i.e.*, finite-size effect. The latter would restrain the growth of any cooperativity lengths and compete with the surface-induced effects, thus moderating the retardation of the dynamics and inducing the observed decrease in Tg. The general trend observed in this study (*i.e.*, the decrease of the glass transition temperature for large pore sizes) suggests the dominance of the finite-size effects over surface effects on the dynamics of toluene in this range. Therefore, our comprehension of the influence of confinement on the liquid behavior is still primitive and based on many macroscopic approximations that are not necessarily true at the nanoscale.

## I.B.3.Effect on Structure

### I.B.3.1. Density Change

A general assumption is often made that the bulk static properties persist upon confinement. Even though this approach proved intrinsic for relating confinement effects to the correlation length of cooperative dynamics, a growing body of literature gives direct evidence to the change in structural properties inside the nanopores of mesoporous systems.[9, 44, 45]

For instance, a method has been proposed to document the variation of the average density of the liquids confined in MCM-41 and SBA-15 silicates.[4, 9] It is based on relating the Bragg peak intensities of the hexagonally ordered mesoporous materials obtained from neutron diffraction experiments to the liquid density by implementing contrast matching methods (Fig. I-8).

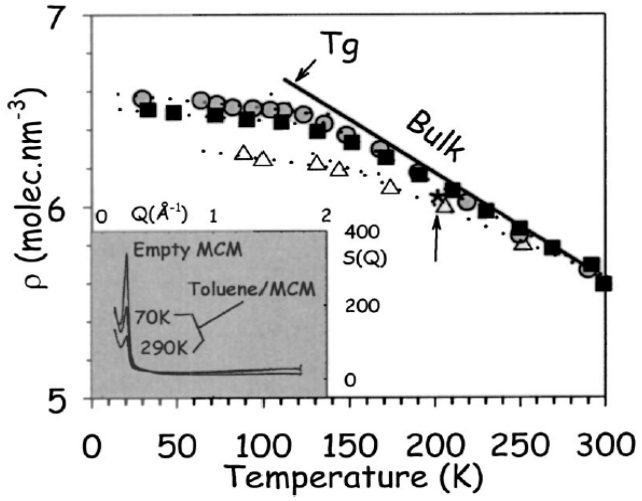


Figure I-8: Temperature dependence of the density of bulk and confined toluene. Pore diameter: Δ: 2.4 nm, ■: 3.5 nm, ●: 4.7 nm. [9]

Tg causes a modification in the thermal expansion from the liquid to the glassy state which is detected by a slope change of ρ versus temperature. The study revealed that the density of the confined toluene may significantly deviate from that of the bulk at the proximity of the Tg.[9] A phenomenon mostly prominent in the smallest pore size where the density of the confined liquid doesn't coincide with that of the bulk. In this case of extreme confinement (D= 2.4nm), which is equivalent to a few molecular diameters, Tg occurs at a much higher temperature indicating a higher thermal energy and volume than the bulk. Regarding larger pore diameters (D= 3.5nm, 4.7 nm), the thermal expansion of the liquid in these confining geometries is lower than that of the bulk leading to a smaller expansion jump resulting in Tgs comparable to the bulk values. This indicates that the density of the confined toluene is smaller than that of the bulk even for pore sizes as big as 10 molecular diameters (D= 4.7nm) where the effect is feeble yet persistent displaying a trend of density change under confinement.

### I.B.3.2. Self-assemblies in Confinement

Density is not the only characteristic affected by confinement. In fact, the structure of H-bonding fluids is more susceptible to confining geometries. This is due to their ability to form networks leading to the development of intermediate range orders (IROs) of a few nanometers in the liquid state (a characteristic which can be hindered by finite size effect for example). Moreover, associative liquids tend to form H-bonding bridges with the interfacial hydrophilic silanols.[46] This surface character is of a great practical significance since it is usually encountered in many popular porous silica materials (SBA-15, MCM-41, Vycor...) granting peculiar features [47] and new structures in the confined geometries (layering, self-association...).

#### *I.B.3.2.i. Inter-pore Layering*

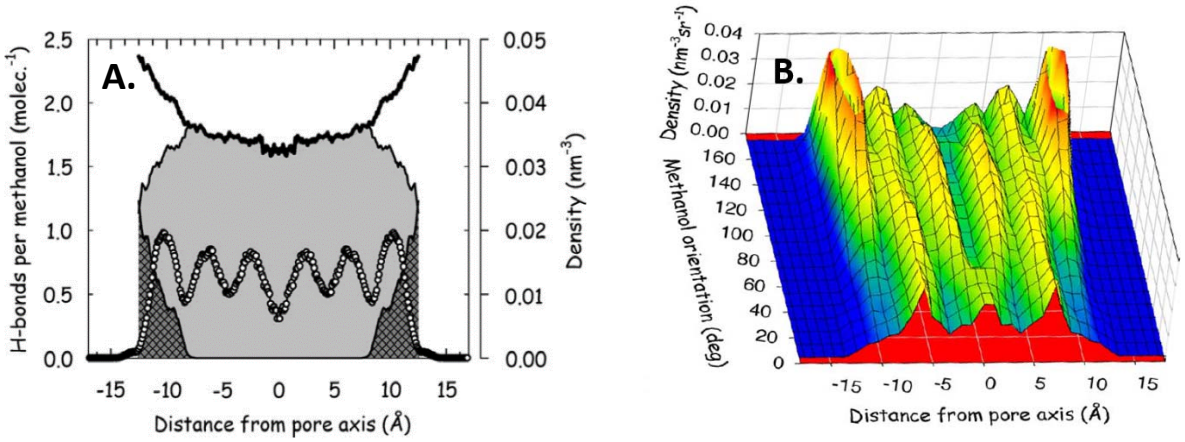


Figure I-9: (A): Radial ρ profile of methanol in silica nanopores. Open circles: local ρ of methanol. Dark shaded area: average number of H-bonds, bounding a methanol and a silanol. Light shaded area: average number of H-bonds linking two methanol molecules. Solid line: average number of H-bonds per methanol molecule; (B): MC simulation of radial ρ profiles vs molecular orientation with respect to the surface. [48]

The structure of nanoconfined methanol was investigated by MD simulation. The study revealed the spatial non-homogeneous distribution of the density of methanol inside the pores of the mesoporous silica. This phenomenon of layering is demonstrated in Fig. I-9 (A) which shows the oscillation of the radial density of methanol's carbon atoms around the typical liquid density ($\rho = 0.014$ nm$^{-3}$) across the pore.[48] The evolution of these layers in the pore reflects the propagation of a translational order from the pore surface towards the center breaking the bulk's translational uniformity. Moreover, the orientational order of the confined methanol shows unusual features as the liquid loses most of its typical isotropy (equal probability of orienting in different possible directions). This is elucidated in Fig. I-9 (B) which displays the radial density profile as a function of the molecular dipole's orientation with respect to the pore surface. It shows that the interfacial layer is anisotropic, with a maximum corresponding to the molecular axis being normal to the surface.[48]

### *I.B.3.2.ii. Self-Association*

Self-association is yet another phenomenon that can be influenced by confinement. Being an outcome of the balance between hydrophilic and hydrophobic forces, one might expect that the introduction of an additional fluid–substrate interaction through confinement can modify the equilibrium of these forces. Furthermore, confinement in MCM-41 and SBA-15 molecular sieves offers the possibility of H-bonding with the interfacial silanols resulting in the formation of new surface-induced self-assemblies.

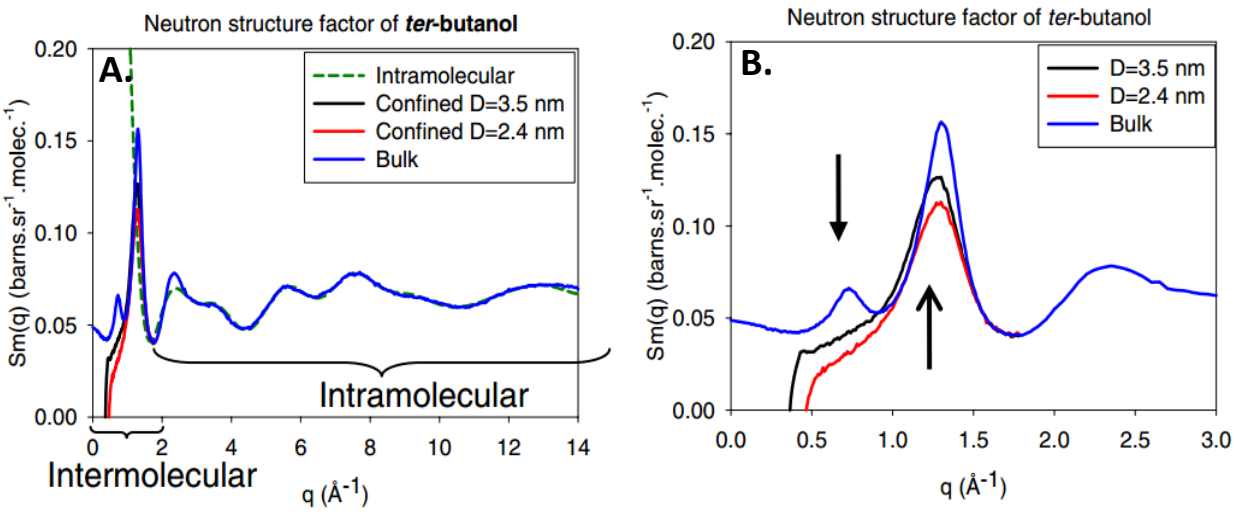


Figure I-10: Neutron structure factor of liquid TBA in bulk and confined in MCM-41. (A): Bulk liquid (blue line), liquid in MCM-41 with D = 3.5 nm (black line), liquid in MCM-41 with D = 2.4 nm (red line), and intramolecular form factor (dashed line); (B): magnified view of the low-q region. [49]

The study of *tert*-butanol (TBA) in MCM-41 mesoporous silicates is a typical example of the structural studies on associating liquids under confinement. The structure factor S(q) of TBA reveals significant changes in the low q region suggesting that the local order of the liquid phase is greatly disturbed by nanoconfinement. The major confinement-induced change is the disappearance of the pre-peak associated to supermolecular assemblies (q= 0.8 $Å^{-1}$) indicating that the supermolecular clustering of TBA is suppressed in the pores (Fig. I-10).[49]

Many interpretations have been approached to explain the absence of the pre-peak in the structure factor of the confined TBA. The first emphasizes the spatial restriction introduced by the porous geometry (pore size and shape) which inflicts severe constraints on the expansion of medium-range ordered nanostructures. The second is based on the fact that the vicinity of the pore wall often promotes specific arrangements in the interfacial fluid (layering, hexatic six-fold orientational order, linear aggregates...) which can compete with the bulk liquid structures.

## I.B.4. Phase Separation of Binary Liquids

So far, we have only discussed the case of simple liquids confined in nanopores. However, the study of the structural and dynamical properties of binary liquid mixtures under confinement has been increasingly gaining interest in many fields.[6, 50] Theoretical studies have focused on the capillary condensation of a mixture of liquids in cylindrical pores. They revealed that for systems with different interactions, the wetting of a component over the other in the pore surface is predominant.[51, 52] A more recent theoretical study indicated the possibility of the binary system to present partially de-mixed thermodynamic states under confinement with several possible configurations: partial wetting leading to the formation of caps, capsules or tubes (complete segregation) with one liquid at the surface and the other being located in the pore.[53]

This segregation in porous media was observed for binary mixtures bearing a miscibility gap in their bulk state.[54-58] A pioneering example of such studies is that of Formisano and Teixeira on the de-mixing of hexane and n-perfluorooctane imbibed into mesoporous Vycor.[54] They developed a model to explain the intensity increase prevailed in their small angle neutron scattering (SANS) results. In their model, they attributed the sharp increase in the scattering intensity at low Qs to concentration fluctuations and associated the appearance of another peak at Q= 0.05 $Å^{-1}$ to the introduction of a new characteristic length related to the formation of an adsorbed layer richer in one of the liquids (B) over the other (A) at the pore wall (Fig. I-11).[54]

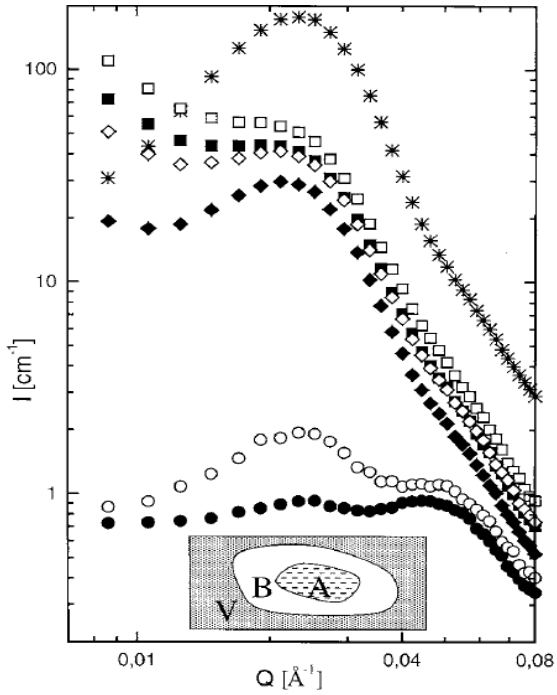


Figure I-11: A logarithmic plot of the intensity scattered from the dry Vycor (stars) and from the samples at the lowest (open symbols) and highest (full symbols) temperature. From the bottom: HD (circles), H (diamonds), and D (squares). [54]

In a similar approach, Findenegg and coworkers investigated the temperature-induced microphase separation of the binary iso-butyric acid+ heavy water mixtures (iBA + $D_2O$) in CPG silica glass.[56, 57, 59, 60] Their SANS results have shown a strong temperature dependence as evident in Fig. I-12. A quantitative analysis of the data using a model similar to that of Formisano and Teixeira relates the rise in intensity with decreasing temperature to growing concentration fluctuations. Furthermore, the decrease of the diffusion coefficient (measured by neutron spin echo experiments) with decreasing temperature was explained by the immobilization of the concentration fluctuations at the pore wall upon reaching pore size and their breakdown into microdomains forming a tube-like structure at low temperatures.

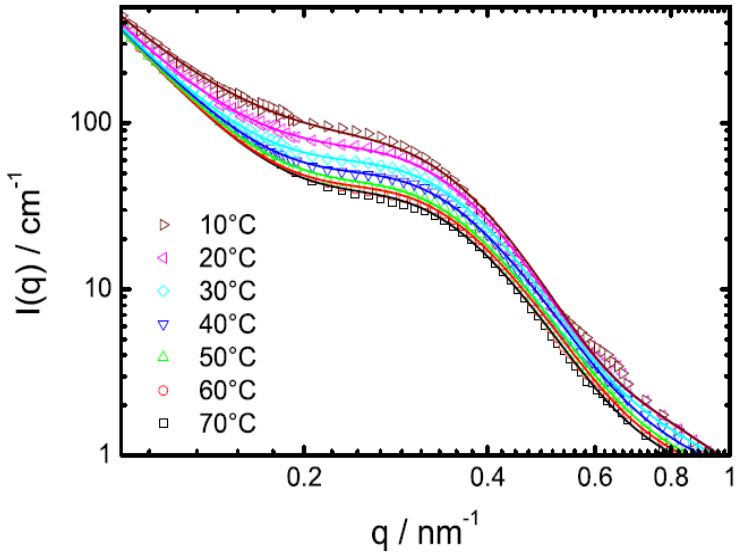


Figure I-12: SANS curves obtained for the 54 wt.% iBA+$D_2O$ sample. [59]

The existence of these nanosegregated regions was interpreted as a consequence of a competition between diverse effects leading to the preferential adsorption of one of the two phases to the host (wetting). However, quenched disorder effects inflicted by the strongly inter-connected pores of Vycor hinder a complete phase separation by trapping the system in a dramatically slowed down critical fluctuations regime deep inside the miscibility gap.

Since the topology of the porous host seems to have a remarkable influence on the phase separation process, new approaches were conducted in an attempt to overcome this effect. This was achieved by the replacement of the interconnected and disordered Vycor and CPG matrices by more ordered materials (Anodic Aluminum Oxides, MCM-41…). For instance, Lefort and coworkers investigated the radial nanostructure of trimethylamine (TEA) /water ($D_2O$) binary mixture confined in the cylindrical pores of anodic aluminum oxide (AAO) membranes as represented in Fig. I-13 (A). [58]

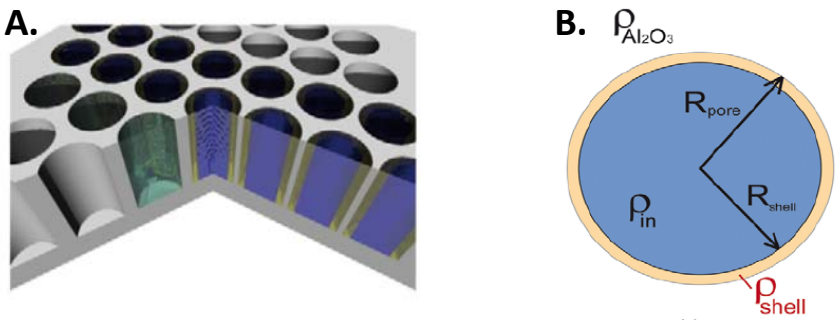


Figure I-13: (A): Schematic representation of cylindrical pores either empty, filled with a homogeneous liquid, or filled with a core-shell structure of a binary solution; (B): A scheme of an ideal core-shell phase separation. The binary solution is supposed to demix in a pore of radius Rpore into a core with radius $R_{shell}$ and of neutron scattering length density $\rho_{in}$, surrounded by a shell of scattering length density $\rho_{shell}$ and surrounded by the AAO matrix of scattering length density $\rho_{Al2O3}$. [58]

The small angle neutron scattering data measured on the confined mixture indicate the existence of a concentration inhomogeneity in the pores well below the bulk phase separation temperature.[58] This inhomogeneous structure was analyzed by the model shown in Fig. I-13 (B) considering a simple core-shell structure. Two scenarios were taken into account the first assuming that the interfacial shell layer is pure $D_2O$ with TEA residing inside the pore and the second assuming the exact opposite configuration. The best agreement was evident for fits with the core-shell model depicting the preferential affinity of water to the AAO pore walls with a TEA-rich phase in the core (as illustrated in Fig. I-14).

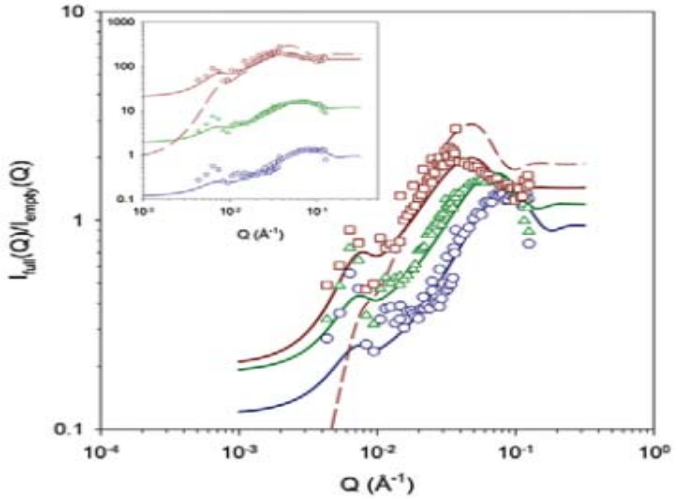


Figure I-14: Best fits of the ratio $\rho(Q) = I_{full}(Q)/I_{empty}(Q)$ of the SANS intensities of filled and empty AAO. The solid lines and dashed lines show the best fits obtained when assuming that this interfacial shell layer is pure D2O and rich in Triethylamine respectively. [58]

In general, it was found that the structure of the nanosegregated phase depends on the confinement geometry and the affinity of one of the two liquids to the pore wall, in particular in the case of possible H- bonding with the surface.

Interestingly, there are recent clues that confinement could induce micro-phase separation of fully miscible binary liquids.[61-65] This situation differs significantly from the studies discussed earlier which have been performed in the vicinity of phase separation or in the two-phase region of critical or non-miscible mixtures. The origin of the phase separation in the former is related to the selective interaction of one of the components with the pore surface rather than the presence of a miscibility gap and critical concentration fluctuations.

An illustrative example on such inspiring studies are the ones conducted by Swenson and coworkers who investigated the dynamics of miscible binary liquids confined in MCM-41. Their studies reveal the non-monotonic dependence of the alcohol dynamics on the water concentration in the binary mixture. A behavior far from an ideal solution and can be explained in terms of the preferential H-bonding of water with the silanol groups at the pore surface and the clustering of the other component in the core leading to phase separation.[61-63] This segregation illustrates that at low concentrations, most of the water resides at the vicinity of the pore wall and doesn't interact with the core liquid. It is only at very high water concentrations that a retardation of the dynamics of the alcohol is witnessed due to the partial remixing of the liquids. The arrested dynamics can be then attributed to the anti-plasticizing effect of the rigid network formed by the different H-bonding entities at high water concentrations.[61, 63]

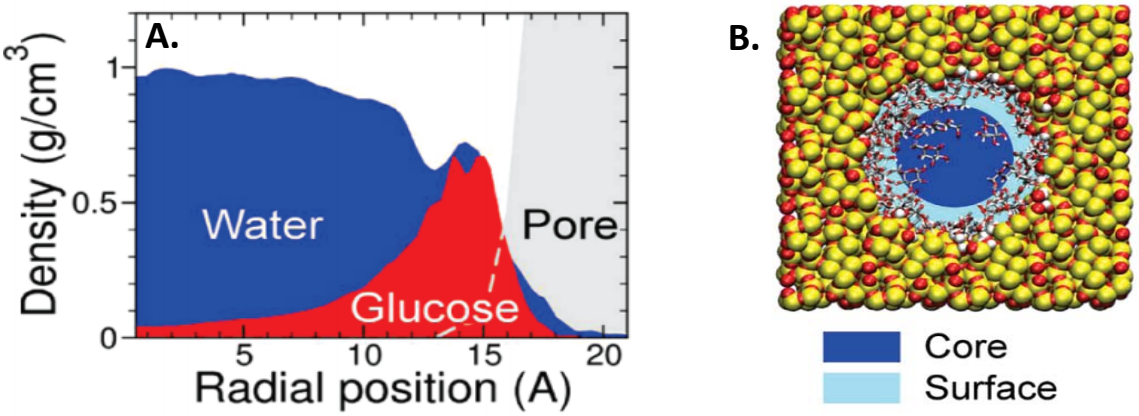


Figure I-15: (A): The density profiles of water (blue), glucose (red) and the silica matrix (grey); (B):a schematic presentation of the pore showing the preferential adsorption of glucose at the pore surface. [64]

Different conclusions stem out of recent MD simulation studies performed on similar binary systems.[64, 65] These studies show the preferential adsorption of the other H-bonding liquid (glucose or ethanol) at the pore surface and the clustering of water at the center of the pore (Fig. I-15). An observation which contradicts with the scenario proposed by Swenson et al.

# I.C. Aim of the Thesis

The disparity of the results obtained by the different techniques in the study of confined binary liquids is one of the main motivations of this work as the possible origin of such divergence is the fact that the mixtures studied comprise two H-bonding liquids. Therefore it would be highly interesting to control such structuring by tuning the affinity of the liquids to the pore wall. The idea is choosing a binary mixture composed of totally miscible liquids in the bulk conditions. However, only one of the components should be capable H-bonding with the interfacial silanol groups and the other should be aprotic. For this reason we chose the notoriously associative *tert*-butanol (TBA) and toluene (Tol). Under such conditions one might expect the selective adsorption of TBA at the surface and the residing of Tol in the core.

This study has also been motivated by two significant observations: the first is the formation of interfacial H-bonded clusters in alcohol-alkane binary mixtures when in contact with hydrophilic surfaces[10-12, 66-71] and the existence of stable supermolecular clusters at the nanoscale in the bulk state of the binary liquids, though fully miscible and homogeneous at the macroscopic scale.[72-74] Moreover, such mixtures (TBA/Tol) have shown the formation of supermolecular assemblies under confinement in MCM-41 type materials, suggesting a surface-induced nanosegregation of the components (core-shell structure).

Since this nano-segregation phenomenon is linked to the nature of the solvent-solute-solid interactions, any modification of the confining matrix in terms of size or chemical nature could lead to different structural and dynamical properties of the nano-segregated systems. Therefore, a main objective of this thesis is altering the pore size and surface properties in an attempt to understand both effects on the phase separation process.

Primarily, tuning the pore size by replacing MCM-41 (D≈ 3nm) by the larger pore-sized SBA-15 (D≈ 8nm) would give an insight to the stability of this nanostructuring and its survival in larger nanochannels. Moreover, tailoring the chemical nature of the surface by going from the strongly hydrophilic MCM-41 and SBA-15 to the hydrophobic carbon porous materials CMK-3 (their graphitic replica) would allow the study of the surface effect and highlight the significance of H-bonding (which is absent in this case) in the formation of such structures.

Another strategy allocated to this thesis is the modification of the liquids in the binary mixture in an attempt to understand the effect of some liquid properties on the nanostructuring. For

instance the impact of steric hindrance can be explored through the substitution of TBA by the smaller methanol/ethanol molecules. Another interesting effect is that of the aromaticity which can be investigated through the replacement of toluene by cyclohexane.

A key objective of this thesis is to achieve a comprehensive vision on the molecular dynamics of the nanosegregated mixtures in order to disentangle the main structural relaxation from the putative distinct modes arising from the different nanosegregated regions. The combination of Quasielastic Neutron Scattering techniques: Backscattering and Time of Flight is essential for the extension of the dynamical range and resolution to cover the broad distribution of relaxation times induced by mixing and confinement.

## I.D. Organization of the Thesis

The thesis consists of five chapters, the structure is as follows: following this introductory chapter, Chapter II presents the liquids used: *tert*-butanol, toluene, methanol, ethanol and cyclohexane and describes the different porous materials used in the literature rationalizing our choice (MCM-41, SBA-15 and CMK-3) in terms of pore size and topology. It then proceeds to illustrate the synthesis and characterization of these materials.

Chapter III is a comprehensive structural study on macroscopically miscible mixtures (TBA/Tol and TBA/ cyclohexane), combining SANS and isotopic contrast effect. We will illustrate our studies on bulk mixtures with different compositions to have an insight on the concentration fluctuations caused by the preferential interactions between similar molecules.

In Chapter IV the mesoscopic scale order of binary liquids in the confined geometry will be addressed. The results suggest the spontaneous nanosegregation of the components of the binary mixtures confined in SBA-15. The SANS measurements will be discussed in the frame of the predictions of a simple core-shell model. Different alcohols, including bulky TBA and the smaller and more hydrophilic methanol and ethanol molecules will be considered in order to discriminate between the interfacial layer scenario and the complete separation of the liquids.

Chapter V focuses on the dynamical properties of binary mixtures under confinement. The study is based on the analysis of Elastic Fixed Window Scans and Mean Square Displacements acquired from Neutron Backscattering measurements. Different TBA/Tol mixture compositions confined in MCM-41(D= 2-3 nm) and SBA-15 (D= 8-9 nm) materials will be compared. HD selective isotopic effects will also be used in order to disentangle the dynamics and relaxation modes coming from the distinct segregated regions.

# References


1. Huczko, A., *Template-based synthesis of nanomaterials.* Applied Physics A, 2000. **70**(4): p. 365-376.
2. Yang, P.P., S.L. Gai, and J. Lin, *Functionalized mesoporous silica materials for controlled drug delivery.* Chemical Society Reviews, 2012. **41**(9): p. 3679-3698.
3. Mancinelli, R., et al., *Multiscale approach to the structural study of water confined in MCM41.* The Journal of Physical Chemistry B, 2009. **113**(50): p. 16169-16177.
4. Morineau, D., et al., *Structure of liquid and glassy methanol confined in cylindrical pores.* The Journal of chemical physics, 2004. **121**(3): p. 1466-1473.
5. Christenson, H.K., *Confinement effects on freezing and melting.* Journal of Physics: Condensed Matter, 2001. **13**(11): p. R95.
6. Gelb, L.D., et al., *Phase separation in confined systems.* Reports on Progress in Physics, 1999. **62**(12): p. 1573-1659.
7. Ellison, C.J. and J.M. Torkelson, *The distribution of glass-transition temperatures in nanoscopically confined glass formers.* Nature Materials, 2003. **2**(10): p. 695-700.
8. Richert, R. and M. Yang, *Surface induced glass transition in a confined molecular liquid.* The Journal of Physical Chemistry B, 2003. **107**(4): p. 895-898.
9. Morineau, D., Y. Xia, and C. Alba-Simionesco, *Finite-size and surface effects on the glass transition of liquid toluene confined in cylindrical mesopores.* The Journal of chemical physics, 2002. **117**(19): p. 8966-8972.
10. Mizukami, M., Y. Nakagawa, and K. Kurihara, *Surface induced hydrogen-bonded macrocluster formation of methanol on silica surfaces.* Langmuir, 2005. **21**(21): p. 9402-9405.
11. Mizukami, M., M. Moteki, and K. Kurihara, *Hydrogen-bonded macrocluster formation of ethanol on silica surfaces in cyclohexane.* Journal of the American Chemical Society, 2002. **124**(43): p. 12889-12897.
12. Yilmaz, N., M. Mizukami, and K. Kurihara, *Molecular macrocluster formation on silica surfaces in phenol-cyclohexane mixtures.* Langmuir, 2007. **23**(11): p. 6070-6075.
13. Kotelyanskii, M. and S.K. Kumar, *Surface transitions for confined associating mixtures.* arXiv preprint cond-mat/9709321, 1997.
14. Radhakrishnan, R. and K.E. Gubbins, *Free energy studies of freezing in slit pores: an order-parameter approach using Monte Carlo simulation.* Molecular Physics, 1999. **96**(8): p. 1249-1267.
15. Radhakrishnan, R., K.E. Gubbins, and M. Sliwinska-Bartkowiak, *Existence of a hexatic phase in porous media.* Physical review letters, 2002. **89**(7): p. 076101.
16. Dosseh, G., Y.D. Xia, and C. Alba-Simionesco, *Cyclohexane and benzene confined in MCM-41 and SBA-15: Confinement effects on freezing and melting.* Journal of Physical Chemistry B, 2003. **107**(26): p. 6445-6453.
17. Radhakrishnan, R., K.E. Gubbins, and M. Sliwinska-Bartkowiak, *Effect of the fluid-wall interaction on freezing of confined fluids: Toward the development of a global phase diagram.* The Journal of chemical physics, 2000. **112**(24): p. 11048-11057.
18. Alcoutlabi, M. and G.B. McKenna, *Effects of confinement on material behaviour at the nanometre size scale.* Journal of Physics-Condensed Matter, 2005. **17**(15): p. R461-R524.
19. Huber, P., *Soft matter in hard confinement: phase transition thermodynamics, structure, texture, diffusion and flow in nanoporous media.* Journal of Physics: Condensed Matter, 2015. **27**(10): p. 103102.
20. Alba-Simionesco, C., et al., *Effects of confinement on freezing and melting.* Journal of Physics: Condensed Matter, 2006. **18**(6): p. R15.
21. Davis, M.E., *Ordered porous materials for emerging applications.* Nature, 2002. **417**(6891): p. 813-821.
22. Klafter, J. and J.M. Drake, *Molecular dynamics in restricted geometries*. 1989: Wiley-Interscience.

23. Jackson, C.L. and G.B. McKenna, *THE MELTING BEHAVIOR OF ORGANIC MATERIALS CONFINED IN POROUS SOLIDS.* Journal of Chemical Physics, 1990. **93**(12): p. 9002-9011.
24. Schüller, J., et al., *Dielectric studies of the glass transition in porous media.* Physical review letters, 1994. **73**(16): p. 2224.
25. Radhakrishnan, R., K.E. Gubbins, and M. Sliwinska-Bartkowiak, *Global phase diagrams for freezing in porous media.* The Journal of chemical physics, 2002. **116**(3): p. 1147-1155.
26. Warnock, J., D. Awschalom, and M. Shafer, *Geometrical supercooling of liquids in porous glass.* Physical review letters, 1986. **57**(14): p. 1753.
27. Alba-Simionesco, C., et al., *Confinement of molecular liquids: Consequences on thermodynamic, static and dynamical properties of benzene and toluene.* The European Physical Journal E, 2003. **12**(1): p. 19-28.
28. Debenedetti, P.G. and F.H. Stillinger, *Supercooled liquids and the glass transition.* Nature, 2001. **410**(6825): p. 259-267.
29. C. A. Angell, K.L.N., and G. B. Wright, *in Relaxations in Complex Systems.* Naval Research Laboratory, 1985. **3**.
30. Sillescu, H., *Heterogeneity at the glass transition: a review.* Journal of Non-Crystalline Solids, 1999. **243**(2): p. 81-108.
31. Böhmer, R., et al., *Nonexponential relaxations in strong and fragile glass formers.* The Journal of chemical physics, 1993. **99**(5): p. 4201-4209.
32. Richert, R., *Homogeneous dispersion of dielectric responses in a simple glass.* Journal of Non-Crystalline Solids, 1994. **172**: p. 209-213.
33. Arbe, A., et al., *Dynamics of glass-forming polymers:"Homogeneous" versus "heterogeneous" scenario.* Physical review letters, 1998. **81**(3): p. 590.
34. Adam, G. and J.H. Gibbs, *On the temperature dependence of cooperative relaxation properties in glass-forming liquids.* The Journal of chemical physics, 1965. **43**(1): p. 139-146.
35. Tracht, U., et al., *Length scale of dynamic heterogeneities at the glass transition determined by multidimensional nuclear magnetic resonance.* Physical review letters, 1998. **81**(13): p. 2727.
36. Donth, E., *The size of cooperatively rearranging regions at the glass transition.* Journal of Non-Crystalline Solids, 1982. **53**(3): p. 325-330.
37. Zorn, R., et al., *Inelastic neutron scattering experiments on the dynamics of a glass-forming material in mesoscopic confinement.* Journal of Non-Crystalline Solids, 2002. **307**: p. 547-554.
38. Scheidler, P., W. Kob, and K. Binder, *The relaxation dynamics of a confined glassy simple liquid.* The European Physical Journal E, 2003. **12**(1): p. 5-9.
39. Dosseh, G., et al., *Fluid–wall interactions effects on the dynamical properties of confined orthoterphenyl.* Journal of Non-Crystalline Solids, 2006. **352**(42): p. 4964-4968.
40. Busselez, R., et al., *Molecular dynamics of glycerol and glycerol-trehalose bioprotectant solutions nanoconfined in porous silicon.* Journal of Chemical Physics, 2009. **130**(21).
41. Arndt, M., et al., *Length scale of cooperativity in the dynamic glass transition.* Physical review letters, 1997. **79**(11): p. 2077.
42. Kivelson, D., et al., *A thermodynamic theory of supercooled liquids.* Physica A: Statistical Mechanics and its Applications, 1995. **219**(1): p. 27-38.
43. Zhang, F.Q., et al., *Understanding effect of wall structure on the hydrothermal stability of mesostructured silica SBA-15.* Journal of Physical Chemistry B, 2005. **109**(18): p. 8723-8732.
44. Patkowski, A., T. Ruths, and E.W. Fischer, *Dynamics of supercooled liquids confined to the pores of sol-gel glass: A dynamic light scattering study.* Physical Review E, 2003. **67**(2): p. 021501.
45. Kilburn, D., et al., *Confinement induces both higher free volume and lower molecular mobility in glycerol.* Applied Physics Letters, 2008. **92**(3): p. 033109.
46. Busselez, R., et al., *Molecular dynamics simulation of nanoconfined glycerol.* Physical Chemistry Chemical Physics, 2009. **11**(47): p. 11127-11133.
47. Dore, J., *Structural studies of water in confined geometry by neutron diffraction.* Chemical Physics, 2000. **258**(2): p. 327-347.

48. Guégan, R., D. Morineau, and C. Alba-Simionesco, *Interfacial structure of an H-bonding liquid confined into silica nanopore with surface silanols.* Chemical Physics, 2005. **317**(2): p. 236-244.
49. Morineau, D. and C. Alba-Simionesco, *Does Molecular Self-Association Survive in Nanochannels?* The Journal of Physical Chemistry Letters, 2010. **1**(7): p. 1155-1159.
50. Schreiber, A., et al., *Effect of surface modification on the pore condensation of fluids: experimental results and density functional theory.* Molecular Physics, 2002. **100**(13): p. 2097-2107.
51. Evans, R., U.M.B. Marconi, and P. Tarazona, *Fluids in narrow pores: Adsorption, capillary condensation, and critical points.* The Journal of chemical physics, 1986. **84**(4): p. 2376-2399.
52. Peterson, B.K., et al., *Lennard-Jones fluids in cylindrical pores: Nonlocal theory and computer simulation.* The Journal of chemical physics, 1988. **88**(10): p. 6487-6500.
53. Liu, A.J., et al., *WETTING TRANSITIONS IN A CYLINDRICAL PORE.* Physical review letters, 1990. **65**(15): p. 1897-1900.
54. Formisano, F. and J. Teixeira, *Critical fluctuations of a binary fluid mixture confined in a porous medium.* European Physical Journal E, 2000. **1**(1): p. 1-4.
55. Formisano, F. and J. Teixeira, *Appearance of critical fluctuations in a binary fluid mixture confined in Vycor glass.* Journal of Physics: Condensed Matter, 2000. **12**(8A): p. A351.
56. Schemmel, S., et al., *Phase separation of a binary liquid system in controlled-pore glass*, in *Dynamics in Small Confining Systems-2003*, J.T. Fourkas, et al., Editors. 2004. p. 215-220.
57. Schemmel, S., et al., *Local structure of a phase-separating binary mixture in a mesoporous glass matrix studied by small-angle neutron scattering.* Journal of Chemical Physics, 2005. **122**(24).
58. Lefort, R., et al., *Phase separation of a binary liquid in anodic aluminium oxide templates.* European Physical Journal E, 2011. **34**(7).
59. Hellweg, T., et al., *De-mixing dynamics of a binary liquid system in a controlled-pore glass.* European Physical Journal E, 2003. **12**: p. S1-S4.
60. Rother, G., et al., *Confinement effect on the adsorption from a binary liquid system near liquid/liquid phase separation.* Journal of Chemical Physics, 2004. **120**(24): p. 11864-11873.
61. Elamin, K., et al., *Different behavior of water in confined solutions of high and low solute concentrations.* Physical Chemistry Chemical Physics, 2013. **15**(42): p. 18437-18444.
62. Elamin, K., H. Jansson, and J. Swenson, *Dynamics of aqueous binary glass-formers confined in MCM-41.* Physical Chemistry Chemical Physics, 2015. **17**(19): p. 12978-12987.
63. Swenson, J., et al., *Anomalous dynamics of aqueous solutions of di-propylene glycol methylether confined in MCM-41 by quasielastic neutron scattering.* Journal of Chemical Physics, 2014. **141**(21).
64. Lerbret, A., et al., *Molecular Dynamics and Neutron Scattering Study of Glucose Solutions Confined in MCM-41.* Journal of Physical Chemistry B, 2011. **115**(5): p. 910-918.
65. Guo, X.Y., T. Watermann, and D. Sebastiani, *Local Microphase Separation of a Binary Liquid under Nanoscale Confinement.* Journal of Physical Chemistry B, 2014. **118**(34): p. 10207-10213.
66. Kurihara, K., *Nanostructuring of liquids at solid-liquid interfaces*, in *Molecular Organisation on Interfaces*, G. Lagaly, Editor. 2002. p. 49-56.
67. Kurihara, K. and M. Mizukami, *Hydrogen-bonded surface macroclusters of carboxylic acid on silica in cyclohexane.* Proceedings of the Japan Academy Series B-Physical and Biological Sciences, 2001. **77**(6): p. 115-120.
68. Mizukami, M. and K. Kurihara, *Hydrogen-bonded macrocluster formation of 1-propanol and 2-propanol on silica surfaces.* Australian Journal of Chemistry, 2003. **56**(10): p. 1071-1080.
69. Mizukami, M. and K. Kurihara, *Ethanol cluster formation on silicon oxide surface in cyclohexane-ethanol binary liquids.* Chemistry Letters, 2000(3): p. 256-257.
70. Mizukami, M. and K. Kurihara, *Alcohol cluster formation on silica surfaces in cyclohexane*, in *Adsorption and Nanostructures*, I. Dekany, Editor. 2002. p. 13-17.
71. Mizukami, M. and K. Kurihara, *Macrocluster Formation of Alcohol on Silica Surface in Cyclohexane: Analysis of Interfacial Energy between Adsorption Layer and Bulk Solution.* e-Journal of Surface Science and Nanotechnology, 2006. **4**: p. 244-248.

72. Sassi, P., et al., *Distributions of H-bonding aggregates in tert-butyl alcohol: The pure liquid and its alkane mixtures.* The Journal of Physical Chemistry A, 2007. **111**(27): p. 6020-6027.
73. Hennous, L., et al., *Crossover in structure and dynamics of a primary alcohol induced by hydrogen-bonds dilution.* The Journal of chemical physics, 2014. **141**(20): p. 204503.
74. Abdel Hamid, A., et al., *Solvation Effects on Self-Association and Segregation Processes in tert-Butanol–Aprotic Solvent Binary Mixtures.* The Journal of Physical Chemistry B, 2013. **117**(35): p. 10221-10230.

# CHAPTER II:

# LIQUIDS AND MATERIALS

# Chapter II: Liquids and Materials

## II.A. Introduction

The most important materials in our daily life happen to be molecular liquids. Surprisingly, the degree of structure and property understanding of these systems barely matches up with their abundance and significance. Therefore, the study of molecular fluids has been a topic of intensive research during the last decades.

More recently, with the development of ordered mesoporous materials, an increasing interest has emerged in the properties of these liquids when confined in nanometer-scale geometry [1] either for a fundamental interest or due to their technological significance and possible application in many scientific areas including microfluidics in biotechnology, engineering of nanomaterials, geology, oil and chemical industry (cracking, catalysis…).

From a fundamental point of view, the nanoscale confinement (introducing fluids into a restricted geometry of a typical size of a few molecular diameters) drastically modifies many of their physical and/or chemical properties compared their bulk counterparts (structure, molecular dynamics, phase transition, reactivity). [2-7]

To further understand the effect of confinement many studies have been conducted on a variety of porous materials which differ in pore size, pore geometry, pore surface regularity, chemical nature… Different approaches for the classifications of porous materials have been suggested; however, the most acknowledged one was conducted by IUPAC (International Union of Pure and Applied Chemistry) according to the pore size into three main categories: microporous (pore diameter between 0.3 and 2 nm), mesoporous (pore diameter between 2 and 50 nm), and macroporous (pore diameter greater than 50 nm).[8]

We describe in the following chapter the features and characteristics of the different types of liquids and porous materials used in our studies and justify the choice of the systems studied in terms of the objectives of the thesis.

# II.B. Liquids

Lower aliphatic alcohols are a prototype of complex molecular liquids which have retained a constant interest throughout the last decades. Their significance originates from their role as very common chemical substances abundantly used as solvents, reagents and raw materials in industries. Although simple in chemical structure, they exhibit a remarkable amphiphilic character bearing both a polar hydroxyl group and a nonpolar alkyl tail. This duality contributes to the complexity of their intermolecular structure as the presence of a hydroxyl group enables them to exhibit a multiplicity of intermolecular orders related to their H-bonding ability. [9-22] The balance between hydrophobic and hydrophilic interactions is a major driving force of an association of different length scaled microstructures in the liquid state.[23] This equilibrium plays an important role in many biological and chemical processes such as the assembly of proteins and the self-organization of microemulsions.[24, 25]

In alcohol-water solutions, a strong deviation of physiochemical properties from ideal mixture approximation is observed which is attributed to the incomplete mixing of the diverse interacting molecules at the microscopic level.[26-29] Despite the complete miscibility of such binary solutions at the macroscopic scale, their heterogeneities are identified in terms of supermolecular alcohol clustering at the microscopic scale. The preferential configuration of alcohol clusters in binary mixtures corresponds to pair combination of tail-to-tail hydrophobic alkyl groups, an arrangement that resembles the micellar structures formed by surfactants in water.[30] The existence of H-bond interactions between the hydroxyl groups at the periphery and water molecules is a critical factor contributing to the stability of such microstructures.

Different strategies have been conducted in the aim of isolating supermolecular aggregates associated by H-bonds in the liquid state. A growing body of experimental results on binary alcohol-alkane solutions suggests that these types of binary liquids would preferentially form spatially separated nanophases. The addition of an aprotic liquid (none H-bonding) acting as a hydrogen bond diluent, is an efficient way of modulating the interaction between these supermolecular aggregates.[31-33]

This phenomenon of segregation was also studied by nanoscale confinement in mesoporous media for liquids that exhibit a miscibility gap i.e., in the presence of a macroscopic phase separation in the bulk phase. [34-36] However, it is striking that the study of the segregation of fully miscible binary systems in confinement is very scare in the literature.[37-39] This has guided our choice of systems to conduct a thorough study of the mesoscopic structure when mixing

alcohol with an aprotic diluent in bulk and under confinement. In this section we shall describe the physicochemical properties of the chosen liquids.

### II.B.1. *Tert*-Butyl Alcohol

*Tert*-butyl alcohol (*tert*-butanol) is the simplest, yet most widely investigated prototypical molecule of many systems exhibiting micelle-like supramolecular clusters related to H-bonding in the liquid state.[40, 41] It is a model system to fundamentally explore the microscopic mechanisms linked to self-association in condensed matter.

A variety of micro-heterogeneous structures have been witnessed for large, cluster forming *tert*-butanol molecules.[15, 16, 19-21] According to the abundant literature on the topic the formation of these clusters is attributed to the amphiphilic nature of *tert*-butanol bearing both hydrophilic hydroxyl moiety and hydrophobic butyl extremity.[14, 17-21, 42] These micellar clusters are centered about the hydroxyl H-bonding groups and surrounded by the *tert*-butyl hydrophobic parts of the molecules. They involve four to six molecules similar to what is observed in various H-bonding liquids.[20, 41] The formation of these supramolecular assemblies has been linked to the frustration of the H-bonding system by steric hindrance due to the bulky repulsive part of the molecule. [15, 16, 19-21]

In many large peripheral group bearing associating liquids [21] (*tert*-butanol, phenol), the cluster correlations could be demonstrated by a unique experimental signature in their pair correlation functions which is the appearance of a pre-peak in the static structure factor obtained by neutron diffraction , X- ray or molecular simulation [12, 18, 20, 21, 40] (See Fig. II-1 for *tert*-butanol).[22]

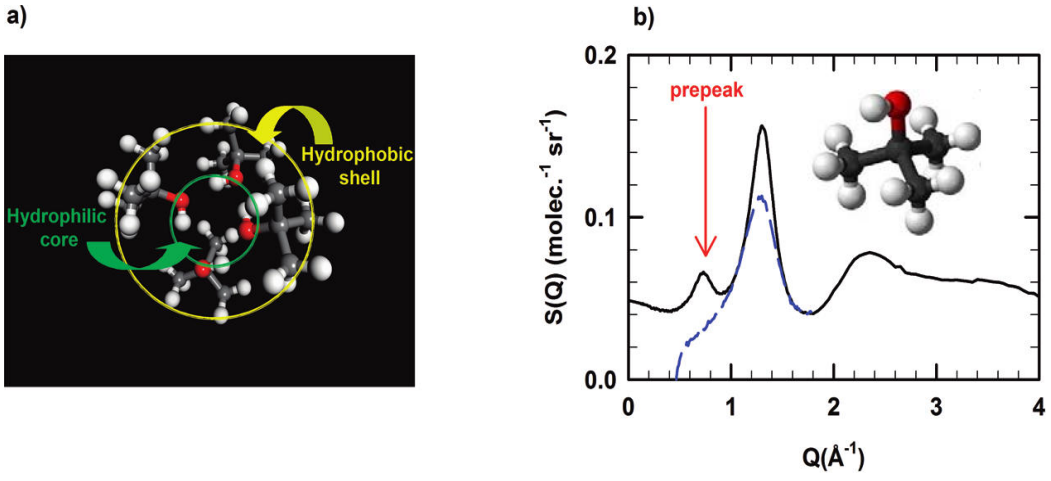


Figure II-1: (a) Cluster of four *tert*-butanol molecules in the liquid state. [22] (b) Structure factor of *tert*-butanol in bulk (solid line) and under confinement (dashed line).[18]

*Tert*-butanol is a mono-alcoholic tertiary organic liquid at room temperature, (above the melting temperature of 25 ° C). It was chosen for its extreme simplicity and the large number of studies that have been devoted recently for the pure compound in bulk or under confinement.[18, 22] A limitation of this choice, regarding the studies in bulk, is its very low capacity to be kept in the super-cooled state. Crystallization usually takes place only a few degrees below its melting point. This area can be extended through working in confined environments which proved capable of eliminating this problem (through crystallization suppression) allowing to work over a wider temperature range.

In this study, *tert*-butanol in its hydrogenated and deuterated forms was used. This has proven particularly important for neutron diffraction measurements to modulate the coherent scattering cross section of the system. It is generally considered that, in a molecule of this size, the isotopic effect on the structural properties of the liquid may be considered negligible.[17]

### II.B.2. Methanol

Methanol with a molecular formula of ($CH_3OH$) is the simplest H-bonding organic liquid. It is considered to be a typical system for the investigation of the short range order of a liquid either under confinement or in the presence of a substrate. The structure of bulk liquid methanol has been widely studied by diffraction methods (neutron or X-rays) [9, 10, 43] and MD simulations.[11, 44] Experimental as well as computational studies have suggested that methanol mostly forms chain-like network structures rather than mesoscopic aggregates attributed to the prevailing hydrophilic interactions in the low molecular weight alcohol.[9-11, 20, 21]

Phase transition and glassy behavior of methanol confined in MCM-41 and SBA-15 silicates have been investigated by X-rays [45] and neutron scattering.[12] A detailed description of the variation of the experimental structure factor with the pore diameter showed the existence of strong contributions arising from methanol–silica spatial correlations.[13]

These studies that emphasize the strong interaction between methanol and silica and more importantly, the smaller size of methanol compared to *tert*-butanol have guided our choice in this particular molecule. The significance of the small size of methanol is that it could allow us to discriminate between the scenario of having one molecular layer of alcohol at the pore surface and that of complete segregation of the mixture upon confinement due to its short alkyl chain.

### II.B.3.Ethanol

Ethanol (EtOH), along with other alcohols with chemically simple molecular composition have widespread use in chemical industry as primary solvents and reagents. Moreover, ethanol has multiple applications in environmental processes, industries and biology. From a more fundamental perspective, it has also proven to be attractive in chemical physics due to its strongly associating (H-bonding) nature. The structure of bulk ethanol is not a trivial subject to investigate as many studies show that it exhibits winding chains in the liquid state, the same unique structure which has been suggested to methanol.

Many studies have been conducted on the alcohol in confinement both in the pure [46, 47] and in binary states[37, 48] in a pursuit of understanding its behavior at the nanoscale. We chose this molecule in our studies due to its resemblance to methanol in terms of structure and chemical composition. The idea is to move from the simplest aliphatic alcohols (methanol) to the slightly more "hydrophobic" ethanol and eventually the most bulky *tert*-butanol in an attempt to study the effect of the molecular and alkyl tail size on the associative capacity of the liquid and thus its behavior when in mixture with aprotic diluent under confinement.

### II.B.4. Toluene

The system chosen as the aprotic H-bond diluent of the alcohols used in this study is toluene. It is an aromatic organic liquid of a hydrophobic nature, weakly polar and none H-bonding. The main expected interactions between toluene and *tert*-butanol, methanol and ethanol are therefore of Van der Waals nature. More specific interactions between the hydroxyl group of the alcohol and the quadrupole moment bearing electron-rich aromatic ring of toluene, shall be considered as well. This aromatic ring gives the liquid the capability of non-covalent π–π stacking which gives it additional stability over its non-aromatic analogues.

Regarding its dynamical properties, toluene is a renowned glass forming liquid which undergoes a highly non-Arrhenius like change in its viscosity with temperature in the super-cooled range. Hence, it is considered among the most "fragile" liquids.

An additional element that guided our choice for this system, other than its hydrophobic properties, is the fact that the *tert*-butanol and toluene are miscible in all proportions at the macroscopic level.[49] This adds another value to the nanophase segregation phenomenon as most of the binary systems investigated under confinement so far have been immiscible.

Toluene is easily vitrified and maintained in its supercooled state. However, its crystallization in alcohol mixtures for the compound in bulk limits its study to some extent below room temperature (depending on composition) and to a wider temperature range under confinement (due to crystallization suppression in confined media). This allowed us to conduct a comprehensive study of the structure and dynamics of the mixtures, in confinement, in the supercooled and glassy states in a temperature range between 2 and 320K.

### II.B.5. Cyclohexane

This system was chosen for being a non-aromatic analogue of toluene (both being aprotic and hydrophobic liquids with very similar structures (see Fig. II-2). According to a previous bulk study on *tert*-butanol-toluene and *tert*-butanol-cyclohexane binary liquids, an enhanced stability of the TBA multimeric clusters was achieved in an aliphatic solvent compared to toluene.[50] This was attributed to the existence of slightly stronger interactions between the aromatic ring of toluene and the hydroxyl group of TBA.

Therefore, in this approach we aim to test the influence of the π-electrons on the interaction between *tert*-butanol (TBA) and the aprotic solvent which could possibly affect the final structure of the mixtures under confinement.

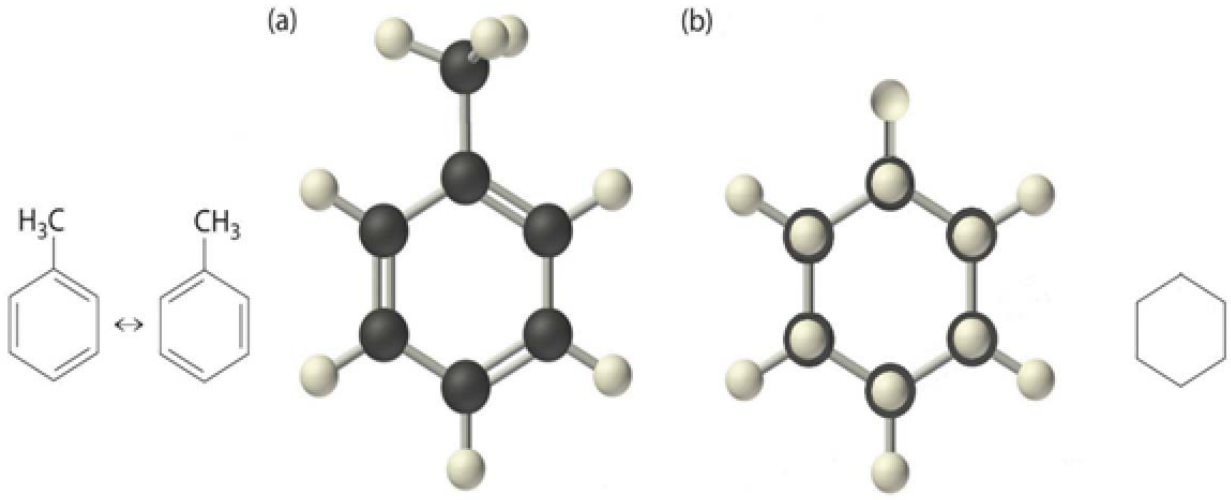


Figure II-2: Structures of the aromatic toluene (a) and the non-aromatic cyclohexane (b).

# II.C. Confining Materials

## II.C.1. Types of Porous Materials

### II.C.1.1. Microporous Materials

#### *II.C.1.1.i. Zeolites*

Microporous systems are typically systems with a pore diameter ranging between 0.3 and 2 nm.[8] Zeolites are a widely renowned type of microporous materials with a central position among the most important materials in contemporary technologies as they have tremendous applications in industrial, petrochemical [51] and many other fields of chemistry in addition to their application in gas separation and storage.[52] Moreover, zeolites are among the most commercially important classes of catalysts [53] with catalytic activities related to their acidic surface and their distinctive properties. For instance, their porosity yields relatively large internal surface areas and the uniformity of their channel sizes and pores accounts for their catalytic selectivity**.** Moreover, their pure inorganic nature makes them extraordinarily robust. A quality which makes them particularly convenient for catalysis under extreme conditions.

The general formula of the zeolite is $M_{x/n}[(A1O_2)_x(SiO_2)_y].zH_2O$, x and y being integers and y/x ratio being greater than or equal to 1, n is the valence of the monovalent cation (M) and finally z is the number of water molecules in each unit cell. Zeolites are crystalline compounds with a 3D structure formed by $TO_4$ tetrahedra, T being either one of the three ions Al, Silicate or phosphate forming a microscopic unit cell.[51] These unit cells connect again in a secondary structure: truncated octahedron, consisting of 8 octahedral faces. This assembly strongly depends on the ratio between Si and Al. Based on this criterion we can differentiate between two commercial zeolites, type A with a ratio of Si/Al=1 and type X and Y having a ratio between one and five, illustrated in Figure II-3.

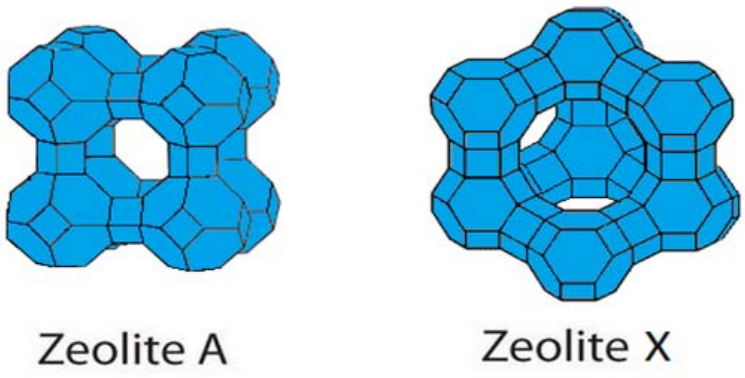


Figure II-3: Two types of zeolites, A and X, with a Si / Al ratio 1 and 1 to 5 for A and B respectively.

#### *II.C.1.1.ii. Metal Organic Framework*

Besides zeolites, a brand new generation of microporous materials, MOF (Metal-Organic Framework) has emerged and advanced extensively during the past years. MOFs are inorganic/organic hybrid materials comprising a self-assembly of coordinating centers of metal ions linked with bridging organic ligands producing adjustable porous host materials. The strong nature of their coordination bonds make them robust solids with high thermal/ mechanical stability and a well-defined geometrical and crystallographic framework structure.

This new family of materials with the 'reticular design' concept enabled the tailoring of novel solids with regular porosity from the micro to nanopore scale. Various architectures can be designed and assembled from a variety of molecular building blocks with different interactions to form a network.[54] This remarkable feature allows facile optimization of the pore structure, surface functionalization and other properties for specific applications which is quite a disguise from zeolites which have steady porous structures and are restricted by rigid tetrahedral oxide skeletons making them difficult to be altered.

MOFs are a vividly explored domain due to their significant properties in many fields including optics, molecular recognition, catalysis and drug delivery. [55-58] Moreover, their most promising applications yet to come is gas storage and separation thanks to their large surface areas, adjustable pore sizes and tunable surface properties which qualify them to be ideal adsorbents.

### II.C.1.2. Mesoporous Materials

Ordered mesoporous materials have attained a great role of importance due to their numerous applications as catalysts and adsorbents in different technological fields (chemistry, biochemistry, environment….). The mainly renowned models of mesoporous materials are oxides (silica, alumina), porous silicon and polymeric membranes. Silica-based mesoporous materials, have particularly attracted further attention in material science due to their textural and morphological properties (large pore volumes, high specific surface areas, narrow pore size distribution and regular pore structure). In this part, we will shortly go over different types of mesoporous materials and highlight the ones used in this study.

Silica aerogels are extremely porous disordered silica (80 to 99% porosity) obtained by hydrothermal condensation of a silica precursor. A limitation of these materials is that although a large variety of sizes is available, they exhibit disorders both in topology and pore size distribution. Aerogels are formed by highly interconnected nanosilica filaments forming a

complex network with a fractal geometry at large scales.[59]This structuration is very interesting in the study of the effects of quenched disorder on phase transitions as well as the study of fundamental aspects of statistical physics: super fluidity of helium, spinodal decomposition, criticality of phase transitions in binary mixtures and liquid crystals…[60, 61]

Vycor is a silica obtained by spinodal decomposition of a $SiO_2$ and $B_2O_3$ mixture. It is a disordered system of interconnected channels yet regular diameter. Another type of materials is Porous silicon (SiP) and anodic aluminum oxide (AAO) which are membranes bearing parallel straight channels among them. The former has a relatively large poly-dispersity with a significant surface roughness and is interesting for studying the effects of unidirectional quenched disorder on the criticality of phase transitions in liquid crystals.[62, 63]

While the physics of the molecules confined in zeolites is essentially dominated by the molecule / adsorbate interaction, confining in mesoporous systems allows exploring a whole new situation, for which the reminiscent collective properties of the bulk phase (cooperative dynamics, phase transitions, and medium-range order) are present in the 'nanophase'.

New families of mesostructured porous silicas have emerged in the beginnings of the 90s.The major innovation in this field was the synthesis of M41S series, including MCM-41 (Mobil Composition of Matter No. 41).[64, 65] More recently, other related families of materials (SBA-15 in 1998 )[66] and their carbon replica CMK-3 [67] were introduced.

#### *II.C.1.2.i. MCM-41*

MCM-41 molecular sieves, the best known representative member of the M41S family of crystalline mesoporous materials have gained enormous interest in the past decades. Their significance is based on their simple, firm yet flexible structure of honeycomb-type lattice with a uniform hexagonal array of parallel cylindrical pores.

This type of mesoporous materials is synthesized via an original hydrothermal synthesis known as the 'template method'. They are obtained by the condensation of amorphous silica ($SiO_2$) in water assisted by the self-assembled micelles of the cationic CTAB surfactant in a basic medium. The resultant pore geometry is obtained from the imprint of the surfactant's liquid-crystal hexagonal template phase. The synthesized materials exhibit specific surface areas, well-defined morphologies and narrow pore size distributions with adjustable pore diameters in the range of 2 to 8 nm. These exceptional structural properties, as well as the precise tuning

of pore size, grant MCM-41 many possible applications in different technological fields: catalytic bulky molecule conversion, adsorptions, separations, host–guest chemistry…

It is considered to be an ideal system for the investigation of the behavior of our confined fluids due to its cylindrical, highly monodisperse and easily tunable pore structure.[64, 68] In addition, its pores are aligned and straight with no intersections. Since it is in the powder form, then it has no macroscopic alignment (like AAO or PSi); however, a compensating advantage is the availability of a large amount of the material which is required for QENS experiments. Another major advantage of this material is the crystalline arrangement of its pores on a lattice, which is a key ingredient for SANS experiments and structure determination of the confined mixtures. Furthermore, it has a meso-size (not micro) which allows bulk reminiscent behaviors of the confined liquids.

Therefore, we chose MCM-41 to be the matrix in which we confine our binary liquids to explore their behavior at the lower mesoporous region (D= 2-4nm) which accounts to a few molecular diameters. The details of the synthetic procedure used in this thesis and the characterization of the materials obtained are given later.

#### *II.C.1.2.ii.SBA-15*

An astonishing turning point in the synthesis of ordered mesoporous materials has been attained by Zhao et al. who managed to synthesize SBA-15 type materials, a brand new type of hexagonal Micelle-Templated Silicas bearing large BET surface areas, large pore sizes (5 to 30 nm), thick pore walls (3.5 to 5.3 nm) and narrow pore size distributions. Such materials are prepared by a template-based sol–gel synthesis where a silica precursor (TEOS) is polymerized in an acidic medium around an amphiphilic nonionic triblock copolymer (Pluronic $P_{123}$): $(EO)_{20}(PO)_{70}(EO)_{20}$ as a template. Thus yielding two-dimensional long range hexagonally ordered (p6mm) silica structures. [66, 69]

The produced solids are subjected to hydrothermal treatments. The judicious choice of thermal parameters can determine the geometrical properties of the resulting SBA-15.[70] For instance, the pore diameter can be easily tuned by varying the temperature of postsynthesis hydrothermal restructuring procedures.[71] These thermal treatments supply SBA-15 with larger pore sizes and thicker pore walls compared to their MCM-41 opponents which provides them with extra mechanical and hydrothermal stability. Furthermore their larger pores make them superior over the latter in catalysis and separation applications.

Nevertheless, several recent studies have shown that SBA-15 silica does not represent such an ideal matrix. Their cylindrical mesopores are renowned to have a complex wall structure, modelled by corrugated pore walls and/or a microporous region close to the pore wall often denoted as a 'microporous corona'.[72-75]

The use of SBA-15 type materials in this thesis is of great importance as the larger pore diameter (D= 8-9 nm) could allow us to distinguish between the scenario of 1 interfacial layer of the hydroxyl-bearing liquid at the pore surface and the total segregation of the liquids confined in the pore. This was difficult in MCM-41 whose diameter (D= 2-4 nm) is equivalent to a few molecular layers which is not sufficient for a true discrimination between the two models.

#### *II.C.1.2.iii. CMK-3*

CMK-3 mesoporous carbon is the hydrophobic replica of SBA-15 retrieved using sucrose as the carbon source.[76] The structure of the carbon comprise a hexagonal arrangement of 1-D carbon rods. The large mesoporous SBA-15 channels are interconnected through smaller pores randomly located perpendicular to the unidimensional pores. Due to the complex 3-D structure, SBA-15 silica can be converted to the negative carbon replica exhibiting the same kind of structure. Our aim is tuning the chemical nature of the pore walls to change the type of liquid-surface interactions which could result in different nanostructuration.

## II.C.2.Synthesis

### II.C.2.1. Synthesis of MCM-41

The porosity of MCM-41 (crystalline arrangement of pores and pore size) is directly linked to the chemical nature and in particular the length of the carbon chain of the surfactant used, as well as the optional addition of organic substances such as 1, 3, 5-trimethylbenzene.[77]

In our case the structuring material used as a template is hexadecyltrimethylammonium bromide (Aldrich $C_{16}$TABr 98%) a water-soluble cationic surfactant whose chain is formed of 16 carbons with $CH_3$ $(CH_2)_{15}N$ (Br) $(CH_3)_3$ as a molecular formula (Fig. II-4). It is in the form of a white powder which forms micellar aggregates when dissolved in water. Tetraethoxysilane (TEOS Aldrich 98%) has a molecular formula of Si $(OC_2H_5)_4$ and is a colorless liquid used as the silica source. In addition, an aqueous ammonia solution $NH_4OH$ (Aldrich 32%) was used as a base catalyst for the chemical reaction of condensation of the silica mesophase.

The samples of MCM-41 used were obtained from a protocol to prepare about 5 g of the porous medium.[78] 4.8g of $C_{16}$TABr was dissolved in 240 ml of distilled water; the mixture was stirred

at a speed of 700 rev / min (rpm) for 15 to 20 minutes until a clear solution was obtained (pH ~ 5.4). To accelerate the chemical reaction the mixture was slightly heated to about 40 °C. 16 mL of aqueous ammonia solution were then added to catalyze and regulate the pH of the reaction (pH ~ 11) followed by 20 mL of TEOS as the silica source. The temperature was maintained at around 40 °C for two hours to ensure that the reaction is complete. To collect the white precipitate obtained, Buchner filtration was done upon simultaneous washing with distilled water (300 ml) to get rid of the remaining base and any excess reactants. The powder was then oven dried at 90 °C for 17 hours to ensure the evaporation of the remaining water. The final step was calcination to eliminate the reminiscent surfactant. It was carried out by rising the temperature gradually from ambient to 550 °C in a 5 hour ramp, followed by a plateau of calcination at 550 °C for another 5 hours.

### II.C.2.2. Synthesis of SBA-15

The structuring material used as a template for SBA-15 synthesis is the nonionic triblock copolymer (Pluronic P123) (Aldrich) (Fig. II-4) which is in a viscous gel form. TEOS (Aldrich 98%) is used as the silica source and HCl (Aldrich 38%) is the acid catalyst for the silica condensation reaction. SBA-15 was prepared using the original procedure reported by Zhao et al.[69] with a few modifications in the thermal treatments during synthesis based on the study of Brodie-Linder et al. on the effect of hydrothermal treatment on the final structure of the mesoporous silica.[70]

A typical synthesis of a SBA-15 material was carried out using the following procedure. Pluronic (4.0 g) was dissolved in a solution of distilled water and concentrated HCl 38% (125 and 25 g, respectively). After stirring for 3 h at $T_1$= 40°C, TEOS (8.6 g) was added. The solution was vigorously stirred for 10 min. Then the flask was stoppered and aged for 24h at the same temperature (40°C). At this point, the temperature was adjusted to $T_2$= 100°C and the mixture was aged again for 24 h under reflux in static conditions. The resulting white solid was Buchner filtered while being washed with 300ml of water (to eliminate the acid and excess reactants), dried at room temperature for 24 h then placed in a furnace where it was heated under air at 550°C for 18 h. A white powder of SBA-15 was thus collected.

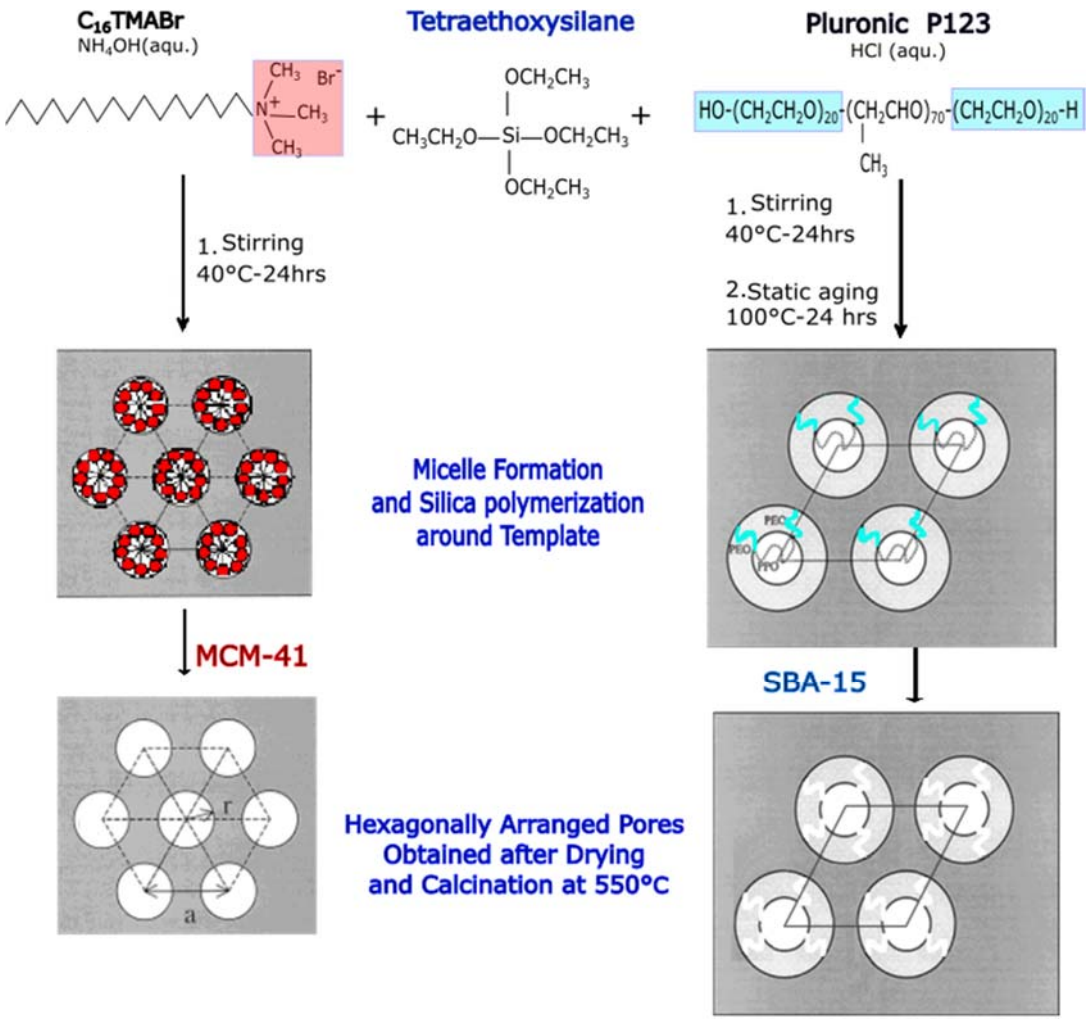


Figure II-4: A scheme for the synthesis of MCM-41 and SBA-15. Some of the figures are taken after [72].

### II.C.2.3. Synthesis of CMK-3

CMK-3 mesoporous carbons were prepared from SBA- 15 template and sucrose carbon source.[76] In a typical CMK-3 synthesis,[76] 1 g of SBA-15 was added to a solution obtained by dissolving 1.25 g of sucrose and 0.14 g of $H_2SO_4$ in 5 g of water. The mixture was maintained in an oven for 6 h at 100 °C. The temperature was then increased to 160 °C for another 6 h. To guarantee full polymerization and carbonization of sucrose within the pores, 0.8 g of sucrose, 0.09 g of $H_2SO_4$ and 5 g of water were added again to the pretreated sample. Afterwards, the sample was subjected to the same thermal treatment. Pyrolysis of the template-polymer composites was carried out at 900 °C under Nitrogen flow to avoid any oxidation reactions. These conditions were maintained for 6 h to ensure complete carbonization of the polymer. It should be mentioned that the last step in the typical synthesis (to eliminate the silica network) was not performed in order to preserve the ordered hexagonal framework of the SBA template.

## II.C.3. Characterization

Five techniques were conducted to characterize the structure and properties of the porous media. Nitrogen adsorption isotherms help us to determine the area of the specific surface, pore volume, pore size distribution and the pore diameter. TEM (Transmission Electron Microscopy) and SEM (Scanning Electron Microscopy) give us a direct vision of the pore channels in terms of organization and morphology of the crystallites of MCM-41 and SBA-15 on complementary spatial scales (from 10 nm to 100 nm). Finally neutron scattering and X-rays reflect the crystalline nature of the hexagonal arrangement of these pores resulting in Bragg peaks which allow us to gain direct access to information about the unit cell parameters. The parameter values obtained are reported in a summary table at the end of this chapter.

### II.C.3.1. Microscopy

#### *II.C.3.1.i. SEM (Scanning Electron Microscopy)*

SEM is a microscopy which allows to provide an insight on the surface topology of the object studied with a resolution of several tens of nm. The image is formed after the bombardment of the sample by a focused electron source. The electron beam interacts with the atoms in the sample causing their excitement and thus emission of secondary electrons which are collected by a detector to form an image. Fig. II-5 shows the images of MCM-41 (A, B, C) and SBA-15 (D, E, F), as measured by scanning electron microscopy (SEM) after calcination.

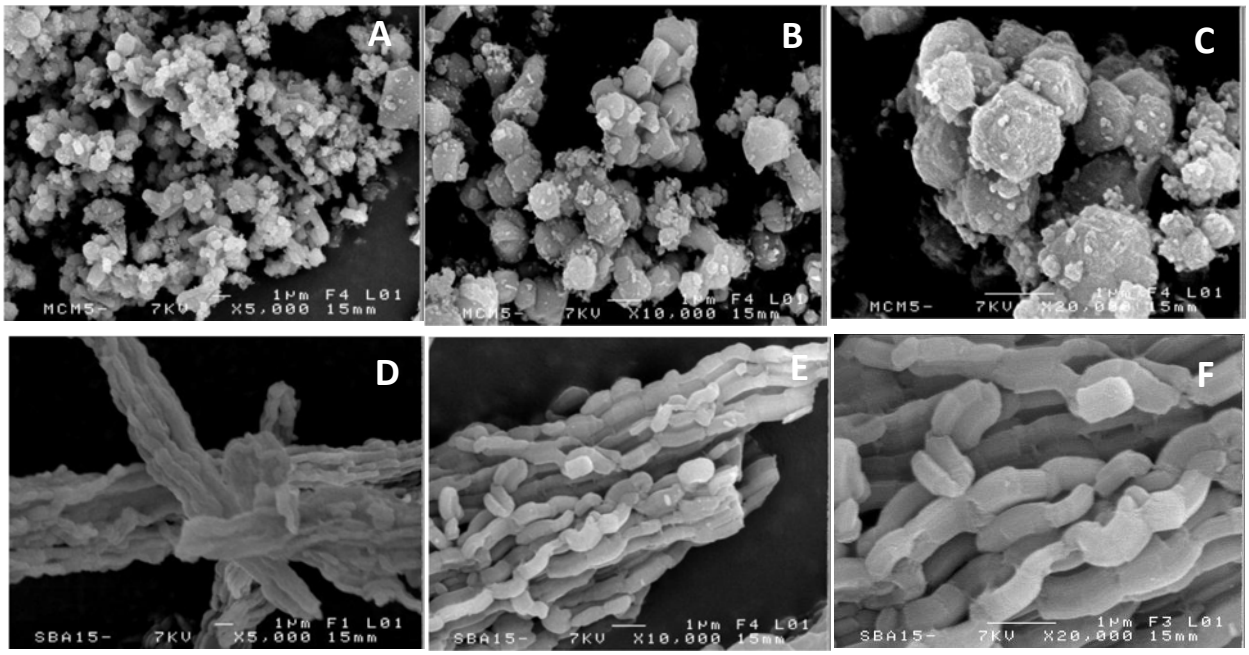


Figure II-5: SEM images of MCM (A, B, C) and SBA (D, E, F) zoomed 5000X, 10000X, and 20000X.

This measurement was conducted at the microscopy platform (CMEBA) of the University of Rennes 1 in collaboration with Joseph Le Lannic. The upper images corresponding to MCM-41 crystallites show the shape and size of the agglomerates suggesting that they are hexagonal (image C) with a size of about 1µm. The SBA-15 images in the bottom show aggregates in the form of braided needle-like rods with "welded" end to end whose lengths (approximately 1,5µm) inform about the length of the pore. Although this technique gives us a concrete vision on the morphology of our materials, it lacks enough resolution to observe pores <10nm, which led us to resort to transmission electron microscopy for complete microscopic characterization.

### *II.C.3.1.ii.TEM (Transmission Electron Microscopy)*

TEM creates images with a much higher resolution than SEM, allowing in some cases to achieve atomic resolution. The measurements for MCM-41 were conducted at the Institute of Materials of Nantes (IMN), as part of a project supported by the Nanofonc network, in collaboration with Nicolas Gautier. As for SBA-15 the measurements were conducted in the Nanobiomedecine center in Poznan in collaboration with Grzegorz Nowaczyk.

Fig. II-6 shows TEM images of MCM-41 (A, B) and SBA-15 (C, D) obtained after calcination. Parts (A, C) are a parallel viewing direction to the axis of the MCM and SBA channels respectively. The former shows the hexagonal arrangement of MCM in the plane perpendicular to their main axis. The latter is; however, a low magnification image where only overlapping of several crystallites is observed. Parts (B, D) are a perpendicular observation to the channel axis of MCM and SBA showing the linear arrangement of the pore channels along their lengths showing that pores in both matrices are aligned in a parallel manner.

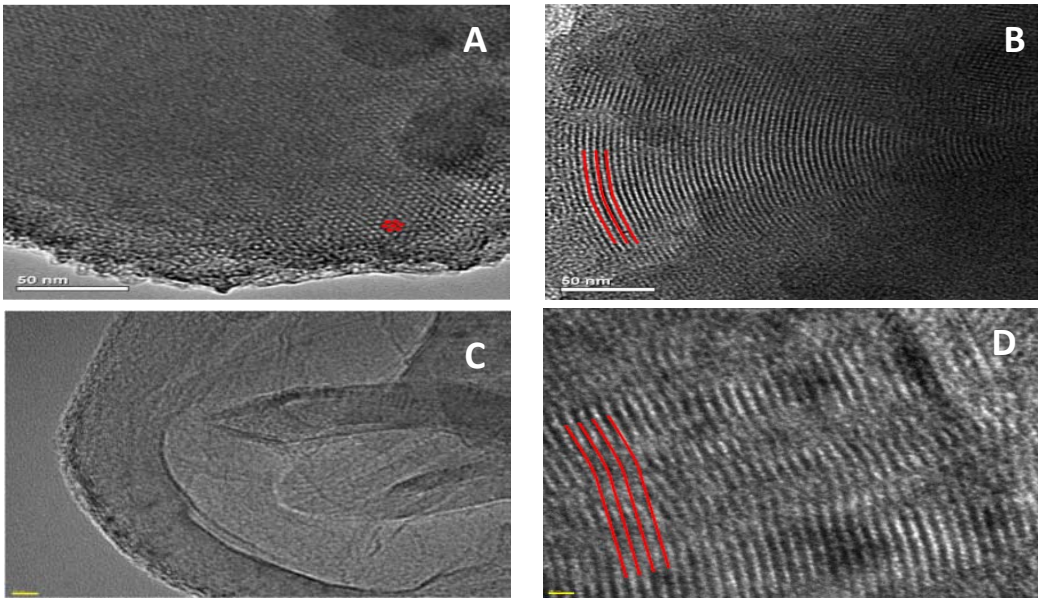


Figure II-6: TEM images os MCM-41 (A, B) and SBA-15 (C, D) with A and C being parallel to pore axis and B and D being perpendicular.

### II.C.3.2. Diffraction

#### *II.C.3.2.i. X-ray Diffraction*

X-ray scattering has been used extensively in the last century as the most effective method for accurate determination of the structure. The advantage of setting at small angles is the ability to probe matter at nanoscale (1 to 100 nm). X-rays interact elastically with the electron cloud of the material and the scattered photons through the material give information about fluctuations in the electron density. The samples studied are hexagonally ordered mesoporous MCM-41 and SBA-15. Therefore the electron density changes from near zero (empty core) to that of silica resulting in a very intense signal of the porous network.

The first Miller index (hk) in a hexagonal lattice is 10, which provides direct information on the long-range order on the organization of the network of pores. It allows the determination the interplanar spacing ($d_{10}$) using the Bragg relationship (II-1):

$$2d \sin\theta = n\lambda$$
$$\text{And } \sin\theta = Q\frac{\lambda}{4\pi}$$
$$\text{Thus } d = \frac{2n\pi}{Q} \qquad \text{(II-1)}$$

For hexagonally packed pores, the interplanar spacing ($d_{10}$) allows the calculation of the unit cell parameter $a$ which is the distance between the centers of two adjacent channels according to the equation (II-2) (see e.g. Kruk et al.) [79]:

$$d(hk) = \frac{a}{\sqrt{\frac{4}{3}(h^2+k^2+hk)}}$$
$$\text{Therefore, } a = \frac{2d_{10}}{\sqrt{3}} \qquad \text{(II-2)}$$

The pore wall thickness is thus deduced as a difference between the unit cell parameter $a$ and mesopore diameter. The measurements were performed at the Institute of Physics of Rennes I in collaboration with Cristelle Mériadec and Franck Artzner at ENSCR on a small angle rotating anode device. The conditions at which the experiment was conducted are: λ= 1.54Å, distance to sample= 423.25mm, T= 25 ° C, I= 40mA and V= 40K. A radial integration allows to measure the diffracted intensity versus scattering vector Q or the scattering angle. Calculations were performed using the "Fit2D" software (developed at ESRF).

The powder X-ray diffraction patterns (see Fig. II-7) obtained for the synthesized SBA-15 and MCM-41 materials exhibit reflections due to the (1 0), (1 1), (2 0) and (2 1) planes which is what to be expected for a hexagonal array of mesopores. The Bragg peaks of MCM-41 appear at higher Q values which indicates the more compact lattice they exhibit. This is related to their smaller pore diameters and thinner walls therefore resulting in a lower unit cell parameter ($a$).

SBA-15 (B) was measured by X-rays. Its diffraction pattern possess several Bragg reflections characteristic for the $p_{6mm}$ symmetry. CMK-3 was synthesized from this SBA-15, its diffraction pattern shows well defined (1 1) and (2 0) reflections. This indicates that the hexagonal structure is not altered by the modification of the SBA surface. However, a decrease in the absolute intensity (the difference is in the order of 5, not shown here for clarity) and the disappearance of the 4$^{th}$ order Bragg peak (2 1), indicates a somewhat lower structural ordering.

It is worth noting; however, that the last observation could also be caused by a coincident zero value of the pore form factor (P(Q)) at the same Q position of the 4$^{th}$ Bragg peak. The latter being indeed modified by the carbon coating. Moreover a shifting to higher Q values is witnessed which indicates a shrinking in the matrix due to the carbon layer formation at the pore wall and the high temperature pyrolysis of the template- polymer composites (900°C).

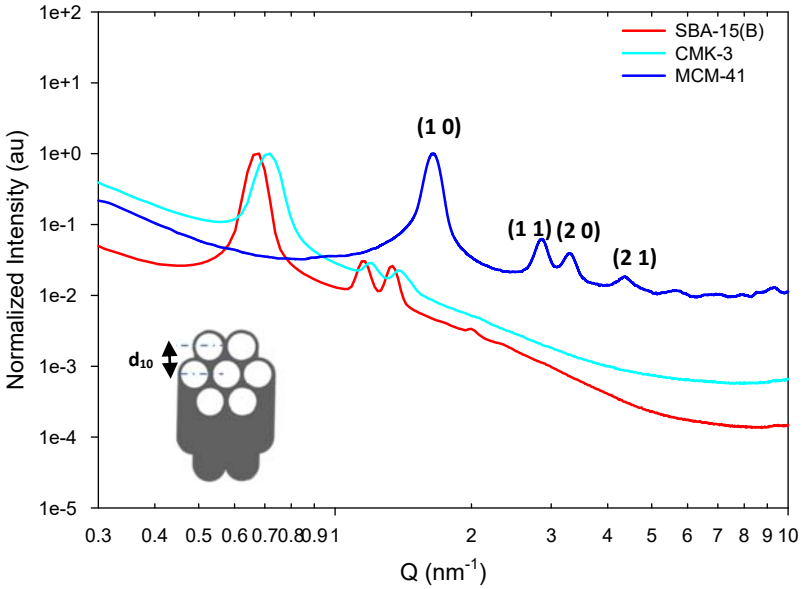


Figure II-7: XRD patterns of and SBA (B) (red), CMK-3 (light blue) and MCM (dark blue). The intensities are normalized to the 1st Bragg peak (Log scale). 4 Bragg peaks are shown for MCM-41 indexed (1 0), (1 1), (2, 0) and (2, 1).

### *II.C.3.2.ii. Neutron Diffraction*

Two different instruments were used for the collection of the diffraction patterns of the materials. MCM-41 was measured on G6.1 spectrometer LLB (Saclay) with an accessible momentum transfer range (Q) of 0.12 to 1.79 $Å^{-1}$. SBA-15 samples were measured on PAXY a SANS instrument at LLB with a Q range ($3x10^{-3}$ $Å^{-1}$< Q < 1 $Å^{-1}$). Isotropic integration was done by an LLB software (Regiso) and the normalization was done using a python script. The detailed information about the theory of the technique as well as the data corrections will be thoroughly illustrated in the corresponding chapters.

Measuring the intensity distribution of MCM-41 and two batches of SBA-15 (A and C) is illustrated in Fig. II-8. Neutron diffraction gives four Bragg peaks which are identified in the spectrum for the three porous media. These peaks confirm their hexagonally ordered crystalline arrangement,[68] which is in accordance with X-ray data.

It should be mentioned that the resolution is worse in the case of neutrons due to a broader wavelength dispersion, making x-rays superior to neutron diffraction with a better resolution of the individual diffraction peaks without overlap.[75] Nevertheless, we used neutron diffraction thoroughly in our studies due to the ability of the manipulation of the scattering length through H/D mixtures. This allows us to highlight one component over the other, a quality of neutrons superior to X-rays.

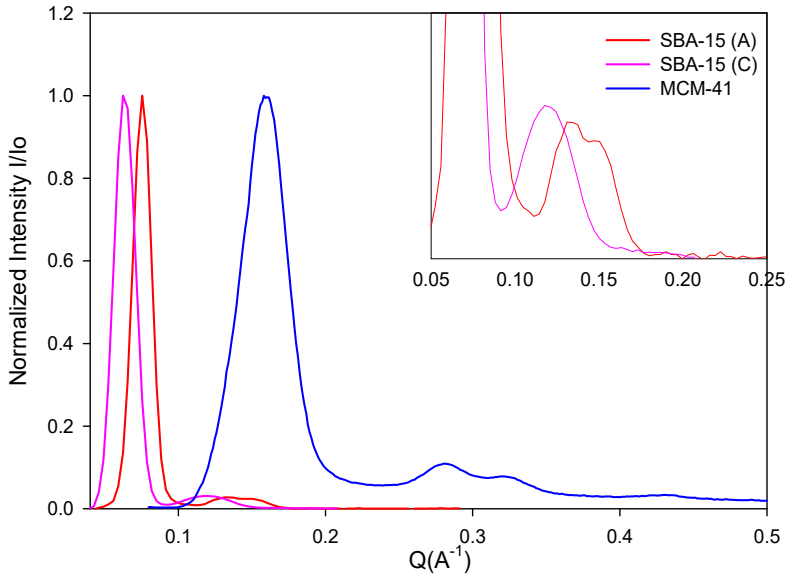


Figure II-8: Normalized static structure factor of SBA-15(A) (red) and SBA-15(C) (pink) and MCM-41(blue). The offset shows the 1st, 2nd and 3rd order Bragg peaks of the two SBA batches.

### II.C.3.3. Adsorption Isotherms

The prolific discovery of ordered mesoporous materials, unleashed new possibilities in the evaluation of surface area and porosity. The new well-defined MCM-41and SBA-15 molecular sieves are particularly suitable as model adsorbents. The reason why these solids are highly adequate for adsorption measurements is because they exhibit a tunable pore size, reproducible surface properties and most importantly highly ordered hexagonal geometry of their uniform cylindrical pores.

The term "adsorption" was created in 1881 by Kayser, which is defined by the increase in the fluid molecular concentration (gaseous or liquid) along the walls of a solid. It is a surface phenomenon that takes place at the interface of a solid adsorbent on one side and a fluid on the other side, as noted by Fontana and Scheele in 1771.

Adsorption is based on the vapor condensation at the surface and the inside of the pores via surface interaction. For a sufficiently large pore size, which is the case of nitrogen /MCM-SBA systems, it takes place as a capillary condensation phenomenon. The latter is associated with a phase change which is reminiscent of the gas -liquid transition appearing at the saturated vapor pressure for the same system in bulk. Capillary condensation takes place at a pressure P smaller than the fluid saturation pressure $P_0$ at a given temperature.[51] The value of $P/P_0$ at which the phenomenon takes place depends on the geometry and size of the pore, the liquid-interface tension as well as the forces of interaction between the fluid and the wall surface.

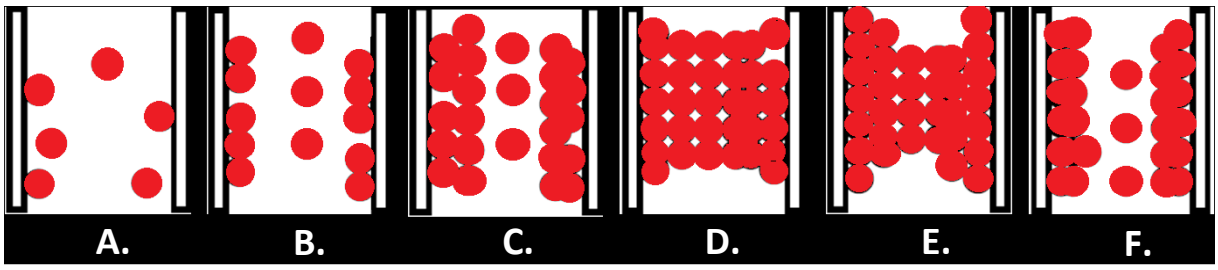


Figure II-9: A schematic representation of the steps of gas adsorption in porous materials.

We performed nitrogen adsorption studies at 77K on ASAP Micromeretics type equipment. These measurements were done in collaboration with Odile Merdrignac and Nathalie Pontais at the Institute of Chemical Sciences of Rennes. Before the measurement was conducted, the sample was degassed under vacuum for several hours. The measurement was performed by successive injections of a calibrated amount of nitrogen after a balance test

up to the saturated vapor pressure $P_0$. The resulting adsorption isotherms (a representation of the adsorbed amount of $N_2$ in terms of the relative pressure) for MCM-41 and SBA-15 are shown in Fig. II-10. Their general profile can be interpreted as expected considering the different regimes in the case of adsorption in a cylindrical mesopore and can be summarized in 5 steps denoted (A) to (F) [51] as demonstrated in Fig. II-9.

In (A), the rapid growth of the amount adsorbed at low pressure is relative to the adsorption of a monolayer of nitrogen localized on the inner surface of the pore. This regime ends with the appearance of phase (B) in which the adsorbed amount of $N_2$ increases slowly. This second stage is associated with the formation of multilayers of the gas. An abrupt increase in the adsorbed amount then appears between (C) and (D). This observation is the signature of the capillary condensation phenomenon which is triggered in the pore center, after reaching a critical thickness of the vapor adsorbed. After point (D), a plateau appears up to saturation pressure, which indicates the complete filling of the pore volume. The desorption curve (marked by the down arrow) is coincident with the adsorption curve in all regions except that corresponding to the capillary condensation. The latter takes place at a lower pressure during desorption, between the points (E) and (F). The existence of a hysteresis loop is characteristic of capillary condensation in the mesopore system and is generally associated with the nature of the first order transition.

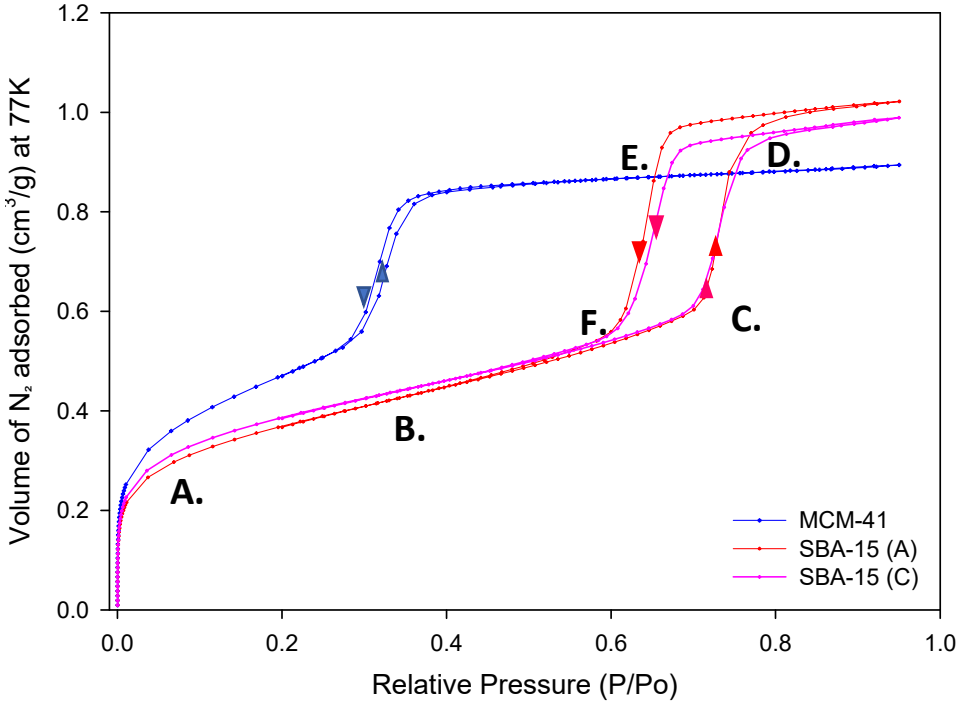


Figure II-10: Adsorption isotherms of MCM-41 (blue), SBA-15 (A) (red), and SBA-15 (C) (pink).

### II.C.3.4. Analysis of the Adsorption Isotherms

The analysis of the adsorption isotherms is abundantly used in materials science for the characterization of the porous media: the specific surface area measured in $m^2/g$, the pore volume measured in $cm^3/g$ and the size distribution of the pores as a function of the average pore diameter.

The total pore volume can be deduced from the amount of adsorbate (gas nitrogen in the most common case) expressed $cm^3$ STP (standard pressure and temperature conditions) measured by the BET theory (Brunauer, Emmett and Teller).[80, 81] The use of this model allowed us to determine the specific surface and pore volume of our materials (summarized in a table at the end of the chapter). Furthermore, the analysis of the part corresponding to the capillary condensation according to the Barret, Joyner and Halenda (BJH) theory allowed us to obtain a first estimate of the value of the pore diameter of MCM-41.[82]

In addition to BJH, it is also possible to combine diffraction data and adsorption isotherms for determining the pore diameter. This method was developed by Kruk et al. [79, 83] and is particularly recommended for mesoporous systems with a hexagonal crystalline order (MCM-41 and SBA-15 ). We used the improved version of the KJS method dedicated for the pore size analysis of larger SBA-15 molecular sieves to determine the pore sizes of our samples.[84] In the following section we will focus on the theoretical framework of these $N_2$ isotherm-based approaches for sample characterization.

#### *II.C.3.4.i.Specific Surface Area (BET):*

The Brunauer - Emmett - Teller theory (BET) in 1938 is the most commonly used method to determine the specific surface area from measuring an adsorption isotherm.[80] It is based on the theorem of Langmuir assuming that the adsorption corresponds to the filling of an entire monolayer on the surface of the pores which allows the calculation of the specific surface area. The BET model applies to other cases in which successive multilayer stacks occur. The values of the specific surface BET ($m^2/g$) for MCM-41, SBA-15 (A) and SBA-15 (B) are mentioned in a characterization table at the end of this chapter. These values were deduced from the model by calculating the amount of the nitrogen adsorbate required for forming a single monolayer, according to equation (II-3) defined by:

$$S_{BET} = \frac{V_m . \sigma . N_A}{m . V_0} \cong \frac{4.35 * V_m(cm^3 STP)}{m(g)} \qquad \text{(II-3)}$$

Where $V_m$ is the volume of the adsorbate ($N_2$) to adsorb to a monolayer, σ is the specific surface area occupied by a gas molecule ($\sigma_{N2}$= 0.1620 $nm^2$), $N_A$ is Avogadro's number, m is the mass of the porous sample and $V_0$ is the molar volume of nitrogen.

Application of the BET model is based on several fundamental assumptions: first, the same forces involved in the condensation of the gas are responsible for the binding energy (in the case of multimolecular adsorption). On the other hand, it assimilates the condensation rate of the gaseous molecules on an already adsorbed layer to the evaporation rate of that layer. By adding an infinite number of layers we can deduce the equation (II-4).[85]

$$\frac{1}{V_A * \left[\left({}^{P_0}/_{P}\right) - 1\right]} = \frac{1}{C.V_m} + \frac{C-1}{V_m.C} \cdot \frac{P}{P_0} \qquad \text{(II-4)}$$

In equation (II-4), $V_A$ is the adsorbed nitrogen volume measured at a given pressure, C is a constant characteristic of the pore surface/adsorbate interaction and $V_m$ is the volume of gas necessary for the formation of a monolayer.

Plotting the isotherm in the new set of coordinates suggested by equation (II-4) gives a straight line in the range of validity of this hypothesis. The values of $V_m$ and C parameters, are thus deduced from the slope and y-intercept of this line respectively.

#### *II.C.3.4.ii. Pore size distribution (BJH):*

The (BJH) method developed by Barret, Joyner and Halenda (1951) is based on the Kelvin equation, which relates the pore size with the capillary condensation pressure. Thus, it can be successfully implemented to virtually all types of porous materials having their adsorption isotherms within a pressure range corresponding to capillary condensation (such as MCM-41 and SBA-15).

A correction to the Kelvin equation was introduced in BJH due to the increased awareness of the importance of thin film formation on adsorption. This model is therefore based on the assumption that the pores have a cylindrical shape and that the pore radius is equal to the sum of the Kelvin radius and the thickness of N stacked layers adsorbed on the pore wall. This method allows modeling the variation of the thickness as a function of the relative pressure. Hence, it is a direct link between the geometric pore data and thermodynamic data deduced from the adsorption isotherms.

This method can also account for pore size distribution, taking into account the fact that the capillary condensation doesn't take place at a single pressure but rather in a domain of pressures associated to the different pore sizes. Therefore, the volume desorbed at a given relative pressure P either comes from the gas condensed in the smaller pores (capillary condensation pressure<P) or the decrease in the thickness of the adsorbed layer on the surface of the larger pores which have been already emptied of the condensed gas (capillary condensation pressure>P) as expressed in equation (II-5). The thickness of the multilayer adsorbed (t) is defined in equation (II-6).[86]

$$dV_{des} = dV_{cond} + t.S_{pore} \quad \text{(II-5)}$$

$$t = 354\left[\frac{-5}{\ln\left(P/P_0\right)}\right]^{1/3} \quad \text{(II-6)}$$

Fig. II-11 shows the narrow pore size distribution of SBA-15 (A) sample obtained from the adsorption and desorption branches of the material. The broadness of the pore size distribution in SBA-15 can be attributed to two factors: The 1st is the heterogeneity of the average diameter of the different channels in the structure and the 2nd is the variation of the channel diameter along single channels.

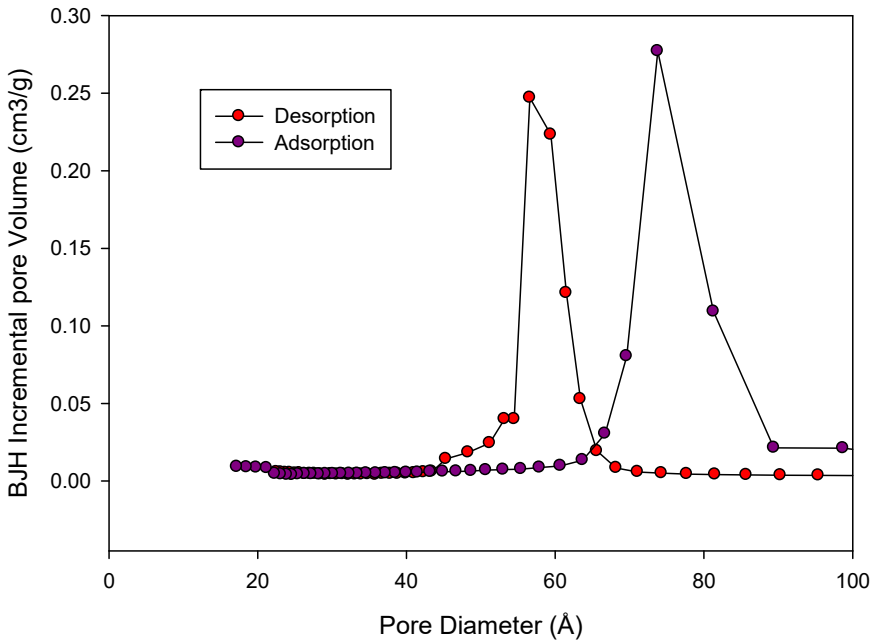


Figure II-11: Pore size distribution of SBA-15(A) obtained from the desorption and adsorption branches.

### *II.C.3.4.iii. KJS Method*

KJS named after Kruk, Jaroniec, and Sayari (KJS) who developed in 1997 a simple method for pore size analysis of ordered mesoporous materials.[79] This method is based on the BJH algorithm.[82] The main development that has been implemented in BJH is the use of XRD measurements and nitrogen adsorption isotherms of hexagonally ordered mesoporous materials in an approach to provide accurate relations for the pore width as a function of the capillary condensation pressure and for the statistical film thickness as a function of the equilibrium pressure.

A major improvement of the KJS method over other methods is the independent evaluation of the pore diameter through its direct relation with the inter-planar spacing equation (II-7).

$$D_p = 1.213 d_{10} \left( \frac{\rho_{SiO_2} . V_0}{1 + \rho_{SiO_2} . V_0} \right)^{1/2} \qquad \text{(II-7)}$$

Where $D_p$ is the pore diameter, $d_{10}$ is the inter-planar spacing (deduced from the first reflection of the diffraction data), $V_0$ is the mesopore volume evaluated from the $\alpha_s$-plots extracted from the adsorption isotherms,[79] (could also be extracted from BET) and $\rho_{SiO2}$ being the density of the silica in the pore wall which is generally assumed to be the same as that of the amorphous silica at atmospheric pressure; *i.e.*, equal to 2.2 ($g.cm^{-3}$).

### *II.C.3.4.iv. Improved KJS method*

The KJS method was initially developed and calibrated for the pore size analysis of small pore widths in the range of 2 to 6.5 nm (characteristic of MCM-41). Therefore its accuracy is highly jeopardized in the characterization of SBA-15 which possesses large pore diameters (D= 8-12 nm). This limitation provided the urge for KJS improvement to extend its applicability to ordered mesoporous silicates with large cylindrical mesopores.

For this purpose, small-angle X-ray scattering (SAXS) structure modeling was used. This permitted an accurate reproduction of experimental diffraction patterns hence allowing an accurate determination of the pore width.[87] An analogous expression to the old KJS method was developed with three adjustable parameter fits where *a*, *b*, and *c* represent the best-fit parameters and are equal to 1.15, 0.875, and 0.27 respectively, (t) is the thickness of the adsorbed multilayer and is calculated according to equation (II-9).
Thus, the resulting equation (II-8) can be used to estimate the pore width of various MCM-41 and SBA-15 samples.[84]

$$D_p = -1.15/\left[\log\left(0.875p/p_0\right)\right] + 2t + 0.27 \quad \text{(II-8)}$$

Where,

$$t(p/p_0) = 0.1\left[\frac{60.65}{0.03071 - \log\left(P/P_0\right)}\right]^{0.3968} \quad \text{(II-9)}$$

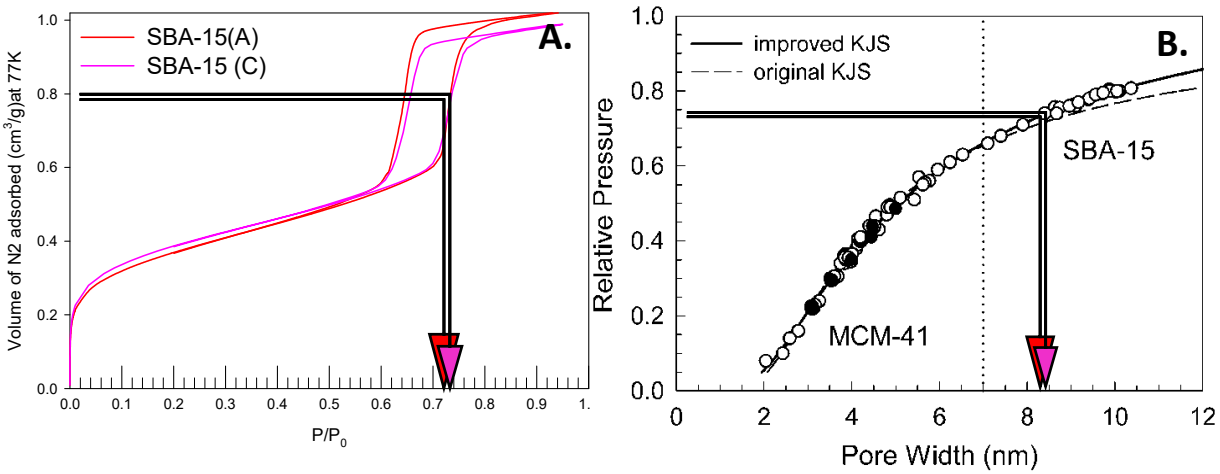


Figure II-12: Improved KJS analysis (determination of capillary condensation relative pressure (A) and its application in (B) [84] to obtain the pore diameter.

### II.C.3.5. Characterization of the Matrices

Table II-1: The $d_{100}$, α, specific surface and pore widths obtained by different techniques.

| | $d_{100}$(nm) | | unit cell parameter(α) (nm) | | Specific Surface ($m^2/g$) | Pore volume ($cm^3/g$) | Pore diameter (nm) | | |
|---|---|---|---|---|---|---|---|---|---|
| | **Xrays** | **Neutron Diffraction** | **Xrays** | **Neutron Diffraction** | **BET** | **(Ads.) at $P/P_0$=0.95** | **BJH (Des.)** | **KJS** | **KJS Improved** |
| MCM-41 | 3.8 | 3.93 | 4.39 | 4.54 | 1106 | 0.67 | 2.9 | 3.9 | 3.9 |
| SBA-15 (A) | | 8.4 | | 9.67 | 822 | 1.02 | 5.7 | 8.7 | 8.3 |
| SBA-15 (B) | 9.52 | | 10.99 | | | | | | |
| SBA-15 (C) | | 9.66 | | 11.1 | 857 | 0.99 | 5.6 | 8.9 | 8.5 |
| CMK-3 | 8.7 | | 10.07 | | | | | | |

# References


1. Frick, B., R. Zorn, and H. Buttner, *1st international workshop on dynamics in confinement.* Journal De Physique Iv, 2000. **10**.
2. Alcoutlabi, M. and G.B. McKenna, *Effects of confinement on material behaviour at the nanometre size scale.* Journal of Physics: Condensed Matter, 2005. **17**(15): p. R461.
3. Alba-Simionesco, C., et al., *Effects of confinement on freezing and melting.* Journal of Physics: Condensed Matter, 2006. **18**(6): p. R15.
4. Morineau, D., Y. Xia, and C. Alba-Simionesco, *Finite-size and surface effects on the glass transition of liquid toluene confined in cylindrical mesopores.* The Journal of chemical physics, 2002. **117**(19): p. 8966-8972.
5. Sliwinska-Bartkowiak, M., et al., *Melting/freezing behavior of a fluid confined in porous glasses and MCM-41: dielectric spectroscopy and molecular simulation.* The Journal of chemical physics, 2001. **114**(2): p. 950-962.
6. Spanoudaki, A., et al., *The dynamics of water in nanoporous silica studied by dielectric spectroscopy.* The European Physical Journal E: Soft Matter and Biological Physics, 2005. **17**(1): p. 21-27.
7. Schildmann, S., et al., *Nuclear magnetic resonance and dielectric noise study of spectral densities and correlation functions in the glass forming monoalcohol 2-ethyl-1-hexanol.* The Journal of chemical physics, 2011. **135**(17): p. 174511.
8. Sing, K., et al., *Physical and biophysical chemistry division commission on colloid and surface chemistry including catalysis.* Pure Appl. Chem, 1985. **57**(4): p. 603-19.
9. Adya, A.K., L. Bianchi, and C.J. Wormald, *The structure of liquid methanol by H/D substitution technique of neutron diffraction.* Journal of Chemical Physics, 2000. **112**(9): p. 4231-4241.
10. Yamaguchi, T., K. Hidaka, and A. Soper, *The structure of liquid methanol revisited: a neutron diffraction experiment at− 80 C and+ 25 C.* Molecular Physics, 1999. **96**(8): p. 1159-1168.
11. Kosztolányi, T., I. Bakó, and G. Pálinkás, *Hydrogen bonding in liquid methanol, methylamine, and methanethiol studied by molecular-dynamics simulations.* The Journal of chemical physics, 2003. **118**(10): p. 4546-4555.
12. Morineau, D., et al., *Structure of liquid and glassy methanol confined in cylindrical pores.* The Journal of chemical physics, 2004. **121**(3): p. 1466-1473.
13. Guégan, R., D. Morineau, and C. Alba-Simionesco, *Interfacial structure of an H-bonding liquid confined into silica nanopore with surface silanols.* Chemical Physics, 2005. **317**(2): p. 236-244.
14. Andanson, J., et al., *Hydrogen bonding in supercritical tert-butanol assessed by vibrational spectroscopies and molecular-dynamics simulations.* The Journal of chemical physics, 2005. **122**(17): p. 174512.
15. Palombo, F., et al., *Spectroscopic studies of the "free" OH stretching bands in liquid alcohols.* Journal of molecular liquids, 2006. **125**(2): p. 139-146.
16. Sassi, P., et al., *Distributions of H-bonding aggregates in tert-butyl alcohol: The pure liquid and its alkane mixtures.* The Journal of Physical Chemistry A, 2007. **111**(27): p. 6020-6027.
17. Bowron, D.T., J.L. Finney, and A.K. Soper, *The structure of pure tertiary butanol.* Molecular Physics, 1998. **93**(4): p. 531-543.
18. Morineau, D. and C. Alba-Simionesco, *Does Molecular Self-Association Survive in Nanochannels?* The Journal of Physical Chemistry Letters, 2010. **1**(7): p. 1155-1159.
19. Kusalik, P.G., et al., *Computer simulation study of tert-butyl alcohol. 1. Structure in the pure liquid.* The Journal of Physical Chemistry B, 2000. **104**(40): p. 9526-9532.
20. Perera, A., F. Sokolić, and L. Zoranić, *Microstructure of neat alcohols.* Physical Review E, 2007. **75**(6): p. 060502.
21. Zoranić, L., F. Sokolić, and A. Perera, *Microstructure of neat alcohols: A molecular dynamics study.* The Journal of chemical physics, 2007. **127**(2): p. 024502.

22. Ghoufi, A., et al., *Hydrogen-bond-induced supermolecular assemblies in a nanoconfined tertiary alcohol.* The Journal of Physical Chemistry C, 2011. **115**(36): p. 17761-17767.
23. Chandler, D., *Interfaces and the driving force of hydrophobic assembly.* Nature, 2005. **437**(7059): p. 640-647.
24. Tabony, J., *Formation of cubic structures in microemulsions containing equal volumes of oil and water.* 1986.
25. Stradner, A., et al., *Equilibrium cluster formation in concentrated protein solutions and colloids.* Nature, 2004. **432**(7016): p. 492-495.
26. Dixit, S., et al., *Molecular segregation observed in a concentrated alcohol–water solution.* Nature, 2002. **416**(6883): p. 829-832.
27. Guo, J.-H., et al., *Molecular structure of alcohol-water mixtures.* Physical review letters, 2003. **91**(15): p. 157401.
28. Wakisaka, A. and K. Matsuura, *Microheterogeneity of ethanol–water binary mixtures observed at the cluster level.* Journal of molecular liquids, 2006. **129**(1): p. 25-32.
29. Dougan, L., et al., *Molecular self-assembly in a model amphiphile system.* Physical Chemistry Chemical Physics, 2010. **12**(35): p. 10221-10229.
30. Bowron, D. and J. Finney, *Association and dissociation of an aqueous amphiphile at elevated temperatures.* The Journal of Physical Chemistry B, 2007. **111**(33): p. 9838-9852.
31. Hennous, L., et al., *Crossover in structure and dynamics of a primary alcohol induced by hydrogen-bonds dilution.* The Journal of chemical physics, 2014. **141**(20): p. 204503.
32. Wang, L.-M., S. Shahriari, and R. Richert, *Diluent effects on the Debye-type dielectric relaxation in viscous monohydroxy alcohols.* The Journal of Physical Chemistry B, 2005. **109**(49): p. 23255-23262.
33. El Goresy, T. and R. Böhmer, *Diluting the hydrogen bonds in viscous solutions of n-butanol with n-bromobutane: A dielectric study.* The Journal of chemical physics, 2008. **128**(15): p. 154520.
34. Formisano, F. and J. Teixeira, *Critical fluctuations of a binary fluid mixture confined in a porous medium.* European Physical Journal E, 2000. **1**(1): p. 1-4.
35. Schemmel, S., et al., *Local structure of a phase-separating binary mixture in a mesoporous glass matrix studied by small-angle neutron scattering.* Journal of Chemical Physics, 2005. **122**(24).
36. Lefort, R., et al., *Phase separation of a binary liquid in anodic aluminium oxide templates.* European Physical Journal E, 2011. **34**(7).
37. Guo, X.Y., T. Watermann, and D. Sebastiani, *Local Microphase Separation of a Binary Liquid under Nanoscale Confinement.* Journal of Physical Chemistry B, 2014. **118**(34): p. 10207-10213.
38. Swenson, J., et al., *Anomalous dynamics of aqueous solutions of di-propylene glycol methylether confined in MCM-41 by quasielastic neutron scattering.* Journal of Chemical Physics, 2014. **141**(21).
39. Elamin, K., H. Jansson, and J. Swenson, *Dynamics of aqueous binary glass-formers confined in MCM-41.* Physical Chemistry Chemical Physics, 2015. **17**(19): p. 12978-12987.
40. Morineau, D., et al., *Experimental indication of structural heterogeneities in fragile hydrogen-bonded liquids.* EPL (Europhysics Letters), 1998. **43**(2): p. 195.
41. Morineau, D. and C. Alba-Simionesco, *Hydrogen-bond-induced clustering in the fragile glass-forming liquid m-toluidine: Experiments and simulations.* The Journal of chemical physics, 1998. **109**(19): p. 8494-8503.
42. Karmakar, A., P. Krishna, and R. Joarder, *On the structure function of liquid alcohols at small wave numbers and signature of hydrogen-bonded clusters in the liquid state.* Physics Letters A, 1999. **253**(3): p. 207-210.
43. Magini, M., G. Paschina, and G. Piccaluga, *On the structure of methyl alcohol at room temperature.* The Journal of chemical physics, 1982. **77**(4): p. 2051-2056.

44. Jorgensen, W.L., J.M. Briggs, and M.L. Contreras, *Relative partition coefficients for organic solutes from fluid simulations.* Journal of Physical Chemistry, 1990. **94**(4): p. 1683-1686.
45. Morishige, K. and K. Kawano, *Freezing and melting of methanol in a single cylindrical pore: Dynamical supercooling and vitrification of methanol.* The Journal of chemical physics, 2000. **112**(24): p. 11023-11029.
46. Takahara, S., et al., *Neutron scattering and dielectric studies on dynamics of methanol and ethanol confined in MCM-41.* Journal of Physical Chemistry C, 2008. **112**(37): p. 14385-14393.
47. Patel, S. and C.L. Brooks, *Structure, thermodynamics, and liquid-vapor equilibrium of ethanol from molecular-dynamics simulations using nonadditive interactions.* Journal of Chemical Physics, 2005. **123**(16).
48. Mizukami, M. and K. Kurihara, *Ethanol cluster formation on silicon oxide surface in cyclohexane-ethanol binary liquids.* Chemistry Letters, 2000(3): p. 256-257.
49. Nikam, P.S., et al., *Densities and viscosities of binary mixtures of toluene with methanol, ethanol, propan-1-ol, butan-1-ol, pentan-1-ol, and 2-methylpropan-2-ol at (303.15, 308.15, 313.15) K.* Journal of Chemical & Engineering Data, 2000. **45**(4): p. 559-563.
50. Abdel Hamid, A., et al., *Solvation Effects on Self-Association and Segregation Processes in tert-Butanol–Aprotic Solvent Binary Mixtures.* The Journal of Physical Chemistry B, 2013. **117**(35): p. 10221-10230.
51. Thommes, M., *Nanoporous materials: science and engineering*, ed. G.Q. Lu, X.S. Zhao, and T.K. Wei. Vol. 4. 2004, London: Imperial College Press.
52. Dong, J., et al., *Hydrogen storage in several microporous zeolites.* International Journal of Hydrogen Energy, 2007. **32**(18): p. 4998-5004.
53. Davis, M.E., *New vistas in zeolite and molecular sieve catalysis.* Accounts of chemical research, 1993. **26**(3): p. 111-115.
54. Yaghi, O.M., et al., *Reticular synthesis and the design of new materials.* Nature, 2003. **423**(6941): p. 705-714.
55. Horcajada, P., et al., *Metal–organic frameworks as efficient materials for drug delivery.* Angewandte Chemie, 2006. **118**(36): p. 6120-6124.
56. Eddaoudi, M., et al., *Modular chemistry: secondary building units as a basis for the design of highly porous and robust metal-organic carboxylate frameworks.* Accounts of chemical research, 2001. **34**(4): p. 319-330.
57. Férey, G., et al., *Crystallized frameworks with giant pores: are there limits to the possible?* Accounts of chemical research, 2005. **38**(4): p. 217-225.
58. Mueller, U., et al., *Metal-organic frameworks - prospective industrial applications.* Journal of Materials Chemistry, 2006. **16**(7): p. 626-636.
59. Schaefer, D.W., *Engineered Porous Materials.* MRS Bulletin, 1994. **19**(04): p. 14-19.
60. Detcheverry, F., et al., *Helium condensation in aerogel: Avalanches and disorder-induced phase transition.* Physical Review E, 2005. **72**(5).
61. Akimov, Y.K., *Fields of application of aerogels (Review).* Instruments and Experimental Techniques, 2003. **46**(3): p. 287-299.
62. Guégan, R., et al., *Evidence of anisotropic quenched disorder effects on a smectic liquid crystal confined in porous silicon.* Physical Review E, 2006. **73**(1): p. 011707.
63. Kityk, A.V., et al., *Continuous paranematic-to-nematic ordering transitions of liquid crystals in tubular silica nanochannels.* Physical review letters, 2008. **101**(18): p. 187801.
64. Kresge, C., et al., *Ordered mesoporous molecular sieves synthesized by a liquid-crystal template mechanism.* Nature, 1992. **359**(6397): p. 710-712.
65. Beck, J., et al., *A new family of mesoporous molecular sieves prepared with liquid crystal templates.* Journal of the American Chemical Society, 1992. **114**(27): p. 10834-10843.
66. Zhao, D.Y., et al., *Triblock copolymer syntheses of mesoporous silica with periodic 50 to 300 angstrom pores.* Science, 1998. **279**(5350): p. 548-552.

67. Ryoo, R., S.H. Joo, and S. Jun, *Synthesis of highly ordered carbon molecular sieves via template-mediated structural transformation.* Journal of Physical Chemistry B, 1999. **103**(37): p. 7743-7746.
68. Lin, H.-P. and C.-Y. Mou, *Tubules-within-a-tubule hierarchical order of mesoporous molecular sieves in MCM-41.* Science, 1996. **273**(5276): p. 765-768.
69. Zhao, D.Y., et al., *Nonionic triblock and star diblock copolymer and oligomeric surfactant syntheses of highly ordered, hydrothermally stable, mesoporous silica structures.* Journal of the American Chemical Society, 1998. **120**(24): p. 6024-6036.
70. Brodie-Linder, N., et al., *SBA-15 synthesis: Are there lasting effects of temperature change within the first 10 min of TEOS polymerization?* Materials Chemistry and Physics, 2008. **108**(1): p. 73-81.
71. Galarneau, A., et al., *True Microporosity and Surface Area of Mesoporous SBA-15 Silicas as a Function of Synthesis Temperature.* Langmuir, 2001. **17**(26): p. 8328-8335.
72. Imperor-Clerc, M., P. Davidson, and A. Davidson, *Existence of a microporous corona around the mesopores of silica-based SBA-15 materials templated by triblock copolymers.* Journal of the American Chemical Society, 2000. **122**(48): p. 11925-11933.
73. Jähnert, S., et al., *Pore structure and fluid sorption in ordered mesoporous silica. I. Experimental study by in situ small-angle X-ray scattering.* The Journal of Physical Chemistry C, 2009. **113**(34): p. 15201-15210.
74. Selvam, P., S.K. Bhatia, and C.G. Sonwane, *Recent advances in processing and characterization of periodic mesoporous MCM-41 silicate molecular sieves.* Industrial & Engineering Chemistry Research, 2001. **40**(15): p. 3237-3261.
75. Zickler, G.A., et al., *Physisorbed films in periodic mesoporous silica studied by in situ synchrotron small-angle diffraction.* Physical Review B, 2006. **73**(18).
76. Jun, S., et al., *Synthesis of new, nanoporous carbon with hexagonally ordered mesostructure.* Journal of the American Chemical Society, 2000. **122**(43): p. 10712-10713.
77. Lindlar, B., et al., *Synthesis of large pore silica with a narrow pore size distribution.* Microporous and Mesoporous Materials, 2001. **44**: p. 89-94.
78. Grun, M., I. Lauer, and K.K. Unger, *The synthesis of micrometer- and submicrometer-size spheres of ordered mesoporous oxide MCM-41.* Advanced Materials, 1997. **9**(3): p. 254-&.
79. Kruk, M., M. Jaroniec, and A. Sayari, *Application of large pore MCM-41 molecular sieves to improve pore size analysis using nitrogen adsorption measurements.* Langmuir, 1997. **13**(23): p. 6267-6273.
80. Brunauer, S., P.H. Emmett, and E. Teller, *Adsorption of gases in multimolecular layers.* Journal of the American Chemical Society, 1938. **60**(2): p. 309-319.
81. Sing, K.S. and S. Gregg, *Adsorption, surface area and porosity*. 1982, London: Academic Press.
82. Barrett, E.P., L.G. Joyner, and P.P. Halenda, *The determination of pore volume and area distributions in porous substances. I. Computations from nitrogen isotherms.* Journal of the American Chemical Society, 1951. **73**(1): p. 373-380.
83. Kruk, M., et al., *Characterization of highly ordered MCM-41 silicas using X-ray diffraction and nitrogen adsorption.* Langmuir, 1999. **15**(16): p. 5279-5284.
84. Jaroniec, M. and L.A. Solovyov, *Improvement of the Kruk-Jaroniec-Sayari method for pore size analysis of ordered silicas with cylindrical mesopores.* Langmuir, 2006. **22**(16): p. 6757-6760.
85. Webb, P.A. and C. Orr, *Analytical methods in fine particle technology*. 1997: Micromeritics Instrument Corp.
86. Lippens, B., B. Linsen, and J. De Boer, *Studies on pore systems in catalysts I. The adsorption of nitrogen; apparatus and calculation.* Journal of Catalysis, 1964. **3**(1): p. 32-37.
87. Solovyov, L., et al., *X-ray structural modeling of silicate mesoporous mesophase material.* Microporous and Mesoporous Materials, 2001. **44**: p. 17-23.

# CHAPTER III:

# SUPERMOLECULAR ORDER IN BULK

# Chapter III: Supermolecular Order in Bulk

## III.A. Introduction

Many alcohol containing binary mixtures display a strong deviation from ideal mixture behavior which can be attributed to the incomplete mixing of the distinct interacting molecules at the microscopic level.[1-4] Although these solutions are sometimes macroscopically miscible, supermolecular alcohol clustering is witnessed due to hydroxyl H-bonding at the microscale. Different strategies were perceived for the isolation of such supermolecular aggregates in the liquid state. The addition of an aprotic liquid, for H-bond dilution, is efficient for modulating interactions between these agglomerates.[5-7]

The segregation and self-association processes have been studied for *tert*-butanol (TBA) - toluene (Tol) and TBA- methyl cyclohexane (MethCyc) systems (the latter being the aliphatic analogue of Tol).[8] For this purpose, two techniques were applied: Raman spectroscopy (to quantify the size distribution of the clusters) and neutron diffraction (to investigate the correlation between such agglomerates). Raman results have shown that the self-association of TBA is dominated by tetramers in the pure form. This trend was gradually reduced upon toluene addition leading to the vanishing of the clusters at low TBA concentrations (Fig. III-1 (A)). Complementary diffraction results reveal a suppression in the inter-cluster correlation pre-peak at TBA concentrations less than 0.7 molar fraction. A signature of the loss of correlation between the different clusters. [8]

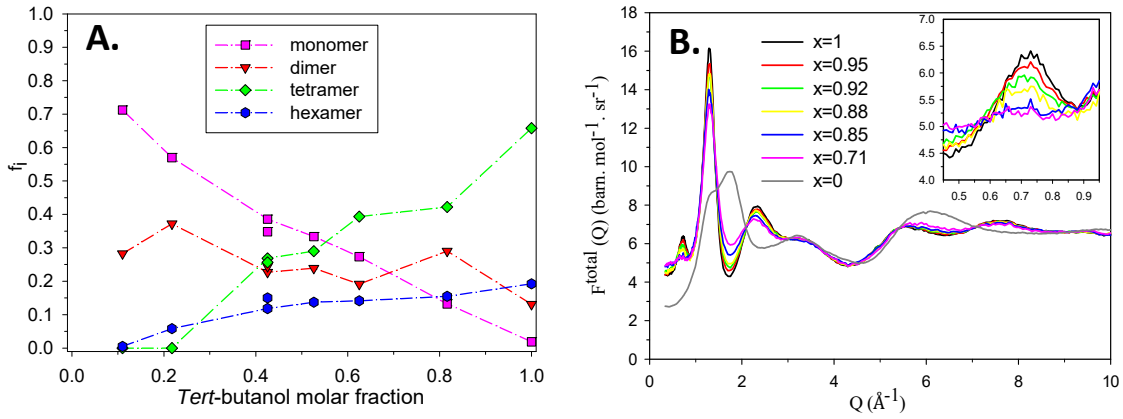


Figure III-1: (A): Population fractions of H-bonded clusters as a function of composition for TBA-Tol mixtures obtained by Raman spectroscopy. (B): Experimental neutron coherent cross section of TBA-Tol mixtures at as a function of the molar fraction of TBA (x). Inset: pre-peak region after [8].

A comprehensive view of the dilution and solvation effects of toluene on TBA is illustrated in Fig. III-2(A) which shows monomeric dominance at low TBA concentrations and it is only at $x_{TBA}>0.4$ that non-correlated tetramers dispersed in Tol prevail. At very high TBA concentrations x>0.8 the TBA clusters segregate in pockets and correlations among them appear. The influence of dilution in this case seems to be more remarkable than in the case of the aliphatic nonpolar MethCyc where tetramers persist even at very high dilution $x_{TBA}=0.1$ indicating an exceptional stability of the clusters and supporting the hypothesis of a specific interaction between the hydroxyl groups and the aromatic nucleus of toluene. Therefore this crossover from diluted clusters to diluted monomers expresses how the cluster stability is influenced upon tuning from a solvating to an inert solvent (Tol and MethCyc respectively).

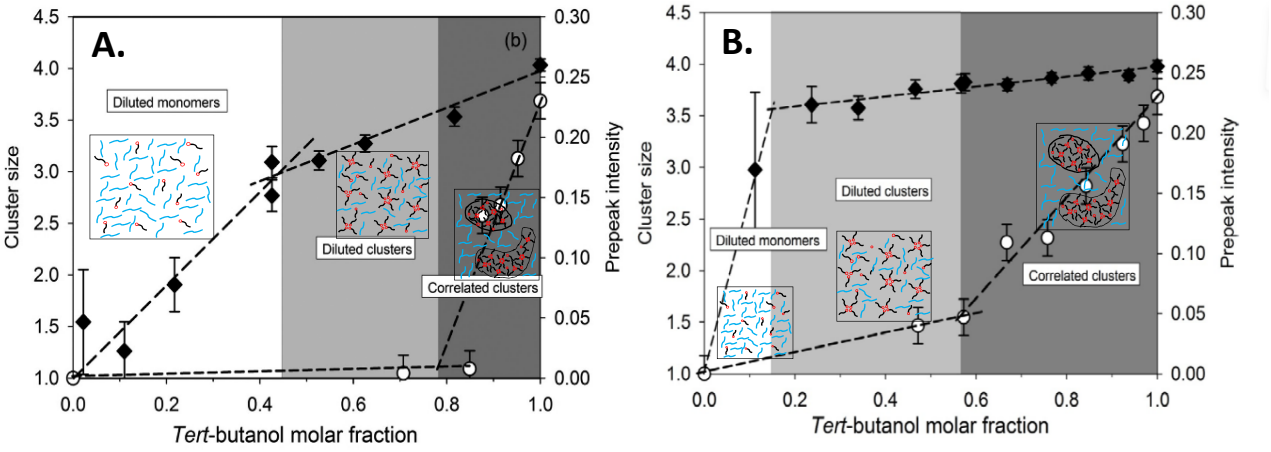


Figure III-2: Cluster size (filled diamond) and pre-peak intensity (open circle) of (A) TBA-Tol and (B) TBA-MethCyc mixtures as a function of the molar fraction of TBA (x). The 3 different microstructures are located by shaded areas. They are separated by two distinct crossovers in the variation of the cluster size and pre-peak intensity respectively as a function of the dilution after [8].

In this chapter, we intend to extend the study of the segregation phenomenon towards a lower Q-region through small angle neutron scattering (SANS). This complementary method addresses the inhomogeneity of the mixtures in terms of concentration fluctuations, which are signatures of single-component-rich domains triggered by selective molecular interactions.

Different H/D isotopic compositions are used to vary the scattering length density of the components of the binary liquids, which amplifies the contrast between domains of different compositions. The characteristic correlation length of the inhomogeneities has been determined using the Ornstein-Zernike model. The formalism of Bhatia and Thornton has been applied to disentangle the different correlation functions related to density and concentration from the total neutron structure factor. Our analysis is based on the assumption that the structure of the

solution can be approximated by a continuous variation of the scattering length density at the mesoscopic scale. This is associated to the variation in the local composition (the different components have different scattering length densities). These fluctuations have been quantified by the evaluation of the Kirkwood-Buff integrals (KBI). In this approach, only the forward scattering is used, so no real structural information can be deduced about the nature of the different molecular aggregates but rather their influence in terms of formation of static domains with different concentrations which might be present in the solution.

The aim of this study is to shed light on the different phenomena, expressed in terms of self-association, long-lived multimers and concentration fluctuations that contribute to the complex microstructure of prototypical alcohols mixed with aprotic solvents. Different systems have been considered to vary their molecular interactions. First, the alcohol-solvent interaction has been tuned by comparing TBA-Tol and TBA-cyclohexane (TBA-Cyc) mixtures. Moreover, the amphiphilic alcohol character has been varied, going from TBA to ethanol and methanol.

# III.B. Methods

## III.B.1. General Background

SANS is an experimental technique implementing elastic neutron scattering at small angles to inspect the mesoscopic structure of matter and determine the time averaged shape and arrangement of particles or agglomerates in a given medium. In a SANS experiment, a beam of collimated radiation is directed to a sample where a part of the incident beam is transmitted by the sample, another is absorbed and the rest is scattered. A detector cell having dx, dy dimensions positioned at a distance L and scattering angle (2θ) from the sample records the flux of radiation scattered into a solid angle ( $\Omega = \frac{dx\,dy}{L^2}$) (Fig. III-3).

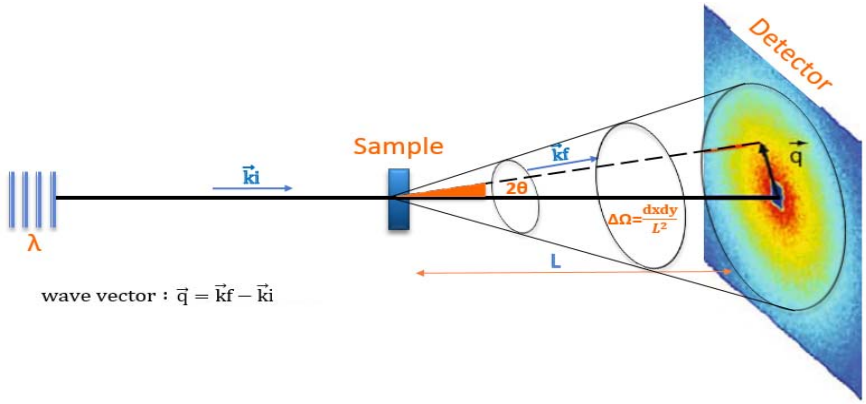


Figure III-3: Schematic representation of a SANS experiment.

The typical momentum exchange (quantifying the reciprocal space lengths) for such experiments, is between $10^{-3}$ and $1Å^{-1}$ allowing structural investigations from nm to a few hundreds of nm length scales. Such scales do not allow the discrimination between individual atoms. The quantity which is therefore assessed is the scattering length density distribution in the sample (ρb) defined by:

$$\rho b = \sum_i b_i . \frac{\rho . N_A}{M_w} \qquad \text{(III-1)}$$

Where $b_i$ is the scattering length of the different nuclei in the sample, ρ is the bulk density of the scattering center and $M_w$ is its molecular weight.

### III.B.2. Experimental

Small-angle scattering experiments were performed on the SANS diffractometer PAXY (LLB, Saclay). The sample detector distance chosen was 1.6m and the neutron wavelength used was 3.5Å allowing the measurement of the diffracted intensity in a momentum transfer range ($0.04 < Q < 0.5Å^{-1}$).

The samples were prepared from hydrogenated *tert*-butanol TBAH mixed with deuterated toluene TolD or with cyclohexane CycD as well as their opposite isotopic compositions: the four types of mixtures are later denoted TBAH-TolD, TBAH-CycD, TBAD-TolH and TBAD-CycH respectively. Methanol and ethanol hydrogenated samples were also prepared with deuterated toluene; *i.e.*, MethH-TolD and EthH-TolD mixtures.

The bulk samples were prepared in volume fraction covering the concentration range $x = 0-1$ ($x$ being the volume fraction of the alcohol). The measurements were conducted at room temperature with a thermal bath regulator set to 22°C. The solutions were filled in 1 mm thick quartz Hellma cells.

### III.B.3. Data Reduction

The determination of the beam's center and the radial isotropic averaging of the different cells were all performed by the Regiso software developed at LLB.

The samples in our experiments were contained inside a container. Therefore, it is crucial to subtract the empty cell contribution from the measured intensity. Both contributions were properly divided by their own measured forward transmission in the aim of correcting for the beam attenuation effects according to:

$$I = K.S(Q) = \left(\frac{I_{sample}}{T_{sample}} - \frac{I_{emptycell}}{T_{emptycell}}\right) \quad \text{(III-2)}$$

The obtained intensity is proportional to the neutron beam incoming flux $I_0$ and the sample's static structure factor S(Q). The subsequent normalization of S(Q) to absolute units is usually performed in two different ways: the first consists of measuring the incoming flux $I_0$ after the removal of the beam-stop and placing an attenuator (to avoid overexposure of the detector). It should be noted that, in this case, the transmission of the latter should also be calibrated and corrected for. Applying this procedure, S(Q) can then be derived from I according to:

$$\frac{I}{I_o} = \Omega.e.S(Q) = \left(\frac{\text{detector area}}{L}\right).e.S(Q) \quad \text{(III-3)}$$

$I_0$ being the flux, e being the cell thickness and Ω signifying the solid angle obtained by the division of the detector cell area by the sample-to-detector distance (L).

In our data treatment we implemented a second method which consists of normalizing the intensity of all the spectra with respect to a standard sample having a high flat signal with a known value of its incoherent cross section ($\Sigma_{(H2O)}/4\pi = .445 cm^{-1}$). We also used the same method (normalization with respect to hydrogenated water) for the correction of the systematic variation in the efficiency of the different cells of the multidetector.

# III.C. Results and discussion

## III.C.1. TBA-Tol/ Cyc Systems

### III.C.1.2. Experimental Results

The results of the SANS experiments show an increase of the scattering intensity at low Q for all the binary solutions (Fig. III-4). Without further analysis, this firmly indicates that the molecular distribution in the liquid is heterogeneous. This inhomogeneous scattering length density distribution causing this increase in the coherent scattering is usually caused by the appearance of domains due to a selective attractive interaction between similar species. These domains seem to be concentration dependent and normally have characteristic sizes in the nanometer range. It should be mentioned; however, that SANS is a low-resolution method, therefore we do not anticipate to attain precise (near-atomic resolution) structures but rather information about the mesoscopic order.

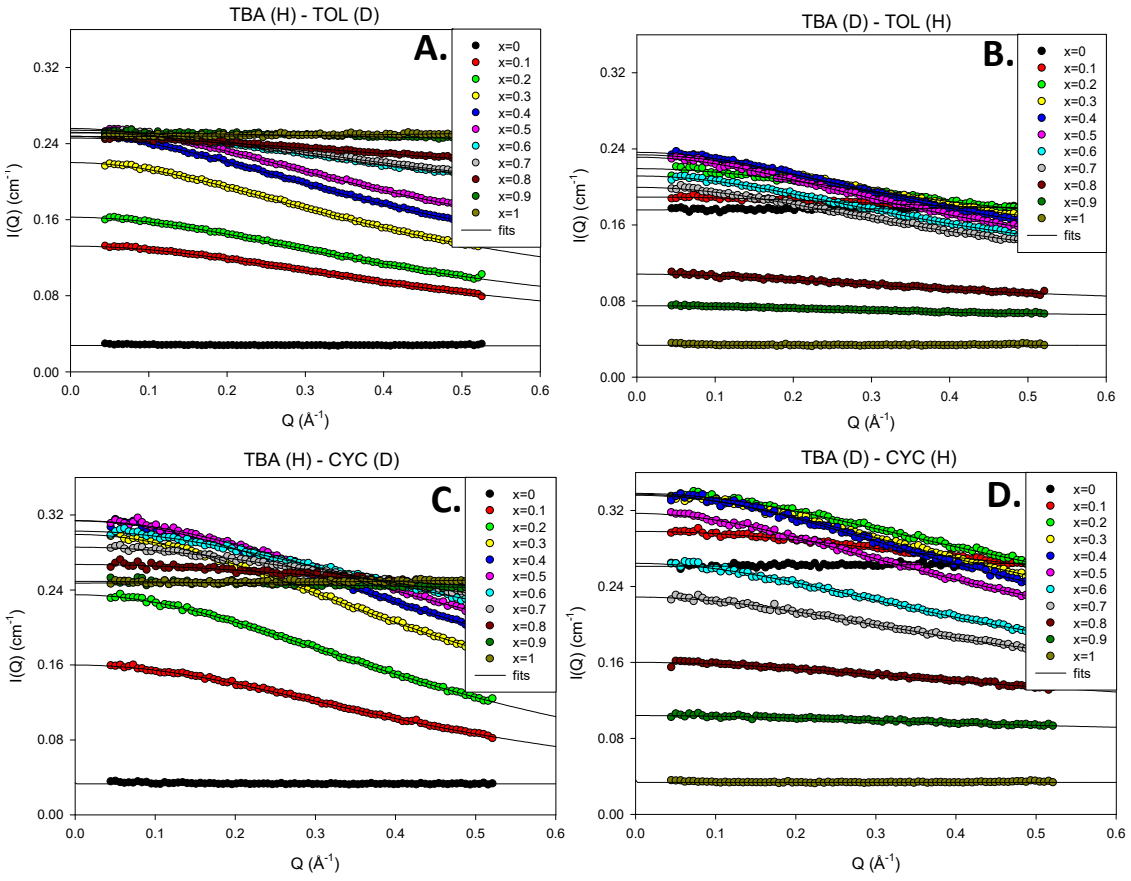


Figure III-4: SANS intensities of TBA-Tol mixtures (A, B) and TBA-Cyc mixtures (C, D), comprising hydrogenated TBA with deuterated Tol and Cyc (A and C respectively) and vice-versa (B and D respectively). The different curves correspond to eleven values of the TBA volume fractions x from 0 to 1. The plotted solid lines are fits to the Ornstein-Zernike model.

### III.C.1.3. Ornstein-Zernike Analysis

The Q-dependence of the scattered intensity depends on the structural arrangement of the scattering centers. Binary mixtures are usually known to bear medium-range fluctuations in composition (and to a lesser extent in density), which eventually diverges for non-miscible systems on approaching phase separation. The scattered intensity obtained by a Fourier transform of the scattering length density distribution in such systems is a Lorentzian function known as the Ornstein-Zernike model.[9] This formalism is known to accurately reproduce the scattering intensity of many non-ideal binary mixtures [10, 11] and can be defined as:

$$I(Q) = \frac{A}{1 + Q^2\xi^2} + B \qquad \text{(III-4)}$$

A expresses the amplitude of the coherent scattering, B represents the Q-independent background and ξ is the correlation length characterizing the spatial extension (correlations) of the scattering length density fluctuations. Such a formalism can be applied for the description of the scattering intensity at zero angle which originates from the distinct scattering length density domains caused by density and concentration fluctuations.

The coherent forward scattering intensity $I_{coh}(0)$ can be obtained from the fitted parameter A. The latter doesn't properly account for contributions from the compressibility term (whose Q-dependences are negligible at moderate temperatures, so they are effectively included in the background parameter B). Therefore $I_{coh}(0)$ can be obtained by adding these terms to A:

$$I_{coh}(0) = A + \rho^2 \, k_B T \, \kappa_T \bar{b}^2 \qquad \text{(III-5)}$$

A fit of the coherent intensity with an Ornstein-Zernike type model was performed and plotted as solid lines in Fig. III-4. The parameters of the Lorentzian (correlation length, amplitude and background) were obtained for the different samples and plotted (Fig. III-5, 6). The correlation length seems to remain almost constant for all compositions in all the samples (ξ= 2Å: close to the molecular scale) and the background increases linearly as expected with the increased Hydrogen content due to the incoherent scattering. Regarding the amplitude, the general trend is characterized by a maximum reached around intermediate compositions and vanishing values are confirmed for pure liquids with no heterogeneities in the scattering length densities.

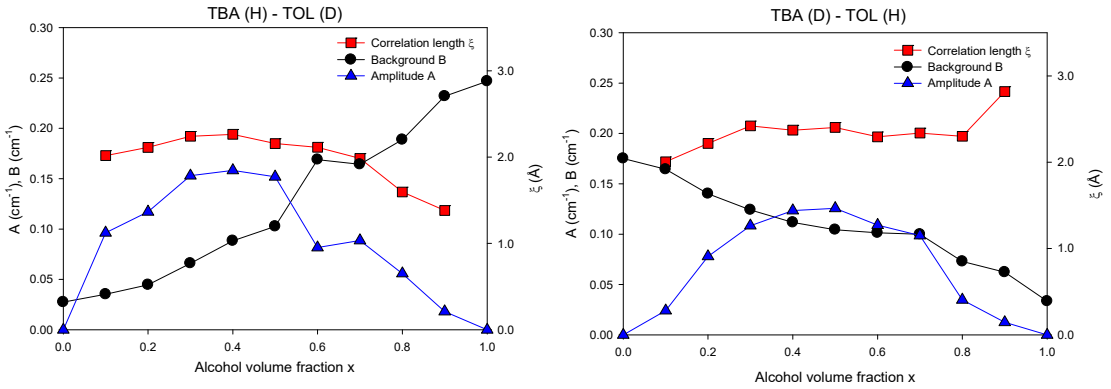


Figure III-5: Parameters (amplitude, correlation length and background) obtained from a fit with the Ornstein-Zernike model of the SANS intensities of *tert*-butanol-toluene mixtures, comprising hydrogenated TBA with deuterated Tol (left panel) and vice-versa (right panel).

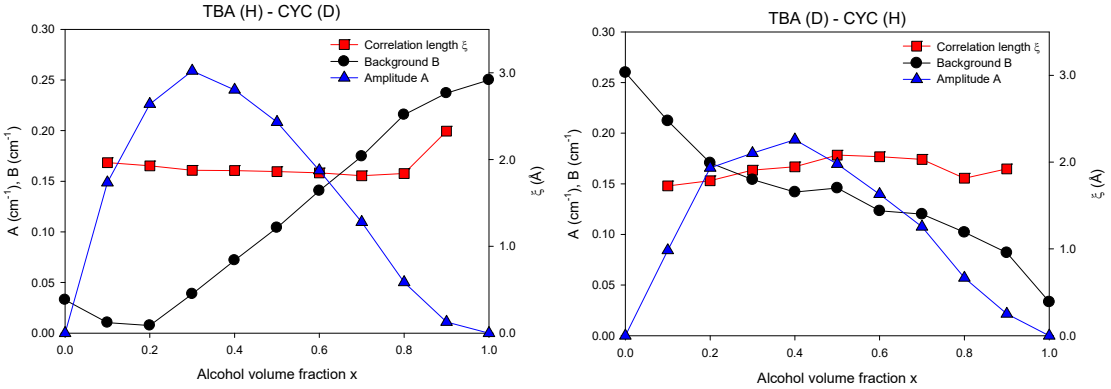


Figure III-6: Parameters (amplitude, correlation length and background) obtained from a fit with the Ornstein-Zernike model of the SANS intensities of *tert*-butanol-cyclohexane mixtures, comprising hydrogenated TBA with deuterated Cyc (left panel) and vice-versa (right panel).

### III.C.1.4. Bhatia and Thornton Analysis

Following Bhatia and Thornton the zero angle coherent scattering of a binary mixture can be expressed as a linear combination of distinct fluctuation terms: [12]

$$\frac{I_{coh}(0)}{\rho} = \bar{b}^2 S_{NN}(0) + (b_1 - b_2)^2 S_{CC}(0) + 2\bar{b}(b_1 - b_2) S_{NC}(0) \quad \text{(III-6)}$$

$\rho$ is the number density of the molecules, $b_1$ and $b_2$ stand for the sums of the coherent scattering lengths of the atoms constituting the two molecules and $\bar{b} = x_1 b_1 + (1 - x_1) b_2$.

$S_{CC}(0)$ represents the fluctuations in the concentration of one molecular type, $S_{NN}(0)$ describes the fluctuations in the molecular number and $S_{NC}(0)$ represents the correlation between the two other fluctuations. The latter terms are linked to the $S_{CC}(0)$ at zero limit of the scattering intensity with relations that can be illustrated as:

$$S_{NN}(0) = \rho\, k_B T \kappa_T + \delta^2 S_{CC}(0) \approx \delta^2 S_{CC}(0) \quad \text{(III-7)}$$

$$S_{NC}(0) = -\delta\, S_{CC}(0) \quad \text{(III-8)}$$

$\kappa_T$ being the isothermal compressibility, $\delta = \rho(\nu_1 - \nu_2)$ being the dilatation factor defined as the product of the average number density $\rho$ and the difference of the partial molar volumes per molecule of the two components ($\nu_1$ and $\nu_2$) and finally $k_B$ is the Boltzmann 's constant.

The slight dependence of $\nu_1$ and $\nu_2$ on the mixture composition, which arises from the excess volume was neglected in our calculation. We checked the validity of this assumption for the mixtures and compositions where these excess quantities were available. For instance, in the case of TBA-Tol mixtures, the excess volume found in the literature is: $V_{excess} < 0.5$ cc/mol[13] and the molar volumes of TBA and Tol are 95 and 105 cc/mol respectively (*i.e.*, $\Delta V = 10$ cc/mol). Therefore the excess volume is less than 5% of $\Delta V$ which is within the precision of our measurements and can thus be safely dismissed.

Furthermore, $S_{CC}(0)$ can be calculated from the forward coherent scattering using the following equation, which is obtained after insertion of eqs. (III-7) and (III-8) into eq. (III-6):

$$I_{coh}(0) = \rho^2 k_B T \kappa_T . \bar{b}^2 + \rho\left[\bar{b}\delta - (b_1 - b_2)\right]^2 S_{CC}(0) \quad \text{(III-9)}$$

The fluctuation terms in the solutions were obtained from the amplitude of the Lorentzian fit combining equations (III-5 and III-9), which gives:

$$S_{CC}(0) = \frac{A}{\varrho\left[\bar{b}\delta - (b_1 - b_2)\right]^2} \qquad \text{(III-10)}$$

No significant density fluctuation takes place upon adding the diluting liquid, as shown in Fig. III-7 ($S_{NN}(0)$ remains small). On the other hand, we witness an increase in the concentration fluctuation term $S_{CC}(0)$ which is directly related to the particle clustering in the mixture. This can be illustrated by the fact that TBA molecules interact preferentially by H-bonds leading to the formation of TBA-rich and Tol-rich regions. The typical volume associated to the local variations of the solute concertation could be estimated from the correlation length deduced from the Ornstein-Zernike analysis. It is striking that it remains close to the molecular scale, which signifies that the concentration fluctuations roughly scale with the size of the multimeric species already characterized by Raman spectroscopy.[8]

Another point of interest is that two systems with the opposite isotopic compositions; *i.e.,* TBAH with TolD versus TBAD with TolH should present the same fluctuation terms $S_{NN}(0)$, $S_{CC}(0)$ and $S_{NC}(0)$ although they exhibit different SANS spectra (Fig. III-4). In fact, this statement is true as long as the isotopic effects on the liquid structure are negligible, which can be safely assumed. Interestingly, Fig. III-7 confirms that the computed fluctuation terms fulfill this requirement, which validates the method and especially the appropriate correction for the isotopic effects on the values of scattering length densities.

A noticeable solvent effect is worth mentioning when comparing TBA-Tol and TBA-Cyc systems (Figs. III-7, 8). The heterogeneous character of the mixture is prevalent around x= 0.4 for TBA-Tol systems (highlighted by a maximum in $S_{CC}(0)$). This position is shifted to lower composition (about x= 0.3) for the TBA-Cyc systems. This observation goes in line with the spectroscopic study mentioned previously, which showed that TBA tetrameric clusters are stable to extreme dilution conditions in aliphatic solvent (x= 0.2) and to a lesser extent in Tol because of a competition between TBA-TBA association and TBA-Tol interaction.[8] Again, the phenomenon underlines the link between concentration fluctuations and the existence of multimeric species.

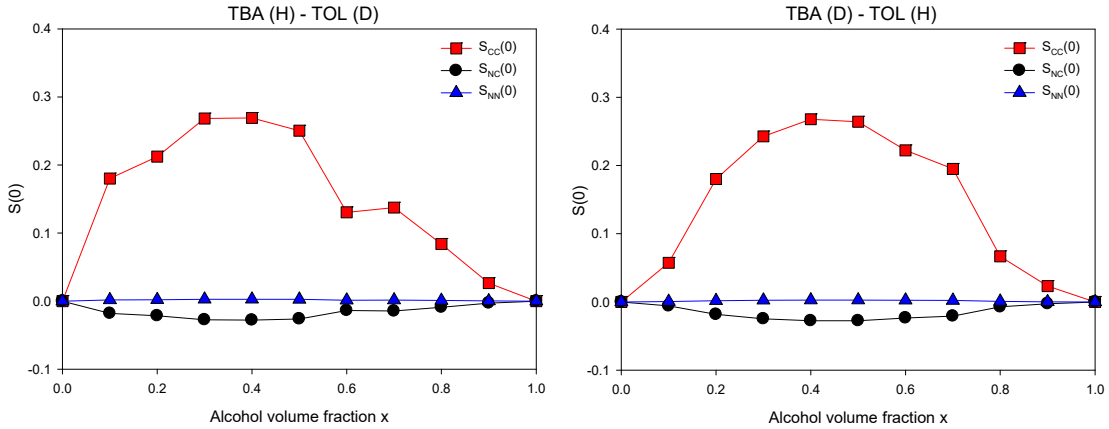


Figure III-7: Bhatia-Thornton fluctuation terms of *tert*-butanol-toluene mixtures, comprising hydrogenated TBA with deuterated Tol (left panel) and vice-versa (right panel). $S_{CC}(0)$, $S_{NN}(0)$ and $S_{NC}(0)$ correspond to concentration fluctuation, density fluctuation and the cross-correlation term, respectively.

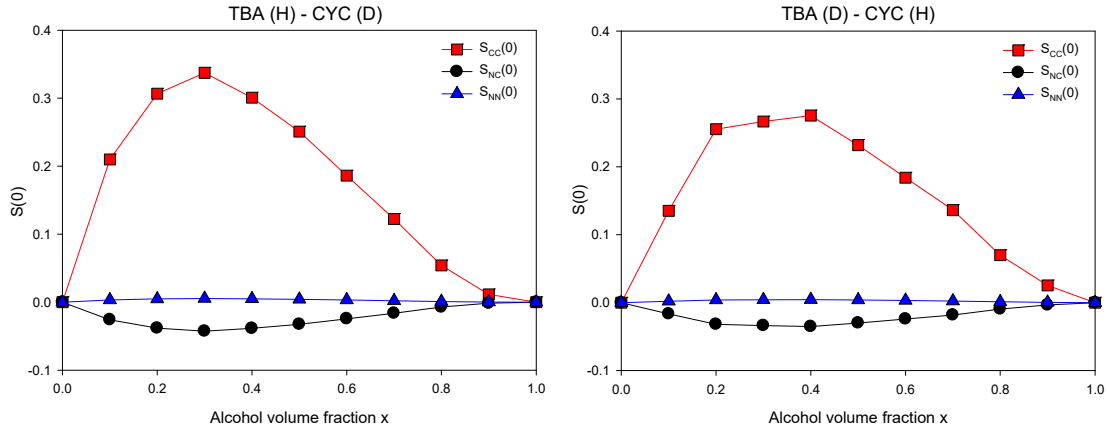


Figure III-8: Bhatia-Thornton fluctuation terms of *tert*-butanol-cyclohexane mixtures, comprising hydrogenated TBA with deuterated Cyc (left panel) and vice-versa (right panel). $S_{CC}(0)$, $S_{NN}(0)$ and $S_{NC}(0)$ correspond to concentration fluctuation, density fluctuation and the cross-correlation term, respectively.

### III.C.1.5. Kirkwood-Buff Analysis

The Kirkwood–Buff theory [14] illustrates the trends of molecular interactions in a solution via the Kirkwood–Buff integrals (KBIs) which can be expressed as:

$$G_{ij} = \int_0^\infty (g_{ij}(r) - 1)\ 4\pi r^2 dr \qquad \text{(III-11)}$$

It is based on the pair correlation functions (gij, gii and gjj), which relate the probability of finding a particle at a given distance from another one, appraising the solute-solute, solute-solvent, and solvent-solvent interactions. The KBIs provide the tendencies of domain formation around a certain type of molecule, by integration of the pair correlation from the molecular to the infinite distance. It is usually applied to investigate domains growth in phase separating systems. SANS has proven to be a suitable technique for a reliable KBIs determination in binary mixtures,[11, 15, 16] where the KBIs can be expressed as linear combination of the different fluctuation terms:[17]

$$G_{11} = \frac{1}{\rho}\left(S_{NN}(0) + \frac{2}{x_1} S_{NC}(0) + \frac{1}{x_1^2} S_{CC}(0) - \frac{1}{x_1}\right) \qquad \text{(III-12)}$$

$$G_{22} = \frac{1}{\rho}\left(S_{NN}(0) - \frac{2}{x_2} S_{NC}(0) + \frac{1}{x_2^2} S_{CC}(0) - \frac{1}{x_2}\right) \qquad \text{(III-13)}$$

$$G_{12} = \frac{1}{\rho}\left(S_{NN}(0) + \frac{x_2 - x_1}{x_1 x_2} S_{NC}(0) - \frac{1}{x_1 x_2} S_{CC}(0)\right) \qquad \text{(III-14)}$$

The KBIs (Figs. III-9, 10) remain generally very small (10 to 100 times smaller than for phase separating binary liquids)[18], with a weak tendency of TBA segregation for low concentrations (revealed by an increase in the magnitude of $G_{22}$ at $x_{TBA}$ <0.2). This observation agrees with the homogeneous character of these mixtures at large scales (*i.e.*, significantly exceeding ξ). The attractive interactions between TBA molecules seem mostly limited to the formation of H-bonded multimeric clusters. As for TBA concentrations close to one, an apparent weak negative interaction between the aprotic Tol or Cyc molecules is observed, which might indicate the presence of solvation effects of the aprotic solute diluted in TBA (though no other experimental indications to support this assumption exist).

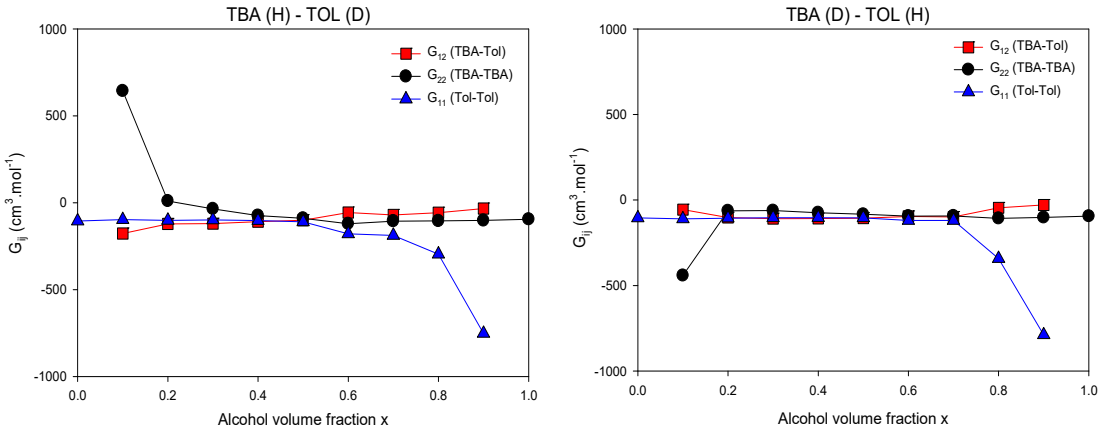


Figure III-9: Kirkwood-Buff integrals of *tert*-butanol-toluene mixtures, comprising hydrogenated TBA with deuterated Tol (left panel) and vice-versa (right panel). $G_{11}$ is the Tol-Tol KB integral, $G_{22}$ is the TBA-TBA KB integral, and $G_{12}$ is the TBA-Tol KB integral.

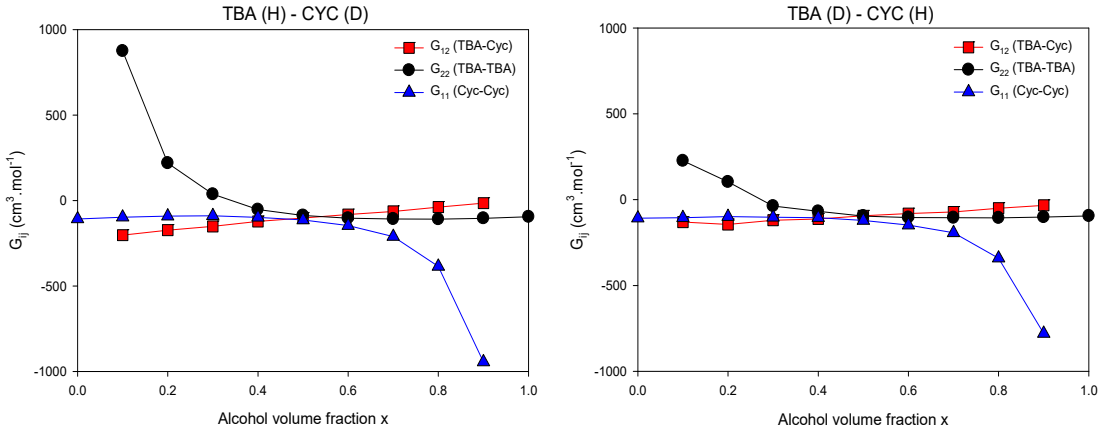


Figure III-10: Kirkwood-Buff integrals of *tert*-butanol-cyclohexane mixtures, comprising hydrogenated TBA with deuterated Cyc (left panel) and vice-versa (right panel). $G_{11}$ is the Cyc KB integral, $G_{22}$ is the TBA-TBA KB integral, and $G_{12}$ is the TBA-Cyc KB integral.

## III.C.2. Meth/Eth-Tol Systems

Intending to tune the amphiphilic character of the H-bonded molecules, a complementary study has been performed in order to follow a series of alcohol molecules with decreasing alkyl group size: from *tert*-butanol (TBA) to ethanol (Eth) and methanol (Meth). The comparison between the three alcohols is performed for alcohol-toluene systems. The SANS spectra of Eth-Tol and Meth-Tol shown in Fig. III-11 exhibit an analogous increase in the intensity at low Q, supplying evidence of aggregation in these solutions too.

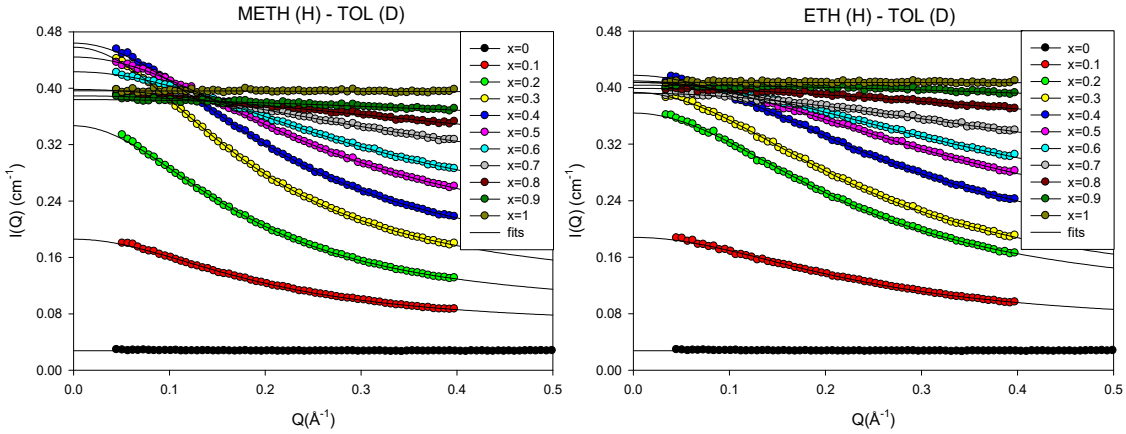


Figure III-11: SANS intensities of methanol-toluene (left panel) and ethanol-toluene (right panel) mixtures, comprising hydrogenated alcohol with deuterated Tol. The different curves correspond to eleven values of the alcohol volume fractions x from 0 to 1. The plotted solid lines are fits to the Ornstein-Zernike model.

The parameters obtained from fits with the Ornstein Zernike model of the SANS spectra (lines in Fig. III-11) are shown in Fig. III-12. Contrary to the TBA systems, the correlation length extracted from the fits varies with the concentration. It is the largest for highly diluted alcohol mixtures and gradually decreases with the increasing quantity of the alcohol. It is also noticeable that the values of the correlation lengths for methanol and ethanol are twice as large as for TBA despite their smaller molecular size. The largest values of the correlation lengths are obtained for the smallest alcohol molecule (methanol).

This different behavior is mostly determined by the balance between hydrophobic and hydrophilic interactions, which depends on the chemical nature of the molecule. A possible interpretation is the formation of extending linear H-bonded clusters in methanol and ethanol, while TBA is known to form cyclic multimers with limited size (typically 4 molecules). [8, 19]

Indeed, experimental and computational studies have reported that methanol forms mostly chainlike structures comprising up to ten molecules. [20-24] They have been related to the

prevailing hydrophilic interaction of small alcohol molecules. A situation that evolves for larger aliphatic groups like TBA where the frustration of the H-bonding network by steric hindrance promote the formation of cyclic micellar multimers.

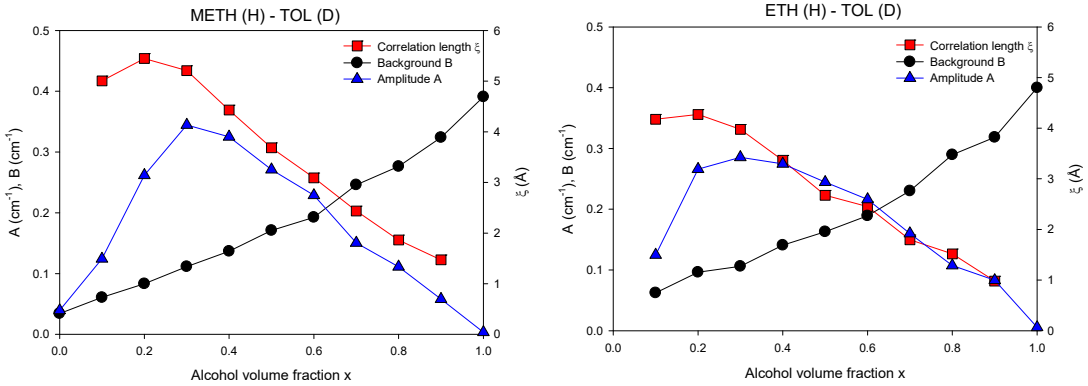


Figure III-12: Parameters (amplitude, correlation length and background) obtained from a fit with the Ornstein-Zernike model of the SANS intensities of methanol-toluene (left panel) and ethanol-toluene (right panel) mixtures, comprising hydrogenated alcohol with deuterated Tol.

The fluctuation terms emphasize the observation of an aggregation process leading to large concentration fluctuation quantified by $S_{CC}(0)$ shown in Fig. III-13. It also reveals that the heterogeneous character of the structure of ethanol-toluene and methanol-toluene solution prevails at lower concentrations (about $x$= 0.2) than for TBA. To understand this result, it is worth mentioning that the strength of the H-bond interaction increases with decreasing the alkyl size of the alcohol, which enhances the stabilization of H-bonded multimers of Eth and Meth diluted in toluene. Hence, the systematic evolution of $S_{CC}(0)$ with the self-association tendency going from TBA, Eth to Meth supports the idea that concentration fluctuations are dominated by the formation of the multimeric clusters themselves.

Moreover a change in the density-density fluctuation $S_{NN}(0)$ is also witnessed in high dilution conditions following the same trend as $S_{CC}(0)$. This observation can be easily interpreted as the coupling between concentration fluctuations and density fluctuations for binary mixtures with constituents having different molar volumes; *i.e.*, large dilatation factor δ according to equation (III-7). This phenomenon was much weaker for TBA-Tol mixtures, both components having comparable molar volumes so their density did not depend significantly on the concentration.

The Kirkwood Buff theory seems to go well with the precedent analysis. Fig. III-14 shows an increase of $G_{22}$ at low alcohol concentrations, demonstrating strong alcohol-alcohol interactions. A phenomenon which is more prevalent in the case of the chain-forming Meth/Eth

molecules compared to the tetrameric bulky TBA. Otherwise, no preferential interactions seem to appear neither between the alcohol nor toluene in the concentration range ($x_{alcohol}$>0.6).

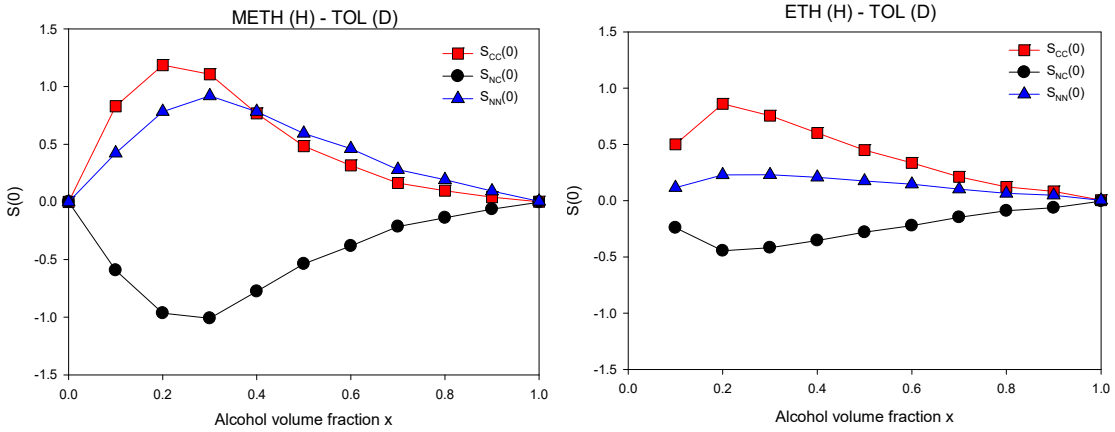


Figure III-13: Bhatia-Thornton fluctuation terms of methanol-toluene (left panel) and ethanol-toluene (right panel) mixtures, comprising hydrogenated alcohol with deuterated Tol. $S_{CC}(0)$, $S_{NN}(0)$ and $S_{NC}(0)$ correspond to concentration fluctuation, density fluctuation and the cross-correlation term, respectively.

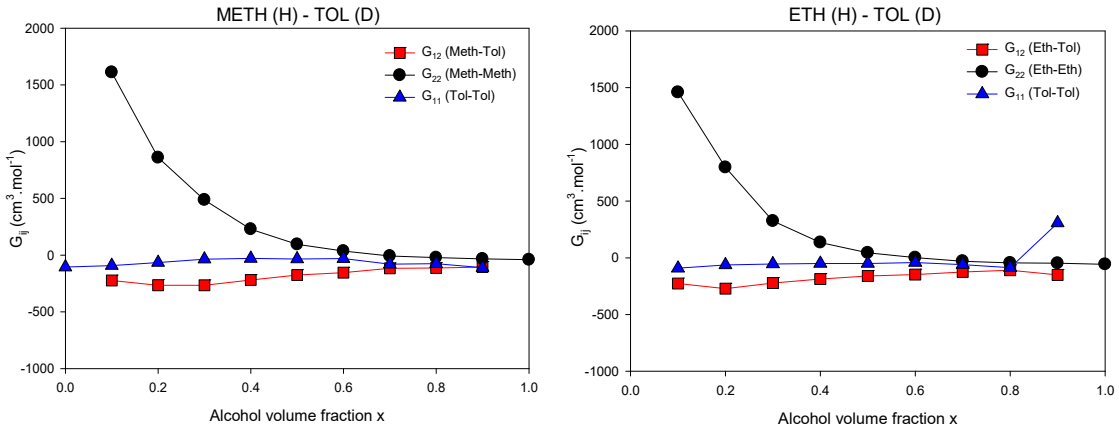


Figure III-14: Kirkwood-Buff integrals of methanol-toluene (left panel) and ethanol-toluene (right panel) mixtures, comprising hydrogenated alcohol with deuterated Tol. $G_{11}$ is the Tol KB integral, $G_{22}$ is the alcohol-Alcohol KB integral, and $G_{12}$ is the Alcohol-Tol KB integral.

# III.D. Conclusion

It is a long-established agreement that alcohol binary liquids are not homogeneous but rather exhibit peculiar molecular organizations. The structural complexity of such systems reflect the interplay between different phenomena related to the H-bond association, the self-aggregation (H-bonded clustering) and mesoscopic correlations or concentration fluctuations.

Different aspects have been assessed in the present study. The SANS experiments performed for a series of TBA-Cyc and TBA-Tol mixtures with different concentrations and isotopic compositions exhibit a systematic increase of the scattered intensity at low-Q indicating a heterogeneity in the liquid's molecular distribution. The characteristic correlation length of the inhomogeneities has been determined using the Ornstein-Zernike model and was found to have values close to the molecular size. The separation between the density and concentration correlation functions has been performed by the application of the Bhatia and Thornton formalism. The behaviors of both the Ornstein-Zernike correlation length and Bhatia and Thornton concentration fluctuation $S_{CC}(0)$ support that concentration fluctuations do not arise from fluctuations of the size and arrangement of the domains of aggregating TBA micellar clusters but rather from the micellar-clusters themselves.

While these conclusions seem to generally apply for the smaller ethanol and methanol alcohols, systematic variations are observed. First, a shift of the maximum concentration fluctuations to smaller alcohol composition could relate to higher H-bond interactions. Moreover, the smaller the molecular size, the larger the values of the correlation lengths. This effect on the concentration fluctuations could be related to the different microstructures, more often expressed in terms of extending linear H-bonded clusters in methanol and ethanol, while TBA is known to form cyclic multimers with limited size (typically 4 molecules).

Therefore, it would be extremely interesting to attempt to manipulate and tune these microstructures through the introduction of a hydrophilic surface. This new condition can be attained by the confinement of the binary mixtures in the straight and monodisperse rigid channels of mesoporous MCM-41and SBA-15 silica molecular sieves and would lead to the formation of new supermolecular ordering which will be the topic of the next chapter.

## References


1. Dixit, S., et al., *Molecular segregation observed in a concentrated alcohol–water solution.* Nature, 2002. **416**(6883): p. 829-832.
2. Guo, J.-H., et al., *Molecular structure of alcohol-water mixtures.* Physical review letters, 2003. **91**(15): p. 157401.
3. Wakisaka, A. and K. Matsuura, *Microheterogeneity of ethanol–water binary mixtures observed at the cluster level.* Journal of molecular liquids, 2006. **129**(1): p. 25-32.
4. Dougan, L., et al., *Molecular self-assembly in a model amphiphile system.* Physical Chemistry Chemical Physics, 2010. **12**(35): p. 10221-10229.
5. Hennous, L., et al., *Crossover in structure and dynamics of a primary alcohol induced by hydrogen-bonds dilution.* The Journal of chemical physics, 2014. **141**(20): p. 204503.
6. Wang, L.-M., S. Shahriari, and R. Richert, *Diluent effects on the Debye-type dielectric relaxation in viscous monohydroxy alcohols.* The Journal of Physical Chemistry B, 2005. **109**(49): p. 23255-23262.
7. El Goresy, T. and R. Böhmer, *Diluting the hydrogen bonds in viscous solutions of n-butanol with n-bromobutane: A dielectric study.* The Journal of chemical physics, 2008. **128**(15): p. 154520.
8. Abdel Hamid, A., et al., *Solvation Effects on Self-Association and Segregation Processes in tert-Butanol–Aprotic Solvent Binary Mixtures.* The Journal of Physical Chemistry B, 2013. **117**(35): p. 10221-10230.
9. Stanley, H.E., *Introduction to phase transitions and critical phenomena.* Introduction to Phase Transitions and Critical Phenomena, by H Eugene Stanley, pp. 336. Foreword by H Eugene Stanley. Oxford University Press, Jul 1987. ISBN-10: 0195053168. ISBN-13: 9780195053166, 1987. **1**.
10. Coulet, M.-V., R. Bellissent, and C. Bichara, *Small-angle neutron scattering study of sulphur–tellurium liquid alloys: structural evidence for a phase separation.* Physica B: Condensed Matter, 2000. **276**: p. 415-416.
11. Almásy, L., L. Cser, and G. Jancsó, *SANS study of 3-methylpyridine–heavy water mixtures.* Physica B: Condensed Matter, 2000. **276**: p. 446-447.
12. Bhatia, A. and D. Thornton, *Structural aspects of the electrical resistivity of binary alloys.* Physical Review B, 1970. **2**(8): p. 3004.
13. Peña, M.P., V. Martínez-Soria, and J. Monton, *Densities, refractive indices, and derived excess properties of the binary systems tert-butyl alcohol+ toluene,+ methylcyclohexane, and+ isooctane and toluene+ methylcyclohexane, and the ternary system tert-butyl alcohol+ toluene+ methylcyclohexane at 298.15 K.* Fluid Phase Equilibria, 1999. **166**(1): p. 53-65.
14. Kirkwood, J.G. and F.P. Buff, *The statistical mechanical theory of solutions. I.* The Journal of chemical physics, 1951. **19**(6): p. 774-777.
15. Almásy, L., G. Jancsó, and L. Cser, *Application of SANS to the determination of Kirkwood–Buff integrals in liquid mixtures.* Applied Physics A, 2002. **74**(1): p. s1376-s1378.
16. Almasy, L. and G. Jancso, *Small-angle neutron scattering and Kirkwood-Buff integral study of aqueous solutions of pyridine.* Journal of molecular liquids, 2004. **113**(1-3): p. 61-66.
17. Shulgin, I. and E. Ruckenstein, *Kirkwood-Buff integrals in aqueous alcohol systems: Comparison between thermodynamic calculations and X-ray scattering experiments.* The Journal of Physical Chemistry B, 1999. **103**(13): p. 2496-2503.
18. Zielkiewicz, J., *Kirkwood-Buff integrals in the binary and ternary mixtures containing heptane and aliphatic alcohol.* The Journal of Physical Chemistry, 1995. **99**(10): p. 3357-3364.
19. Ghoufi, A., et al., *Hydrogen-bond-induced supermolecular assemblies in a nanoconfined tertiary alcohol.* The Journal of Physical Chemistry C, 2011. **115**(36): p. 17761-17767.
20. Adya, A.K., L. Bianchi, and C.J. Wormald, *The structure of liquid methanol by H/D substitution technique of neutron diffraction.* Journal of Chemical Physics, 2000. **112**(9): p. 4231-4241.

21. Yamaguchi, T., K. Hidaka, and A. Soper, *The structure of liquid methanol revisited: a neutron diffraction experiment at− 80 C and+ 25 C.* Molecular Physics, 1999. **96**(8): p. 1159-1168.
22. Zoranić, L., F. Sokolić, and A. Perera, *Microstructure of neat alcohols: A molecular dynamics study.* The Journal of chemical physics, 2007. **127**(2): p. 024502.
23. Perera, A., F. Sokolić, and L. Zoranić, *Microstructure of neat alcohols.* Physical Review E, 2007. **75**(6): p. 060502.
24. Kosztolányi, T., I. Bakó, and G. Pálinkás, *Hydrogen bonding in liquid methanol, methylamine, and methanethiol studied by molecular-dynamics simulations.* The Journal of chemical physics, 2003. **118**(10): p. 4546-4555.

# CHAPTER IV:

# LOCAL ORDER OF CONFINED BINARY LIQUIDS

# Chapter IV: Local Order of Confined Binary Liquids

## IV.A. Introduction

The properties of molecular fluids under confinement interest a wide range of technological applications and are subjected to a pronounced number of fundamental studies. It is a well acknowledged fact that, at the nanoscale, the physical and chemical properties (structure, dynamics, phase transitions...) of the molecular species depend on the size of the studied system. A case that ceases to exist at the sufficiently large macroscopic scale. A widely open question, which is the core of this chapter is to describe and understand how the manipulation of fluids in nanochannels is likely to induce new supramolecular organizations. As demonstrated in chapter III, associated liquids are naturally likely to form highly ordered supramolecular structures. It has been shown that the formation of clusters in the studied binary mixture models can be modulated by the dilution of an amphiphilic compound (alcohol) in an aprotic solvent (toluene/ cyclohexane).

The objective of this chapter is to illustrate the phenomenon of the spontaneous nanostructuring even more remarkably observed under confinement in nanochannels. In this situation, the nanosegregation of the components inside nanochannels leads to a core-shell tubular structure. These nanostructurations may amount to an interface induced nanodemixion, although the mixtures studied (*tert*-butanol/toluene, *tert*-butanol/cyclohexane, methanol/toluene and ethanol/toluene) are all miscible in all proportions at the macroscopic scale. Interestingly, there is recent dynamical evidence that confinement in MCM-41 could induce micro-phase separation of fully miscible binary liquids.[1-3] This nanosegregation phenomenon has been already shown in MCM type materials.[4] In this study, we intend to particularly investigate the relevant characteristic lengths associated with the stability of this core-shell organization. This could be conducted through a controlled change in the pore diameter (from MCM to SBA-15).

Besides the fundamental significance of this phenomenon in terms of grasping the original states of matter at the nanoscale, the observation of such structures could provide possible applications for selective adsorption or self-assembled material synthesis in nanochannels (nanowires, nanotubes)…

# IV.B. Methods and Principles

## V.B. 1. the Concept of Contrast variation:

The structure factor of a liquid is related to the coherent scattering length of its atoms (b), which is a characteristic of each element in the molecule. Similarly, the b value can vary between isotopes of the same atom. One of the most significant examples is Hydrogen (H) and its isotope, deuterium (D), with $b=-0.374.10^{-12}$ cm for H and $b=0.667.10^{-12}$ cm for D. Therefore, the substitution of H atoms by D in a given molecule, causes a modification in the molecular structure factor of the molecule without significantly altering its physicochemical properties.

This phenomenon is exploited in a method known as the isotopic contrast effect which can vary or even cancel the contribution of a specific chemical entity to the total structure factor measured (contrast matching). This can be done by the simple adjustment of its scattering length through a manipulation in its H/D isotopic composition.

This method provides access to some partial structure factors for different spectra measured with different isotopic compositions. An exclusive characteristic of neutron diffraction which allows unique structural studies of complex systems, especially in soft matter and biology.

## V.B.2. the Contrast Effect

In the case of empty SBA-15, the contrast is given as the difference between the scattering length densities of the atoms in the pore and the atoms forming the walls of the matrix (silica) (if empty, $\rho b_{empty}= 0$). The latter is obtained, while assuming that the silica forming the walls has a density equal to that of amorphous silica ($\rho= 2.2$ g.cm$^{-3}$).

The structure factor of empty SBA measured by PAXY small angle neutron scattering spectrometer at LLB shows four Bragg peaks indexed in a triangular lattice (10, 11, 20, 21) as shown in Fig. IV-1. These peaks represent the organization of the pore channels in a honeycomb-like hexagonal lattice. The most intense peak (10) being related to the interplanar distance, offering direct access to the center-center distance of two neighboring pores.

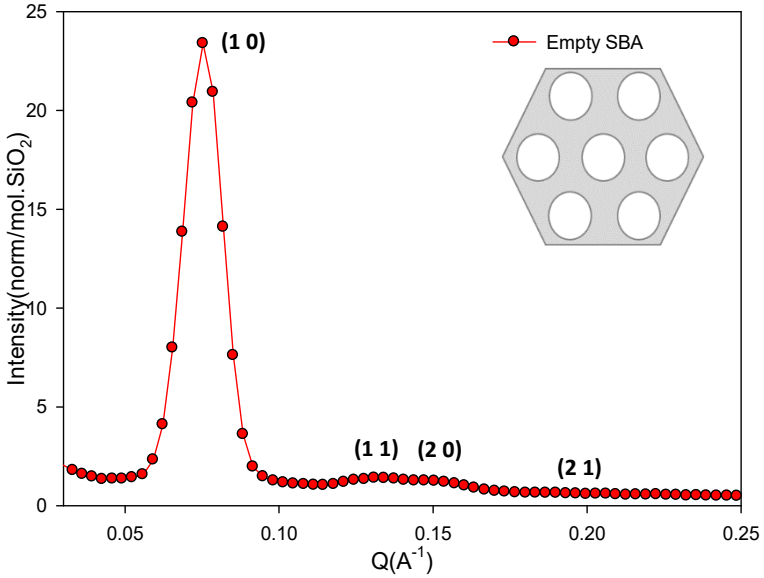


Figure IV-1: The Structure Factor of empty SBA-15 which shows the 4 Bragg peaks corresponding to the hexagonal arrangement of the pores. A triangular lattice is shown at the upper right of the figure.

Filling the empty matrix does not change the position of the Bragg peaks of SBA; however, it leads to a significant variation in their intensity due to the contrast effect. Indeed, the intensity of the Bragg peaks is proportional to the square of the contrast, the latter being defined as the difference in mean scattering length density of coherent scattering centers ($\rho\bar{b}$) between the wall and the inside of the pore according to the equation (IV-1).

When SBA-15 is filled with the liquid, the intensity of the Bragg peaks of the mesoporous materials becomes proportional to the square of the difference in the scattering length density between the liquid (in the pore) and the silica.

$$\begin{aligned} I_{peak(empty))} &= k\left[(\rho\bar{b})_{SiO_2} - 0\right]^2 \\ I_{peak(filled))} &= k\left[(\rho\bar{b})_{SiO_2} - (\rho\bar{b})_{liquid}\right]^2 \end{aligned} \qquad \text{(IV-1)}$$

Where $I_{peak}$ is the intensity of SBA-15's (10) peak measured by neutron diffraction, k is a constant, ρ is the density of the molecule constituting the studied medium, $\bar{b}$ is the sum of all the coherent scattering lengths of the atoms in the molecule and $(\rho\bar{b})$ is the molecular scattering length density.

According to equation (IV-1), the intensity of the Bragg peaks is proportional to the square of the difference in scattering length density between the pore walls and the confined liquid. The latter can be modulated by adjusting the H/D isotope ratio of the molecules.

A special case is obtained when we choose an isotopic composition so that the scattering length density of the liquid becomes equal to that of the pore walls. The liquid is then in a contrast-matching condition (CM) with the matrix and the Bragg peak intensity is expected to vanish.

The "no contrast" compositions can be simply calculated from the liquid's density and chemical formula. (Fig. IV-2) shows the variation of the Bragg Intensity as a function of the liquid density.

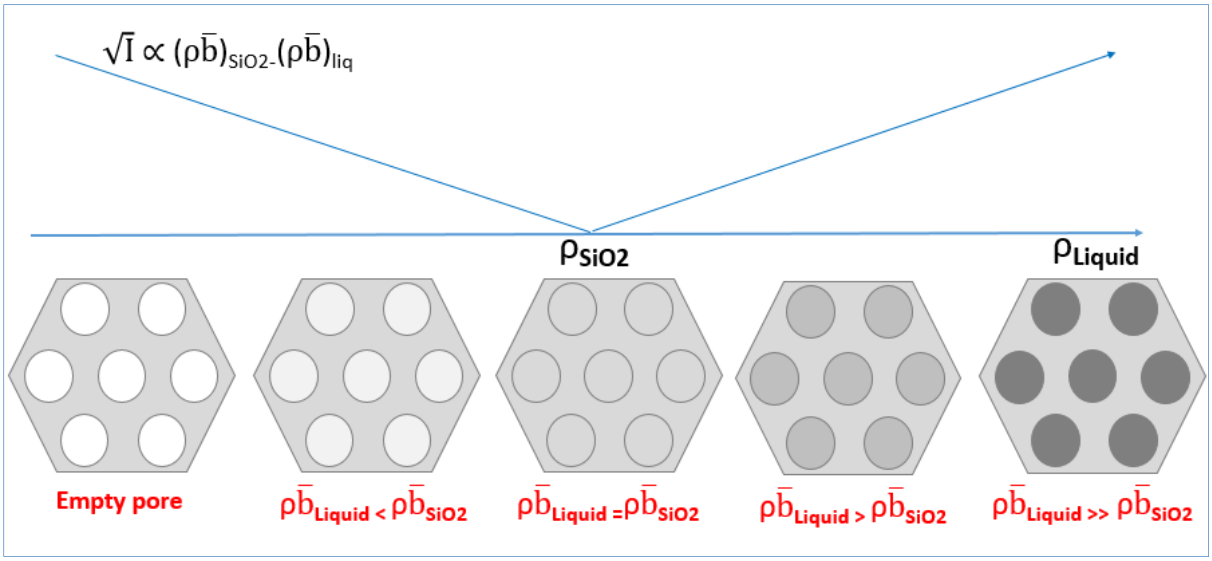


Figure IV-2: The evolution in the scattered Intensity as a function of the liquid's scattering length density relative to the density of silica. The empty pore corresponds to a scattering length density= 0.

This method has been used to determine the variation of the liquid density as a function of temperature for fully deuterated systems.[5, 6] In our approach, the purpose isn't to tune the liquid density but rather adjust the scattering length $(\bar{b})$ through the modification of the H/D composition of the liquid mixtures involved.

# IV.C. SANS Measurements on Confined Mixtures

## IV.C.1. Sample Preparation and Data Treatment

SBA-15, diameter ~ 8.5nm was synthesized following the procedures described in Chapter II. Heating at 120 °C under vacuum for 24h prior to the experiments was performed to remove possible traces of water molecules or other volatile molecules adsorbed. The matrix was then packed into a Hellma quartz cell of 1mm of thickness. The cell was filled SBA compacted so that the dispersion of the powder is homogeneous in the cell. The height of the porous medium (50mm) must be larger than the diameter of the neutron beam (7.6mm). Thus, knowing the total height of SBA and its mass, we were able to estimate equivalent quantity of the empty matrix for later normalization. The measurement was conducted at a wavelength λ= 6 Å and sample-detector distance= 1.5m.

For each of the 4 binary systems studied (TBA-Tol, TBA-Cyc, Meth-Tol, and Eth-Tol) eight samples with different concentrations and isotopic compositions were prepared:

.1-Two samples with one component (alcohol or solvent) each prepared with a specific H/D composition to tune the scattering length so that the scattering length density is equal to that of silica (*i.e.* in CM condition with the matrix).

.2-Two binary mixtures with scattering length densities equivalent to that of the matrix (hydrogenated alcohol + deuterated solvent and deuterated alcohol + hydrogenated solvent).

.3-Two symmetrical systems with the exact same concentration composition but different isotopic composition having the same overall scattering length densities. One of the components is deuterated and the other is contrast matched with the silica matrix.

.4-The last two samples have a constant 30-70 alcohol-solvent composition. Again one of the components is deuterated and the other is contrast matched with silica. It should be mentioned that all eight samples were prepared in volume fraction. The different binary mixture samples studied and their corresponding HD compositions are illustrated in Table IV-1.

Table IV-1: The HD compositions of the different samples and systems measured.

| Binary Systems | TBA-Tol | TBA-Cyc | Meth-Tol | Eth-Tol |
|---|---|---|---|---|
| **Contrast-Matched** | TBAH37TolD63<br>TBAD51TolH49 | TBAH46CycD54<br>TBAD57CycH43 | MethH37TolD63<br>MethD52TolH48 | EthH37TolD63<br>Eth49DTolH51 |
| **Symmetrical** | TBAD43TolCM57<br>TBACM43TolD57 | TBAD53CycCM47<br>TBACM53CycD47 | MethD49TolCM51<br>MethCM49TolD51 | EthD46TolCM54<br>EthCM46TolD54 |
| **alcohol30-solvent70** | TBAD30TolCM70<br>TBACM30TolD70 | TBAD30CycCM70<br>TBACM30CycD70 | MethD30TolCM70<br>MethCM30TolD70 | EthD30TolCM70<br>EthCM30TolD70 |

The different samples were injected into the SBA containing cells with volumes about 90% of the pore volume measured by nitrogen adsorption (Chapter II). Filling the empty matrix does not change the position of its Bragg peaks, it rather causes a significant change in the total structure factor, typically concerning the intensity of Bragg peaks especially noticeable for the most intense (10).

Immediately after the injection of liquid into the cell containing the empty SBA, the imbibition kinetics were followed through the variation in the measured Bragg intensity with time at room temperature. Fig. IV-3 shows the evolution for contrast matched Tol versus time. As observed in the figure, the adsorption of the liquid in SBA and the filling of the pores over time is accompanied by a progressive decrease in the Bragg intensity to a stable value reached after 6 hours indicating that the density in the pores has reached a state of equilibrium corresponding to the complete filling of the pores. This allowed the measurement of the characteristic time of adsorption and the definition of a well-adapted procedure for the subsequent samples.

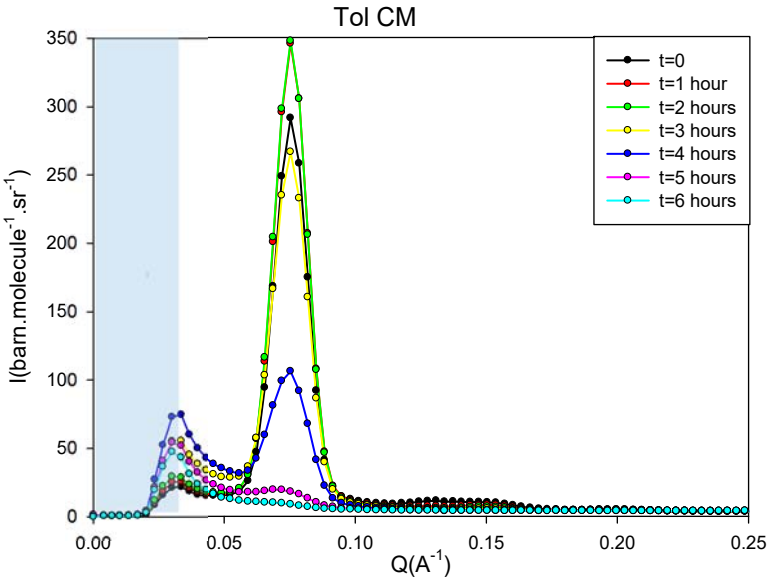


Figure IV-3: Evolution of the total structure factor S(Q) of SBA-15 filled with toluene in contrast matching condition as a function of time. The shaded area represents the beam stop.

Therefore, after the injection of the mixtures, each sealed cell was maintained for a minimum waiting period of 6 hours at room temperature in order to assure that the impregnation has reached a steady state and that the system is thus in equilibrium. This is important to ensure that the change in the measured intensity is connected to the nanostructuration of liquids confined in the pores of SBA rather than the adsorption kinetics. We have also verified that for each sealed cell there was no loss of liquid by evaporation, by sample weight control before and after the measurement.

Finally, regarding the data treatment, it was applied using the standard procedures thoroughly explained in Chapter III where the spectra were corrected from the empty cell contribution (transmission corrections), normalized to the right amount of SBA-15 and corrected for detector efficiency (through the normalization to a constant incoherent diffuser: $H_2O$) to eventually obtain intensities in absolute units.

# IV.D. Experimental Results

## IV.D.1. Contrast effect of the mixture of one single isotope liquid (D / H)

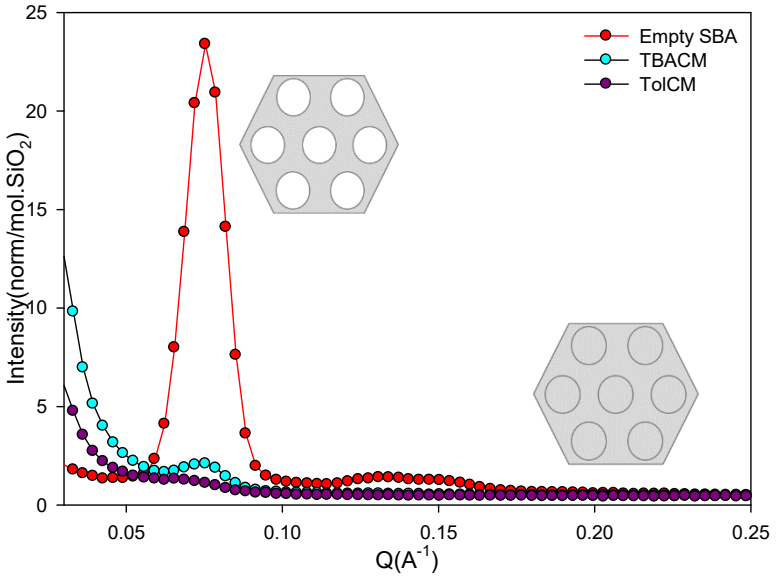


Figure IV-4: The structure factors of empty SBA (red), SBA filled with TBA in CM (blue) and Tol in CM (purple) where a total suppression of the Bragg peaks is observed.

As mentioned earlier, a suppression in the intensity of the Bragg peaks is expected for isotopic mixtures having their scattering length densities equivalent to that of the pore walls. Such a measurement was performed for an isotopic D/H mixture of *tert*-butanol (TBA) with a composition of 55/45% and toluene (Tol) with an isotopic concentration of 54/46% both being in CM conditions with the confining matrix.

Fig. IV-4 shows the structure factor of both mixtures in comparison to the empty matrix. A total extinction of the Bragg peak intensities of SBA is witnessed validating the zero contrast condition as well as the appropriate choice of the density of silica ($2.2 g.cm^{-3}$). This observation also demonstrates that the sample preparation protocol allows the achievement of a complete and homogeneous filling of the pores in the case of pure liquids.

## IV.D.2. Contrast Effect in Binary Mixtures Satisfying CM Condition

The CM method has been verified by the total extinction of the Bragg peaks of SBA filled with an isotopic mixture of pure liquids (Tol or TBA) in CM condition. In the current approach, we want to verify the validity of zero contrast for isotopic mixtures of two different liquids. For this purpose, we used a binary mixture of hydrogenated *tert*-butanol (TBAH) and deuterated toluene (TolD) and another with TBAD and TolH so that the scattering length densities of both mixtures is equal to that of silica. The CM condition is attained for a TBAH/TolD composition of 37/63 and TBAD/TolH composition of 51/49.

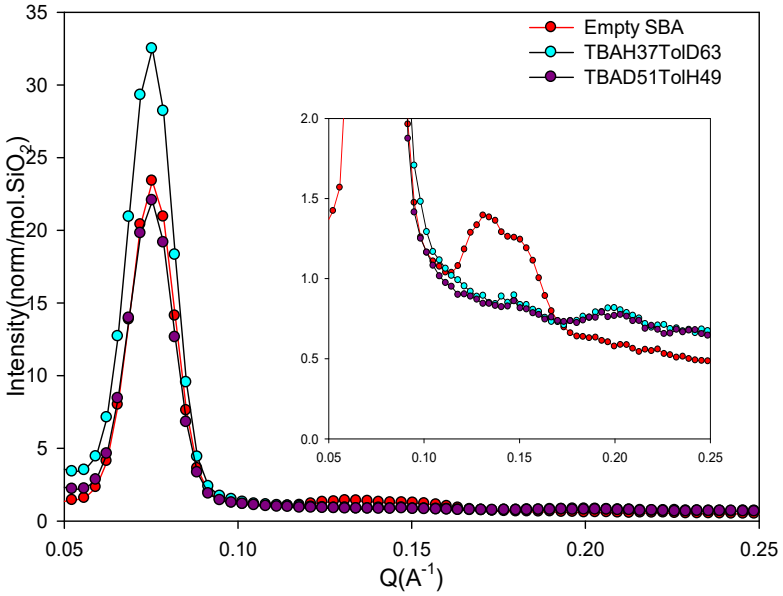


Figure IV-5: The structure factors of empty SBA (red), SBA filled with TBAH/TolD (blue) and TBAD/TolH (purple) both mixtures being in CM where a modulation in the Intensity is observed.

The experimental S(Q) of the isotopic mixture of the binary system in comparison to that of empty SBA is illustrated in Fig. IV-5. The figure shows that no Bragg peak extinction is observed in the case of the contrast matched binary mixtures. In contrary, the peak intensity (10) of SBA filled with the H/D mixture is even higher than that of the empty matrix. Moreover, an extinction of the 2$^{nd}$, a strong decrease in the 3$^{rd}$ and a significant increase in the intensity of the 4$^{th}$ order peaks is observed in both mixtures. A scenario very distinct from that of pure substances indicating a modulation in that form factor rather than a simple contrast related scaling in its intensity.

This observation is quite remarkable because it provides a direct evidence that the binary mixture doesn't homogeneously fill the pores. This indicates the existence of a heterogeneous distribution of the concentration of the mixture which can be associated to a structuration of the liquids or more specifically the nanosegregation of the components in the SBA-15 pores.

## IV.D.3. Symmetrical Mixtures with Equivalent Scattering length Densities

To further investigate the heterogeneity in the pore in the case of TBA/Tol binary mixture, a new strategy was adopted. In this approach two mixtures were prepared. In each of the two mixtures only one of the components is visible being deuterated while the other component is isotopically contrast matched with the matrix.

The significance of these mixtures is that they are chemically equivalent bearing the exact same composition. In addition, and probably the most interesting characteristic of the symmetrical mixtures is the fact that they have the same scattering length density *.i.e.* they should give the exact same diffraction patterns in the case of uniform filling and can therefore give a conclusive evidence of heterogeneity otherwise.

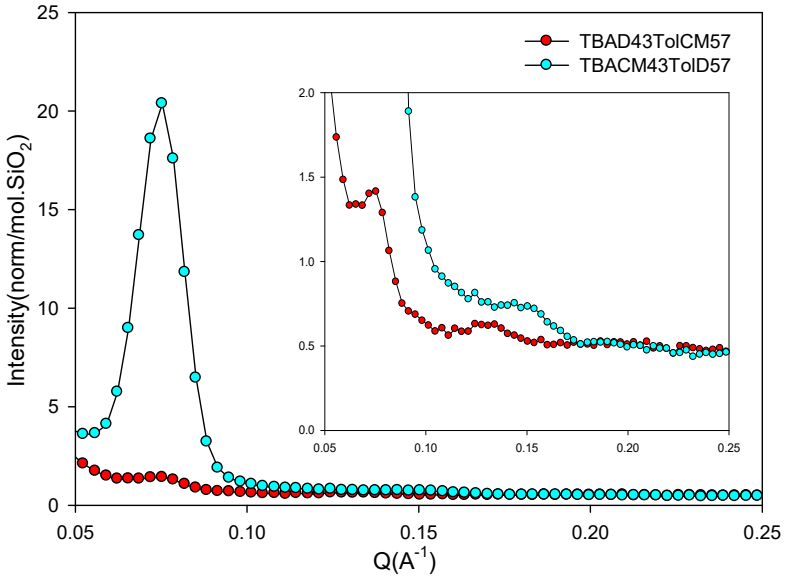


Figure IV-6: The structure factors of SBA filled with TBADTolCM (red), SBA filled with TBACMTolD (blue) both mixtures having the same composition 43/57 and same scattering length densities.

This has been demonstrated in Fig. IV-6 where the symmetrical mixtures peculiarly give very distinct structure factors with that of TBADTolCM having almost a total extinction of all but the 2$^{nd}$ order Bragg peak (even though the system is not in CM) while the other sample displays high intensities in the 1$^{st}$ and 3$^{rd}$ order Bragg peaks. This different modulation of the intensities and alternation between the 2$^{nd}$ and 3$^{rd}$ order Bragg peaks between the two samples unambiguously indicates the non-uniform filling and heterogeneity of the binary mixtures inside the pore.

# IV.E. Structural Models

## IV.E.1. Choice of Model

To reveal the nature of the nanostructuring in confinement we have developed a theoretical model. The aim of the latter, described in the following paragraphs, is to predict quantitatively the Bragg peak intensity for a given structure in order to estimate the density distribution within the pores for phase-separating mixtures. Different forms of binary liquid nanostructuring in cylindrical pores were predicted theoretically.[7] Even though these predictions were developed for mixtures with a miscibility gap (a case distinct than ours), they can identify different possible structures and can still be relevant to our study. Three microstructures corresponding to different thermodynamic states (capsules, plugs and tubes) were considered as shown in Fig. IV-7.

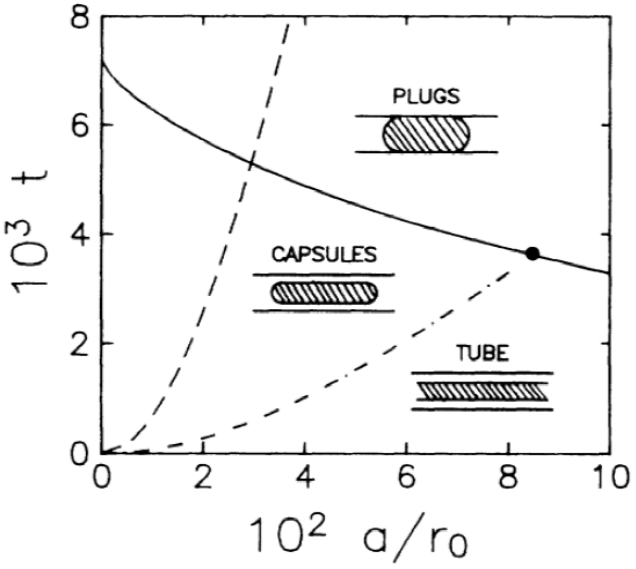


Figure IV-7: Prediction of the phase diagram of the different visible structures as a function of the reduced temperature (t) and the inverse pore radius ($r_0$) (case of a de-mixed mixture with a non-wetting component.

It is important to note that this nanosegregation must have a component that modulates the concentration profile in the radial direction*; i.e.,* perpendicular to the pore axis, to affect the Bragg peak intensity. A simple modulation of the concentration in the direction parallel to the pore axis may give an additional diffuse component but wouldn't influence the intensity of the Bragg peaks. For instance, in neutron scattering, the plug should not have any effect on the intensity of the Bragg peaks and would be difficult to detect because it doesn't lead to a concentration modulation in the (xy) plane perpendicular to the channels in which lies the two crystallographic axes of the hexagonal array of SBA. The only possibility for detecting this

plug structure is if the cap positions along the z axis are correlated from one channel to another forming a 3-D ordered structure. However, this possibility may be eliminated because it is highly improbable to have sufficient interactions between liquids in adjacent channels, separated by a silica wall. On the other hand, "capsules" and "tubes" generate a radial modulation concentration upon an average projection on the (xy) plane. However, since the two structures lead to the same type of average radial concentration profile they are experimentally indistinguishable contributing to the same core-shell type profile. This cylindrical symmetry profile is characterized by two domains: one corresponding to a peripheral layer, located at the pore surface and another at the pore center.

Confined liquids are known to be highly susceptible to geometrical as well as surface effects.[8-10] Interfacial phenomena induced by a strong interaction of one of the components with the pore surface are likely to lead to core-shell like concentration profiles. Launching from this idea together with the cylindrical symmetry induced by the pore shape, a preferential interaction of the liquid with the pore wall may facilitate its adsorption at the surface leaving the pore core free for the second liquid (with lower affinity to the pore surface) to reside in .

In order to grasp the essence of the physical phenomenon revealed by the diffraction experiments, we chose the simplest model with the least number of adjustable parameters. The latter assumes that a liquid is completely adsorbed on the surface and the second is located at the center *i.e.* confinement induced complete segregation of the two components (core-shell structure). The local molar fraction thus passes strictly from x= 0 to x= 1 upon crossing the two segregated regions. This nanoscale organization could itself be considered as a thermodynamic phase, having a non-homogeneous distribution of its concentration (and not a two phase system) as the characteristic sizes involved are comparable to those of an interface between two separated liquids.

It is obvious that this extremely simplified model is not designed to quantitatively reproduce the data. In fact, in the case of an interfacial segregation, it is expected that the concentrations in the two fields are not strictly 0 and 1, but rather correspond to mixtures more rich in one constituent or the other. Moreover, the existence of such a sharp interface between the two regions, at the atomic scale, is very simplistic. However, this model has the enormous advantage of having no adjustable parameters and therefore having a predictive nature. Furthermore, the robustness of this model will allow us to extract the main physical elements leading to this nanostructuring phenomenon.

### IV.E.2. Theoretical Background

The intensity measured by neutron scattering is proportional to the product of the form factor of the object (pore) and the structure factor (pore distribution) using the formula:

$$I(Q) = KS(Q).|F(Q)|^2 = KS(Q).P(Q) \quad \text{(IV-2)}$$

For a perfect 2-D hexagonal array of cylindrical pores, the structure factor S(Q) is given by:

$$S(Q) = \frac{1}{Q^2}\sum_{hk} M_{hk}\,\delta(Q_{hk}) \quad \text{(IV-3)}$$

$M_{hk}$ being the multiplicity factor of the diffraction peaks where $M_{hk}$ =12 for diffractions of mixed Miller indices (hk), and $M_{hk}$ =6 for (h0) and (hh), Q is the scattering vector and $\delta(Q_{hk})$ are Dirac (δ) functions at specific reciprocal lattice points corresponding to the Bragg peak positions obtained by:

$$Q_{hk} = \frac{4\pi}{a\sqrt{3}}\sqrt{(h^2 + k^2 + hk)} \quad \text{(IV-4)}$$

In the case of an empty matrix:

$$F(Q) = \frac{\rho_{SiO_2} {R_{pore}}^2 Z(QR_{pore})}{\rho_{SiO_2} {R_{pore}}^2} \quad \text{(IV-5)}$$

Where $Z(QR_i) = \frac{2J_1(QR_i)}{(QR_i)}$, ($J_1$ being a first order Bessel function). In this approach we made the choice to normalize F(Q) to the total number of scatterers of the empty SBA, i.e. F(0)=1.

#### IV.E.2.1. Homogeneous Filling

In the case of a matrix filled in liquid:

$$F(Q)^{Filled} = \frac{(\rho_{liq} - \rho_{SiO_2}){R_{pore}}^2 Z(QR_{pore})}{\rho_{SiO_2} {R_{pore}}^2} = \frac{(\rho_{liq} - \rho_{SiO_2})}{\rho_{SiO_2}} F(Q)^{Empty} \quad \text{(IV-6)}$$

Filling the pores with a liquid will affect F(Q) rather than S(Q).

I(Q) is the same yet having a different prefactor (*i.e.*, simple rescaling in the intensity). This result is illustrated by the Contrast Matching (CM) experiments according to equation (IV-1).

### IV.E.2.2. Core-Shell Model

In this case, a simple generalization of the homogeneous filling is implemented (again we apply the same normalization to the number of scatterers of the empty matrix).

$$F(Q)^{Core-Shell} = \frac{1}{\rho_{SiO_2} R_{pore}{}^2} \sum_{i=1}^{2} (\rho_i - \rho_{(i-1)}) R_i{}^2 Z(QR_i) \qquad \text{(IV-7)}$$

Where, $\rho_0 = \rho_{SiO_{2(matrix)}}$, $\rho_1 = \rho_{shell}$, $\rho_2 = \rho_{core}$, $R_{1=}R_{pore}$ and $R_{2=}R_{core}$ (based on the core-shell model for a cylinder illustrated in Fig. IV-8). At the center, the shape of the pore is demonstrated by a cylinder (gray) consisting of two liquids with different densities: core (red) for the liquid at the center and shell (blue) for the liquid at the surface. The diagrams in the same figure show the different possibilities for structuring liquid in the pores for this model.

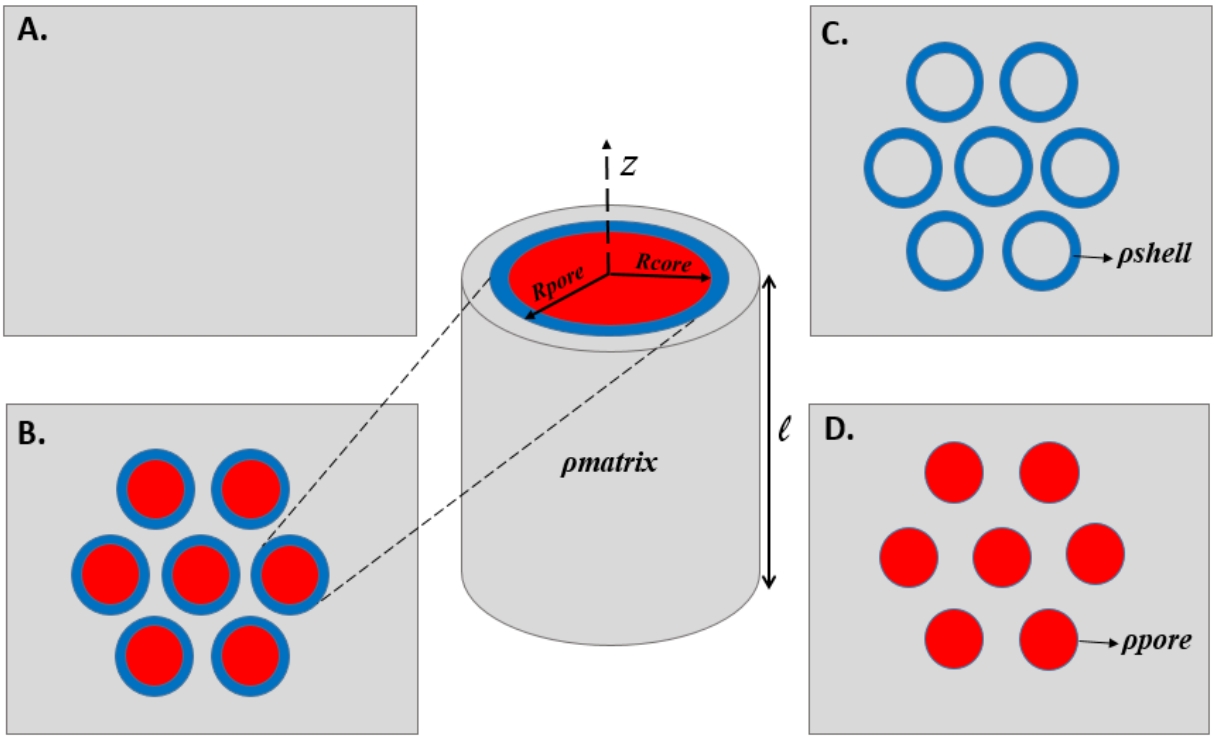


Figure IV-8: Core-shell model of a pore in the center, in the form of a cylinder (gray) formed by two different density liquids, core (red) and shell (blue). The contrast variation depending on the variation of the scattering length density; (a) in zero contrast, (b) the densities of the two constituents of the binary liquid are different from each other and from that of the matrix, (c) and (d) two symmetrical mixtures with one of two liquids in CM condition.

Contrast variation depending on the change in the density of the pore is illustrated for different situations: A.: contrast matching (zero contrast condition), *i.e.* scattering length density of the liquid in the pores is equivalent to that of silica (gray), B.: the case where the densities of the binary liquid components and the matrix are all different, C. and D.: symmetrical mixtures having one of the two liquids is in CM and the other being deuterated making the latter selectively visible to neutrons.

Fig. IV-9 shows the distribution of the scattering length density of the four situations (A, B, C and D). 1 and 2 are the components of the binary liquid segregated at the center and adsorbed at the pore surface respectively, r is the pore radius and $\rho_{SiO2}$ is the density of the silica.

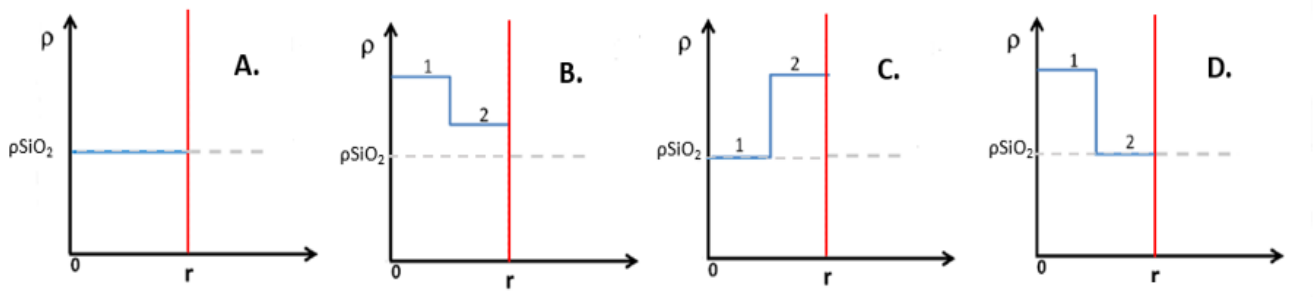


Figure IV-9: Schematic representation of the scattering length density distribution corresponding to 4 cases represented in Figure IV-8. Liquids 1 and 2 are respectively located in the center and at the surface of pore, (r) is the pore radius and $SiO_2$ is the scattering length density of the silica

### IV.E.2.3. Debye Waller Factor Model

In this section, we try to analyze the diffraction intensities of SBA in terms of various structural models of the hexagonal unit cell. The different parameters of these models are the dimensions and scattering length densities of each part in the unit cell. After choosing the core-shell model as the simplest model possible to describe the heterogeneities in the pore, we have to take into account the fact that our confining matrix is not ideal.[11-13]

The positions of the cylinders in the unit cell may be randomly displaced from their ideal 2-D hexagonal positions. This is usually due to the thermal fluctuations frozen by silica polymerization (static lattice distortions) which are illustrated in Fig. IV-10.

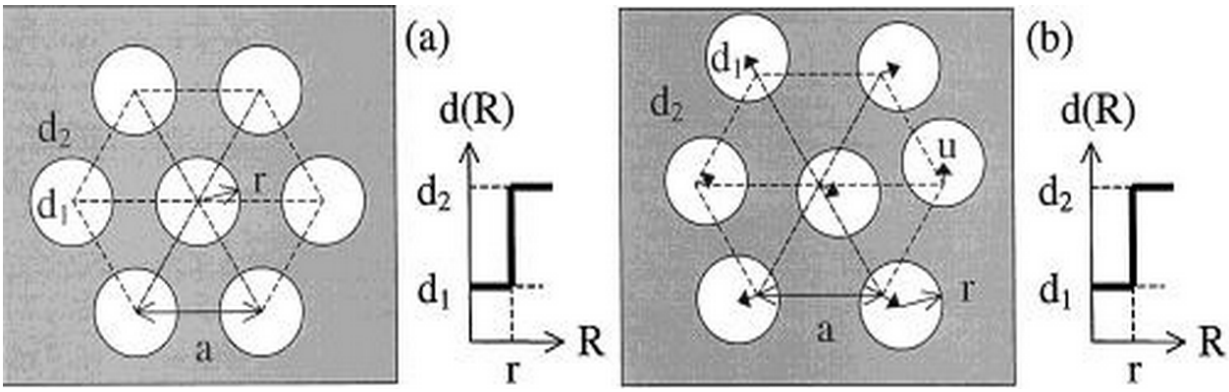


Figure IV-10: Schematic representation of the structure in terms of different models based on (a) two density levels and (b) two density levels and a DWF. Arrows indicate a random displacement of the pore centers. [11]

The frozen random disorder in the pore position with respect to the ideal lattice will affect S(Q). This is approximated by the DWF in the harmonic approximation:

$$I(Q) = \frac{K}{Q^2}\sum_{hk} M_{hk}\,\delta_{(Q_{hk})}|F(Q)|^2 e^{-\frac{\langle u^2\rangle Q^2}{2}} \qquad \text{(IV-8)}$$

$< \bar{u}^2 >$ is the normalized mean-squared displacement (MSD) of the cylinders.

This DWF effect can be introduced into a modified form factor P(Q) to yield the following equation:

$$I(Q) = \frac{K}{Q^2}\sum_{hk} M_{hk}\,\delta_{(Q_{hk})}\left|F(Q)e^{-\frac{\langle u^2\rangle Q^2}{4}}\right|^2 = \frac{k}{Q^2}\sum_{hk} M_{hk}\,\delta_{(Q_{hk})}.P(Q) \qquad \text{(IV-9)}$$

Therefore the intensities of the higher order reflections are expected to be significantly reduced by this DWF effect.

### IV.E.2.4. Microporous Corona Model

In addition to static defects, SBA diverges from an ideal matrix in terms of pore structure. Its cylindrical mesopores are notorious to have a complex wall structure, modelled by corrugated pore walls and/or an interfacial microporous region denoted as a 'corona' (Fig. IV-11).

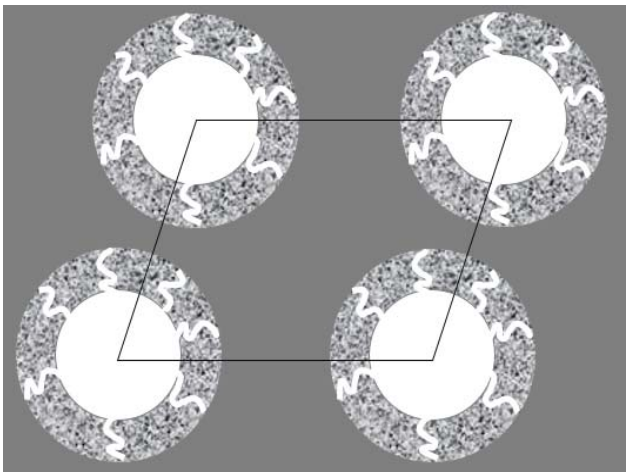

Figure IV-11: A scheme of SBA pores having a lower density corona region and wall corrugations.

Therefore, a model accounting for a reduced density sponge-like corona around the pores, following the studies of Impéror-Clerc *et al.*,[11] was introduced. It is based on the assumption that the cylindrical mesopores belong to a perfect 2-D hexagonal lattice with monodispersed mesopores bearing a perfectly circular cross section, but surrounded by a microporous corona of a reduced (constant) density, with dense silica constituting the outer region.

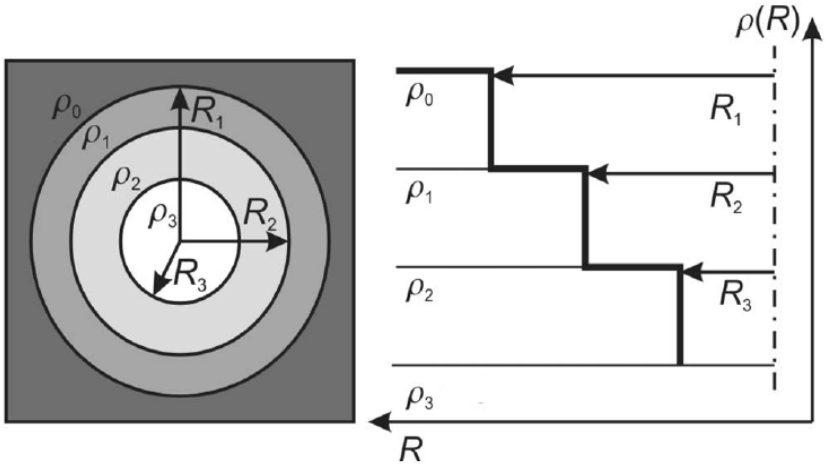


Figure IV-12*:* Four density levels model of the pore structure of SBA-15 with electron densities: dense silica matrix $\rho_0$, microporous corona $\rho_1$, shell $\rho_2$, and the core of the $\rho_3$. $R_1$, $R_2$, and $R_3$ represent the radii of the different shells. [12]

This step-density model developed by Zickler et al. [13] is probably the simplest way to account for this complex situation in which both the corona, the shell and the core in our core shell model are assumed to have uniform densities. However, based on this model it is not possible to discriminate explicitly between a microporous corona and highly corrugated pore walls.[13]

Mathematically, this model is defined by four density levels as shown in Fig. IV-12. The 1st region represents the core in the center of the pore with scattering length density $\rho_3$, the 2nd represents the shell of a uniform density $\rho_2$, the 3rd region represents the porous corona of uniform length density $\rho_1$, and the 4th representing the matrix of uniform density $\rho_0 = \rho_{SiO2}$.

It is worth mentioning that the corona density $\rho_1$ must be considered carefully, due to the introduction of the porosity of the microporous corona $\left(p = \frac{V_{micropore}}{V_{corona}}\right)$.

When SBA is empty, $\rho_1 = (1-p)\rho_{SiO_2}$; otherwise, $\rho_1 = p\rho_{surf} + (1-p)\rho_{SiO_2}$ where $\rho_{surf}$ is the scattering length density of the liquid occupying the microporous surface of the SBA.

As for the normalization, the same convention is applied, i.e., normalization to the total scatterers in empty SBA which is now equal to the mesoporous volume + microporous volume:

$$\rho_{SiO_2} {R_2}^2 + p\rho_{SiO_2}\left({R_1}^2 - {R_2}^2\right) = \rho_{SiO_2}\left[p{R_1}^2 + (1 - p{R_2}^2)\right] \qquad \text{(IV-10)}$$

Therefore the normalized form factor can now be expressed as:

$$F(Q) = \frac{1}{\rho_{SiO_2}\left[p{R_1}^2 + (1 - p{R_2}^2)\right]} \sum_{i=1}^{3} (\rho_i - \rho_{(i-1)}) {R_i}^2 Z(QR_i) \qquad \text{(IV-11)}$$

And indeed, we have F(0)=1 for the empty SBA with this appropriate normalization.

# IV.F. Data Analysis

## IV.F.1. Data Treatment

### IV.F.1.1. Background Corrections

We recall that: a) $I(Q) = \frac{K}{Q^2}\sum_{hk} M_{hk}\, \delta(Q_{hk}).\, P(Q)$

The spectra comprise a background which was removed by fitting with a pseudo Voigt function. The correction was done using Sigmaplot software where the position, width, and height of the peaks were kept free. The experimental data, best fits and background corrected data are plotted in Fig. IV-13.

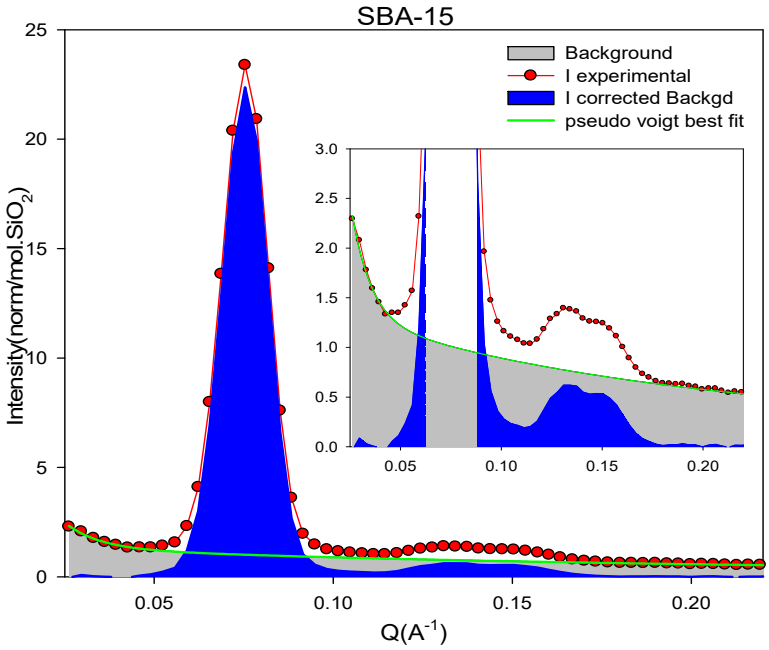


Figure IV-13: Background correction of experimental intensity.

### IV.F.1.2. Analysis of Bragg Scattering

The Bragg peaks are not Dirac but rather broadened due to the instrumental finite resolution and sample imperfections. In order to get their total intensities, they were fitted by 4 Gaussian functions in order to extract their integration, as shown in Fig. IV-14.

We fitted with the function b) $I(Q)^{fit} = \frac{1}{Q^2}\sum_{hk} M_{hk}\, \tilde{I}_{hk} G_{hk}(Q - Q_{hk}) + I(Q)^{Bckgd}$

Where $G_{hk}$ are unitary Gaussians (with weakly varying width related to the instrument resolution), $\tilde{I}_{hk}$ giving a measure of the integrated intensity of the (hk)-Bragg peaks.

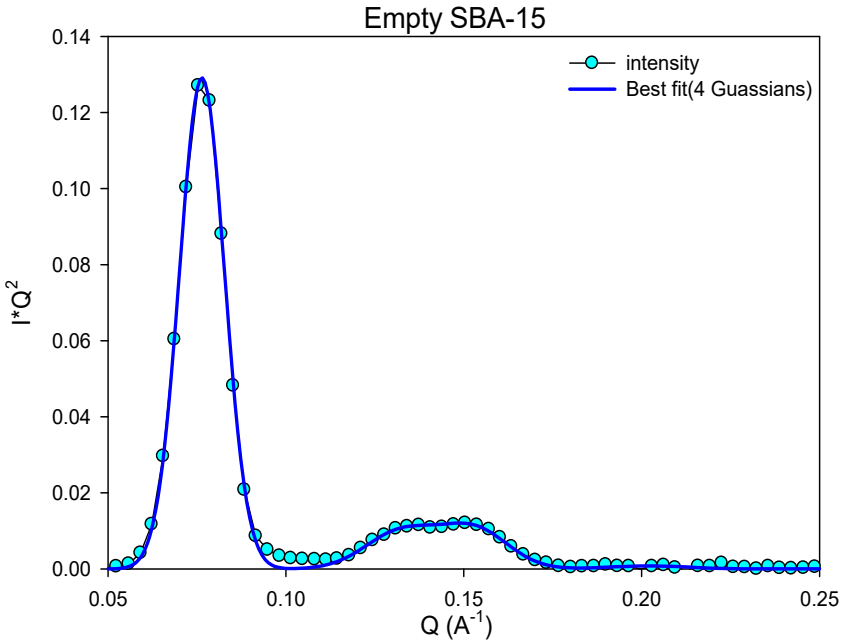


Figure IV-14: Best fit (4 Gaussians) of the experimental intensity after background correction.

Comparing a) and b) one should obtain:

$$\tilde{I}_{hk} = K.P(Q_{hk}) \qquad \text{(IV-12)}$$

Where K is an instrumental normalization factor. It has been determined by rescaling with respect to (1 0) Bragg peak of the empty SBA-15 and kept fixed for all the other samples.

### IV.F.1.3. Model Calculations

Our analysis was based on equation (IV-12) as we were testing the ability of the form factor P(Q) (which carries information about the radial density distribution in the cylindrical pores) to reproduce the extracted intensities $\tilde{I}_{hk}$.

It should be mentioned that for the different models the empty matrix is fitted and the parameters obtained from the best fit are kept fixed and used conjointly with the pore radius obtained from the adsorption isotherms in the calculation of the form factors of the filled samples. Therefore, no parameters were kept free in an attempt to examine the capacity of the models in the prediction of the Bragg reflection intensities for the filled samples.

Table IV-2: Different parameters (radii and densities) for the different models approached (TBA-Tol systems are taken as a prototype but the same calculation was implemented on other systems).

| Model | Densities of Different Levels | Values of Different Radii |
|---|---|---|
| **Homogeneous** | $\rho_1 = \rho_2 = \rho_{SiO2}$ | $R_1 = R_2 = R_{pore}$ |
| **Core-Shell TBA surface** | $\rho_1 = \rho_{TBA}$<br>$\rho_2 = \rho_{Tol}$ | $R_1 = R_{pore}$<br>$R_2 = R_{core} = R_{pore}\left(\sqrt{(1-x)}\right)$ |
| **Core-Shell TBA layer** | $\rho_1 = \rho_{TBA}$<br>$\rho_2 = \left(x - \frac{e^2}{Rpore^2}\right)\rho_{TBA} + \rho_{Tol}$ | $R_1 = R_{pore}$<br>$R_2 = R_{core} = R_1 - e$ |
| **Core-Shell Tol surface** | $\rho_1 = \rho_{Tol}$<br>$\rho_2 = \rho_{TBA}$ | $R_1 = R_{pore}$<br>$R_2 = R_{core} = R_{pore}\sqrt{x}$ |
| **Corona TBA surface** | $\rho_1 = \rho_{surf} = \rho_{TBA}$<br>$\rho_2 = \rho_{shell} = \rho_{TBA}$<br>$\rho_3 = \rho_{core} = \rho_{Tol}$ | $R_1 = R_{pore} - 0.5t$<br>$R_2 = R_{pore} + 0.5t$<br>$R_3 = \sqrt{\left[(R_1{}^2 p(1-x)) + (R_2{}^2(1-p)(1-x))\right]}$ |
| **Corona Tol surface** | $\rho_1 = \rho_{surf} = \rho_{Tol}$<br>$\rho_2 = \rho_{shell} = \rho_{Tol}$<br>$\rho_3 = \rho_{core} = \rho_{TBA}$ | $R_1 = R_{pore} - 0.5t$<br>$R_2 = R_{pore} + 0.5t$<br>$R_3 = \sqrt{\left[(x.R_1{}^2 p) + (x.R_2{}^2(1-p))\right]}$ |

The different calculations for the different models are illustrated in Table I, where, depending on the isotopic composition $\rho_{TBA}$ is either equal to $\rho_{TBAD}$, $\rho_{TBAH}$ or $\rho_{SiO2}$ (when satisfying the CM conditions). The same could be applied to $\rho_{Tol}$.

Moreover, the term x corresponds to the TBA volume fraction, t and p correspond to the thickness and porosity of the corona respectively and finally the term e corresponds to the thickness of one molecular layer of the liquid. The values of e used were obtained from the literature and are 6, 3.8 and 3.5 Å for TBA,[14] ethanol[15] and methanol[16] respectively.

## IV.F.2.Discussion of Data in Terms of Reliability of Models

### IV.F.2.1.Debye Waller Factor Model

#### *IV.F.2.1.i.Tert-butanol -Toluene Systems*

The data treated by the procedures described in the previous section were fitted with the models illustrated earlier. I shall start the data analysis with the DWF model in general and proceed to demonstrate different scenarios within the same model. This is an attempt to qualitatively assess the nature of the witnessed nanostructuring phenomenon. As mentioned earlier, the models taken into account are oversimplified and are thus not designed for a quantitative description of the data. However, the great advantage of the lack of adjustable parameters grants the model a privileged predictive nature.

The best fit for the empty SBA is represented in Fig. IV-15 (A), the pore size was fixed by the value obtained by the adsorption isotherms (D= 8.3nm). The value of the MSD obtained is 50 Å$^2$ which corresponds to average displacements in the order of 0.7 nm, *i.e.* about 7% of the unit cell parameter (a) which is in a good agreement with the literature.[11] These parameters, now fixed, were used for the calculation of the P(Q) for all the filled samples.

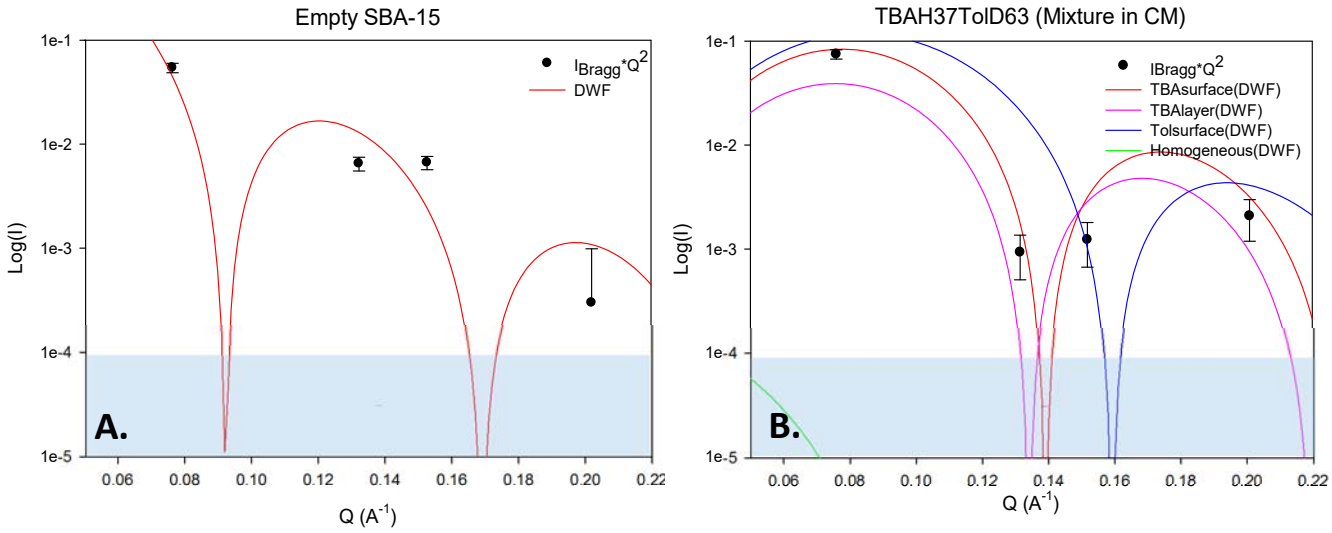


Figure IV-15: DWF model predictions (solid lines) and experimental Bragg intensities $\tilde{I}_{hk}$ (circles) for (A): empty SBA used for TBA-Tol/Cyc systems (batch1) and (B): TBAH37TolD63 (CM mixture) the shaded area represents the undetectable intensity limit.

We recall a total extinction of the Bragg peak intensity in the case of one-component isotopic liquid in CM, which wasn't the scenario obtained in the case of binary isotopic mixture also satisfying the CM condition with the confining matrix.

In the purpose of understanding the physical phenomenon behind this behavior, the change of the intensity of the sample was modelled by different scenarios within the DWF model (Fig. IV-15 (B)).

First the homogeneous model was ruled out as it anticipates a zero intensity of the peaks (which is not consistent with the experimental results). The three other models taken into account different segregation possibilities:

-1. The 1st model (denoted *TBA@surface,* in red) supports the possibility of a total separation of the liquids inside the pore with TBA (the alcohol) being at the surface of the pore and Tol (the solvent) in the center of the pore.

-2. The second model (denoted *TBA-layer,* in pink color) is rather a special case of the first model as it represents the scenario of one exclusive TBA-layer on surface and the rest of the TBA (not constituting the layer) would, therefore, mix with the Tol inside the pore.

-3. Finally, the third model (denoted *Tol@surface,* in blue) considers the same segregation phenomenon as the 1st model; however, it considers Tol (the solvent) to be at the surface and hence TBA (the alcohol) will reside in the core.

All the models related to the segregation phenomenon successfully expect a high intensity in the 1st order Bragg peak. The models agreement with the higher order peaks seems to be more discriminative, as the *Tol@surface model* incorrectly predicts a high intensity of the 2nd order Bragg peak (which is obviously not the case), at the time that both *TBA-layer* and *TBA@surface* models seem to properly reproduce the experimental intensities.

A clearer image emerges from the symmetrical systems having the same scattering length density. As discussed in the experimental results section, the two samples were supposed to give the same diffraction pattern in the case of homogeneous filling. Remarkably, the two core-shell DWF models *TBA@surface* and *TBA-layer* seem to be in a good agreement with the unexpected difference in the Bragg peak intensities between the two samples (Fig. IV-16 (A and B)) and can accurately reproduce the very low intensities (near Bragg extinction) in the TBADTolCM symmetrical sample (as shown in Fig. IV-16 (A)).

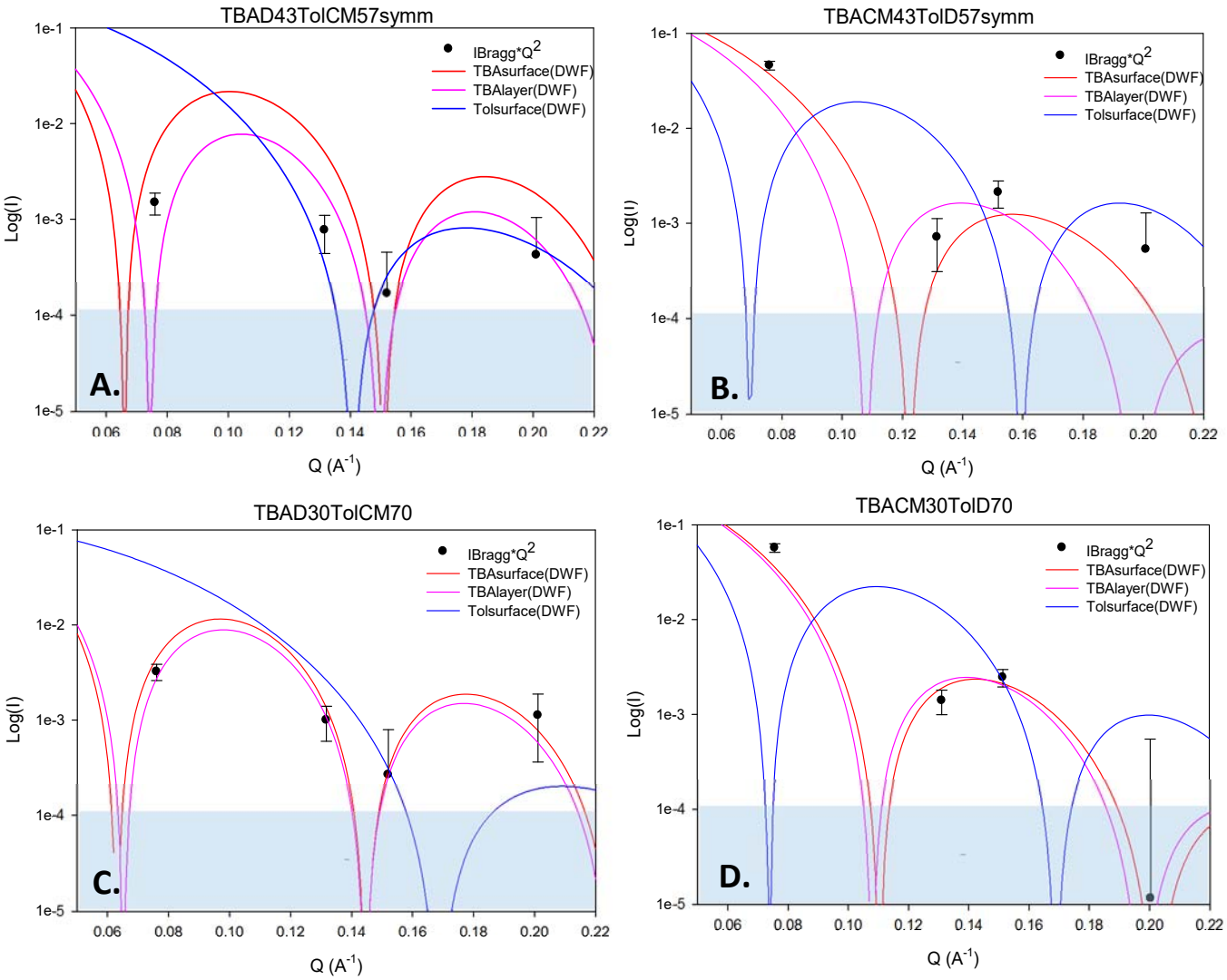


Figure IV-16: DWF model predictions (solid lines) and experimental Bragg intensities $\tilde{I}_{hk}$ (circles) for the symmetrical TBATol samples (A and B) and TBA30 Tol70 samples with opposite isotopic compositions (C and D).

The most remarkable agreement is in the 1st order Bragg peak as they correctly anticipate low and high intensities for the TBADTolCM and TBACMTolD symmetrical samples respectively. Moreover, both models give good anticipation for the higher order peaks and explain the alternation in the intensities of 2nd and 3rd order Bragg peaks between the 2 samples as the minimum in the models comes at to the position of the 3rd order peak in the TBADTolCM symmetrical sample leading to its extinction and close to the 2nd order peak in the TBACMTolD sample leading to its reduced intensity. The *Tol@surface* model, on the other hand, falsely expects high intensity for the 1st order peak of TBADTolCM symmetrical sample and low intensity of the same peak in the other symmetrical sample and can therefore be dismissed (Fig. IV-16 (A, B)).

The TBA30Tol70 sample corresponds to TBA concentration comparable to one-layer of TBA at the surface making the *TBA@surface* and *TBA-layer* models mathematically equivalent. This can be illustrated by Table IV-1 (in the Model Calculations section) where in the case of one TBA-layer $R_{core}= R_{pore}$-e (with $R_{pore}= 8.3/2= 4.15$nm and $e_{TBA}=0.6$nm) yielding $R_{core}= 3.55$ nm. As for *TBA@surface* model, $R_{core}=R_{pore}$ $(\sqrt{1 - x_{TBA}}) = 4.15(\sqrt{0.7}) = 3.47$nm. *i.e.*, equivalent core radii.

Both models seem to be in an excellent agreement with the corrected experimental data successfully expecting low intensities in the 1st and 3rd Bragg peaks and high intensities in the 2nd and 4th order peaks TBAD30TolCM70 sample and reproducing the high intensity in the (1,0) peak in the opposite 3070 sample (Fig. IV-16 (C and D)). Again the *Tol@surface* model fails to reproduce the experimental intensities as it wrongly anticipates a high intensity in the 1st order Bragg peak in TBAD30TolCM70 and low intensity of the same peak in TBACM30TolD70.

To conclude, Fig. IV-17 shows the agreement of the different models with the experimental Bragg intensity. As shown in Fig. IV-17 (A), *TBA@surface* model, although not fully quantitative, succeeds to qualitatively reproduce the main patterns in the data being able to anticipate the main modulations in the Bragg peak intensities. In contrary, the *Tol@surface* model can be safely eliminated as it falsely predicts the intensities for the (10) Bragg peak in the measured samples.

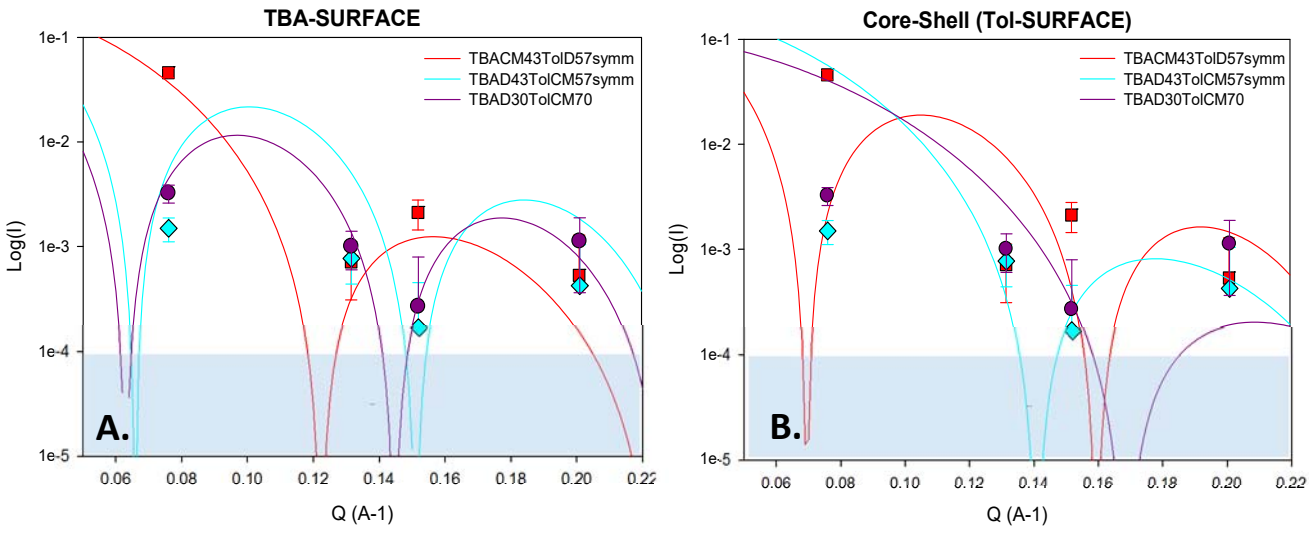


Figure IV-17: The agreement of the different models (DWF *TBA@surface* (A) and DWF *Tol@surface* (B)) with the experimental Bragg intensities $\tilde{I}_{hk}$ in TBATol systems.

The core shell model with *TBA@surface* and toluene core is demonstrated for the different samples in Fig. IV-18 where TBA is represented in blue, Tol in red and silica in grey.

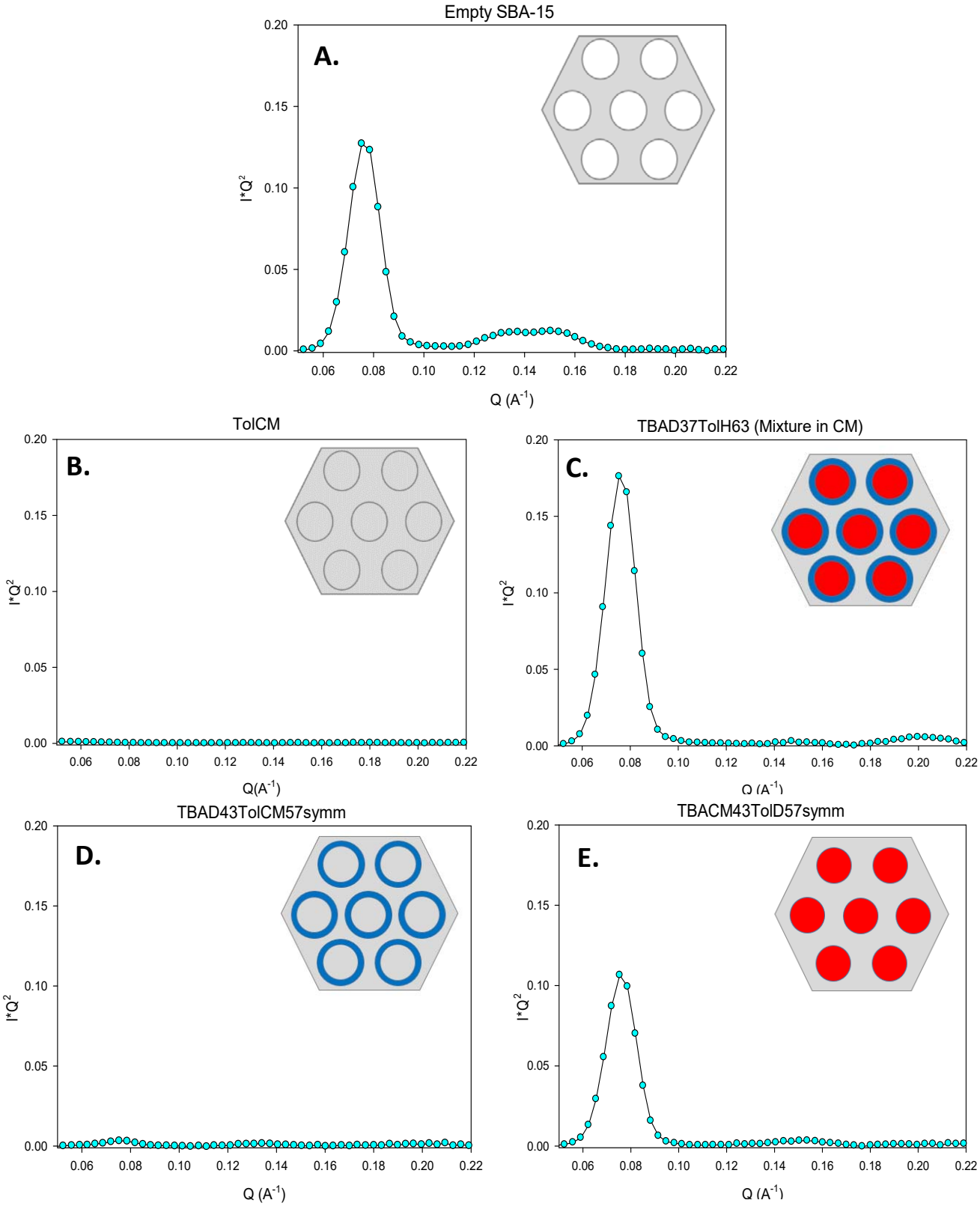


Figure IV-18: The treated experimental intensities and their corresponding (*TBA@surface*) core shell schemes for the different samples measured in the TBATol system.

### *I.V.F.2.1.ii. Tert-butanol -Cyclohexane Systems*

The main reason for the choice of this TBA-Cyclohexane (Cyc) was to test the influence of the interaction between the TBA and the aprotic solvent. According to the bulk study discussed in chapter III, [17] an enhanced stability of the TBA multimeric clusters was achieved in an aliphatic solvent compared to Tol. This was attributed to the existence of slightly stronger interactions between the aromatic ring of toluene and the hydroxyl group of TBA. Therefore, the following study on Cyc was motivated by the emerging question about a hypothetical better segregation of the two components in confinement, allowed by a weaker solute-solvent TBA-Cyc interaction.

The diffraction patterns obtained for the different TBA-Cyc samples are shown in Figs. IV-19. The overall features are in general agreement with the case of TBA-Tol systems and indicate a similar nanostructuring phenomenon inside the pore. The key-observations are the following:

-1. *The absence of Bragg peak extinction for contrast matching compositions*. This is exemplified in Fig. IV-19 (A and B). Note also that the H/D and D/H contrast matching mixtures (Figs. A and B respectively) exhibit very different patterns. The upmost signature of nanosegeragtion is the high intensity of the (10) Bragg peak of the H/D mixture, while ten times weaker for the D/H system.

-2. *The observation of very different signals arising from the two 'symmetrical' mixtures.* This is shown in Fig. IV-19 (C and D) for the two mixtures with the same chemical composition ($x_{TBA}$= 0.53), the same scattering length density and comprising a deuterated compound mixed with contrast matching one. The TBADCycCM system (Fig. IV-19 (C)) exhibits an almost extinction of its (10) Bragg peak, although it is far from the contrast matching composition. On the other hand, the TBACMCycD counterpart system exhibits an intense (almost 100 times more intense) Bragg peak (Fig. IV-19 (D)). Again, this rules out the homogeneous filling which would have predicted the same patterns.

-3. A different composition (*i.e.*, 30/70) in Fig. IV-19 (E and F), comprising a deuterated compound mixed with a contrast matching one also reveals interesting features that are in line with the TBATol systems and will help distinguishing between the different models.

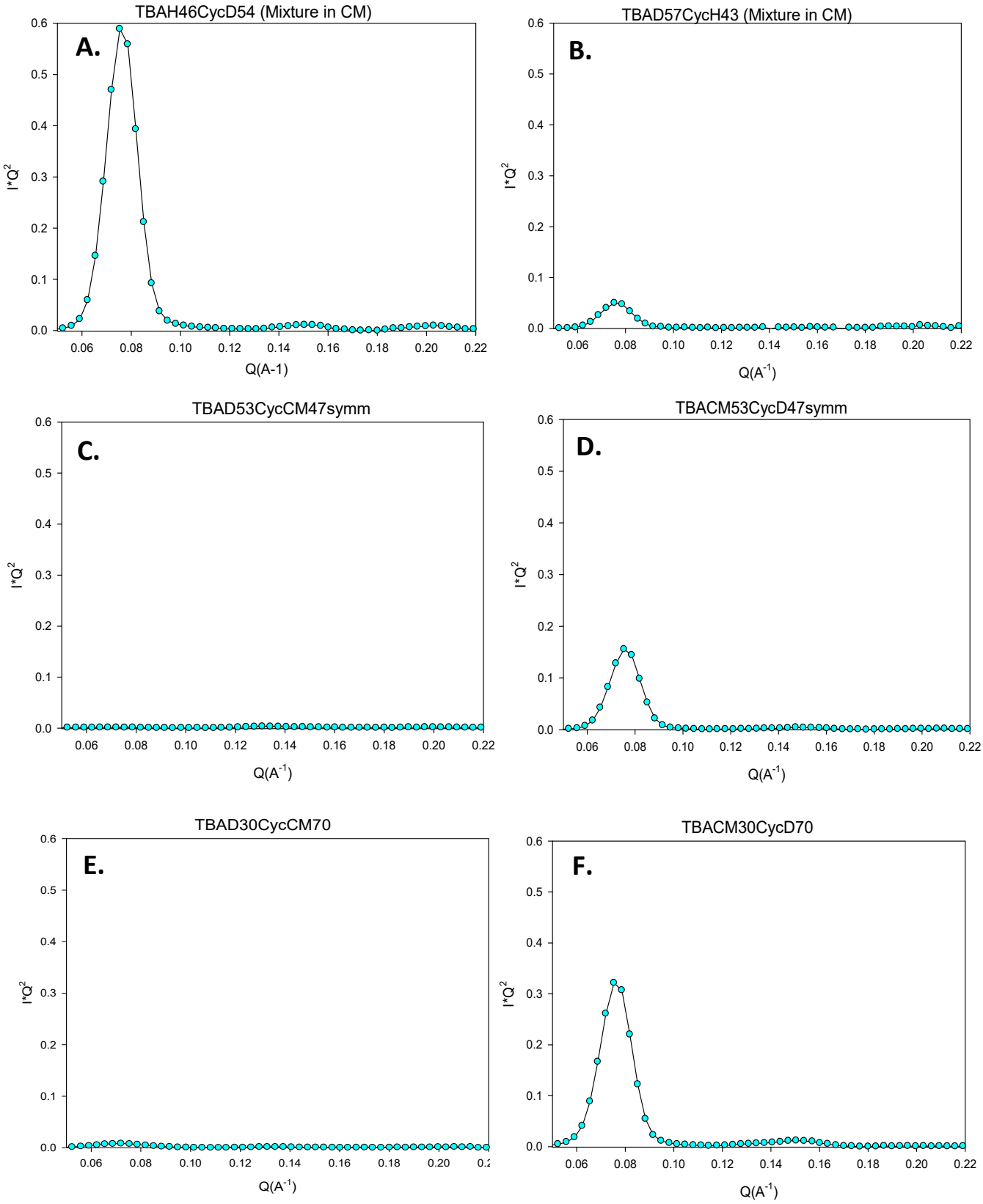


Figure IV-19: The treated experimental Bragg intensities for the different samples of the TBACyc system.

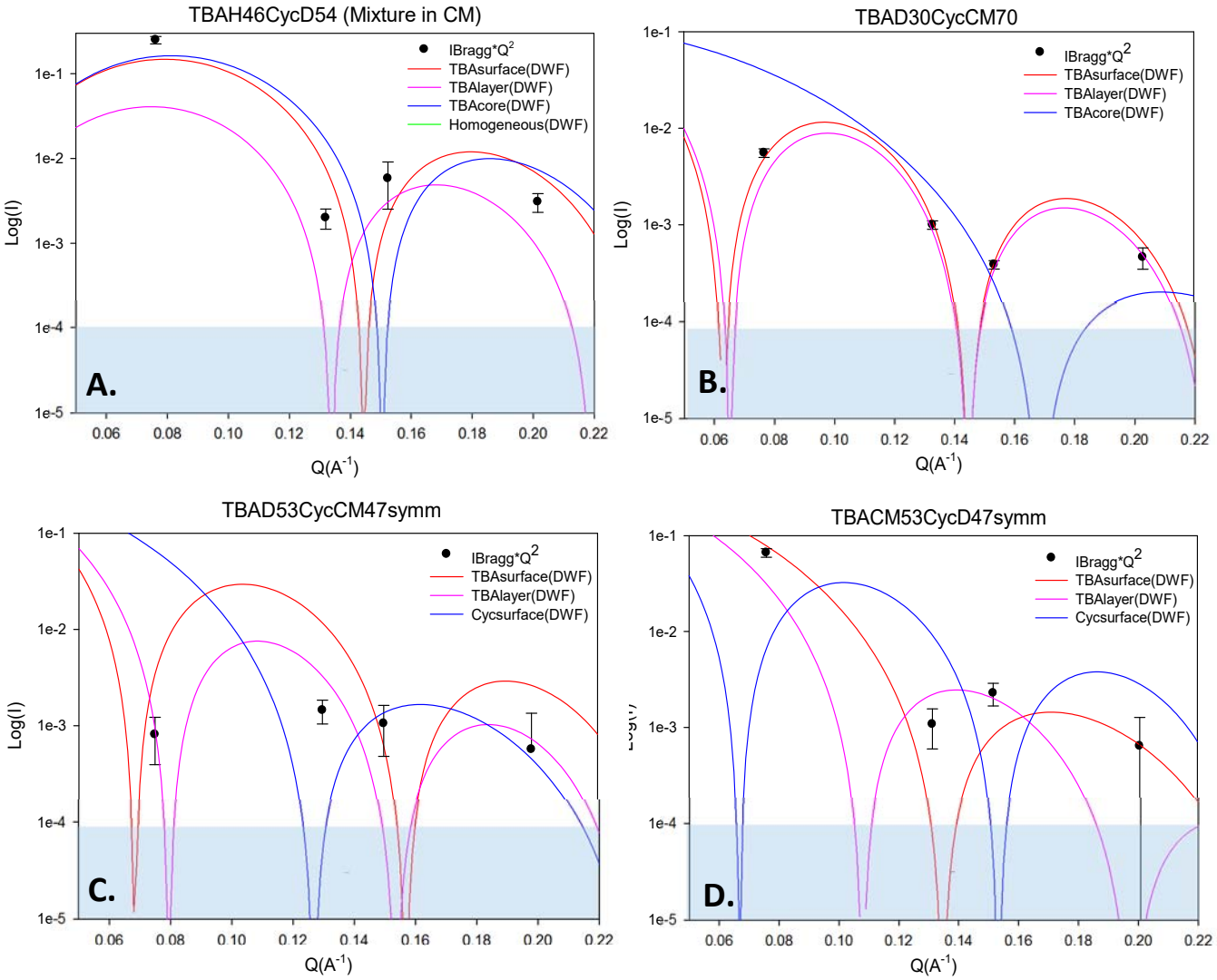


Figure IV-20: DWF model predictions (solid lines) and experimental Bragg intensities $\tilde{I}_{hk}$ (circles) for (A): TBAHCycD mixture in CM, (B):TBAD30 CycCM70 and the symmetrical TBACyc samples (C and D).

The different predictions from the core-shell models were compared to experimental intensities in (Fig. IV-20). First, concerning the contrast matching composition shown in Fig. IV-20 (A), it is obvious that the homogeneous model could be again knocked out due to its failure in the prediction of the non-zero (and indeed huge!) intensities of the CM binary mixture.

On the contrary, both core-shell models are able to predict such pattern. It should be noted also that the predictions from both *TBA@surface* and *Tol@surface* models are practically undistinguishable. Indeed, in this particular case (*i.e.*, contrast-matching mixture with composition around 50-50) the density profiles of the two models are almost the same, except for a change in their sign. They should indeed lead to equivalent values of the form factor since the square of the density profile entering in the equation doesn't allow a discrimination between different signs.

However this distinction between the different models can be made with the two symmetrical systems (Fig. IV-20 C and D). On the first hand, they show low (almost extinction) intensity in the TBADCycCM symmetrical system (Fig. IV-20 (C)) and a high intensity of the 1st order peak in the second symmetrical system (Fig. IV-20 (D)). This modulation was again successfully reproduced by the form factors associated to both *TBA@surface* and *TBA-layer* models and poorly reproduced by the *Tol@surface* model anticipating the opposite to what's experimentally obtained.

Finally, Fig. IV-20 (B) shows a 3rd sample that emphasized the superiority of the *TBA@surface* model over its *Tol@surface* counterpart which is TBAD30CycCM70. Interestingly, both the *TBA@surface* and the *TBA-layer* models are equally capable of a quantitative reproduction of the Bragg intensities. It is noteworthy that for this specific composition (30/70), the calculated thickness of the TBA shell corresponds indeed to one molecular layer, so that the two models are strictly equivalent (same illustration as for the TBA30Tol70 sample discussed earlier).

Fig. IV-21 shows the accordance of the *TBA@surface* model with the experimental data for 3 different samples (A) and the conflicting *Tol@surface* model with the same diffraction data (B) indicating that the core shell with *TBA@surface*, although not fully quantitative, can still succeed to give a plausible physical picture to the nano-induced structuration of the mixture. Fig. IV-22 is a schematic representation of the core-shell *TBA@surface* model of the different samples involved.

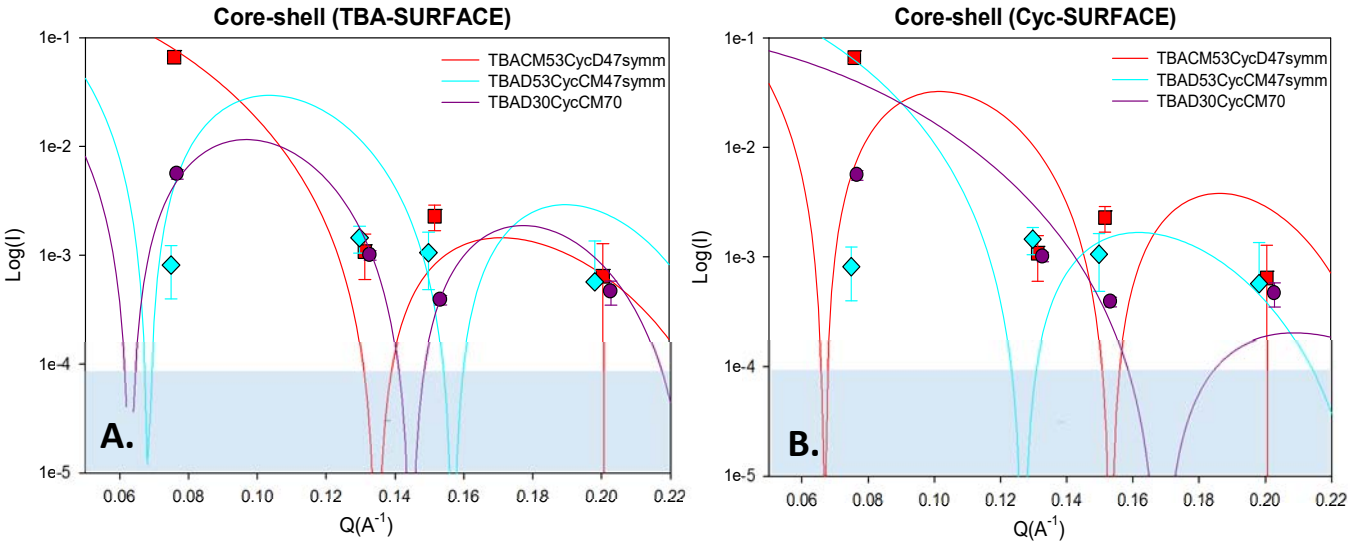


Figure IV-21: The agreement of the different models (DWF *TBA@surface* (A) and DWF *Cyc@surface* (B)) with the experimental Bragg intensities $\tilde{I}_{hk}$ in TBACyc systems.

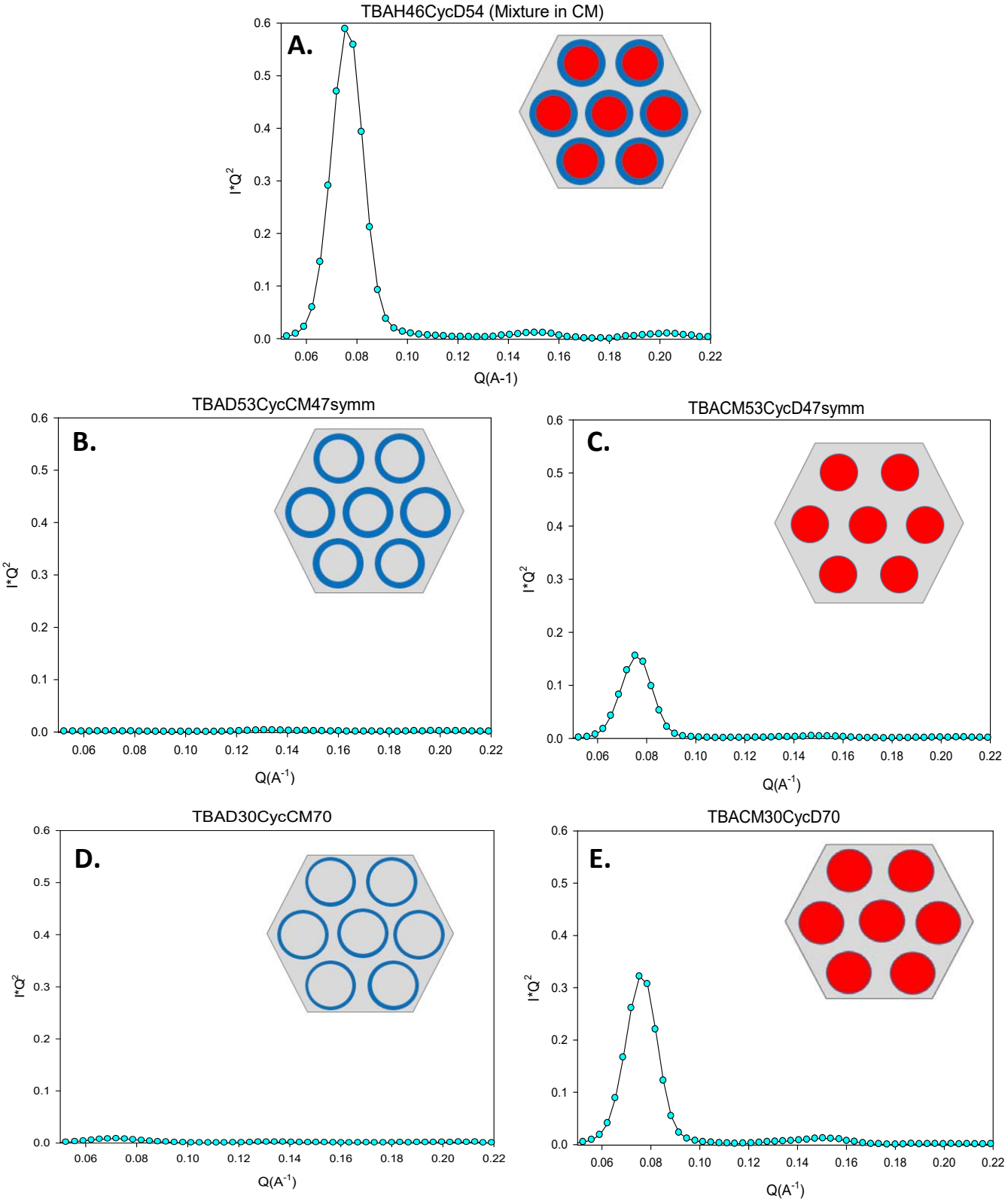


Figure IV-22: The treated experimental intensities and their corresponding (*TBA@surface*) core shell schemes for the different samples measured in the TBACyc system.

### *IV.F.2.1.iii.Methanol/Ethanol –Toluene Systems*

Another batch of SBA-15 was used for the methanol (Meth) and ethanol (Eth) /Tol series of experiments (D= 8.5nm). Better fits are obtained with the DWF model than the 1st batch (Fig. IV-23). The value of the MSD obtained from the best fit is 30 Å$^2$ corresponding to average displacements in the order of 0.55 nm which is consistent with the literature.[11]

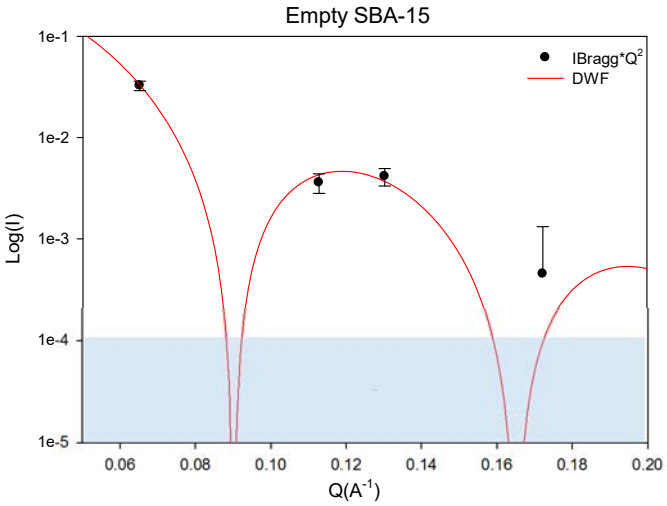


Figure IV-23: DWF model fits of the empty SBA used in the Meth/Eth-Tol systems (batch 2).

In this series of experiments we faced a major problem for some of the samples due to the high volatility of Meth and Eth. This volatility lead to lower filling percentages when targeting 100% porosity and lead instead to values as low as 75%. The unfilled pores normally have little influence on high intensities. Their scattering; however, leads to a remarkable increase in the intensity close to CM condition (*Eth@surface* and *Eth-layer* models prediction) as shown in Fig. IV-24 (A, B).

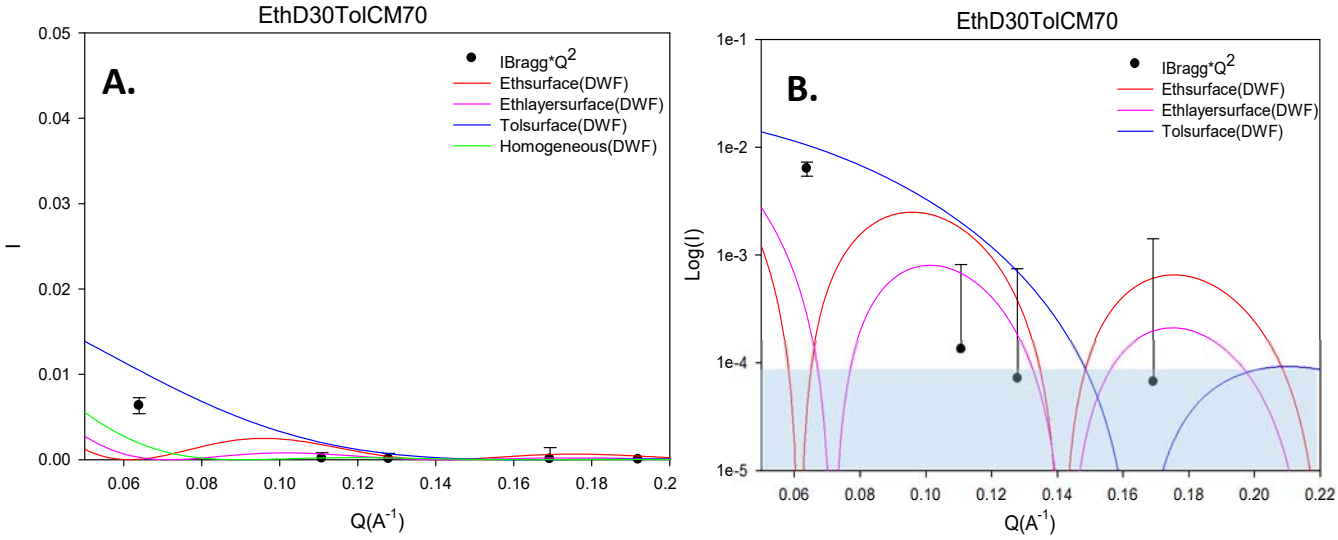


Figure IV-24: A and B show DWF model fits of an example of EthTol system at near CM concentration showing an increase in intensity due to the incomplete pore filling.

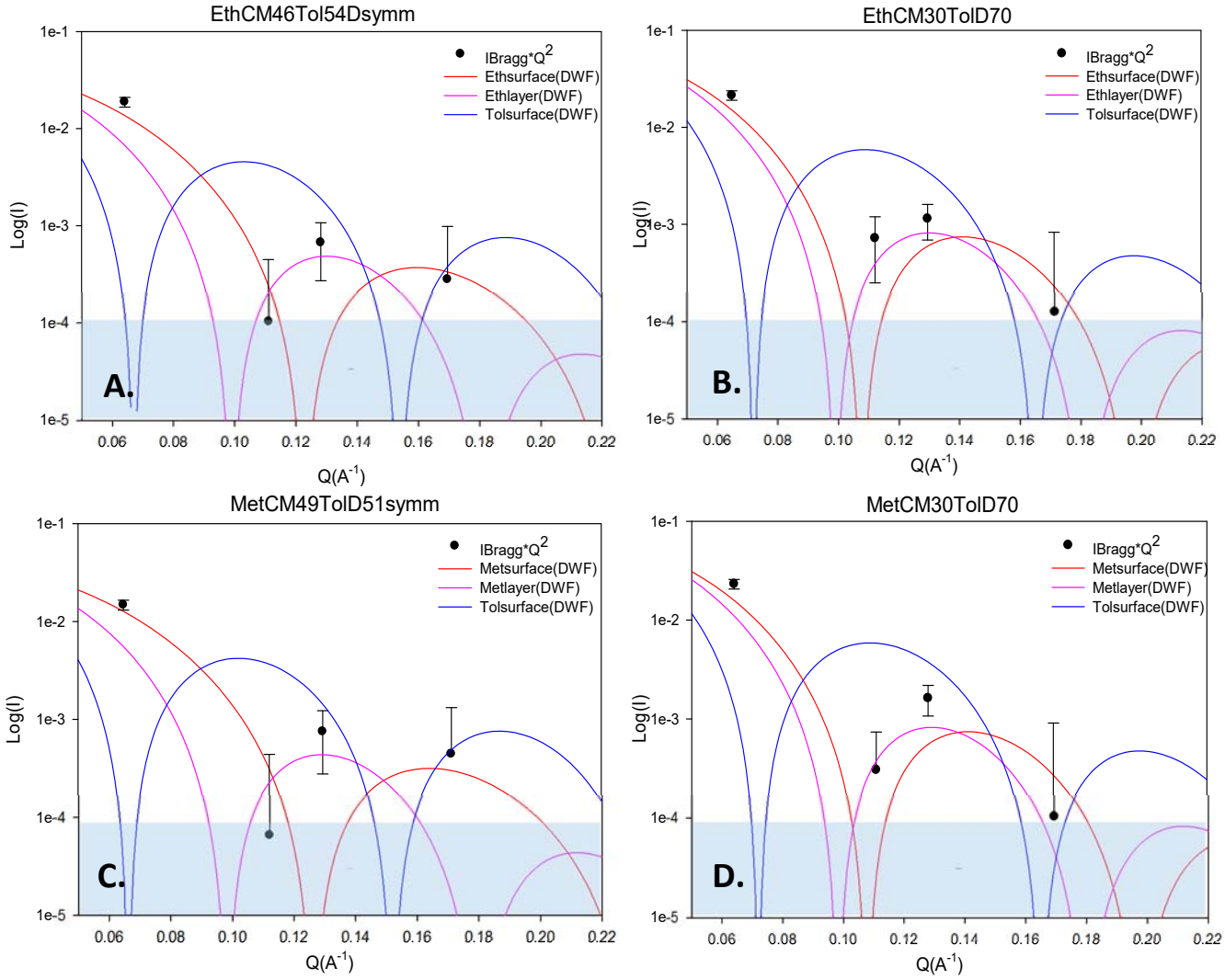


Figure IV-25: DWF model predictions for the EthCMTolD samples (A and B) and MethCMTolD samples (C and D).

The real story was revealed by the samples that do not give a CM prediction but rather anticipate high intensities which are resistant to the empty pore scattering effects. The emergent image from these samples is of a great resemblance to the previous results. For all Eth-Tol and Meth-Tol samples, the *alcohol@surface* and *alcohol-layer* core-shell DWF models give the best Bragg intensity agreement. In contrary, the *Tol@surface* model fails to predict the high (10) amplitude.

It should be noted that the main target of replacing TBA with the smaller Meth or Eth is to check whether the smaller molecular size could favor the alcohol monolayer model leading to a real discrimination from the total segregation (alcohol surface) model as both have been equally good so far. An aim not fully achieved as although *alcohol@surface* model better reproduces the (10) peak, the higher order peaks are slightly better reproduced with the monolayer model (Fig. IV-25).

### IV.F.2.2.Microporous Corona Model

Many studies have shown that SBA-15 is far from being a perfect 2-D hexagonal lattice. The presence of a microporous corona has been exploited in the literature.[11-13, 18-21] This motivated our approach of implementing a microporous corona within our core-shell model. This approach worked quite well for the two empty SBA-15 batches giving a very good fit (better and equivalent to the DWF fits for the 1st and 2nd batches as shown in Fig. IV-26 (A and B respectively).

Again, the porosity (p) and thickness (t) were fixed by the best empty fits and the pore size was fixed by adsorption isotherms. The values of (t) and (p) parameters are 14nm and 0.13, and 10nm and 0.6 for the 1st and 2nd batch respectively.

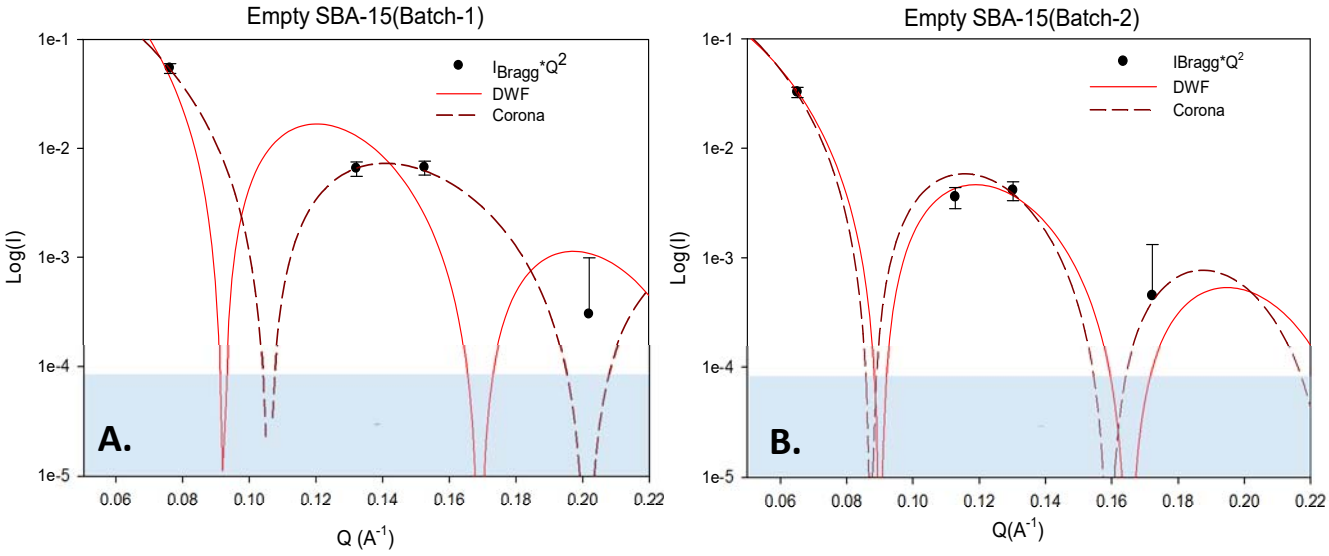


Figure IV-26: DWF and corona model fits of the empty SBA used in the TBA-Tol/Cyc systems (batch 1) and Meth/Eth-Tol systems.

As a general trend, an introduction of a corona leads to a shifting in the F(Q)s to higher Qs ; *i.e.,* same effect as a reduction in pore size. The quality of the corona model was compared to the *TBA @surface* DWF model considered the most eligible DWF model with best data agreement. Two corona models are represented: alcohol and aprotic solvent at the surface. In both cases, we assumed that all the porosity of the corona was filled by the liquid present at the surface, the remaining fraction of this liquid forming the shell.

For the TBA-Tol systems (Figs. IV-27), the corona *TBA@surface* model manages to reproduce the main trends in the diffraction data, unlike the corona *Tol@surface*, which is systematically far from agreement. Looking into more details, the corona *TBA@surface* anticipates low intensities for the 1st order Bragg reflection of the TBADTolCM systems (Fig. IV-27 (A and

C)) and predicts high intensities in the (10) reflection of the TBACMTolD samples where, indeed, the intensity is high (Fig. IV-27 (B and D)). As a first conclusion, one can state that both DWF and corona models seem to agree on the preferential segregation of TBA at the surface and Tol in the core.

As for the higher order peaks, it seems they are systematically better reproduced with the simpler DWF model. For instance, in Fig. IV-27 (D), according to the corona model, the intensity of the 2nd order peak in the TBACM30TolD70 sample should have been jeopardized by the minimum of the form factor, which is not the case. The DWF factor for the same sample predicts the right intensities of the diffraction peaks. In addition the general accordance of the Bragg intensities and the form factors seems to be much more evident in the DWF model.

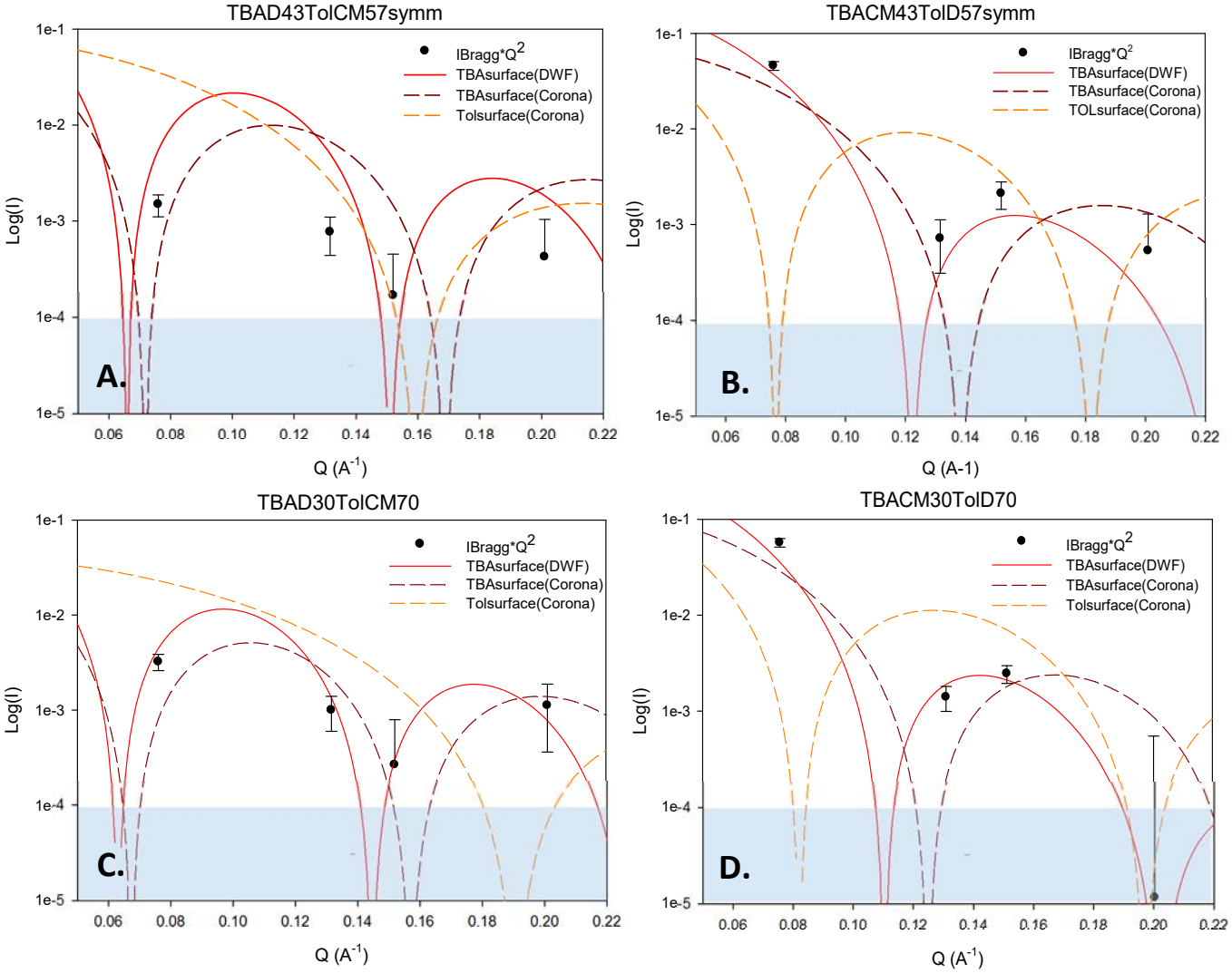


Figure IV-27: DWF (*TBA@surface*) and corona model predictions (lines) and experimental Bragg intensities $\tilde{I}_{hk}$ (circles) for the symmetrical TBATol samples (A and B) and TBA30Tol70 samples (C and D).

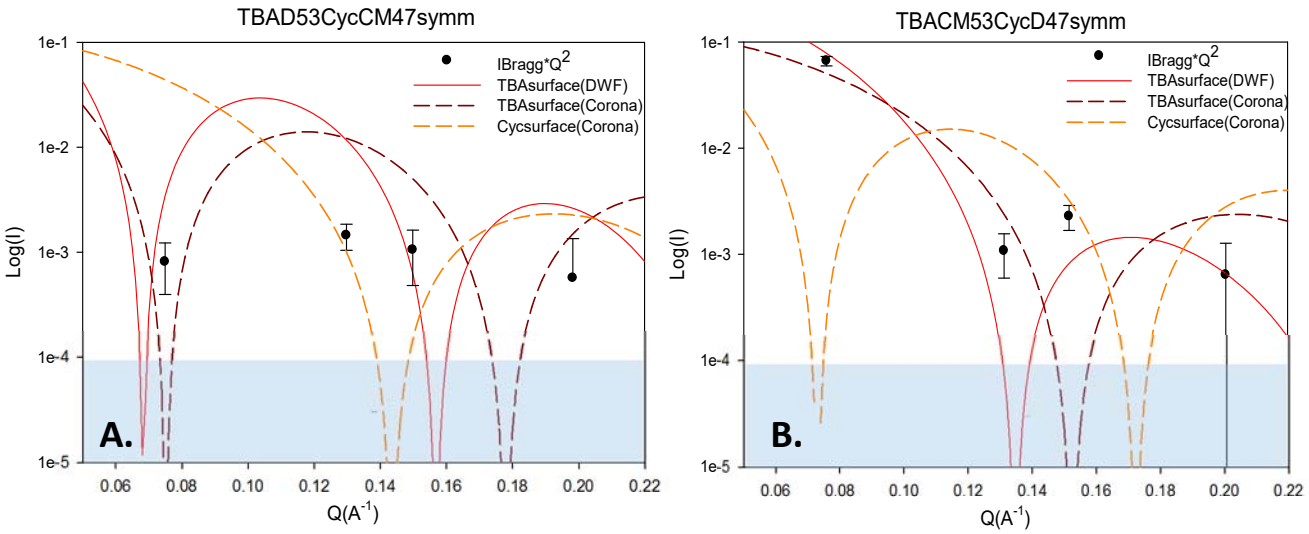


Figure IV-28: DWF (*TBA@surface*) and corona model predictions (lines) and experimental Bragg intensities $\tilde{I}_{hk}$ (circles) for symmetrical TBACyc samples (A and B).

Regarding the TBACyc system samples (Figs. IV-28), again the segregation of Cyclohexane at the surface is ruled out by the discrepancy between experiments and the predictions from the *Cyc@surface* corona model. Both the corona *TBA@surface* and the DWF *TBA@surface* models are able to reproduce the main diffraction patterns where the low intensity in the TBADCycCM 1st peak and the high intensity in that of TBACMCycD was indeed predicted.

However, for the higher order peaks, a comparative appraisal of the corona *TBA@surface* and the DWF *TBA@surface* is difficult to establish as their predictions decrease in quality and often remain at the qualitative level. The most obvious differences between the two models could be pointed out for the TBACMCycD system (Fig. IV-28 (B)), where the *TBA@surface* corona model falsely predicts an extinction of the 3rd order Bragg peak. This difference seems to add again to the figure of merit of the DWF *TBA@surface* model.

Finally, concerning the Methanol/Ethanol-Toluene systems, the same conclusions can be withdrawn from the data (the agreement of both corona and DWF models with alcohol at surface with the experimental data and the failure of the *Tol@surface* models in the reproduction of any trend, in particular for the 1st Bragg peak). It should be noted; however, that unlike the previous samples with the 1st SBA batch, the Meth/Eth systems display a slight preference for the corona model over the DWF model as the former better reproduces the higher order diffraction (Fig. IV-29).

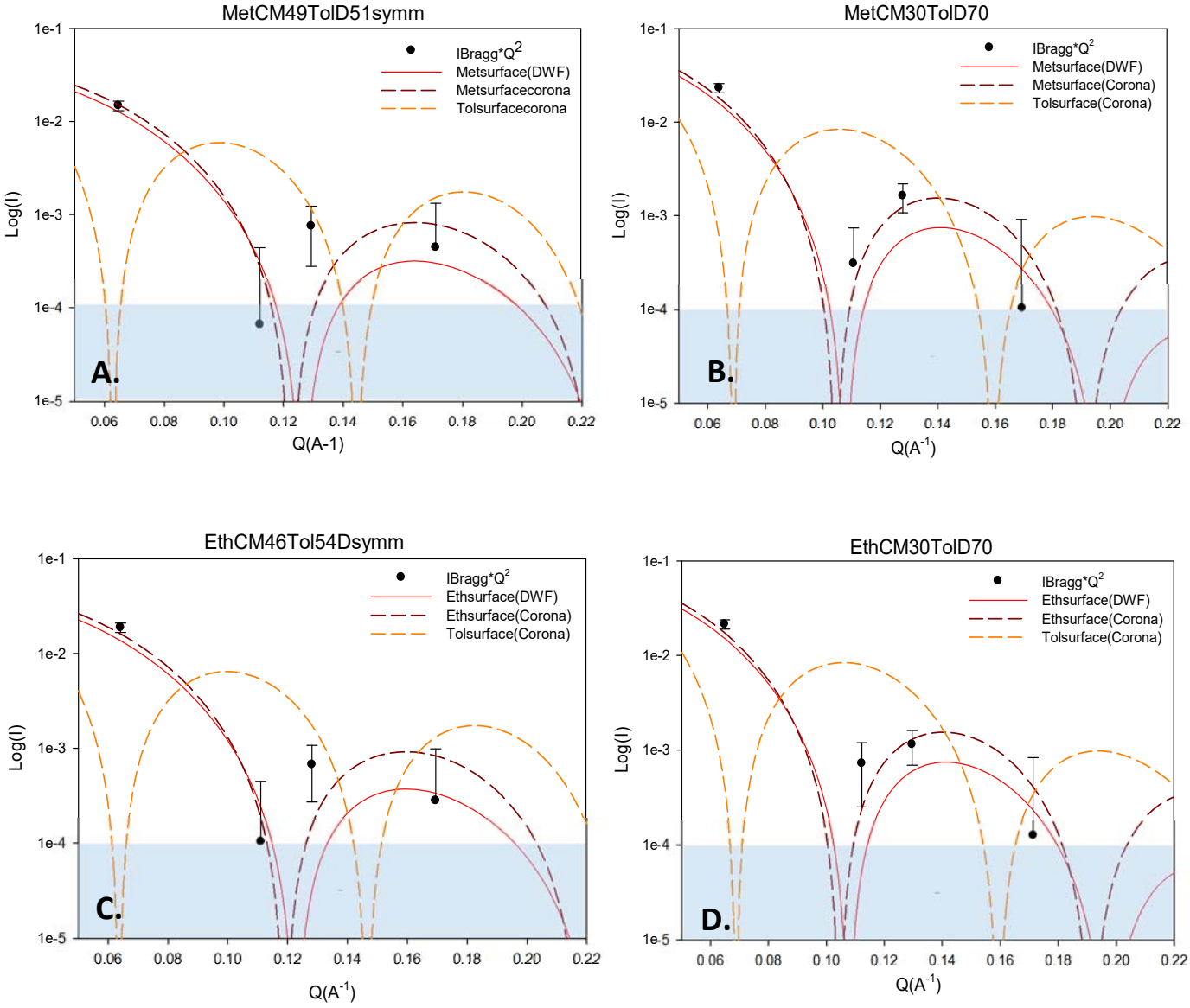


Figure IV-29: DWF (*TBA@surface*) and corona model predictions for the symmetrical MethCMTolD samples (A and B) and EthCMTolD (C and D)

# IV.G. Conclusion

As a general conclusion of this chapter, we propose to summarize the main implications of this structural study. We showed the existence of a spontaneous structuring phenomenon appearing under confinement in SBA-15 materials. This phenomenon of nanosegregation inside nanochannels leads to a stable concentric core-shell tubular structure. This modulation of the mixture concentration resembles a nanodemixtion induced by a preferential interaction of one component (*tert*-butanol, methanol, ethanol) with the silanol interface.

These prolific results open an original field in the studies of confined binary liquids which have conventionally focused on wetting effects and changes in pre-transitional concentrations upon approaching phase separation or the existence of equilibrium structures in the mesostructured biphasic domain of a non-miscible blend. In this context, we have shown that the use of isotopic effects in neutron diffraction, combined with the use of organized porous matrices, helps achieve a unique level of description.

Experimentally, several perspectives have been considered. In an attempt to study the effect of the interaction of the aromatic ring with the hydroxyl group of the alcohol, toluene was substituted by cyclohexane. However, the results have shown no true distinction between the two cases strongly indicating that the interactions of the hydroxyl group with the silanol surface is much more efficient than that with the ring of the aromatic toluene.

Another approach was considered in a trial to discriminate between the complete nanosegregation of the constituents and a monolayer of the alcohol at the surface. For this purpose the bulky TBA was replaced by the smaller methanol and ethanol molecules. In this aspect, one would expect the preferential monolayer formation and the homogeneous filling of the core. Nevertheless, the quality of the predictions obtained doesn't allow a proper distinction between the two models without any ambiguity.

It should be mentioned that a third approach had been attempted in this thesis but wasn't discussed in the manuscript. This approach was the replacement of the hydrophilic matrix by the hydrophobic CMK-3 replica. The idea was to change the nature of the interfacial interactions leading to new core shell structures. This ordeal turned illusive due to the low intensity of the diffraction data obtained which doesn't allow a real assessment of the quality of the different models.

Although some of the approaches turned out to be partially disappointing, they bring a very strong message about the rather general character of the phenomena of nanosegregation observed in nanoporous silicates that we were able to reproduce for a variety of binary systems. Going beyond the structural study of these revealed original nanophases, it seems of a great interest to study their dynamics. This perspective is the subject of the next chapter, in which we present a study of the relaxational dynamics and glass transition of the nanostructures by quasielastic neutron scattering.

# References


1. Elamin, K., et al., *Different behavior of water in confined solutions of high and low solute concentrations.* Physical Chemistry Chemical Physics, 2013. **15**(42): p. 18437-18444.
2. Swenson, J., et al., *Anomalous dynamics of aqueous solutions of di-propylene glycol methylether confined in MCM-41 by quasielastic neutron scattering.* Journal of Chemical Physics, 2014. **141**(21).
3. Elamin, K., H. Jansson, and J. Swenson, *Dynamics of aqueous binary glass-formers confined in MCM-41.* Physical Chemistry Chemical Physics, 2015. **17**(19): p. 12978-12987.
4. A. R. Abdel Hamid, R. Mhanna, R. Lefort, A. Ghoufi, C. Alba-Simionesco, B. Frick, D. Morineau, *Structural evidence of core-shell formation in a binary liquid confined in MCM-41.* Journal of Physical Chemistry, 2015. to be submitted.
5. Morineau, D., Y. Xia, and C. Alba-Simionesco, *Finite-size and surface effects on the glass transition of liquid toluene confined in cylindrical mesopores.* The Journal of chemical physics, 2002. **117**(19): p. 8966-8972.
6. Alba-Simionesco, C., et al., *Confinement of molecular liquids: Consequences on thermodynamic, static and dynamical properties of benzene and toluene.* The European Physical Journal E, 2003. **12**(1): p. 19-28.
7. Liu, A.J., et al., *WETTING TRANSITIONS IN A CYLINDRICAL PORE.* Physical review letters, 1990. **65**(15): p. 1897-1900.
8. Marković, I. and R. Ottewill, *Small angle neutron scattering studies on non-aqueous dispersions of calcium carbonate. Part III. Concentrated dispersions.* Colloid and Polymer Science, 1986. **264**(5): p. 454-462.
9. Formisano, F. and J. Teixeira, *Critical fluctuations of a binary fluid mixture confined in a porous medium.* European Physical Journal E, 2000. **1**(1): p. 1-4.
10. Schemmel, S., et al., *Local structure of a phase-separating binary mixture in a mesoporous glass matrix studied by small-angle neutron scattering.* Journal of Chemical Physics, 2005. **122**(24).
11. Imperor-Clerc, M., P. Davidson, and A. Davidson, *Existence of a microporous corona around the mesopores of silica-based SBA-15 materials templated by triblock copolymers.* Journal of the American Chemical Society, 2000. **122**(48): p. 11925-11933.
12. Jähnert, S., et al., *Pore structure and fluid sorption in ordered mesoporous silica. I. Experimental study by in situ small-angle X-ray scattering.* The Journal of Physical Chemistry C, 2009. **113**(34): p. 15201-15210.
13. Zickler, G.A., et al., *Physisorbed films in periodic mesoporous silica studied by in situ synchrotron small-angle diffraction.* Physical Review B, 2006. **73**(18).
14. Ghoufi, A., et al., *Hydrogen-bond-induced supermolecular assemblies in a nanoconfined tertiary alcohol.* The Journal of Physical Chemistry C, 2011. **115**(36): p. 17761-17767.
15. Saiz, L., J. Padro, and E. Guardia, *Structure and dynamics of liquid ethanol.* The Journal of Physical Chemistry B, 1997. **101**(1): p. 78-86.
16. Morineau, D., et al., *Structure of liquid and glassy methanol confined in cylindrical pores.* The Journal of chemical physics, 2004. **121**(3): p. 1466-1473.
17. Abdel Hamid, A., et al., *Solvation Effects on Self-Association and Segregation Processes in tert-Butanol–Aprotic Solvent Binary Mixtures.* The Journal of Physical Chemistry B, 2013. **117**(35): p. 10221-10230.
18. Galarneau, A., et al., *Microporosity and connections between pores in SBA-15 mesostructured silicas as a function of the temperature of synthesis.* New Journal of Chemistry, 2003. **27**(1): p. 73-79.
19. Findenegg, G.H., et al., *Analysis of pore structure and gas adsorption in periodic mesoporous solids by in situ small-angle X-ray scattering.* Colloids and Surfaces a-Physicochemical and Engineering Aspects, 2010. **357**(1-3): p. 3-10.

20. Pollock, R.A., et al., *Size and Spatial Distribution of Micropores in SBA-15 using CM-SANS.* Chemistry of Materials, 2011. **23**(17): p. 3828-3840.
21. Findenegg, G.H., et al., *Fluid adsorption in ordered mesoporous solids determined by in situ small-angle X-ray scattering.* Physical Chemistry Chemical Physics, 2010. **12**(26): p. 7211-7220.

# CHAPTER V:

# DYNAMICS OF CONFINED BINARY MIXTURES

# Chapter V: Dynamics of Confined Binary Mixtures

## V.A. Introduction

The dynamics of nanoconfined glass-forming liquids has been a topic of intensive research[1-13] due to their significance in many technological and industrial applications including catalysis, chromatography and separation.[9] However, very little is known about the case of nanosegregated mixtures comprising amphiphilic interactions in contact with a hydrophilic surface. A few approaches on this topic have been recently conducted on a number of binary mixtures confined in MCM-41.[14-17] These quests reveal behaviors far from ideal solutions and supply dynamical evidence of microphase separation under confinement. However, such studies were performed on liquids with comparable hydrophilicity which doesn't allow a conclusive perception on the physical behavior of confined binary liquids.

In another approach, it has been shown that *tert*-butanol (TBA) molecules spontaneously form mesoscopic supramolecular assemblies when dispersed in an inert solvent toluene (Tol).[18] Moreover, confinement and surface-induced structuring of the fully miscible (TBA/Tol) solutions in the straight and monodisperse rigid channels of mesoporous MCM-41[19] and SBA-15 silica molecular sieves (D= 3.7 and 8.3nm respectively) revealed the nanosegregation of the components into a core shell structure (as shown in the previous chapter).

This segregation mechanism induced by the amphiphilic character of TBA has raised many questions regarding the dynamical behavior of such complex liquids in nanoconfinement. One could speculate that the phase separation of the components could lead to spatially separated dynamics. Therefore, a key objective of the work conducted in this chapter is to investigate by QENS the molecular dynamics of the nanosegregated super-cooled fluids, with the objective of disentangling the main structural relaxations related to the 'macroscopic' glass transition from putative distinct modes arising from the different nanosegregated regions.

# V.B. Glass Transition Measurements

## V.B.1. Tg from Differential Scanning Calorimetry

### V.B.1.1. Tg in Pure Compounds

The phase behavior of the samples was determined by Differential Scanning Calorimetry. Under the conditions of handling, all the measurements were conducted under isobaric conditions, therefore we can consider that the heat flux is proportional to the enthalpy:

$$\frac{dH}{dt} = + m.C_p.\frac{dT}{dt} + f(t,T)$$

With m representing the sample mass, $\frac{dH}{dt}$ the Heat flow, $C_p$ the Heat capacity, $\frac{dT}{dt}$ the heating rate and f (t, T) function associated with events such as phase transitions or irreversible processes (chemical reactions, aging ...)

DSC measurements were performed on bulk and confined TBA and Tol liquids both in the pure state and in mixtures. The apparatus was set on a cooling rate of 10 K.min$^{-1}$ along a range varying from 320 K to 100 K, followed by a rise to the same temperature at the at same rate. However, only heat flow acquired on heating are shown on the thermograms (Figs. V-1, 2).

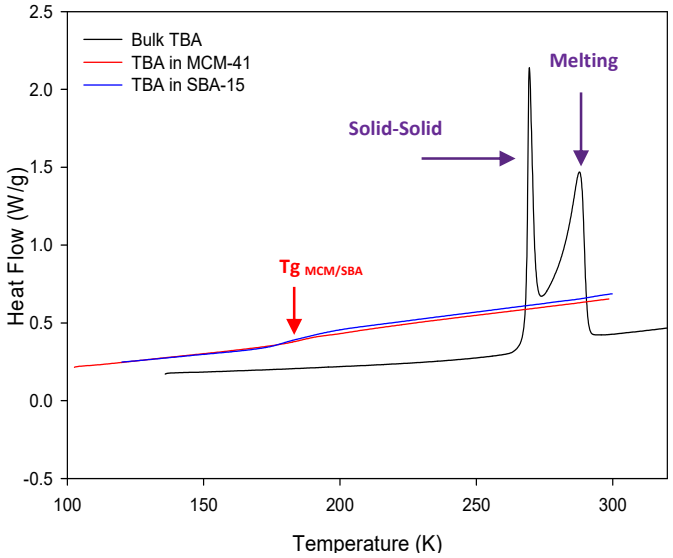


Figure V-1: Differential Scanning calorimetry measures on TBA in bulk and confined in MCM-41 and SBA-15 where the heat flow was measured as a function of temperature.

The DSC measurements on pure components show that TBA is not a glass-former in the bulk, it readily crystallizes on cooling, giving rise to an exothermic peak (not shown). The transformation of the formed crystalline phase gives rise to two endothermic peaks upon

heating, the 1st being a solid-solid transition (phase IV to phase II), the 2nd being melting. However, a true Tg appears in confinement revealed by a small step in the heat flow in both confining matrices at around 180 K. Tol, on the other hand, is a glass-former in bulk. Its glass recrystallizes on heating in the bulk but remains glassy or liquid in confinement (Fig. V-2).

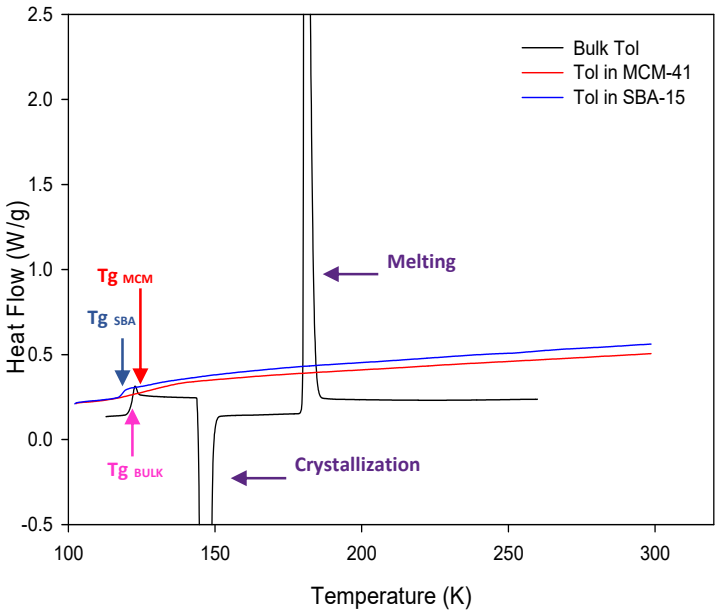


Figure V-2: DSC measures on Tol in bulk and confined in MCM-41 and SBA-15

Table V-1 shows the different Tg values obtained by the DSC measurements where Tg is defined as the maximum of the heat flux derivative and ΔTg is obtained from the HWHM of the heat flux derivative and quantifies the broadening of the glass transition.

The Tg broadening upon confinement can be interpreted in terms of dynamical heterogeneities induced by surface interaction and the distribution of different environments. Moreover, the non-monotonic change in the Tg of Tol in confinement is in agreement with previous studies [1] and has been attributed to a competition between surface, size and density effects.

Table V-1: Tg values for TBA and Tol in bulk and under confinement in MCM and SBA.

| Tg values | Tol | TBA |
|---|---|---|
| **Bulk** | 121.5 +/-1 K | No Tg |
| **SBA-15** | 118.5 +/-2 K | 185 +/-12 K |
| **MCM-41** | 127 +/-12 K | 185 +/-8 K |

### V.B.1.2. Tg in Binary Mixtures

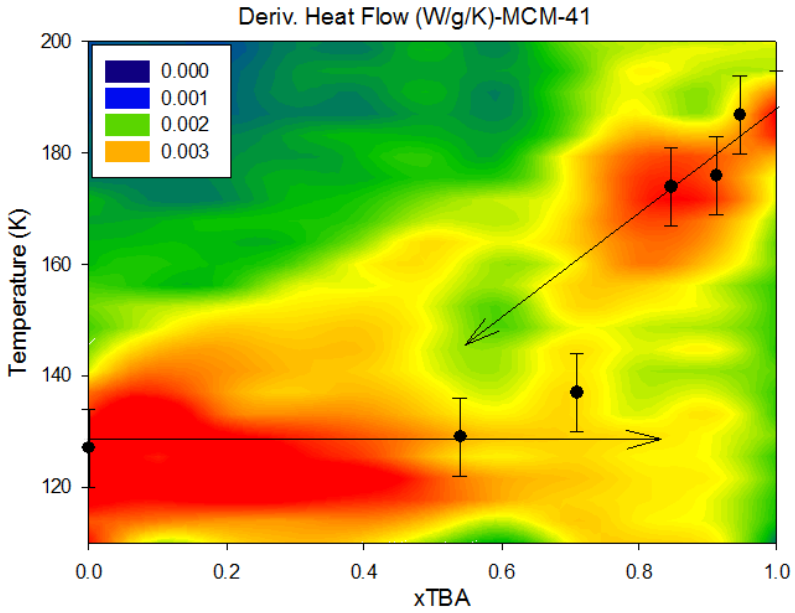


Figure V-3: The change in the heat flow vs temperature and TBA fraction. (The black solid circles correspond to the Tgs obtained by neutron scattering after [21]).

The DSC measurements, emphasized by neutron scattering density measurements of the Tg (solid black circles), reveals the presence of two apparent Tgs: one close to the pure confined Tol and another close to pure TBA but decreasing upon increasing the amount of Tol. At intermediate concentrations, a large broadening and an overlap of the different signals is witnessed (the two arrows highlight the simultaneous presence of the two Tgs).

This duality in the Tg has been demonstrated in the literature, [2, 20] and is usually associated to heterogeneous dynamics caused by the interfacial interactions in restricted geometries. In particular, it indicates the presence of separated dynamical processes, consistent with two distinct spatial regions corresponding to the interface (shell) and the pore center (core).

The 1st transition is faster (lower Tg) and is less affected by dilution. It could be therefore related to the core Tol whose amplitude decreases upon increase in $x_{TBA}$ as a consequence of the decreased core volume. The 2nd could be related to the interfacial TBA, slowed down by the surface interaction. A scenario compatible with our SANS data on the core-shell structure.

## V.B.2. Dielectric Studies of Mixtures

### V.B.2.1. Decoupling of the Different Modes

Dielectric measurements were performed for TBA-Tol systems in MCM-41 by Abdel Hamid and coll.[21] For each of the studied systems, the frequency at the maximum of the main relaxation peak is used for the extraction of the relaxation times (τ) which are plotted as a function of the inverse temperature. The obtained curves can be extrapolated to τ=100 seconds (corresponding to the DSC time scale) to extract the Tgs for the different systems.

DSC and dielectric measurements yield similar Tg values for Tol. On the contrary, TBA gives very distinct values of Tgs (around 45K difference) between the two techniques (Fig. V-3). This observation indicates a coupling of the dielectric mode to the main structural relaxation probed by DSC for Tol and a decoupling of the modes in TBA. It is noteworthy that the dielectric spectroscopy probes dipolar dynamics usually related to rotation modes. This arouses speculations concerning a possible "Plastic Glass" phase in the case of confined TBA [21] where the degrees of freedom allow the persistence of rotational dynamics deep within the glass.

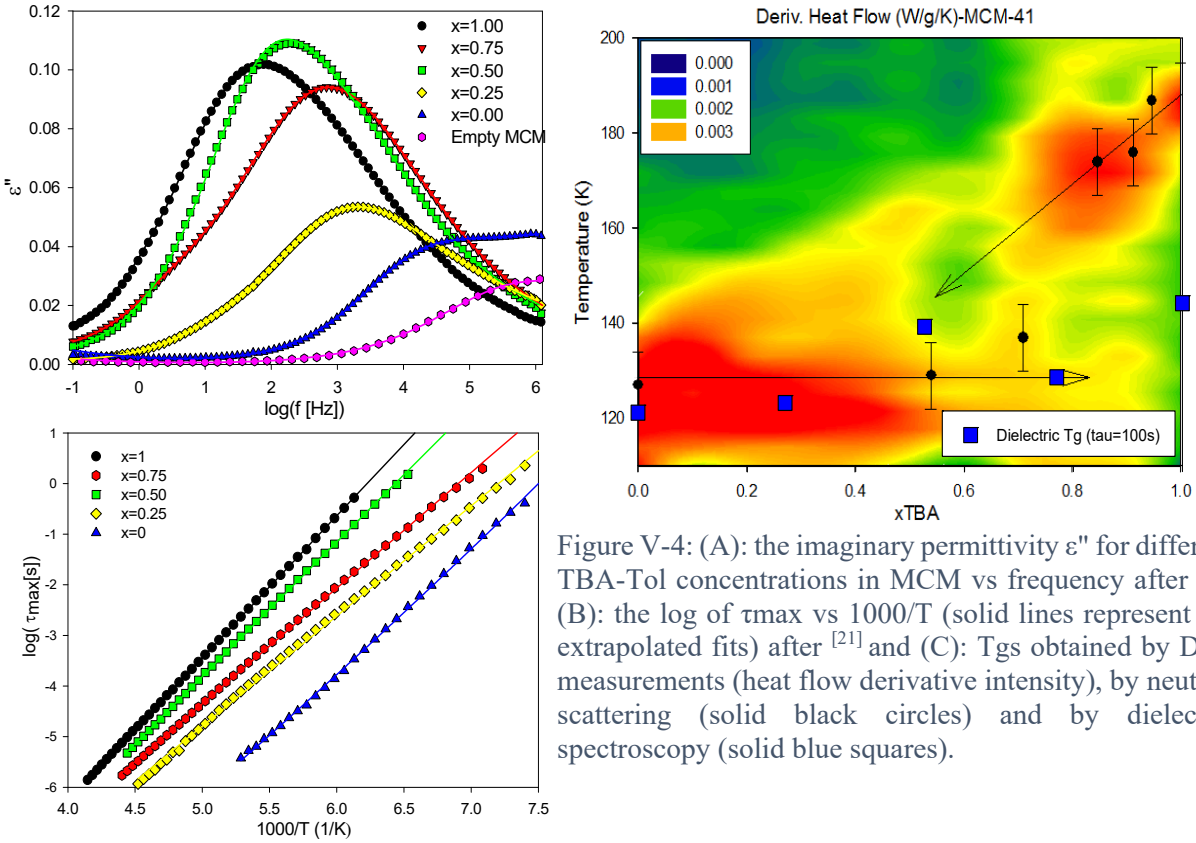


Figure V-4: (A): the imaginary permittivity ε" for different TBA-Tol concentrations in MCM vs frequency after [21]. (B): the log of τmax vs 1000/T (solid lines represent the extrapolated fits) after [21] and (C): Tgs obtained by DSC measurements (heat flow derivative intensity), by neutron scattering (solid black circles) and by dielectric spectroscopy (solid blue squares).

In order to validate/complement the DSC and dielectric studies, QENS with isotopic labelling is the ideal method to disentangle the different dynamics arising from the different compounds and the different modes (structural relaxation, rotation, secondary relaxation, etc...).

# V.C. Quasielastic Neutron Scattering

## V.C.1. Theoretical Background

Quasielastic neutron scattering (QENS) represents a specific case of inelastic neutron scattering investigating small energy (around zero) transfers with respect to the incident neutron energy. Therefore, it refers to processes attributing to an elastic line broadening rather than true inelastic peaks. This small energy transfer corresponds to the energies of the stochastic translational, rotational, and vibrational motions of the atoms. Generally, in a neutron scattering experiment we obtain the double differential cross section:

$$\frac{d^2\sigma}{d\Omega d\omega} = \frac{k_f}{k_i}.\frac{1}{2\pi}.\sum_i\sum_j \int_{-\infty}^{+\infty} \frac{1}{N}\langle b_i b_j e^{\{iQR_{i(t)}\}} \times e^{\{-iQR_{j(0)}\}}\rangle . e^{(-i\omega t)}dt \qquad (V\text{-}1)$$

$k_i$ and $k_f$ are the incident and final wave vectors of the beam, Q is the momentum transfer vector, ω is the angular frequency to energy transfer ($\omega=\frac{E_f-E_i}{\hbar}$), Ω is the solid detection angle, $b_i$ and $b_j$ are the scattering lengths of atoms i and j and N is the number of scattering atoms.

In the case of a single isotope, the same expression can be simply defined by:

$$\frac{d^2\sigma}{d\Omega d\omega} = \frac{1}{4\pi N}.\frac{k_f}{k_i}[\sigma_{coh}S_{coh}(Q,\omega) + \sigma_{inc}S_{inc}(Q,\omega)] \qquad (V\text{-}2)$$

Where $\sigma_{coh}$ and $\sigma_{inc}$ are the coherent and incoherent cross sections of the isotope respectively. The dynamical structure factor S(Q, ω) measured in a neutron scattering experiment is divided into two parts, coherent and incoherent. Each obtained from the Fourier transform of the coherent and incoherent intermediate scattering functions $I_{coh}(Q, t)$ and $I_{inc}(Q, t)$ as follows:

$$S_{coh}(Q,\omega) = \frac{1}{2\pi}\int_{-\infty}^{+\infty} I_{coh}(Q,t)\, e^{(-i\omega t)}dt \qquad (V\text{-}3)$$

$$S_{inc}(Q,\omega) = \frac{1}{2\pi}\int_{-\infty}^{+\infty} I_{inc}(Q,t)\, e^{(-i\omega t)}dt \qquad (V\text{-}4)$$

The intermediate scattering functions $I_{coh}(Q, t)$ and $I_{inc}(Q, t)$ can be respectively expressed as: (The < > notation present in both expressions signifies the thermal averages). [22]

$$I_{coh}(Q,t) = \frac{1}{N}\sum_{i=1}^{N}\sum_{j=1}^{N}\langle e^{iQ.r_i(0)}e^{-iQ.r_j(t)}\rangle \quad \text{(V-5)}$$

$$I_{inc}(Q,t) = \frac{1}{N}\sum_{i=1}^{N}\langle e^{iQ.r_i(0)}e^{-iQ.r_i(t)}\rangle \quad \text{(V-6)}$$

$I_{coh}(Q, t)$ is related by inverse FT to the Van Hove pair correlation function [23] which illustrates the probability the presence of a scattering particle at position r and time t given that another particle is at position r=0 at t=0:

$$G(r,t) = \frac{1}{(2\pi)^3}\int_{-\infty}^{+\infty} e^{-i(Qr-\omega t)}\, I_{coh}(Q,t)d^3Qd\omega = \frac{1}{N}\sum_{i=1}^{N}\sum_{j=1}^{N}\delta\left(r - r_i(0))\delta(r - r_j(t)\right) \quad \text{(V-7)}$$

On the other hand, $I_{inc}(Q, t)$ is related by inverse FT to the self-correlation function i.e. the probability that a scattering particle which was at position r=0 at t=0 has moved at time t to the location r and can be expressed as:

$$G_s(r,t) = \frac{1}{(2\pi)^3}\int_{-\infty}^{+\infty} e^{-i(Qr-\omega t)}\, I_{inc}(Q,t)d^3Qd\omega = \frac{1}{N}\sum_{i=1}^{N}\delta\big(r - r_i(0))\delta(r - r_i(t)\big) \quad \text{(V-8)}$$

However, in a hydrogen-containing sample, almost exclusively the proton motions are highlighted due to the high incoherent cross-section of Hydrogen dominating any coherent contributions which can be, therefore, neglected. Therefore in quasielastic neutron scattering we essentially measure the scattering intensity corresponding to the incoherent scattering function $S_{inc}(Q, \omega)$, allowing to probe the self-correlation of the individual dynamics of the scattering particles. In this incoherent approximation $S_{inc}(Q, \omega)$ is commonly expressed as:

$$S_{inc}(Q,\omega) = e^{\left(-\frac{\langle u^2\rangle Q^2}{3}\right)}\big[A(Q).\delta(\omega) + (1 - A(Q))S_{quasi}(Q,\omega)\big] \quad \text{(V-9)}$$

$A(Q)$ represents the elastic incoherent structure factor emerging from restricted dynamics, [22, 24] $S_{quasi}(Q, \omega)$ stands for the quasielastic response of slow molecular relaxations, and the exponential term is the fast vibrational modes approximated by the Debye-Waller factor.

## V.C.2. Neutron Backscattering (BS)

High energy resolution QENS measurements are usually required to investigate the large scale motions and slow relaxational processes of molecular liquids typically taking place at ns time scales. Since the resolution of a spectrometer is restricted by the selectivity of the monochromator, a high resolution could only be achieved through the monochromation of the incoming and the scattered beam by adopting a backscattering geometry of the crystals.

This can be explained by the fact that the spread of the wave length $\Delta\lambda/\lambda = \cot\vartheta.\Delta\vartheta$ obtained from the differentiation of the Bragg law ($\lambda = 2\sin\vartheta/d$) becomes zero for $2\vartheta$=180°. This means that the wavelength spread becomes minimal when the beam is perfectly reflected (180°) i.e. backscattering geometry. The latter thus optimizes the energy resolution yielding values of FWHM≈1μeV for Si (1 1 1) monochromator.

Fig. V-5 shows a schematic setup of a backscattering spectrometer which illustrates its principle. The incident neutron beam is first deflected by a low wavelength selectivity crystal to the monochromator. The beam then reflects in a backscattering position and is afterwards scattered by the sample to the analyzers which again backscatter. The reflected neutrons then pass through the samples to the detector bank. A Doppler drive oscillates the monochromatic crystals leading to the modification of the incident energy allowing quasielastic measurements.

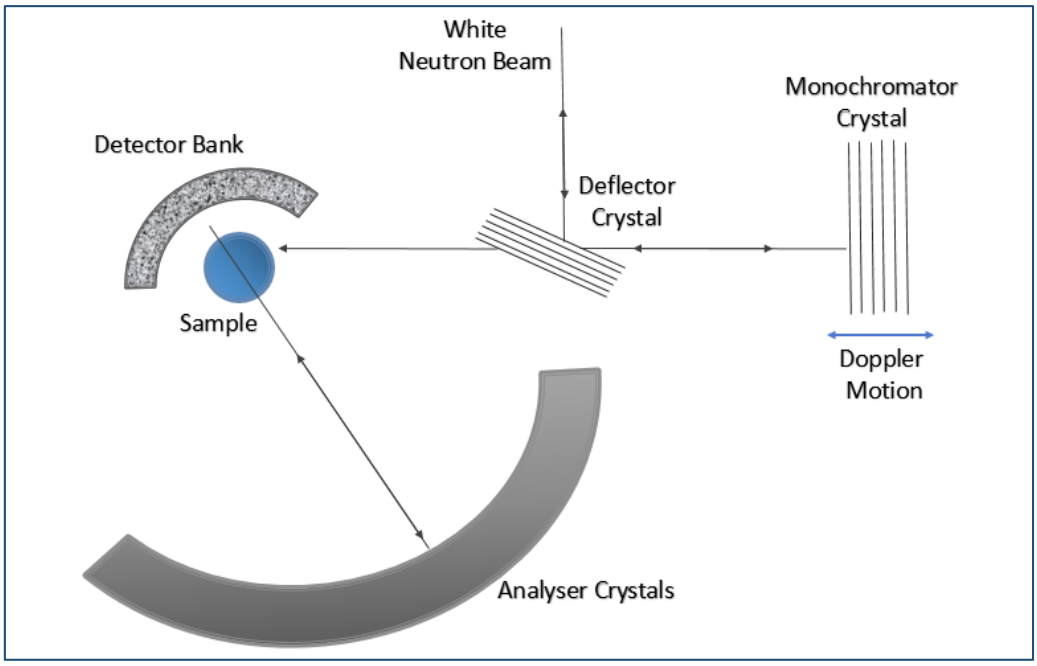


Figure V-5: A simplified schematic setup of a backscattering spectrometer.

### V.C.2.1. Elastic-Inelastic Fixed Window Scans

Fixed Window Scans (FWS) give a quick overview over the temperature dependence of the dynamics of the system of interest. If set to zero energy transfer (i.e. Doppler drive arrest, ΔE=0), the scans are then called Elastic Fixed Window Scans (EFWS). The measured intensity is essentially $S_{inc}$ ($Q$, ω=0) which integrates all purely elastic (A(Q)) or quasielastic contributions slower than the energy resolution defining the "fixed window" of the instrument's resolution.

This integrated intensity is measured versus a chosen temperature range (as shown in Fig. V-6). EFWS can therefore reveal the temperature range where the dynamics reach relaxation times comparable to the resolution.

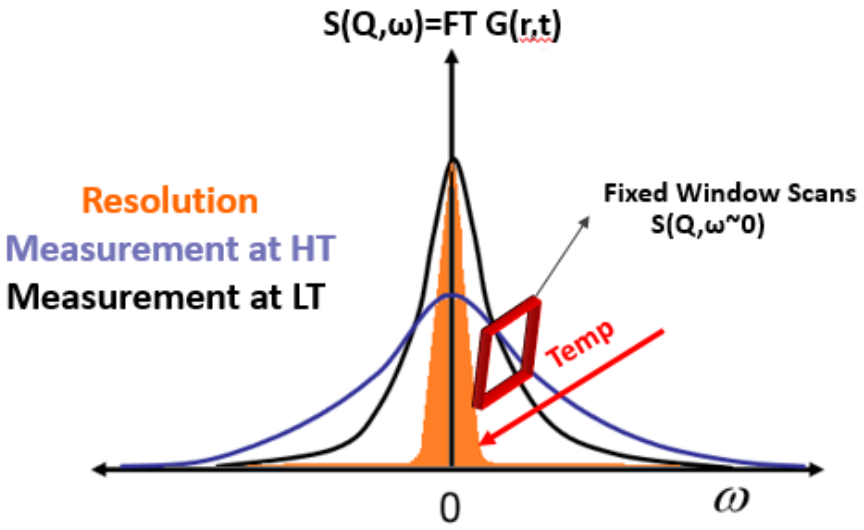


Figure V-6: A scheme showing the incoherent dynamic structure factor, the Quasielastic response at high and low temperatures and the EFWS at ω=0 measured versus temperature (axis directed by the red arrow).

Inelastic fixed window scans IFWS, measure the spectral function $S_{inc}(Q, \omega)$ at a chosen energy offset ω=ct by allowing the monochromator to periodically oscillate at a certain speed at alternating $\pm v_{Doppler}$. The count rate is then recorded as function of sample temperature. A maximum count rate at $T_{max}$ signify that the relaxation function has its maximum spectral weight in the selected energy window. The Q-dependence of the scattering holds the information about the nature of the dynamical processes involved (local or diffusive).

# V.D. Experimental Details

## V.D.1. Sample Preparation

Sample preparation was similar for all the confined samples. A constant amount of the mesoporous materials (MCM-41, SBA-15) was filled into a standard flat aluminum cell for both liquid and confined samples. The liquid binary mixtures (prepared in volume fraction for different isotopic and concentration compositions) were filled using a well calibrated micropipette. The targeted volume of the filling is 100% of the porous volume of the confining matrix determined by adsorption isotherms illustrated in Chap. II (0.67 $cm^3/g$ for MCM and 1 $cm^3/g$ for SBA). An indium wire was introduced to fill the gaps of the sample holder and secure the sealing of the sample. This was done to ensure the absence of any leakage of the volatile liquids. Finally the samples were put in the oven at around 25 °C for a few hours to equilibrate the system and assure the homogeneous filling of the different pores, in agreement with the SANS kinetic measurements.

It is crucial to note that, in order to avoid multiple scattering the sample thickness was carefully chosen to be 0.1 mm and 1mm for the bulk and confined samples respectively resulting in a transmission of roughly 90% depending on the density and exact composition of the sample.

It should be noted that the samples were prepared with different isotopic compositions where the dynamics of the hydrogenated constituent are specifically highlighted due to the high incoherent cross section of the proton. This is a very powerful feature of neutron scattering and this method was used to label one of the two components of our mixtures and specifically follow its dynamics.

## V.D.2. Experimental Conditions

The EFWS experiments on MCM-41 confined systems were performed on IN10 and IN16 backscattering instruments at the ILL. On the other hand, the measurements on the binary liquids confined in SBA-15 were conducted on spheres at FRMII. All the mentioned instruments share a comparable high resolution; however, they differ in their flux, energy range and Q grid having different number of detectors**.** The most significant characteristics of the distinct instruments used in our experiments are illustrated in the table below:

Table V-2: The characteristics of the different high resolution backscattering instruments used.

| | Number of Detectors | Q range ($A^{-1}$) | Resolution (μeV) | Energy Transfer(μeV) |
|---|---|---|---|---|
| **IN10** | 7 | 0.07-2.0 | 1-1.2 | ±15 |
| **IN16** | 22 | 0.2-1.9 | ~0.9 | ±15 |
| **Spheres** | 16 | 0.2-1.8 | ~0.65 | ±31 |

In our elastic fixed window scans measurements only one configuration was used with Si (1 1 1) crystals; therefore, all the experiments were performed at a fixed wavelength of 6.27 Å. Moreover, for elastic measurements, the outgoing flux was measured at the same energy *i.e.* the Doppler was set to zero velocity. The elastic scattering was measured versus temperature in a temperature range from 2 K to around 320-350 K (differing between one instrument and another). For all the systems and on all instruments the measurements were done in cooling in the aim of avoiding the crystallization of the liquids with a cooling rate of 0.5 K/min.

### V.D.3. Data Treatment

The EFWS raw data measured are total elastic intensities at distinct Q values. For the MCM systems, the preliminary treatment of the data was performed using the standard ILL software sqwel. The latter successfully performs corrections for sample self-absorption and the subtraction of the aluminum sample holder. A subsequent treatment was achieved by a home written Scilab script which subtracts the appropriate amount of the confining matrix (by introducing a correcting coefficient with respect to the silica mass in the empty MCM sample). The treated intensity was then normalized to low temperature based on the assumption that the molecules have zero-point movement at low temperatures. Under this assumption all the incoherent scattering is contained within the elastic resolution i.e. $S_{inc}(Q,0)_{2K} = \int S(Q,\omega)d\omega$. Similarly, the SBA-15 data were treated using the FRM-II slaw software which converts raw neutron counts into S(Q, ω), subtracts empty-cell contributions, corrects from the empty matrix and normalizes to low temperatures.

# V.E. Results and Discussion

## V.E.1 Pure components in SBA-15

### V.E.1.1. Elastic Fixed Window Scans

EFWS measure the elastic contribution from localized motions (Elastic Incoherent Structure Factor A(Q)) and the fraction of quasielastic contribution of both localized and non-localized modes which is slower than the instrumental energy resolution R(Q,ω), which is later assimilated to the value of the dynamic structure factor at zero energy S(Q,0).

$$\text{EFWS} = \int \mathrm{R}(\mathrm{Q},\omega)\mathrm{S}(\mathrm{Q},\omega)\mathrm{d}\omega \approx \mathrm{S}(\mathrm{Q},0)$$

The increases of S(Q,0) from 0 to 1 on cooling illustrates the gradual slowdown of the different dynamical modes, which are active in the liquid and frozen in the glass or even at a lower temperature. The Q dependence is determined by the geometry of the localized modes i.e. A(Q) and the dispersion of the quasielastic lines *i.e.* Γ(Q)

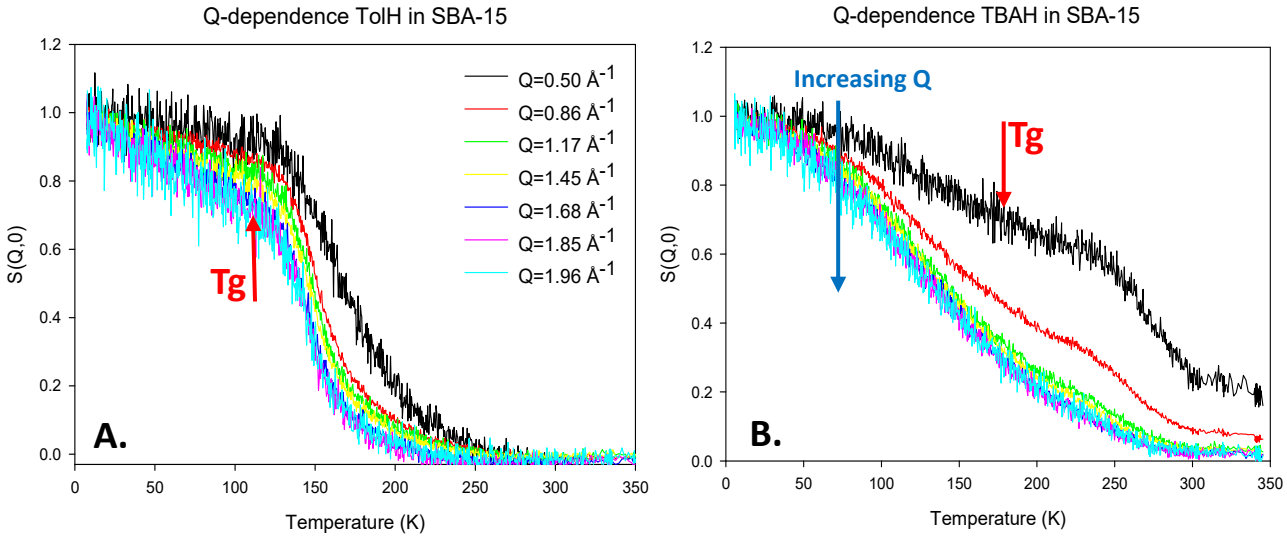


Figure V-7: (A) and (B): Q-dependence of the EFWS of TolH and TBAH in SBA-15 respectively.

The EFWS of TBA and Tol show common features including: an increase in elastic intensity upon cooling from about 0 at high temperatures to 1 at T= 2K. Moreover, both scans show a sigmoidal shape (step) which occurs a few ten K above Tg followed by a gradual increase upon further cooling. Finally the intensity in both scans decreases with increasing Q.

Regardless of the resemblance, Tol and TBA are very different at the quantitative level as for Tol the amplitude of the step is large and sharp (S(Q,0)= 0.6-0.85) at Tg and S(Q,0) is weakly Q dependent around and below Tg (Fig. V-7 (A)). As for TBA, the amplitude of the step is

small for the lowest two detectors (S(Q,0)= 0.2-0.4) and null elsewhere. In the vicinity and below Tg, $S(Q,0)_{TBA}$ is very Q dependent as it broadly ranges between 0.25 and 0.7 at Tg as shown in Fig. V-7 (B).

### V.E.1.2. Mean Square Displacement (MSD)

The Mean Square Displacement (MSD) is a complementary way to study the Q-dependence of the dynamic structure factor. At low temperatures, the quasielastic lines related to relaxation processes are narrow enough not to be discriminated from a true elastic peak within the given experimental resolution.

Moreover, vibrational modes lead to an inelastic component and a purely elastic one. The former stands outside the energy range of Backscattering and is not observable by this technique. The latter being convoluted with the dynamic structure factors of the other modes appears as a damping factor, also denoted by the Debye Waller factor.

In the frame of the harmonic approximation, which is usually valid in the low temperature range, this intensity reduction gives the opportunity of measuring the temperature dependence of the Mean Square Displacement MSD, $\langle u^2 \rangle$ of the vibrational modes from the slope of the logarithm of the elastic intensity versus $Q^2$:[22]

$$\frac{S_{inc}(Q,0,T)}{S_{inc}(Q,0{,}5K)} = e^{-\frac{\langle u^2 \rangle (T) Q^2}{3}} \qquad \text{(V-10)}$$

In this section we report the Mean Square Displacement at the nanosecond timescale measured by Elastic Fixed Window Scans which has proven to be a very efficient method in the determination of the effective MSDs particularly in the context of the glass transition investigations. In this section, MSDs were studied as a function of temperature for pure TBA and Tol confined in SBA-15 as shown in Fig. V-8.

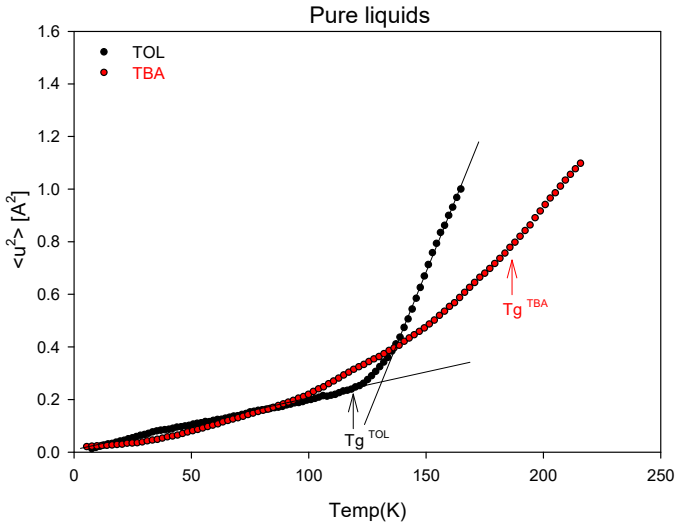


Figure V-8: MSD measurements of TBAH and TolH confined in SBA-15.

The MSDs of Tol and TBA reveal remarkably distinct behaviors:

The MSD of Tol is almost linear and weakly varying up to Tg. At Tg, its value is equal to 0.2 Å$^2$ and a crossover takes place with a rapid increase of a few tens of degrees above the transition. This indicates that, below Tg, the dynamics of Tol are frozen except for modes with very small amplitude (MSD<0.3 Å$^2$) such as vibrations and methyl librations-rotations in accordance with the harmonic approximation.

The picture changes above Tg, as a rapid activation of many degrees of freedom of large amplitude motions takes place (*i.e.* translation, molecular rotations...) coupled to the structural relaxations and the harmonic approximation becomes, therefore, invalid.

On the other hand, TBA displays a gradual increase of MSD with a bended shape (*i.e.* no clear crossover). This observation is consistent with a distribution of modes in the glass (at T< Tg) that must be, however, localized because no diffusion occurs below Tg. Moreover the MSD of TBA rises within the glass well below Tg and is remarkably large at Tg being equal to 0.8 Å$^2$ indicating the activation of degrees of freedom with large amplitudes and a large deviation from the harmonic approximation in the glass. We can infer the existence of various active modes in the glass of TBA such as methyl rotations, molecule or cluster rotations and secondary relaxation processes….

### V.E.1.3. Conclusion

The previous observations can be interpreted in a simple picture: a distinction between localized modes (which are still active below Tg) and slower modes coupled to the structural relaxations and frozen upon approaching the glass transition.

It is crucial to note that below Tg, only localized modes are possible; *i.e*., comprising a purely elastic component, also denoted Elastic Incoherent Structure Factor (EISF), for which the Q dependence reflects the long-time trajectory of the localized mode.

Above Tg, both are possible, such as localized rotation and diffusive translation for instance. However, we consider that their convolution to diffusion mode ultimately gives rise to an only quasielastic contribution. Applying this approximation, the following equation is obtained, where the DWF stands for the EISF counterpart of vibrational (inelastic) modes:

$$S_{inc}(Q,\omega) = e^{\left(-\frac{\langle u^2\rangle Q^2}{3}\right)}\left[A^{loc}(Q).\delta(\omega) + \left(1 - A^{loc}(Q)\right)S_{loc}(Q,\omega)\right] \otimes [S_{relax}(Q,\omega)] \quad \text{(V-11)}$$

$A^{loc}(Q)$ and $S_{loc}(Q,\omega)$ are the EISF and the quasielastic component of the localized modes, respectively. $S_{relax}(Q,\omega)$ is the purely quasielastic contribution from modes coupled to the main structural relaxation of the liquid. It should be mentioned that $\otimes$ represents the convolution product of the two terms.

<u>At the glass transition:</u>

The jump in $S(Q,0)$ on approaching Tg is due to the slowing down of $S_{relax}(Q,\omega)$ (where $S_{relax}(Q,0) = 0$ at high T and 1 in the glass). Noting that local modes remain much faster than the relaxation modes approaching Tg ( $S_{loc}(Q,0) = 0$). Thus $S_{inc}(Q,0)$ becomes:

$$S_{inc}(Q,0) = e^{\left(-\frac{\langle u^2\rangle Q^2}{3}\right)}A^{loc}(Q)S_{relax}(Q,0) \quad \text{(V-12)}$$

This means that, in the vicinity of the glass transition, the amplitude of the jump in the EFWS is proportional to $A^{loc}(Q)$.

Below the glass transition:

All structural relaxations are frozen ( $S_{relax}(Q,0) = 1$), therefore $S_{inc}(Q,0)$ is expressed by:

$$S_{inc}(Q,0) = e^{\left(-\frac{\langle u^2\rangle Q^2}{3}\right)}\left[A^{loc}(Q) + \left(1 - A^{loc}(Q)\right)S_{loc}(Q,0)\right] \qquad \text{(V-13)}$$

This interpretation allows the understanding of the features observed in the EFWS and the Mean Square Displacements.

Concerning Tol: the prominent jump in EISF around 120-200K, at all Q-values, reflects the slowdown and freezing of most of the degrees of freedom, which are coupled to the structural relaxations $S_{relax}(Q,\omega)$ (Fig. V-7 (A)). The behavior is rather typical for glass-forming systems, the distributions of these modes is commonly represented by a phenomenological Kohlrausch relaxation function.

The case of TBA: the EISF is dominated by a distribution of localized modes with large amplitude on the entire temperature range (as observed in the MSDs in Fig. V-8 (B)). $S_{relax}(Q,\omega)$ is highly damped by $A^{loc}(Q)$ and its jump is only accessible around 200-300K for the lowest two Q-values (Fig. V-7 (B)).

It should be mentioned that this analysis of the origins of the different characteristics observed in the EISF and MSD, should be complemented by TOF to study the quasielastic contribution from these modes and shall serve as the basis for the discussion about the confined mixtures.

## V.E.2. Binary Mixtures in SBA-15

### V.E.2.1. Contribution from Deuterated Components

As mentioned earlier, we used isotopic labelling to specifically highlight the dynamics of a chosen component (which is hydrogenated) over the other (which is deuterated). This technique is very useful and serves as a very efficient method to disentangle the different dynamical contributions of the different constituents. Nevertheless, it might be problematic in certain cases where the contribution of the deuterated component is significant and can't be neglected. In this approach we shall illustrate the degree of significance of this effect in our systems, which will help in the interpretation of the EFWS of the confined binary mixtures in the following sections.

Table V-3: The coherent, incoherent and total scattering sections of TBA (H-D) and Tol (H-D).

| | Sig Inc | Sig Coh | Sig Scat Tot |
|---|---|---|---|
| **TBA D** | 20 | 82 | **103** |
| **TBA H** | 799 | 44 | **843** |
| **Tol D** | 16 | 84 | **100** |
| **Tol H** | 639 | 53 | **692** |

Table V-3 gives the coherent, incoherent and total scattering sections of TBA and Tol (hydrogenated and deuterated). The calculations were done based on their atomic compositions.

It should be mentioned that the intensity of the coherent contribution is modulated by $S_{coh}(Q)$, while $S_{inc}(Q)$ is constant. In the subsequent estimation, we neglected this Q variation (*i.e.* we assumed $S_{coh}(Q) = \frac{\sigma_{coh}}{4\pi}$). According to previous diffraction experiments[18, 25] one can assume that $S_{coh}(Q) < \frac{\sigma_{coh}}{4\pi}$ up to Q= 1.05Å$^{-1}$. Thus the contribution from the deuterated compound in the binary liquid is likely to be smaller than our estimation.

Using this approximation of the coherent scattering, we were able to calculate the contribution of TolD and TBAD to the total scattering of the sample using the following equations respectively:

$$\frac{(1-x)\sigma_{tot}^{TolD}}{(1-x)\sigma_{tot}^{TolD} + x\sigma_{tot}^{TBAH}} \quad \text{(V-14)}$$

$$\frac{x\sigma_{tot}^{TBAD}}{(1-x)\sigma_{tot}^{TolH} + x\sigma_{tot}^{TBAD}} \quad \text{(V-15)}$$

x represents the molar fraction of TBA in the mixture and ($\sigma_{total}=\sigma_{coh}+\sigma_{inc}$). The contributions from the different deuterated compounds in the samples are illustrated in Table V-4.

Table V-4: Contribution of the deuterated liquids to the overall scattering of the different samples.

| | **TBAH/TolD samples** | **TBAD/TolH samples** |
|---|---|---|
| **$x_{vol}$ TBA** | **Sig TolD scatt. /Sig Tot** | **Sig TBAD scatt. /Sig Tot** |
| **0** | | 0.00 |
| **0.3** | 0.20 | 0.07 |
| **0.5** | 0.10 | 0.14 |
| **0.7** | 0.04 | 0.28 |
| **1** | 0.00 | |

Although the EWFS curves of mixtures will be discussed in details in the next part, we would like to have a first overview of the significance of possible contributions arising from the deuterated component with respect to the intended incoherent contribution from the hydrogenated counterpart of the mixture. This is illustrated for one Q value (Q= 0.86Å$^{-1}$) and for different compositions of TBAHTolD and TBADTolH mixtures in Fig. V-9 (A and B respectively).

The solid lines represent the measured EFWS and exhibit significant dependences with the composition, which are intended to illustrate changes in the dynamics of the hydrogenated compound. However, the scattering section of the deuterated liquids relative to the total scattering calculated in Table V-4 was used to quantify the possible contribution to the elastic fixed window scans arising from the deuterated component. The vertical bars at T=0 in graphs A and B signify the level of scattering arising from TolD and TBAD respectively. Furthermore,

the dotted curves correspond to the EFWS of pure Tol (Fig. V-9 (A)) and TBA (Fig. V-9 (B)), scaled to the levels of Tol and TBA in the mixtures respectively.

In the TBAHTolD systems (Fig. V-9 (A)): we can conclude that the contribution of TolD to the jumps of intensity observed at high T (T>180K) can be safely ruled out, because its intensity is expected to be extremely small in this range. However, the contribution to the features observed at low T is possible, but only partially and therefore can't be enough to explain the changes observed in the EFWS. Therefore, some changes in the dynamics of TBAH have to be invoked to explain the high T variation and the essential part of the low T variation of S(Q,0).

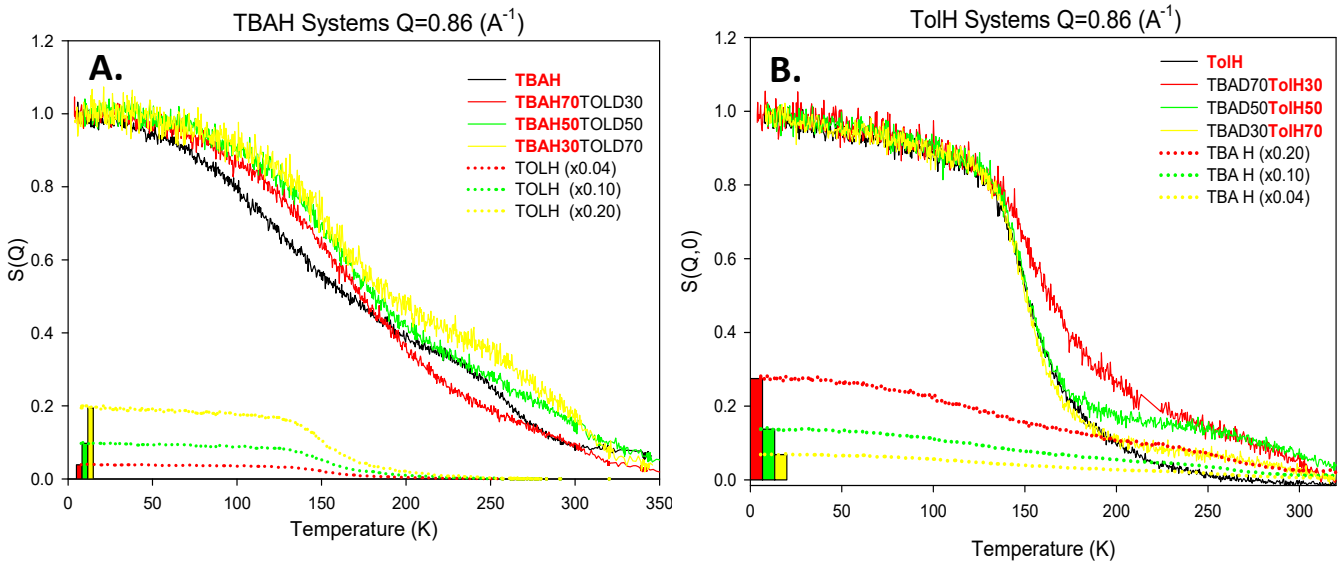


Figure V-9: (A): the contribution of TolD and (B): TBAD to the total intensity of the EFWS where the vertical bars at T=0 signify the level of scattering arising from TolD and TBAD respectively. The dotted curves correspond to the EFWS of the pure components scaled to their level in the mixtures.

In the TBADTolH systems (Fig V-9 (B)): the TBAD contribution to the features observed at high T is possible mostly for the lowest Tol composition (see red curve for $x_{TBA}$= 0.7) but secondary otherwise. Therefore, changes in the TolH dynamics bring indeed the most significant contributions to the concentration dependence of the EFWS in TBADTolH systems.

### V.E.2.2 Elastic fixed Window Scans

Our discussion of the EFWS in mixtures will be limited to two Q-values where the Q dependence will be rather illustrated by the MSDs (the figures of the EFWS at all Q values will be shown in the annex). The two momentum transfer values chosen are: Q= 0.86Å$^{-1}$ which represents the features observed at low Q and is close to the TBA pre-peak and Q= 1.45Å$^{-1}$ which is representative of the features observed at high Q. The latter Q value is close to the main diffraction peak of TBA and Tol.

#### *V.E.2.1.i. High Momentum Transfer: Q= 1.45Å$^{-1}$*

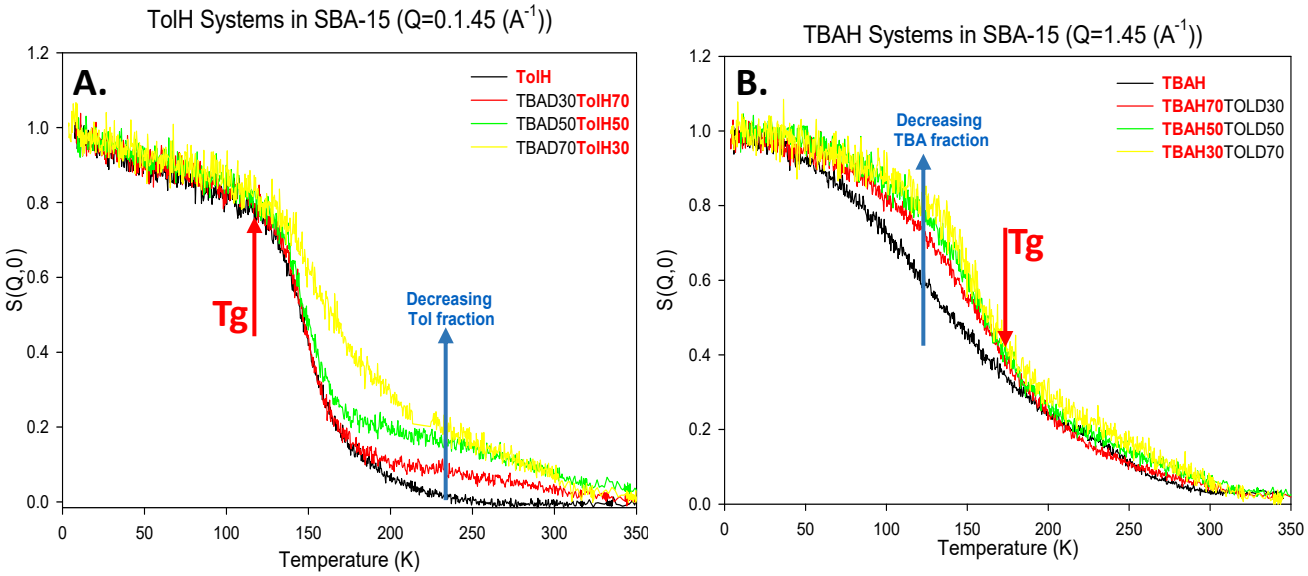


Figure V-10: FWS for (A): TBADTolH and (B) TBAHTolD systems with different compositions in SBA-15 at Q= 1.45A$^{-1}$.

The EFWS of the TBADTolH samples reveal a systematic increase of intensity, above Tg, in the high T range (150-300K) with decreasing Tol fraction which is a representative of $S_{relax}(Q, 0)$ of Tol. It seems like an emergence of a second slower (high T) component to $S_{relax}(Q, 0)$ which apparently increases with the decrease in the Tol fraction. However, no effect is observed in the low T range (0-150K), below Tg, which is a signature of the $S_{loc}(Q, 0)$ in the vitreous state of Tol (Fig. V-10 (A)). The EFWS of the TBAHTolD samples display a very different behavior which is characterized by the absence of any effect in the high T range (185-300K), *i.e.* above Tg, which is representative of $S_{relax}(Q, 0)$ of TBA and a systematic increases of intensity in the low temperature range (50-185K), which is representative of $S_{loc}(Q, 0)$ of TBA. Furthermore, a sharper crossover near the glass transition is observed in the mixtures compared to the gradual decrease in the pure TBA (Fig. V-10 (B)).

The conclusions that could be made from the analysis of the EFWS at high Q are given is the following part, sequentially for the two different constituents.

- Tol dynamics:

In the glass, Tol has no visible change in the local dynamics, which are essentially vibrational and conformational, and are therefore, weakly sensitive to changes in the molecular environment. As for the Liquid phase, a growth of a slow component coexisting with a "pure-Tol-like" relaxation component takes place. This observation agrees with the persistence of a rich-Tol region in the pore (core) which behaves like pure Tol (Fig. V-11). The slow component could arise from the interfacial region (between the core and the shell), where the dynamics are reduced by the interaction of Tol with the TBA molecules forming the more viscous shell region. Its contribution increases with $x_{TBA}$ because it scales like the surface to volume ratio of the core (Fig. V-11 (B and C)). Moreover, the vitrification of the TBA shell below 185K could also act as an effective reduction of the confinement radius of the Tol core.

Regarding the smallest composition $x_{Tol}$= 0.3, the 2 components broaden and merge, indicating that for such small core radius, the distinction between interfacial and core molecules becomes illusive: $R_{core} = R_{pore}\sqrt{(1 - x_{TBA})} = 4.1\sqrt{(0.3)} = 2.2$nm; *i.e.*, equivalent to a few molecular diameters (reference: see Chap. IV, Table IV-1). It should be mentioned; however, that for this particular composition a contribution from the TBAD dynamics is also possible (as discussed previously) which could enhance this broadening in temperature.

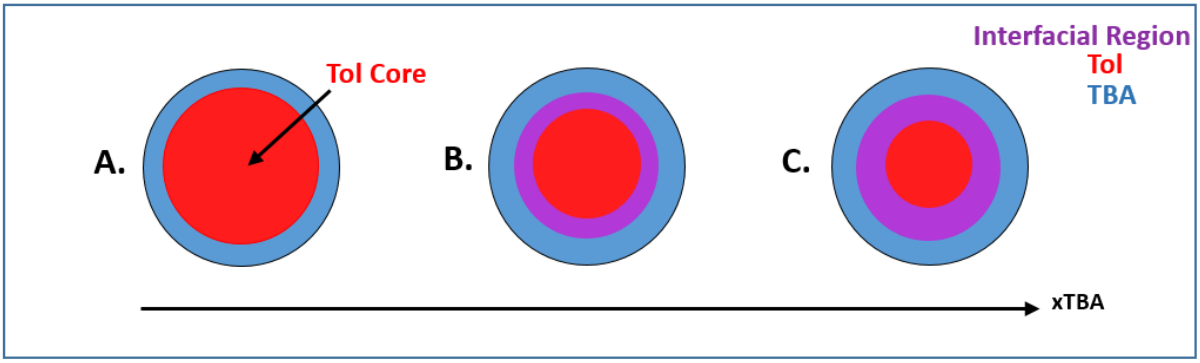


Figure V-11: A representation of the core-shell structure in the pore where the concentric shells represent the different liquid constituents. Where the blue, red and purple represent the TBA-rich phase, the Tol-rich phase and the developing liquid interfacial region between the two respectively.

- TBA dynamics:

The absence of any change in the relaxation dynamics of liquid TBA is simply because they are not visible at this Q, being damped by the EISF of localized modes. Below Tg, a change in the local dynamics (molecule or cluster rotation) takes place as the dynamics slow down and become less distributed (sharper kink) upon Tol addition.

Interestingly this result is contradictory to expectations from simple mixing arguments: Tol being less viscous than TBA, it should have plasticizing effects and the TBA relaxation should be, therefore, accelerated. Moreover, mixing should complexify the molecular environments, leading to a broader distribution of the relaxation modes rather than the observed sharpening.

On the other hand, all these observations are in full agreement with the core-shell structure: in this situation the slowdown agrees with the segregation of TBA at the surface where its strong H-bond interaction with the silanol groups limits its rotational dynamics. Moreover, the distribution of dynamical modes in TBA could be attributed to the different environments, comprising TBA molecules adsorbed at the pore wall with reduced dynamics and TBA molecules located in the pore center (for pure TBA) or interacting with Tol in the liquid interfacial region between the core and the shell (Fig. V-12 (A)). As $x_{TBA}$ decreases, the population of TBA molecules located at or near the pore center decreases, and it eventually leads to a unique population consisting of TBA molecules adsorbed at the pore surface as shown in Fig. V-12 (B).

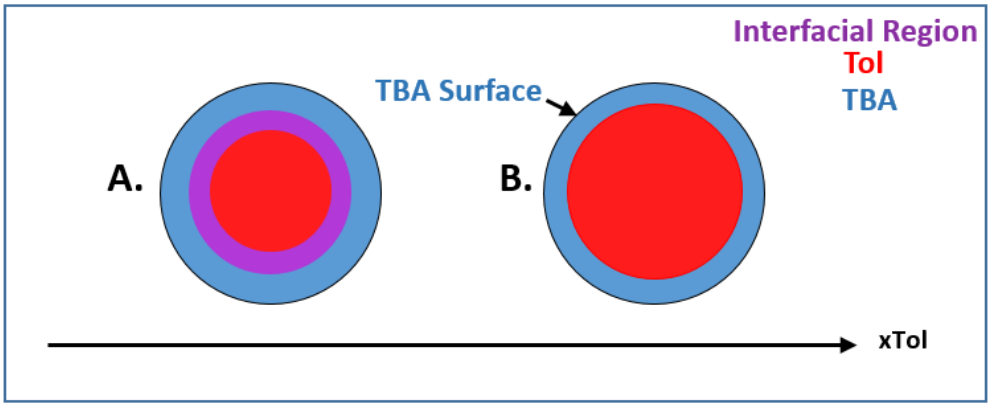


Figure V-12: A representation of the core-shell structure in the pore where the concentric shells represent the different liquid constituents. Again the blue, red and purple represent the TBA-rich phase, the Tol-rich phase and the developing liquid interfacial region between the two respectively.

### *V.E.2.1.ii. Low Momentum Transfer: Q= 0.86 Å$^{-1}$*

The same main patterns in the EFWS are reproduced at low Q for TBADTolH samples (Fig.V-13 (A)) indicating a similar behavior to that discussed earlier. This further supports that the hypothetical contributions arising from the deuterated molecules, which should be maximized around the main diffraction peak (at Q= 1.45Å$^{-1}$), are indeed small compared to the incoherent scattering.

Concerning the TBAHTolD samples (Fig.V-13 (B)), the glass (T<200K) also shows the same behavior as discussed for a high Q-value. As for the liquid phase (T>200K), new features emerge around the small jump, which has been attributed to $S_{relax}(Q, 0)$. As discussed previously for the pure TBAH, this relaxation mode is accessible only at low Q, being damped by A(Q) otherwise. The step due to the slowdown of $S_{relax}(Q, 0)$ on approaching Tg for TBA is firstly blurred by the addition of a small amount of Tol (x= 0.3 being the smallest used). Nevertheless, further Tol addition causes a systematic increase of a high temperature (slow) component (see Fig.V-13 (C)), where pure TBA was removed for clarity). This non-monotonous behavior highlights the existence of at least two competing effects that shall be discussed again in relation with the structure.

The low Q results provide supplementary information about very interesting phenomena, which are the following: the addition of small amount of Tol to TBA initially highlights a conventional "plasticizing effect" of Tol on the relaxation dynamics of the confined liquid TBA. This leads to the observed faster and broadened relaxation dynamics of TBA in the liquid phase. This is expected because Tol is an aprotic solvent which can dilute the H-bond interactions between the TBA molecules. In addition, Tol having a lower Tg can also reduce the viscosity of the mixture.

Then for $x_{Tol}$>0.3, an opposite effect emerges, consistent with the formation of the core-shell structure. The liquid TBA dynamics is then gradually dominated by the contribution from the population of adsorbed molecules, which are slower and spatially restricted.

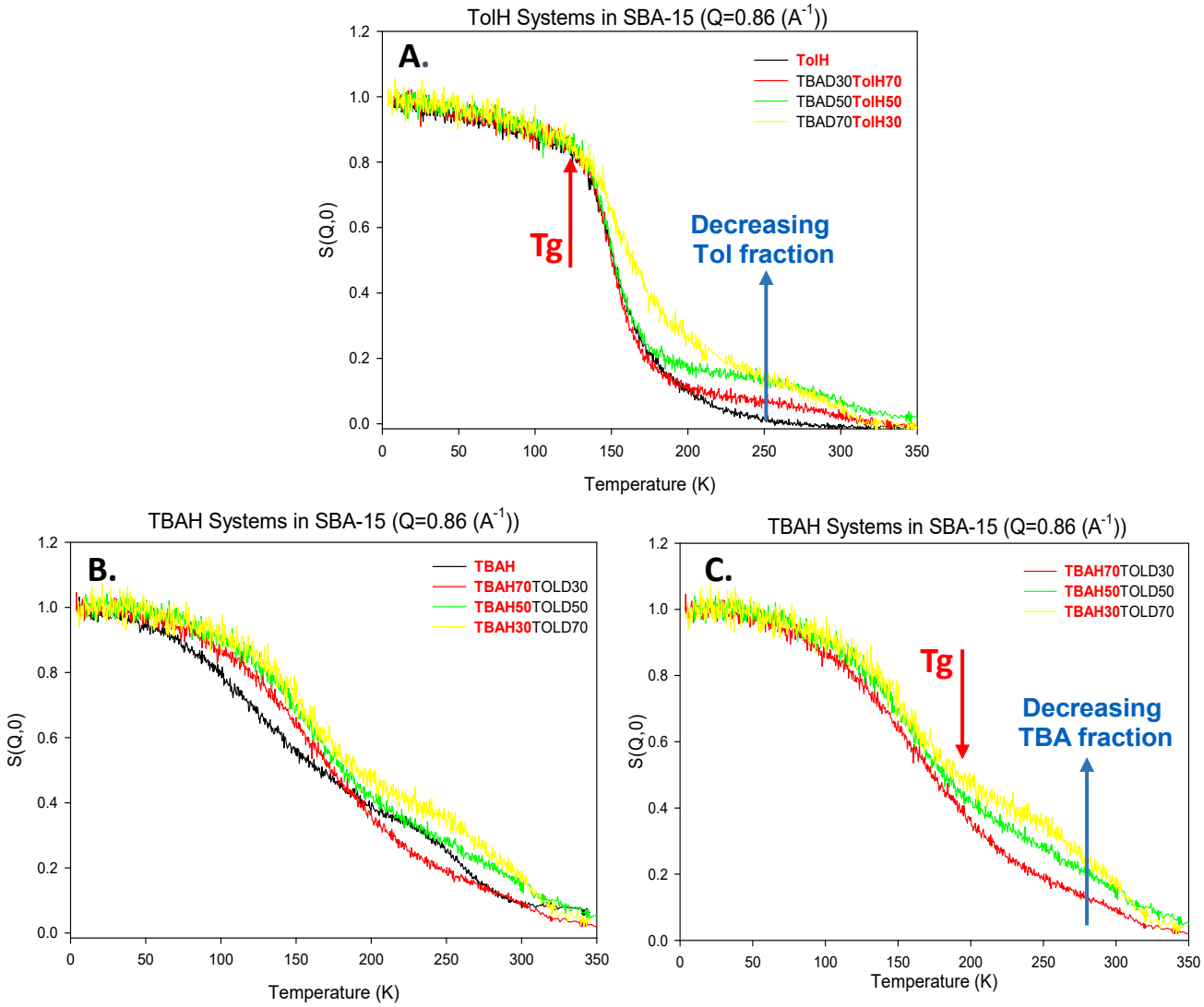


Figure V-13: EFWS of (A): TBAHTolD and (B): TBADTolH systems with different compositions in SBA-15 at Q= 0.86 $A^{-1}$, (C) is same as (B) but pure TBAH is removed for clarity.

These results agree with and go one step further than existing results in the literature where studies on confined binary mixtures have shown dynamical evidence of microphase demixion contributed to the different affinities of the liquids to the pore walls leading to the preferential absorption of one of the mixture constituents at the surface.[7, 14-17] The labeling of the dynamics of the different constituents by H/D isotopic effect and the correlation of dynamics to structural determination provide a unique comprehensive view on the different intervening phenomena.

### V.E.2.3. Mean Square Displacement (MSD)

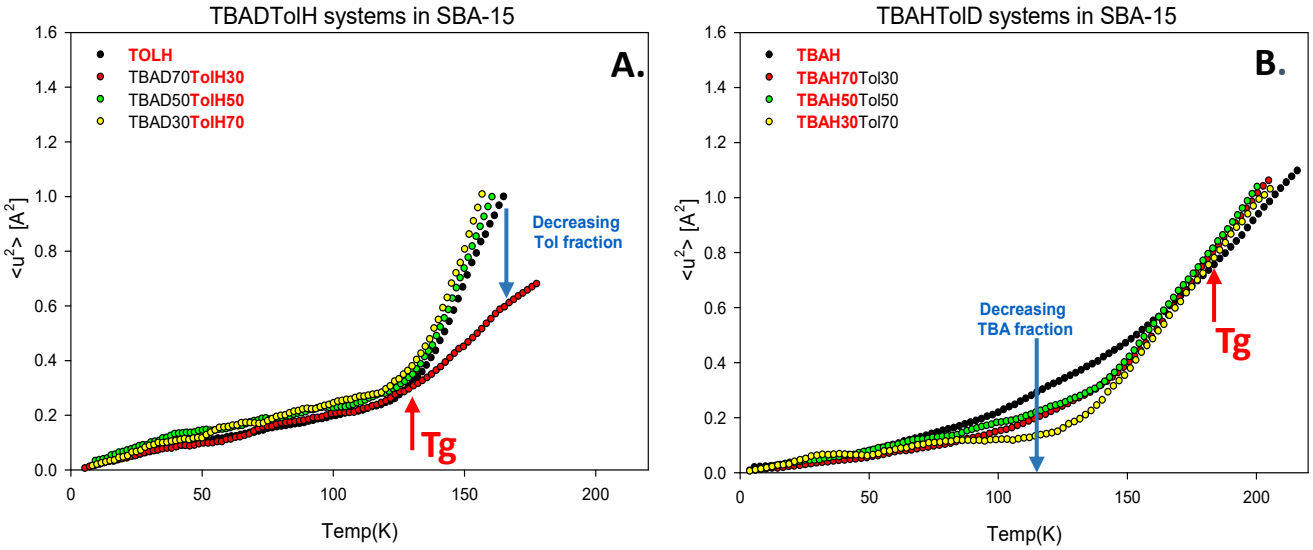


Figure V-14: MSDs vs T for (A): TBADTolH systems and (B): TBAHTolD systems confined in SBA.

The MSD of the different mixtures have been obtained from a quadratic fit of the logarithm of the EFWS intensity. Fits of good quality were obtained, especially in the low temperature range, attesting the applicability of the harmonic approximation and the absence of noticeable coherent scattering. It should be noted that the data were normalized to the lower temperature. Therefore the coherent S(Q) contributions are removed as long as they are not T-dependent.

For TBADTolH samples (Fig. V-14 (A)), no dilution effects take place in the glass. This is obviously in agreement with the EFWS, which emphasizes that the dynamics of vitreous Tol mainly comprise conformational modes, which are barely sensitive to the environment.

Above Tg, the same deviation from the harmonic approximation is due to onset of structural relaxation.[22] This is true for all samples but the one with the highest dilution (x= 0.3), which displays a smaller effective MSD. In agreement with EFWS already shown in Fig. V-13 (A), for T< 170K, only a "Pure Tol-like" relaxation dynamics was observed. As such, it is attributed to the Tol-rich region located in the core, which is not dependent on $x_{TBA}$. The slower interfacial component only appears at even higher temperatures (above 180K), which is a temperature range not accessible to the MSD measurements. There is one exception for x= 0.3 where the typical timescales of the core Tol and interfacial Tol relaxation merge, which could explain the reduced MSD. In addition, it is important to note that for this particular sample, one should also consider a possible contribution from TBAD to the reduced MSD (as discussed before for the EFWS).

Regarding the TBAHTolD samples, (Fig. V-14 (B)) a systematic variation of the MSD is observed in the temperature range 100K<T<150K. For pure TBA, the MSD variation with T shows a gradual increase. The smaller $x_{TBA}$ is, the more distinct the crossover between the two regimes becomes.

It is worth recalling that in this T range for TBA, the MSD is only probing the local glassy dynamics of the vitreous state. This observation is consistent with the EFWS: the reduction of the broadening of the population of the different local (especially rotational) modes in the glassy TBA, as well as the reduction of their motion amplitude by the localization of TBA at the silica surface.

## V.E.3. Binary Mixtures in MCM-41

### V.E.3.1. Elastic Fixed Window Scans

#### *V.E.3.1.i. Momentum Transfers: Q= 1.45 and 0.86 Å$^{-1}$*

The same qualitative behavior has been generally confirmed for the smaller pore sized MCM-41(D= 3.5 nm). However, these observations are blurred in the case of the latter due to a broadening in the signal (Fig. V-15 (A to D)).

The most obvious observable feature (still identified regardless of the broadening) is the relaxation of Tol above Tg in the TBADTolH systems (Fig. V-15 (A and C)). A systematic increase of a second slower relaxation component appear a temperature above T= 200K, indicating the slower dynamics of Tol molecules interacting with the TBA shell.

The two other weaker effects observed for TBAHTolD samples in SBA are hardly visible in MCM-41 ((Fig. V-15 (B and D)). The first concerns a steeper variation of the EISF related to the local dynamics in the glassy state, which could still be perceived in MCM at Q= 1.45Å$^{-1}$ (Fig. V-15 (B)). The second is the change in the liquid TBA's structural relaxation, only visible at high temperature and low Q, whose observation is essentially within the statistical noise.

This broadening of the signals is attributed to the size reduction, leading to overlapping (undistinguishable) contributions from pore/core and interfacial regions which become ill-defined as the pore size decreases and approaches the molecular size.

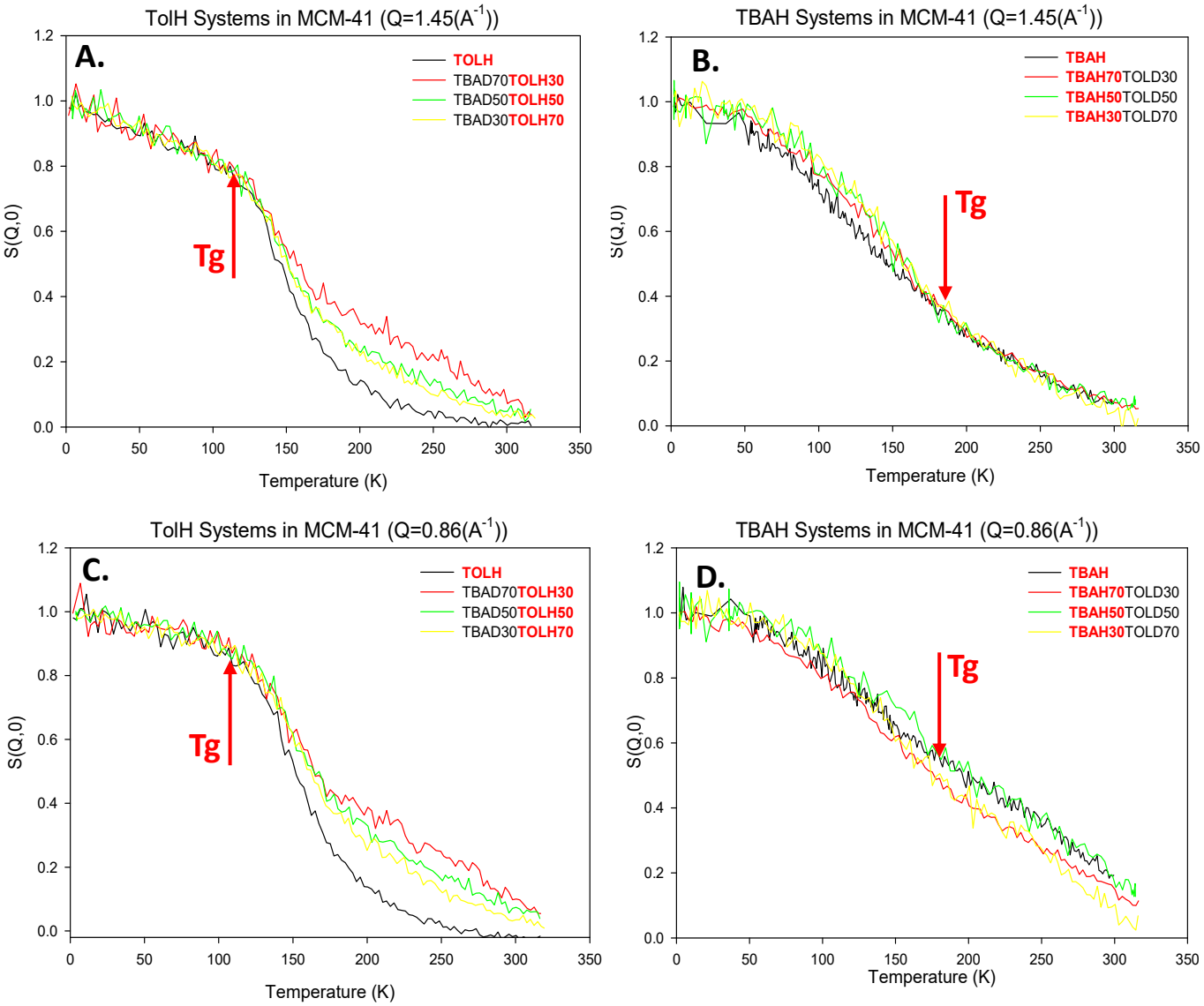


Figure V-15: EFWS of (A): TBADTolH and (B): TBAHTolD systems with different compositions in SBA-15 at Q=1.45 $A^{-1}$. (C) and (D) represent the same systems at Q=0.86 $A^{-1}$ respectively.

## V.F. Conclusion

The dynamics of binary liquids confined in the straight and monodispersed channels of MCM-41 and SBA-15 ordered mesoporous materials were investigated by elastic fixed window scans, which are usually conducted to probe the transition from the liquid to the glassy state and give an insight on the T-dependence of the dynamics at the nanosecond timescale.

The results obtained for TolH show a growth of a slow component coexisting with a "pure-Tol-like" relaxation component for Tol above Tg, in agreement with a rich-Tol region in the core of the pore. Moreover, a slow component appears upon the addition of TBA which could emerge from a liquid interfacial region in the pore (between the core and the shell), where Tol could interact with more viscous TBA which acts as an anti-plasticizer causing a reduction of the dynamics of the former.

On the other hand, TBAH displays a slowdown of the liquid relaxation dynamics above Tg and a suppression of parts of the local modes in the glass upon Tol addition. Both phenomena generally contradict a simple plasticizing scenario, which would be expected for ideal mixing of Tol with TBA and which could be perceived only for small amounts of Tol (x=0.3). The slowing in the dynamics of liquid TBA and the suppression of glassy modes can be attributed to the segregation of TBA and its H-bonding interaction with the pore surface.

The obtained observations seem to confirm the structure we proposed through modeling the SANS data in chapter IV. They provide a rather unique comprehensive viewpoint on properties of confined binary liquids, making the direct correlation between spatially segregated dynamical heterogeneities and the formation of original core shell nanostructures induced by preferential interactions.

It should be noted; however, that this dynamical image is maintained qualitative. A subsequent quantitative analysis is therefore essential for a complete insight of the physical image of the behavior of such complex system under confinement, an objective we are currently pursuing.

## References


1. Morineau, D., Y. Xia, and C. Alba-Simionesco, *Finite-size and surface effects on the glass transition of liquid toluene confined in cylindrical mesopores.* The Journal of chemical physics, 2002. **117**(19): p. 8966-8972.
2. Schüller, J., et al., *Dielectric studies of the glass transition in porous media.* Physical review letters, 1994. **73**(16): p. 2224.
3. Richert, R. and M. Yang, *Surface induced glass transition in a confined molecular liquid.* The Journal of Physical Chemistry B, 2003. **107**(4): p. 895-898.
4. Busselez, R., et al., *Molecular dynamics simulation of nanoconfined glycerol.* Physical Chemistry Chemical Physics, 2009. **11**(47): p. 11127-11133.
5. Frick, B., et al., *Inelastic neutron scattering for investigating the dynamics of confined glass-forming liquids.* Journal of Non-Crystalline Solids, 2005. **351**(33-36): p. 2657-2667.
6. He, F., L.-M. Wang, and R. Richert, *Dynamics of supercooled liquids in the vicinity of soft and hard interfaces.* Physical Review B, 2005. **71**(14): p. 144205.
7. Lerbret, A., et al., *Molecular Dynamics and Neutron Scattering Study of Glucose Solutions Confined in MCM-41.* Journal of Physical Chemistry B, 2011. **115**(5): p. 910-918.
8. Patkowski, A., T. Ruths, and E.W. Fischer, *Dynamics of supercooled liquids confined to the pores of sol-gel glass: A dynamic light scattering study.* Physical Review E, 2003. **67**(2): p. 021501.
9. Scheidler, P., W. Kob, and K. Binder, *The relaxation dynamics of a confined glassy simple liquid.* The European Physical Journal E, 2003. **12**(1): p. 5-9.
10. Yamamoto, R. and K. Kim, *Heterogeneity and finite size effects in the dynamics of supercooled liquids.* Journal De Physique Iv, 2000. **10**(P7): p. 15-20.
11. Zorn, R., et al., *Inelastic neutron scattering experiments on the dynamics of a glass-forming material in mesoscopic confinement.* Journal of Non-Crystalline Solids, 2002. **307**: p. 547-554.
12. Alba-Simionesco, C., et al., *Confinement of molecular liquids: Consequences on thermodynamic, static and dynamical properties of benzene and toluene.* The European Physical Journal E, 2003. **12**(1): p. 19-28.
13. Morineau, D., et al., *Structure of liquid and glassy methanol confined in cylindrical pores.* The Journal of chemical physics, 2004. **121**(3): p. 1466-1473.
14. Elamin, K., et al., *Different behavior of water in confined solutions of high and low solute concentrations.* Physical Chemistry Chemical Physics, 2013. **15**(42): p. 18437-18444.
15. Swenson, J., et al., *Anomalous dynamics of aqueous solutions of di-propylene glycol methylether confined in MCM-41 by quasielastic neutron scattering.* Journal of Chemical Physics, 2014. **141**(21).
16. Elamin, K., H. Jansson, and J. Swenson, *Dynamics of aqueous binary glass-formers confined in MCM-41.* Physical Chemistry Chemical Physics, 2015. **17**(19): p. 12978-12987.
17. Guo, X.Y., T. Watermann, and D. Sebastiani, *Local Microphase Separation of a Binary Liquid under Nanoscale Confinement.* Journal of Physical Chemistry B, 2014. **118**(34): p. 10207-10213.
18. Abdel Hamid, A., et al., *Solvation Effects on Self-Association and Segregation Processes in tert-Butanol–Aprotic Solvent Binary Mixtures.* The Journal of Physical Chemistry B, 2013. **117**(35): p. 10221-10230.
19. A. R. Abdel Hamid, R.Mhann, R. Lefort, A. Ghoufi, C. Alba-Simionesco, B. Frick, D. Morineau, *Structural evidence of core-shell formation in a binary liquid confined in MCM-41.* Journal of Physical Chemistry, 2015. to be submitted.
20. Le Quellec, C., et al., *Influence of surface interactions on the dynamics of the glass former ortho-terphenyl confined in nanoporous silica.* The European Physical Journal Special Topics, 2007. **141**(1): p. 11-18.

21. Hamid, A.R.A., *Nanosegregation of binairy liquids confined in mesoporous materials* 2012, Rennes 1.
22. Bée, M., *Quasielastic neutron scattering.* 1988.
23. Van Hove, L., *Correlations in space and time and Born approximation scattering in systems of interacting particles.* Physical Review, 1954. **95**(1): p. 249.
24. Bee, M., *Localized and long-range diffusion in condensed matter: state of the art of QENS studies and future prospects.* Chemical Physics, 2003. **292**(2-3): p. 121-141.
25. Morineau, D. and C. Alba-Simionesco, *Does Molecular Self-Association Survive in Nanochannels?* The Journal of Physical Chemistry Letters, 2010. **1**(7): p. 1155-1159.

# GENERAL CONCLUSION

With the advancements in nanotechnology, the manipulation of complex liquids in nanochannels has brought new opportunities for fluidic applications and the design of nanomaterials. Therefore, the study of the effect of confinement on the behavior of molecular condensates has been a highly active research field over the past few years. One particular attraction of this topic, aside of its promising technological applications, is the invalidity of many of the well acknowledged macroscale arguments at the nanolevel. In fact, many studies have supplied prevailing evidence indicating that the properties of confined liquids can't be simply interpreted in terms of their bulk counterparts as confinement has proven capable of the drastic modification of the static and dynamical properties of molecular systems.

Since the late 90s, a growing body of research has been done in the aim of understanding the differences between the physicochemical properties of liquids in bulk and under confinement. However, most of these studies have basically focused on relatively simple liquids. It is only until recently that studies on more complex H-bonding liquids have emerged. These protic liquids are associated with the formation of self-assembled microstructures often related to the balance between hydrophobic and hydrophilic interactions in the bulk phase. Thus, the geometrical constrains imposed by confinement, as well as the surface interactions with the pore walls of the confining matrix can readily disturb this balance, consequently leading to the formation of unanticipated structures and the development of new surface-driven phases.

In this thesis, we pushed this topic to a whole new level of complexity through the dilution of the hydrogen bond-forming liquid with an apolar solvent and the confinement of the resulting binary mixture in distinct mesostructured porous silicates (SBA-15, MCM-41 and CMK-3) which either differ in pore size or surface nature. By manipulating these parameters, we were able to control the formation of supramolecular structures of the mesoscopic mixtures under confinement. This approach allowed the study of new physical phenomena related to the behavior of binary mixtures in channels of a few nanometers in diameter. To investigate the structure of these systems, we used neutron small angle scattering with an extended range of momentum transfer. This allowed us to gain an insight on medium-range ordered structures (clusters and the modulation of concentration in the case of nanosegregated systems).

The primary study of the mixtures in bulk, revealed the presence of inhomogeneities which are usually associated to the phenomenon of aggregation. This supermolecular organization in the alcohol-aprotic solvent binary mixtures has been illustrated in the form of clustering of the

species of the same type upon dilution. An observation demonstrating a strongly non-ideal behavior of the mixtures. Another piece of information acquired in this study is the spatial extension of the resulting one-component rich-domains which barely exceeds the molecular size, confirming that the solutions exhibit a heterogeneous microstructure but remain macroscopically homogeneous.

An even more remarkable spontaneous nanostructuring phenomenon was observed under confinement in nanoscale channels. This specific behavior of the nanoconfined mixture leads to the formation of core-shell type structures. The stability of such structures is connected to the existence of preferential interactions with the hydrophilic surface of the confining matrix (SBA-15) which can indeed overcome the size of the alkyl part of the amphiphilic alcohol involved (*tert*-butanol, methanol, ethanol). It is important to note that the formation of such structures has been discussed so far in the case of mixtures having a macroscopic phase separation in bulk. In the latter, the existence of a macroscopic demixing or mesoscopic concentration fluctuations related to the approaching of this transition could be considered necessary ingredients. On the contrary, all our studied binary mixtures are macroscopically miscible in all proportions. Indeed, our study suggests that for certain types of mixtures, nanostructuring can appear as a confinement effect in itself and is not related to any classical thermodynamic phase transition. Moreover, it seems essential at this level to stress that the study of the radial profile of the concentration is based on a quite original approach, combining the contrast effects in isotopic neutron diffraction and the crystallinity of the arrangement of the mesoporous channels.

Unlike the case of bulk mixtures, confinement suppresses crystallization allowing the study of the dynamical properties of the original nanosegregated mixtures in the supercooled state at the proximity of the glass transition. The molecular dynamics the confined binary liquids were investigated by quasielastic neutron scattering and more specifically elastic fixed window scans acquired on backscattering instruments which give an insight on the T-dependence of the dynamics at the nanosecond timescale. The presence of different types of relaxation under confinement and non-trivial dependencies of dynamical properties with the concentration of the mixtures were observed. The global dynamical signatures obtained seem to be consistent with the core-shell structure. For instance, TBA in the systems confined in SBA-15 displays a general slowdown of the liquid relaxation dynamics and a suppression of some local modes upon Tol addition. These observed phenomena contradict with a simple plasticizing scenario,

which would be expected for ideal mixing of Tol with TBA and is rather consistent with the segregation of TBA and its interaction with the pore surface. In addition, the dynamics of Tol seem to be compatible with the presence of a Tol-rich region in the core of the pore and its slowing down upon the increase in the TBA fraction in the mixture can be simply explained in terms of an interfacial region of the two liquids (between the core and the shell) where the viscous TBA plays an anti-plasticizing role. This general view has also been confirmed to MCM-41 systems. Therefore, the obtained observations do not only confirm the structure we proposed through modelling the SANS data, but rather provide a unique comprehensive viewpoint on the properties of confined binary liquids, establishing a direct correlation between spatially segregated dynamical heterogeneities and the formation of original core shell nanostructures induced by preferential interactions. Furthermore, this study has successfully validated previous speculations on the possible existence of a prolific "plastic glass" type phase in *tert*-butanol. This confirmation was established through a comparison of the Tgs measured by different techniques (dielectric spectroscopy, neutron diffraction, EFWS and DSC) which suggested, in the case of totally associated system (*i.e*., neat *tert*-butanol), the presence of a decoupling between the mesoscopic relaxational dynamics and the rotational dynamics.

To our knowledge, there isn't a comparable study that examined the nanostructuring of binary miscible blends under confinement. This work has provided a thorough overview of such a phenomenon both from structural and dynamical points of view. It has therefore helped in the definition and emphasis of several experimental and modelling strategies whose implementation would highlight this phenomenon in other families of materials. We have emphasized several aspects that seem to play a leading role in this nanostructuring and could guide future research orientations. One particular role is that of the surface interaction in the modification of the balance of the hydrophobic/hydrophilic interactions within the mixture. This interaction, combined with the spatial geometry of confinement are, in our opinion, the main triggering elements in the nanosegregation. Therefore, the modulation of these elements could open limitless possibilities and provide new opportunities in supermolecular structuring.

A potential approach would be the tailoring the chemical nature of the surface by going from the strongly hydrophilic (MCM-41 and SBA-15) to the hydrophobic replica which is expected to allow the study of the surface effect and highlight the significance of H-bonding (which is absent in this case) in the formation of such structures and might even eventually lead to new core-shell structures. This possibility was attempted in this thesis; however, the obtained

hydrophobic materials lacked sufficient order to be successfully modeled. A future perspective would thus be implementing the same idea on different types of matrices with a better crystalline order than the used CMK-3. In another perspective, we supplied a solid qualitative dynamical image on the dynamical behavior of such nanostructures. This approach provides a very strong motivation for a subsequent quantitative analysis in the objective of achieving a comprehensive vision on the molecular dynamics of the nanosegregated mixtures. This requires the combination of the quasielastic neutron scattering and time of flight data for the extension of the dynamical range and resolution to cover the broad distribution of relaxation times induced by mixing and confinement. An aim we are still pursuing.

# ANNEX:

# Q-DEPENDENCE OF EFWS

# Annex: Q-Dependence of EFWS

## N.A. Dynamics in SBA-15

### N.A.1. TBAH TolD Systems Confined in SBA-15

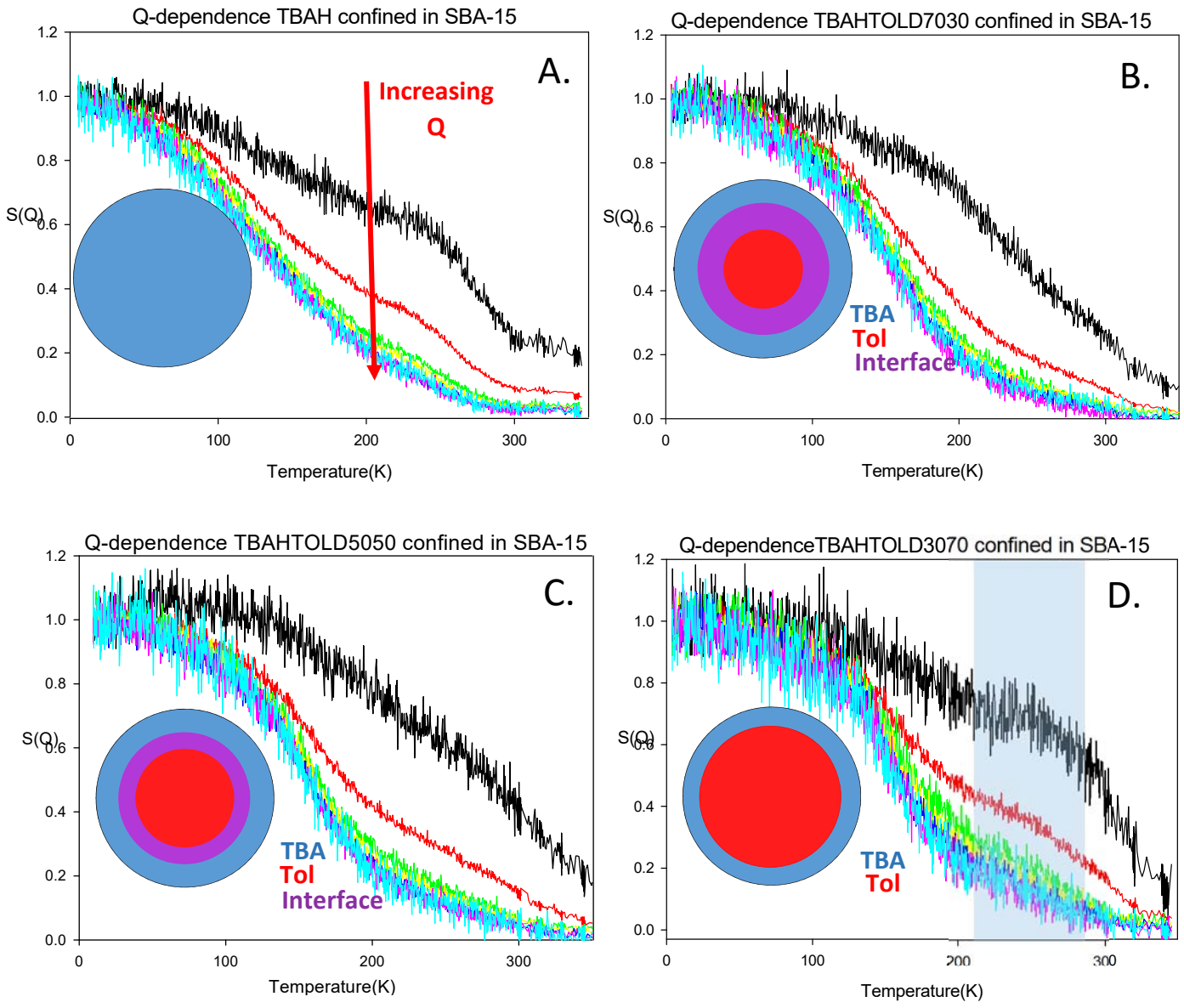


Figure N-1: Q-dependence of the EFWS of TBAHTolD mixtures confined in SBA-15, TBAH concentration decreases from A to D. The circular shape represents the pore and the concentric shells represent the constituents based on the color code. Where the blue, red and purple represent TBA, Tol and the interface region of the two respectively.

## N.A.2. TBADTolH Systems Confined in SBA-15

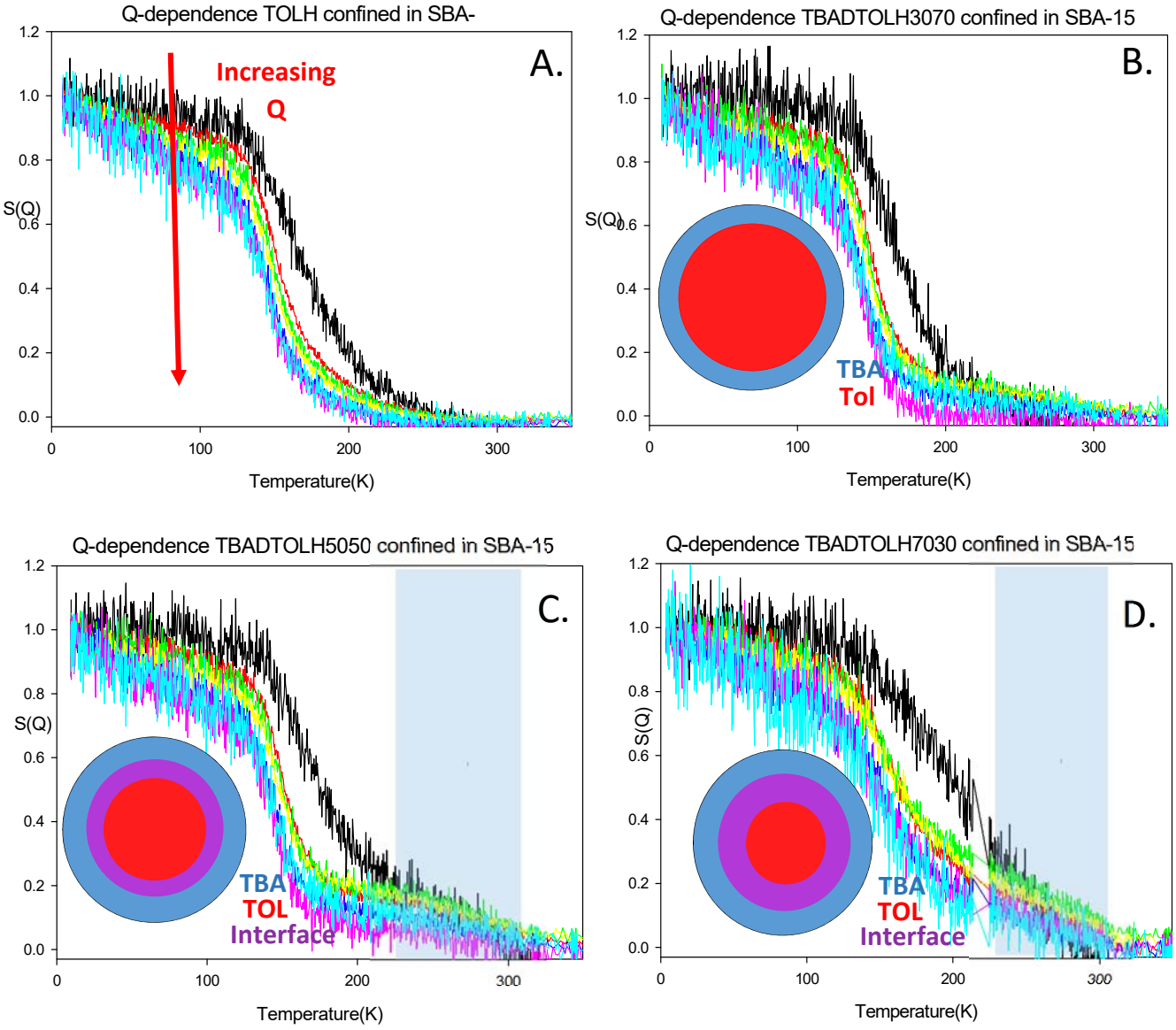


Figure N-2: Q-dependence of the EFWS of TBADTolH mixtures in SBA-15, TolH concentration decreases from A to D. The circular shape represents the pore and the concentric shells represent the constituents based on the color code. Where the blue, red and purple represent TBA, Tol and the interface region of the two respectively.

# N.B. Dynamics in SBA-15

## N.B.1. TBAH TolD Systems Confined in MCM-41

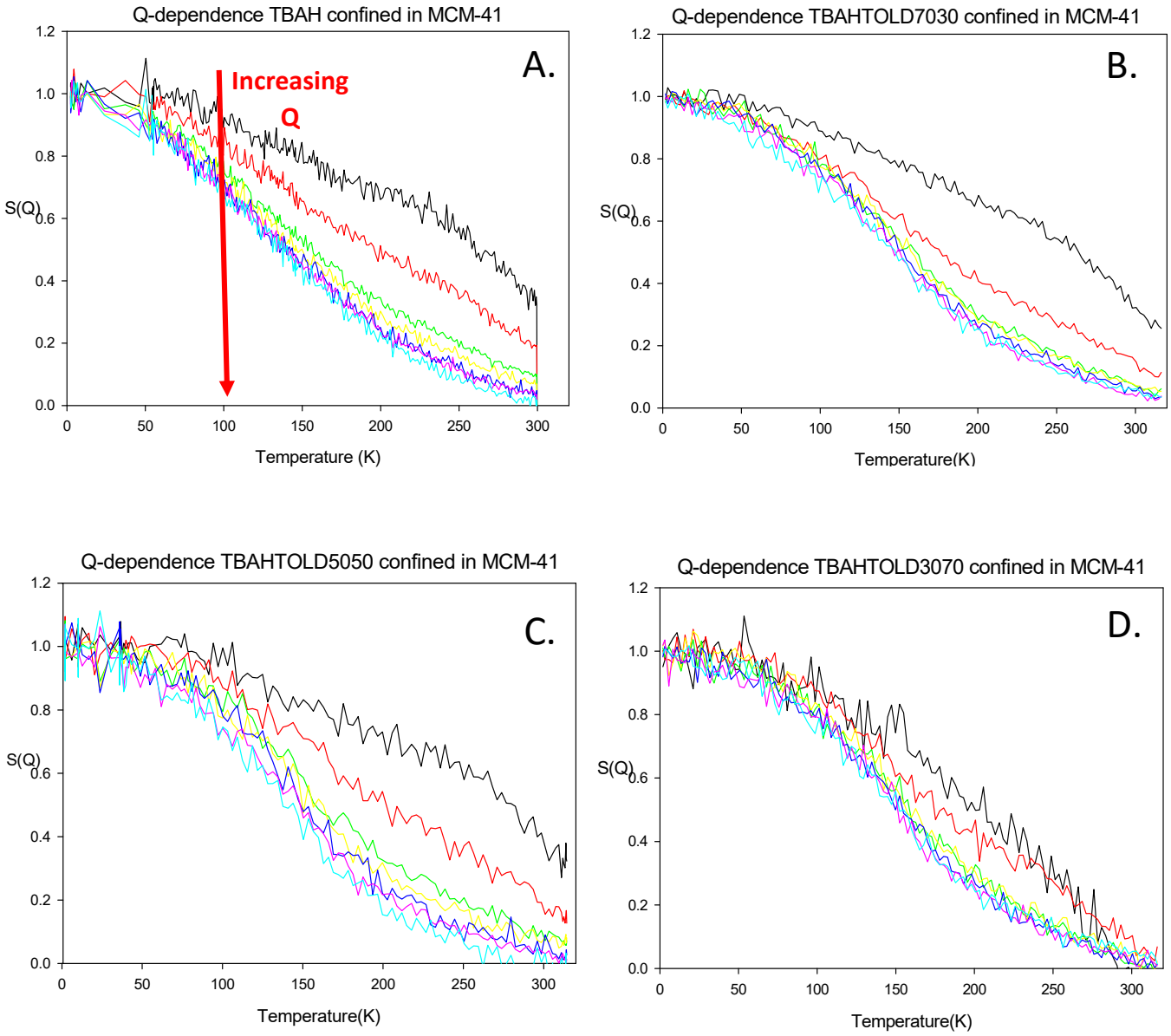


Figure N-3: Q-dependence of the EFWS of TBAHTolD mixtures confined in MCM-41, TBAH conc. decreases from A to D.

## N.B.2. TBAD TolH Systems Confined in MCM-41

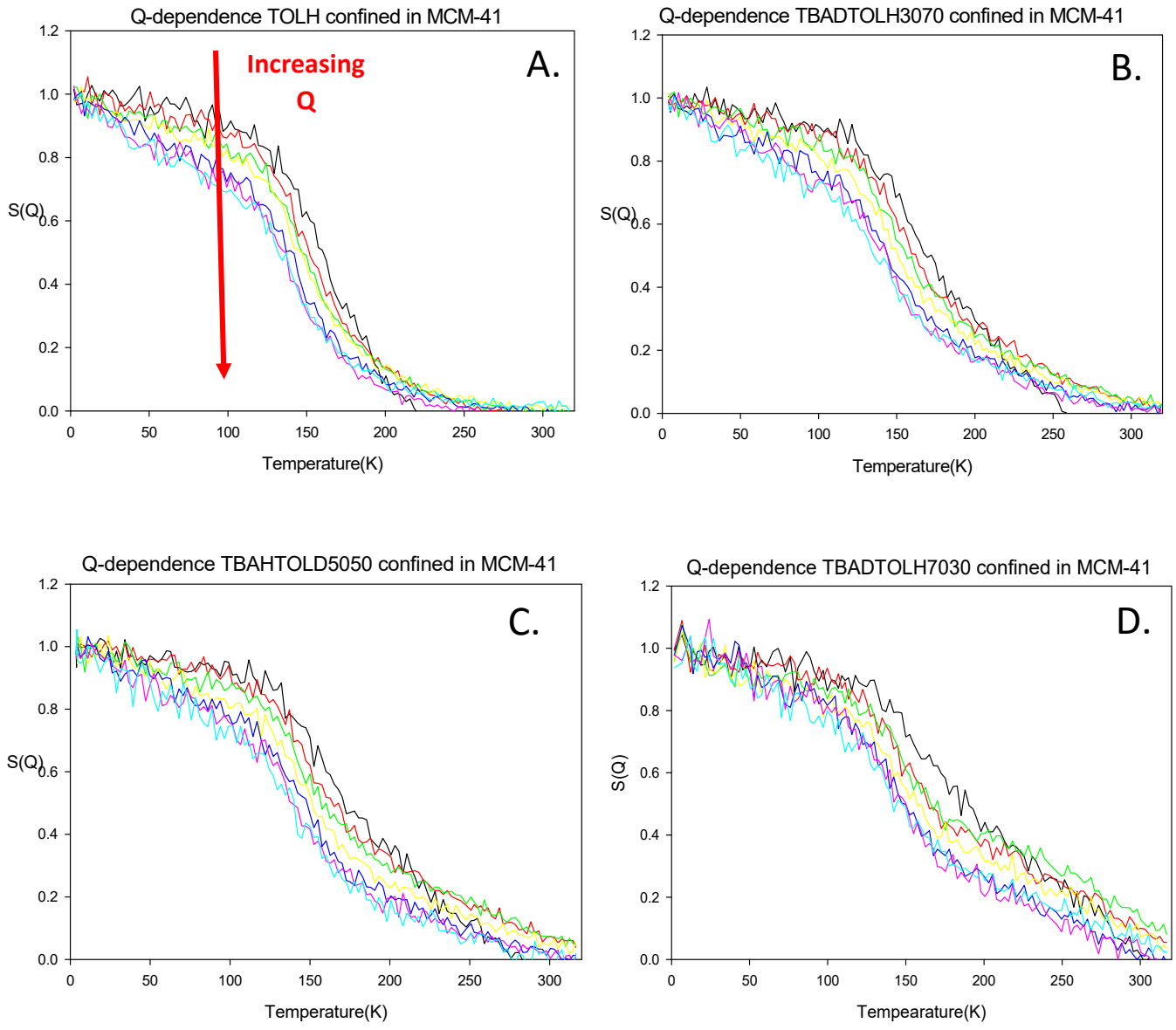


Figure N-4: Q-dependence of the EFWS of TBADTolH mixtures confined in MCM-41, TolH conc. decreases from A to D.

**Abstract:** The objective of this thesis is tuning the formation of ordered supramolecular structures of an H-bonded liquid alcohol, either by dispersion in an aprotic solvent or by confinement in mesoporous silicates (MCM-41 and SBA-15). In the bulk, a strong perturbation from ideal mixing depicted in terms of clustering between similar species is observed by small angle neutron scattering. Under confinement, a remarkable nanosegregation phenomenon of the mixture is observed in the pores, leading to concentric tubular structures of core-shell type, which are striking for macroscopically homogeneous and fully miscible binary systems. The molecular dynamics of these original glassforming nanostructures is studied by quasielastic neutron scattering in the liquid and vitreous states, revealing different types of relaxation modes under confinement with non-trivial concentration dependencies. Isotopic HD labelling of the mixtures components provides a unique comprehensive viewpoint on the properties of these confined binary liquids, establishing a direct correlation between spatially segregated dynamical heterogeneities and the formation of original core shell nanostructures induced by preferential interactions.